The Future of Markets and DERs: Providing Essential Grid Services and Managing Performance Risk

Final Project Report

M-44

Power Systems Engineering Research Center

Empowering Minds to Engineer
the Future Electric Energy System

The Future of Markets and DERs: Providing Essential Grid Services and Managing Performance Risk

Final Project Report

Project Team
Kory W. Hedman, Project Leader
Mojdeh Khorsand
Arizona State University

Shmuel S. Oren
University of California Berkeley

Graduate Students
Trishant Roy
Hari Krishna Achuthan Parthasarathy
Arizona State University

Tomas Valencia Zuluaga
University of California Berkeley

PSERC Publication 25-01

December 2025

For information about this project, contact:

Kory W. Hedman
Arizona State University
School of Electrical. Computer, and Energy Engineering
P.O. Box 875706
Tempe, AZ 85287-5706
Phone: 510-225-5987
Email: khedman@asu.edu

Power Systems Engineering Research Center

The Power Systems Engineering Research Center (PSERC) is a multi-university Center conducting research on challenges facing the electric power industry and educating the next generation of power engineers. More information about PSERC can be found at the Center's website: http://www.pserc.org.

For additional information, contact:

Power Systems Engineering Research Center
Arizona State University
527 Engineering Research Center
Tempe, Arizona 85287-5706
Phone: 480-965-1643
Fax: 480-727-2052

Notice Concerning Copyright Material

Acknowledgements

The authors would like to thank all the industry collaborators: Oluwaseyi Akinbode (MISO), Guillermo Bautista Alderete (CAISO), Sumit Bose (GE), Hong Chen (PJM), Yonghong Chen (MISO), Kwok Cheung (GE), Richard Dillon (SPP), Erik Ela (EPRI), Jesse Gantz, (GE), Anthony Giacomoni (PJM), Bo Gong (SRP) Majid Heidarifar (EPRI), Avnaesh Jayantilal (GE), Akshay Korad (MISO), Sobia Naqvi (APS), Dane Schiro (ISO-NE), Nikita Singhal (EPRI), Yohan Sutjandra (The Energy Authority), Arun Nair (Eaton), Clyde Loutan (CAISO), and Harvey Scribner (SPP).

Executive Summary

FERC Order 2222 mandates incorporation of distributed energy resources (DERs) in wholesale markets. With this new requirement, one main power systems change is the push towards not just DER integration but also the reliance on these resources to be able to provide essential grid services. Electricity markets, grid operations, and reliability requirements are designed for classical assets, not emerging assets with distinct characteristics, i.e., higher probability of failure, lower capacity firmness, and lower impact of failure. This project addresses the concern of DER integration from multiple fronts: a) effective aggregation and management of DERs to ensure their profitability and the quality of services provided by these aggregated resources, b) essential market and operational reform, and c) coordination of transmission and distribution services provided by DERs.

Part I: Intra-day DER Risk Assessment

Driven by climate goals and the transition to cleaner sources of energy, it is evident that the modern electric grid is undergoing a significant transformation in both its generation resource mix and demand-side management. The current reliability practices, however, were designed for classical assets and not fully suited for emerging resources. This part of the work presents intra-day risk assessment frameworks to complement existing practices and support the effective inclusion of DERs in wholesale electricity markets. Suitable decision-making frameworks to model uncertainty, risk, and correlation have been examined from perspective of various stakeholders in the DER management process.

In the first portion of the work, key challenges associated to participation of DERs in wholesale markets has been addressed from the perspective of a profit-maximizing Virtual Power Plant managing an aggregation of solar photovoltaic, electric storage, and residential load resources. It is shown that aggregation of DERs can perform comparably to conventional resources, despite their distinct uncertainty and variability characteristics. To address sequential decision-making under uncertainty, two modeling frameworks are explored: Markov Decision Processes (MDP) and robust optimization using Mixed Integer Linear Programming (MILP). The approaches are modeled to align with existing day-ahead and real-time market operations. While MDP modeling is conceptually consistent with sequential decision-making, it is impractical due to intrinsic assumptions about the system probabilities and computational intractability in VPP decision-making. In contrast, the MILP-based framework aligned with existing steady-state power system practices and demonstrates satisfactory performance. The modeling emphasizes risk preference of aggregators and time frames of rolling forecasts for solar and load resources. Detailed insights about modeling intricacies and associated computational requirements have been analyzed and presented in the report.

In the latter portion, intra-day situational awareness frameworks have been explored. Emerging resources such as behind-the-meter renewables and electric storage resources often lack full controllability and visibility to system operators managing the electric grid. To address this gap, an intra-day lookahead assessment framework is proposed that leverages historical performance of electric storage resources along with weather and price information. The framework predicts future state-of-charge (SOC) level and categorizes it into three zones: *low*, *medium*, and *high*. This

framework is aimed to assist system operators with downstream reserve procurement decisions and ensure reliability in the grid. A data-driven approach is employed to explore three statistical and machine learning models: (i) Seasonal ARIMA with eXogenous parameters (SARIMAX), (ii) Extreme Gradient Boosting (XGBoost), and (iii) Long Short-Term Models (LSTM). Detailed performance evaluation and comparison of the three models are presented.

Part II: DER and Smart Inverter Management for Coordinating Transmission - Distribution Services and Enhancing Distribution System Flexibility

The increasing penetration of residential roof-top photovoltaic (PV) and other Distributed Energy Resource (DER) units causes severe power quality issues including voltage violation and voltage unbalance within the distribution feeder and the transmission system. Legacy VAr devices, which were conventionally used to mitigate voltage violation issues within the distribution feeder, are incapable of providing a solution due to the fast voltage fluctuations caused by inverter-based resources. The sparsity and cost of installation and maintenance of these devices also prevent them from being an effective solution. The swift adoption of Electric Vehicles (EVs) also contributes to voltage unbalance issues, where the rapid change in demand due to multiple charging loads rules out conventional solutions to voltage balancing.

Apart from this, with the introduction of FERC order 2222, the inclusion of DER aggregators in the wholesale markets compounds on the previously mentioned problem, posing a challenge to the safe and reliable operation of the transmission and distribution systems. Due to the active nature of modern distribution systems and modeling complexities, the ISO has no visibility over the DS limits while making decisions on the DER aggregator's energy and ancillary service awards, leading to distribution system violations. Therefore, there is an emerging need for coordinating DER aggregators and transmission-distribution operations.

With the introduction of the IEEE 1547-2018 standards, Smart Inverters (SIs) are enabled to provide reactive power support using four different operational modes and voltage support using one active power operational mode. The fast control action, and the distributed and localized presence of these SIs enable them to provide a solution to all the shortcomings mentioned above. To maximize the efficiency of these SIs to mitigate the issues feeder-wide, an efficient DER scheduling tool is required. The consequent work presented investigates the popularly utilized reactive power and active power operational modes, by creating a DER scheduling tool utilizing a robust Distribution Optimal Power Flow (DOPF) model, the Current Voltage ACOPF (IVACOPF). Furthermore, a comprehensive Unified Mode Selection (UMS) framework is presented to optimally select the mode and set point of operation within the DER scheduling tool to minimize operational cost and mitigate voltage issues. The main objective of this work is to maximize deliverability subject to reliable and nominal distribution system operation.

Learnings from this work are then leveraged in improving distribution system hosting capacity, managing voltage violations and, effectively, improving overall distribution system flexibility. In this work, using statistical information obtained from different distribution system conditions and data-mining algorithms, an ISO-DSO-DERA coordination framework is proposed, which allows DER aggregators to participate in the wholesale electric market, having visibility into the distribution system and considering distribution system limitations. The performance of this

framework is compared with the case where the ISO has no visibility over the distribution system limits while making decisions on the aggregator's energy and ancillary service awards. A detailed unbalanced AC optimal power flow based on IVACOPF model is utilized for emulating DSO-DERAs coordinated operations to manage distribution system limits while considering DERAs promised services to ISO. The effect of VAr support capability of roof-top PV unit SI is evaluated in increasing the distribution system flexibility to improve the deployability of the aggregators promised awards. The VAr capability of PV SIs is based on the IEEE 1547-2018 standard, formulated by mixed-integer linear constraints. An IEEE 118-bus system and unbalanced 240-bus distribution test system are used to compare performance of the different ISO-DSO-DERA coordination architectures and, transmission and distribution management during uncertain events.

Part III: Stable and Fair Uniform Price Allocations of Community Aggregation Gains in Retail Electricity Markets

The research, conducted at UC Berkeley, consists of two distinct works: a) Data-driven sizing of col-located storage for uncertain renewable energy, and b) Stable and fair market design in peer-to-peer electricity markets.

In the first work, a high-level stochastic steady-state model is proposed to analyze the value of co-located energy storage systems for wind power producers that participate in an electricity market through forward contracts and use storage to unlock access to capacity payments. In particular, the goal is to find optimal storage and contract sizing, as well as stationary operating policies for profit maximization in the long run. We propose a Markovian stylized model calibrated to actual wind power production that allows us to obtain limiting distributions of battery storage levels, assess the value of storage size and perform a sensitivity analysis on key parameters such as contract prices, capacity payments and storage efficiency. We develop the case with contracts of constant price, outline how this model can be extended to a variable-price setting and discuss potential challenges in that avenue.

The advent of differentiated prices for consuming (buying) and injecting (selling) electricity at the residential level promotes the emergence of local peer-to-peer electricity markets for prosumers, which can deliver savings to participants as long as an attractive cost sharing mechanism can be designed. Building on cooperative game theory models that have been proposed in the literature, we define the uniform price core, a class of desirable distribution of savings in this context, and prove constructively that it is not empty. We propose the shadow price imputation, a computationally efficient stable uniform price imputation, which we show to be equivalent to a dual imputation in the sense of cooperative linear production games. In the second part of the chapter, we compare the shadow price imputation to other imputations in the uniform price core through the lens of fairness. To overcome the challenge of tractability for larger numbers of participants, we extend an existing sampling methodology and apply it to optimization problems devised to obtain a fair imputation. The long-term incentive implications for different stakeholders, as well as a generalization to a stochastic case where the uncertainty in renewable production and local demand is considered, are also discussed. We present theoretical results and numerical experiments and examples to illustrate our approach.

Project Publications:

[1] T. Roy, A. K. Jana, and K. W. Hedman, "Optimization of Aggregated Energy Resources using Sequential Decision-making," in *2022 North American Power Symposium (NAPS)*, 2022, pp. 1–6. doi: 10.1109/NAPS56150.2022.10012186.

[2] T. Roy and K. W. Hedman, "Risk Quantification with Management of Aggregated Energy Resources," in *2024 IEEE Power & Energy Society General Meeting (PESGM)*, 2024, pp. 1–5. doi: 10.1109/PESGM51994.2024.10689045.

[3] T. Roy and K. W. Hedman, "A Sequential Decision-making Framework for Management of Aggregated Energy Resources," - *Under preparation*.

[4] T. Roy and K. W. Hedman, "Intra-day Lookahead Models for Energy Storage Resources Using Time Series Prediction," - *Under preparation*.

[5] H. K. A. Parthasarathy, Z. Soltani and M. Khorsand, "Operational DER Scheduling Tool for Unbalanced Distribution Systems Considering Watt-VAr Controllers of PV Smart Inverters" 2023 NAPS, NC, USA, pp. 1-6.

[6] H. K. A. Parthasarathy, M. Ghaljehei, Z. Soltani and M. Khorsand, "Qualification and Disqualification of Aggregator's Energy and Ancillary Service Awards in Wholesale Markets", Submitted for review, IEEE Open Access Journal of Power and Energy.

[7] H. K. A. Parthasarathy, Z. Soltani and M. Khorsand, "Unified Mode Selection Framework for Real-Time VAr Optimization Tool in Unbalanced Distribution Systems" , To be submitted.

[8] T. V. Zuluaga and S. S. Oren, "Data-Driven Sizing of Co-Located Storage for Uncertain Renewable Energy," in IEEE Transactions on Energy Markets, Policy and Regulation, vol. 1, no. 4, pp. 348-359, Dec. 2023, doi: 10.1109/TEMPR.2023.3277844.

[9] T. V. Zuluaga and S. S. Oren, "Cost Sharing Mechanism with Statistical Learning for Peer-to-Peer Energy Trading," 2023 IEEE Power & Energy Society General Meeting (PESGM), Orlando, FL, USA, 2023, pp. 1-5, doi: 10.1109/PESGM52003.2023.10253145.

[10] T. V. Zuluaga and S. S. Oren, "Sizing co-located storage for uncertain renewable energy sold through forward contracts," arXiv preprint arXiv:2207.12619, 2022.

Student Theses:

[1] T. V. Zuluaga, "Optimization of electricity systems under uncertainty," Ph.D. dissertation, UC Berkeley, 2024.

[2] H. K. A. Parthasarathy, "A Unified Mode Selection Framework for DER Scheduling Tool Considering Unbalanced Distribution Systems" Order No. 31336937, Arizona State University, United States -- Arizona, 2024. (Student is pursuing a PhD in Power and Energy Systems at Arizona State University)

[3] T. Roy, "Modeling and Characterization of Distributed Energy Resources in Electricity Markets". PhD dissertation. Expected Graduation: 2026.

Part I

Intra-day DER Risk Assessment

Kory W. Hedman
Trishant Roy, Graduate Student

Arizona State University

For information about this project, contact

Kory W. Hedman
Arizona State University
School of Electrical. Computer, and Energy Engineering
P.O. Box 875706
Tempe, AZ 85287-5706
Phone: 510-225-5987
Email: khedman@asu.edu

Power Systems Engineering Research Center

The Power Systems Engineering Research Center (PSERC) is a multi-university Center conducting research on challenges facing the electric power industry and educating the next generation of power engineers. More information about PSERC can be found at the Center's website: http://www.pserc.org.

For additional information, contact:

Power Systems Engineering Research Center
Arizona State University
527 Engineering Research Center
Tempe, Arizona 85287-5706
Phone: 480-965-1643
Fax: 480-727-2052

Notice Concerning Copyright Material

Table of Contents

List of Figures

List of Tables

1. Introduction

In the modern world, electricity is a fundamental necessity in the world, and electric grids are the infrastructure backbone for energy supply [1]. These electric grids have been developing and incorporating the environmental, economic, and technical requirements of society.

In recent times, there has been an increased demand for sustainable energy and efficient use of resources. Hence, distributed energy resources (DERs) will be a significant part of the future electric grid. According to International Energy Agency (IEA), the global renewable resource capacity is expected to rise to over 4800 GW by 2026 - equivalent to the combined current global capacities of fossil fuels and nuclear resources [2]. Other DERs, like demand-side management, standalone storage devices, and electric vehicles, are also gaining popularity for achieving the goal of an efficient electric grid. Hence, future grid operations is a crucial research area for the power engineering community.

One of the primary objectives, operating cost of the electric grid, is largely dependent on the decisions taken by grid operators. These decisions include generator dispatch schedules, procurement of reserves, maintenance scheduling, etc. The grid operators must ensure that electricity is delivered efficiently, reliably, and securely while meeting the energy needs of society at all times. To ensure this, system operators protect the grid against uncertainties such as weather events, equipment failures, cyber-attacks, and other disruptions. Hence, accurate modeling and efficient use of resources are essential for cost-effective grid operations. These can be achieved through effective risk management strategies.

The introductory chapter provides a brief overview of the key topics covered in the report. It introduces a brief background of risk management, reliability modeling, and distributed energy resources and their interdependence with modern electric system operations. The chapter also highlights the main challenges that will be addressed in the report and the expected contributions of the research.

1.1 Background

1.1.1 Conventional Mindset for Managing Risk

From the beginning of human history, our ancestors, i.e., early humans were exposed to various risks [3]. They had to protect themselves against dangerous animals, various diseases, and natural hazards. The ancestral mentality to tackle these challenges was primarily to avoid them. For instance, if there was a wild animal in the vicinity, human would relocate and the community would abandon the whole area. Similarly, the sick individuals were isolated to prevent infection in the rest of the community. These were "risk-averse" strategies, i.e., avoiding potential dangers wherever possible.

The origin of risk management is briefly described in Peter L. Bernstein's book "Against the Gods: The Remarkable Story of Risk" [4]. The author describes how humans questioned that the future does not occur by random events generated by Gods, and how people began to understand risks.

He also argues that the ability to measure and manage risk has been a key driver of economic growth and technological progress, which has enabled human society to overcome many of the challenges and dangers that once seemed insurmountable.

Risk management has evolved, both theoretically and technically, over the years. It is used as a tool to identify, assess, and manage risks in various areas of daily life, and helps to reduce potential financial losses, environmental damage, and human casualties. In modern times, it is widely used in project management, financial applications (e.g., trading, loans, and insurance), and operational problems like electric systems, transportation, manufacturing, etc.

1.1.2 Reliability Modeling in Power Systems: N-1

Electric grids are interconnected networks of transmission lines, connected generators, and loads. Failure of any of these components can restrict energy supply and can also damage other components. Hence, electric grid operators need to consider and model the unplanned interruptions or damages of these components. Similar to our ancestors, engineers in the 19th century developed a risk-averse criteria to protect the electric grid from "beasts" i.e. the outages in the electric network. This criterion was termed as N-1 security. By definition, a system is N-1 secure if it can maintain its normal operations in the event of a single loss of a generator, transmission line, or transformer.

Apart from the ancestral risk preference, there were various technical factors that led to the adoption of N-1. First, traditional power plants have been bulk/large in nature with a low probability of failure. Second, an outage in traditional generators occurs due to faults, which leads to generator getting disconnected from the grid. This leads to complete loss of generation from the generator. Third, the outages of traditional generators are generally uncorrelated. This is because faults in the network are often independent, i.e., one fault does not generally induce another fault at a different location due to existing protection schemes. Due to these reasons, protecting against one outage protects the system against the most probable outage events. Mathematically, if the probability of an outage is 2%, then the probability of two simultaneous outages is 0.04% (i.e., 2% of 2%). However, with the rapid integration of renewable-based technologies and developments in energy management, there are arising challenges in operations of modern electricity grids.

1.1.3 Distributed Energy Resources

Distributed Energy Resources (DERs) present various operational challenges for modern electric grids. Fossil fuels like coal and natural gas have been the conventional sources of generating electricity since the 19th century. As the world shifts towards more sustainable and clean energy sources to conserve natural resources and reduce the carbon footprint, the same is reflected in electrical power systems. Examples of clear energy sources include solar, wind, biomass, hydroelectric, etc. While the pros of using renewable and sustainable energy sources outweigh the cons, it poses some technical and financial challenges to the electrical power grid. Technologies like battery storage and demand-side management are also developing to support the electric grid. These technologies help the grid by shifting the demand profile, reducing the peak demand, and providing emergency services. Figure 1.1 depicts the conventional resources like coal power

plants, natural gas plants, and diesel generators, and newer technologies like electric vehicles, solar PV, wind, demand response, etc.

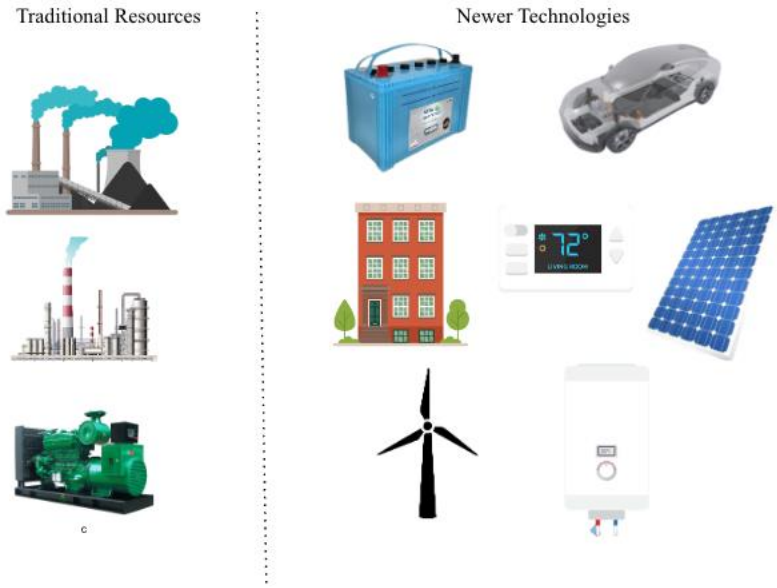

Figure 1.1 Resources integrated in modern electricity grids

1.1.3.1 Fundamental Challenges

One of the main challenges in including renewable energy sources in the power grid is the uncertainty associated with the energy source itself. The inability to forecast the energy accurately makes the system stochastic. For example, solar energy, the renewable source considered in the current work, has two kinds of variability associated with the sunshine - predictable and stochastic variability [5]. The sunrise and sunset times in an area can be predicted accurately. Similarly, we can also predict that the sunshine hours in the winter will be less than in summer. These come under predictable variability. On the other hand, on a cloudy day, it is challenging to predict the sunshine even within an hour. This comes under the category of stochastic variability, i.e., uncertainty. We are mainly concerned with the stochastic variability because if we connect the solar energy source to the grid directly as per the predicted sunshine values, and there is a significant deviation of the actual sunshine from the predicted value, this will create a supply-demand gap in the system. The consequences could go both ways - one, if the actual solar power generated is less than the predicted value, there will be a shortage in supply while the demand will be high. To balance the system, load shedding will happen, leading to a loss of customer trust in the utility. The possible scenario is when the actual solar power generated is more than the predicted solar power; this means excess power is pushed into the grid, which may result in grid instabilities (like line overflows). As we understand, the consequences can be both financial and technical, so a mechanism is needed to mitigate these concerns.

Moreover, traditional energy sources like coal and natural gas plants have a firm capacity and are fully dispatchable. On the hand, renewable sources are non/semi-firm and semi-dispatchable. This is due to the variable nature of renewables. Also, there is limited visibility and control for distribution utilities and system operators, especially for the renewable resources owned by

residential or commercial customers. These limitations pose concerns related to reliability in the integration of renewables in power system operations.

Other distributed energy resources like demand response, storage, electric vehicles, etc. also have the fundamental problems of stochastic variability, limited visibility and control. It is challenging to predict the behavior for human-in-the-loop resources like demand response and electric vehicles. For these resources, modeling either variability, predictable or stochastic, is challenging since they are primarily dependent on user preferences. This lack of knowledge limits their usage, especially during emergency operations. Aggregation of these resources can help in better management and increase in reliability for the system.

1.2 Challenges with N-1 and Need for Better Risk Management

The N-1 security criterion is a modeling technique that has ensured sufficient reliability for decades. The simplicity of the criteria in managing the operations despite unforeseen failures is remarkable. Similar to transmission lines and traditional generators, N-1 can accurately model the complete failure of an aggregator - for instance, due to an electrical fault leading to disconnection of the aggregator. N-1 can also model outages in DERs that are independent of one another. For example, a large solar PV plant's generation is independent of aggregated wind plants.

However, the assumptions due to which N-1 sufficed are not valid anymore with the introduction of newer technologies. An outage in traditional generators leads to a complete loss of generation from the generator. However, there is generally a partial loss of generation in the case of DERs due to unknown or unforeseen events. Moreover, the probability of failure is not insignificant due to the intrinsic dependence on the environment and user preference. Also, there is a correlation of outputs between DERs. For example, a decrease in the generation of a solar plant would likely lead to a decrease in nearby solar plants. Correlation between different types of assets, like storage and renewables, is also possible. The difference is illustrated in the figure below, where three key characteristics: probability of failure, impact of failure, and correlation with other assets are modeled for DERs and the scope of N-1 criteria. We observe that DERs are high-probability, high-correlation-type resources, whereas N-1 can only accurately model low-probability, low-correlation resources.

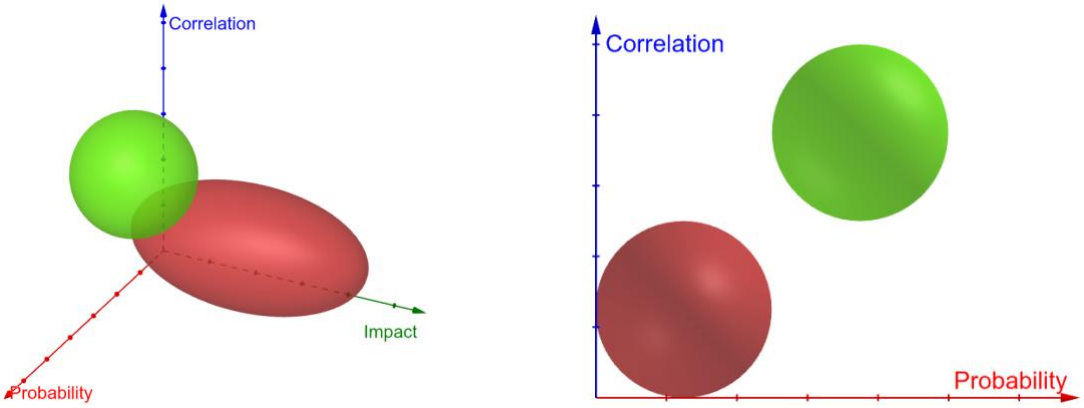

Figure 1.2 Illustration of operational characteristics modeled by N-1 (red) and of DERs (green) (i) Orthographic projection (ii) Planar depiction

The differences between DERs and traditional generators are further highlighted in Table 1.1. There are other unknown events, like deviation due to weather events, changes in user behavior, etc., for which N-1 was not designed. Moreover, additional modeling considerations, including dependence on weather, user preferences, and correlation with other assets, are required to reliably and efficiently operate DERs. In conclusion, although N-1 can model unplanned failures in conventional generators, it is insufficient to model DERs. Therefore, proper risk management and reliability criteria are required to ensure energy security and efficient economics of the electric grid. Also, there is a need to develop reasonable models to characterize the dependencies and correlations mentioned earlier.

Table 1.1 Modeling of various events/features using N-1 criterion for different assets

Assets	Characteristics	Events/features not modeling in N-1	Degree of match with N-1
Conventional Generators	Firm capacity, dispatchable, controllable	Probabilistic nature of failures	High
Renewables	Intermittent, non-dispatchable, uncertain	Weather events, correlation with other assets	Medium
Energy Storage	Controllable	Charging behavior, correlation with other assets	Low
Electric Vehicles	Non-firm, uncertain, mobile, user dependent	Charging/user behavior, correlation with other assets	Low
Demand-side Management	Semi/non-controllable, user dependent	User behavior, correlation with other assets	Low

1.3 Report Organization

The organization of the remaining report is as follows:

- Chapters 2 and 3 address the inclusion of DERs from an aggregator/Virtual Power Plant perspective. Two popular and effective modeling frameworks, namely, Markov Decision Processes and Mixed-Integer Linear Programming, have been explored.
- Consequently, Chapter 4 address operational challenges from the system operator's perspective. It presents intra-day lookahead models to predict and assess future storage level of electric storage models in the electric network.
- Chapter **Error! Reference source not found.** summarizes the various methodologies and the key findings of the report.

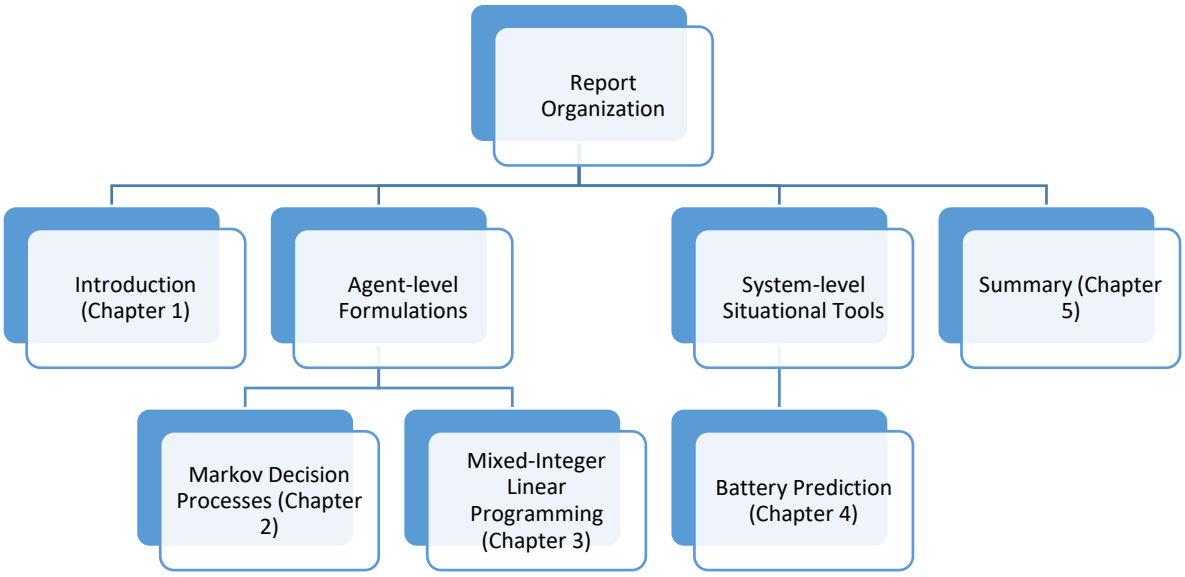

Figure 1.3 Overview of the report organization

2. Agent-Level Decision-Making using Markov Decision Processes

In this chapter, a decision-making strategy is formulated for aggregators with multiple resources such as solar PV, battery, and demand. This chapter presents our first approach in developing a suitable decision-making framework for DER aggregators. The problem is analogous to decision-making by an aggregator in the real-time stage of wholesale electricity markets, i.e., it bids in the real-time market to procure/sell the deficit/excess energy after accounting for the expected net demand and bid from the day-ahead market.

A Markov Decision Process (MDP) model is used to describe the aggregated system, including defining the objective function, state variables, action variables, transition probabilities, and constraints for the problem. Two sequential decision-making algorithms, dynamic programming and Q-learning, are then implemented and compared for deterministic and stochastic case studies.

The aggregation management problem can be related to other real-world problems, and we look to leverage prior efforts to develop a decision-making approach. On the one hand, some research works have used the reinforcement learning approach to solve problems such as strategy optimization in algorithmic trading [6], cost optimization in stochastic shortest-path problems [7] and net power-bill optimization for residential households [8]. On the other hand, there is another set of research works, [9], [10], [11], [12], [13], [14], which have tried to solve similar energy storage capacity problems with dynamic programming. Motivated by both categories of past research, our work focuses on using two state-of-the-art techniques - dynamic programming (DP) and reinforcement learning to solve the aggregated resource management problem. We have used dynamic programming [15], [16], [17] and Q-learning [15], [18], [19], [20] approaches in this chapter and compared their performance.

In the further sections, more details about the implementation and performance of the algorithms are presented. Section 2.1 presents the mathematical modeling of the system. The methodologies and algorithms implemented to determine a suitable policy are presented in Section 2.2. The case studies and their results are discussed in Section 2.3 and summarized in Section 2.4.

2.1 Mathematical Model of the System

The decision-making framework is formulated as a Markov Decision Process (MDP) in this work. The framework is motivated by [21]. Let the length of the time horizon be T, i.e., the time horizon is from $t = 1$ to $t = T$. Let R_t, E_t, D_t, and P_t denote the battery level, solar generation, total demand, and electricity price respectively at time t.

The battery parameters considered in the model are: (i) battery capacity (R_{max}), (ii) maximum charging and discharging rate (γ^c, γ^d), (iii) charging and discharging efficiency (β^c, β^d).

2.1.1 State and Action Variables

The state variable consists of the battery level (R_t), solar generation (E_t), total demand (D_t), and electricity price (P_t), i.e.,

$$S_t = (R_t, E_t^S, D_t^S, P_t^S) \tag{2.1}$$

Among these, the solar generation, total demand, and electricity price are stochastic in nature and independent of the action chosen by the utility.

The action/decision variable is the set of the various possible interactions between resources in the system. The interactions considered in this work are depicted in Figure 2.1.

$$x_t = \left(x_t^{sd}, x_t^{gd}, x_t^{rd}, x_t^{sr}, x_t^{gr}, x_t^{rg}, x_t^{sg}\right) \geq 0 \tag{2.2}$$

Please note that the formulation presented in [21] did not consider the solar to grid interaction (x_t^{sg}) in the action variables. The effect on the total profit of considering x_t^{sg} is presented through case studies in Section 2.3.

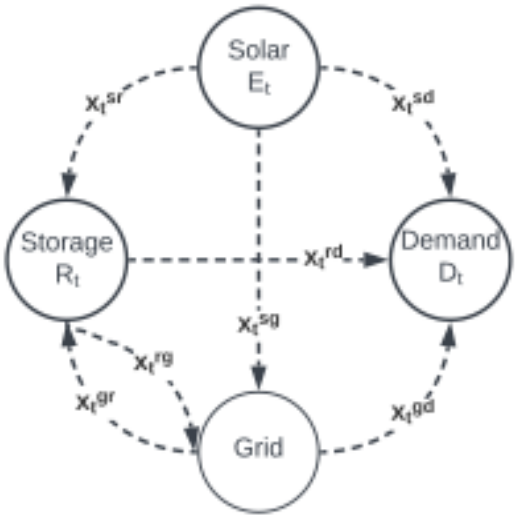

Figure 2.1 Action variables considered in the formulation

The next state of the battery from battery state, R_t, and action, x_t, is:

$$R_{t+1} = R_t + \beta^c\left(x_t^{gr} + x_t^{sr}\right) - x_t^{rg} - x_t^{rd} \tag{2.3}$$

2.1.2 Constraints

The feasible action space, $X_t(S_t)$, for any state S_t is found through the constraints presented below. The cumulative energy transfer from solar, battery and grid to the load will be used to satisfy the demand. Hence,

$$x_t^{sd} + \beta^d x_t^{rd} + x_t^{gd} = D_t \tag{2.4}$$

Since the battery cannot dispatch more than its current level, the exchange of battery to demand and battery to grid variables are constrained.

$$x_t^{rd} + x_t^{rg} \leq R_t \tag{2.5}$$

Also, since the battery cannot be charged more than its rated value, the energy flowing to the battery is constrained.

$$x_t^{sr} + x_t^{gr} \leq R_{max} - R_t \tag{2.6}$$

Balancing the energy from solar generation,

$$x_t^{sr} + x_t^{sd} + x_t^{sg} = E_t \tag{2.7}$$

Maximum charging and discharging power limits are also considered as follows:

$$x_t^{sr} + x_t^{gr} \leq \gamma^c \tag{2.8}$$

$$x_t^{rd} + x_t^{rg} \leq \gamma^d \tag{2.9}$$

2.1.3 Objective Function

The profit when action x_t is chosen at state S_t is given by:

$$r(S_t, x_t) = P_t\left(D_t + \beta^d x_t^{rg} - x_t^{gr} - x_t^{gd}\right) \tag{2.10}$$

Overall, the goal of the utility is to find the optimal policy (μ) to maximize its total profit

$$V_\mu(s) = \max_{\mu \mathrm{E}_\mu} \left[\sum_{t=1}^{T-1} r\left(S_t, \mu_t(S_t)\right)\right] \tag{2.11}$$

Hence, the resulting problem is of the undiscounted finite horizon type and a non-stationary (i.e. time dependent: $\mu = (\mu_1, \ldots, \mu_{T-1})$) policy is required for this problem.

Given the sequential nature of the problem, dynamic programming and Q-learning (a reinforcement learning strategy) are tested and analyzed.

2.2 Methodologies/Algorithms

2.2.1 Dynamic Programming

Dynamic programming is a powerful method to determine the optimal policy for a Markov Decision Process. It divides the problem (2.11) into several one-stage sub-problems [22].

Let's define a value function, $V_t(S_t)$, to denote the expected profit for the utility starting from state S_t and time t. According to the Bellman equation:

$$V_t(S_t) = \max_{x_t \in \mathrm{X}_t(S_t)} \left(r(S_t, x_t) + E\left[V_{t+1}\left(f(S_t, x_t)\right)\right]\right) \tag{2.12}$$

where $r(S_t, x_t)$ is the profit of the utility when action x_t is applied at state S_t, and $S_{t+1} = f(S_t, x_t)$. Starting from the last time period, the Bellman equation is used to iteratively evaluate the value function for all states and all time periods.

The algorithm is summarized in Algorithm 1. The $next\_value$ (defined in line 7, equal to $E\left[V_{t+1}\left(f(S_t, x_t)\right)\right]$) is calculated as follows:

$$next\_value = \sum_{S_{t+1} \in S} p(S_{t+1}|S_t, x_t) \cdot V_{t+1}(S_{t+1}) \tag{2.13}$$

where $p(S_{t+1}|S_t, x_t)$ is the transition probability of reaching state S_{t+1} when current state, S_t, and action x_t are given.

Algorithm 1: Dynamic Programming

Result: Returns policy $\mu = (\mu_1, \ldots, \mu_{T-1})$ and value function $V_t(S_t)\ \forall t, S_t \in S$.
Given: r: function to calculate profit
f: function to calculate next state

1. Initialize: $V_T(S_T) \leftarrow 0 \quad \forall\, S_T$

2. **for** $t = T - 1$ to 1 do
3. **for** S_t in S do
4. *action_space* ← *get_action_space*(S_t)
5. *best_value* ← $-\infty$
6. for *action* in *action_space* do
7. *next_value* ← *get_next_value*(S_t, *action*)
8. if *best_value* < *r*(S_t, *action*) + *next_value* then
9. *best_value* ← *r*(S_t, *action*) + *next_value*
10. *best_action* ← *action*
11. **end**
12. **end**
13. $V_t(S_t)$ ← *best_value*
14. $\mu_t(S_t)$ ← *best_action*
15. **end**
16. **end**

2.2.2 Q-learning

A property of Q-learning over dynamic programming is that it does not require the information of state transition probabilities. This is an advantage since, in many applications, this information may not be available or may not be accurate. Moreover, different stakeholders may consider different values in applications where the costs and profits are associated with the probability metrics.

The Q-learning algorithm has been summarized in Algorithm 2. The main principle of the strategy is that Q-factors for all state-action pairs are updated through a series of runs on the system. The update uses previous Q-values, current profit, and the best Q-value of the next state (line 9).

A trade-off between exploration and exploitation is present in this strategy. The ε-greedy approach [23] has been used to choose the actions. First, a random number between 0 and 1 is generated. If

the random number is less than a pre-defined threshold (ε), the best action using the current Q-values is chosen. Else, a random action is chosen. Mathematically,

$$x_t = \begin{cases} \underset{x}{arg\,max}\, Q\,(S_t, x), & if\ random\ number < \varepsilon \\ choose\ random\ action, & else. \end{cases} \tag{2.14}$$

Algorithm 2: Q-learning

Result: Returns Q-values, $Q_t(S_t, x_t)\ \forall t, S_t \in \mathrm{S}, x_t$.

Given: numEpisodes, batt_start_state

Initialize: $Q_t(S_t, x_t)$, $NCount_t(S_t, x_t) \leftarrow 0 \quad \forall S_T, x_T \in \mathrm{X}_T(S_T)$

for $episode$ in $1, \ldots, numEpisodes$ **do**

    $S_1 \leftarrow batt\_start\_state$

    for $t = 1\ to\ T-1$ **do**

        action $\leftarrow \epsilon$-greedy_approach(S_t)

        apply action: get reward, $r(S_t, x_t)$ and next state, S_{t+1}

        $NCount_t(S_t, x_t) \leftarrow NCount_t(S_t, x_t) + 1$

        $Q_t(S_t, x_t) \leftarrow Q_t(S_t, x_t) + \left\{r(S_t, x_t) + Q_t(S_t, next\_best\_action) - \frac{Q_t(S_t, x_t)}{NCount_t(S_t, x_t)}\right\}$

    end

end

2.3 Case Studies and Results

The scenarios used in the case studies are summarized in Table 2.1. D1 is a deterministic scenario where the solar generation and price generation are known apriori. Two stochastic scenarios, S1 and S2, are also considered where the solar generation and electricity prices are non-deterministic. The range and step size of the data are also tabulated in the table. The charging and discharging efficiencies of the battery are assumed to be 90%, and the maximum power charge/discharge is assumed as 20 units.

Table 2.1 Scenarios considered in this work

Scenario	Battery energy		Solar generation		Electricity price	
	Range	Step-size	Range	Step-size	Range	Step-size
D1	0-10	1	-	-	-	-
S1	0-10	5	3-7	2	30-70	20
S2	0-30	5	1-7	1	30-70	4

Without loss of generality, the demand is assumed to be deterministic in the analysis. It is considered to be sinusoidal, and the variation is given by:

$$D_t = \max\left\{0{,}3 - 4\sin\left(\frac{2\pi}{T}(t-1)\right)\right\} \tag{2.15}$$

2.3.1 Deterministic Scenario

The motivation for analyzing the deterministic scenario is two-fold: first, to compare the results with/without solar to grid energy transfer (x_t^{sg}), and second, to analyze the results of dynamic programming in a deterministic scenario. The data considered in the scenario is tabulated in Table 2.2.

Table 2.2 Data for scenario D1

Time	Solar generation (units)	Total demand (units)	Electricity price ($/unit)
1	5.0	3.00	30
2	2.0	0	50
3	6.0	0.65	38
4	1.0	5.35	70
5	3.0	6.80	42

On implementing the dynamic programming approach, the total profit obtained when x_t^{sg} is not considered is \$1020.11 whereas it is \$1039.11 when x_t^{sg} is included in the action variables. Hence, the total profit is higher when the solar to grid energy transfer is considered.

Figure 2.2 depicts the actions using the policy from dynamic programming. Few observations from the actions:

- The battery gets fully charged at $t = 1$ and $t = 3$ and then fully discharged at $t = 2$ and $t = 4$. This is expected because the electricity price at $t = 1$ and $t = 3$ are lower than at $t = 2$ and $t = 4$ respectively. Therefore, the decision-making algorithm suggests these actions in order to maximize the total profit.
- In the case of Figure 2.2 (a), the solar generation is transferred to the grid through the battery, which introduces energy losses due to battery efficiencies of less than 1. Hence, the total profit is higher when x_t^{sg} is considered since it allows energy to be directly transferred from solar generation to the grid.
- The battery completing discharges itself in the last stage in order to maximize the profit. End conditions can be added to the battery stage (like the battery should end with the same state as the initial state) by modifying the terminal costs, $V_T(S_T)$.

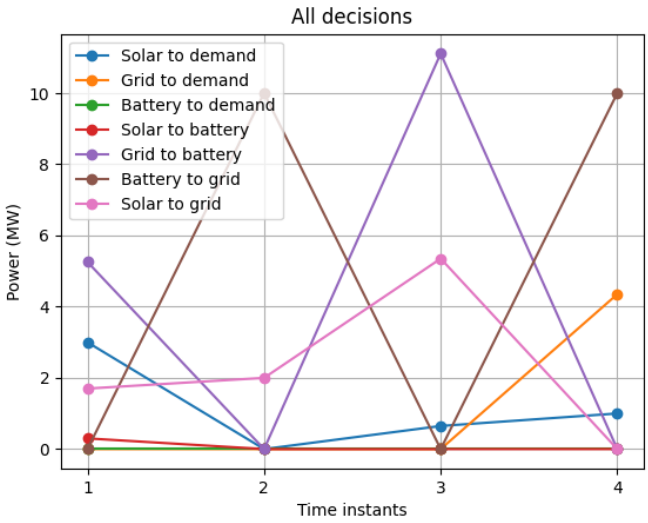

(a) Without solar-to-grid (x_t^{sg}) transfer variable

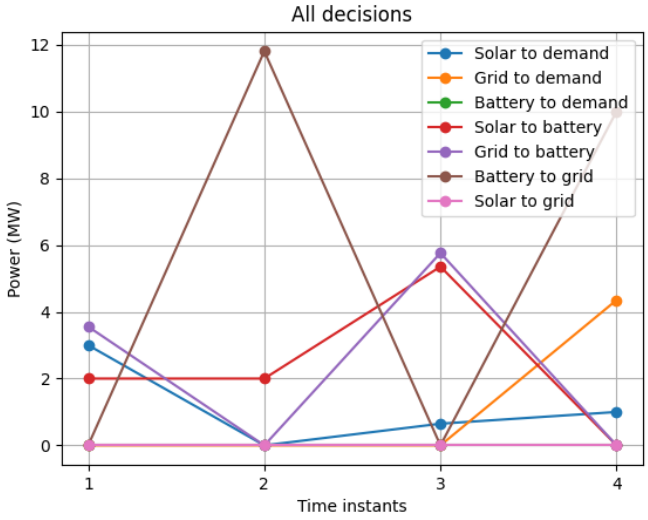

(b) With solar-to-grid transfer variable

Figure 2.2 Comparison of dynamic programming results for scenario D1

2.3.2 Performance of DP in Stochastic Scenarios

The dynamic programming algorithm presented above was tested for stochastic scenarios, S1 and S2. The computation time and expected profit results are summarized in Table 2.3. As expected, the computation time increases significantly with increase in states in the scenario.

Table 2.3 Performance of dynamic programming on stochastic scenarios

Scenario	Computation time (secs)	Expected profit ($)

S1 S2	0.11 26.95	1373.33 1701.58

2.3.3 Performance of Q-learning in Stochastic Scenarios

The results of the Q-learning algorithm presented in Algorithm 2 are analyzed in this section.

2.3.3.1 Dependence on ϵ

First, the dependence on the parameter ϵ in the ϵ -greedy approach is analyzed. Figure 2.3 depicts the variation of the expected profit over episodes when ϵ is varied from 0.1 to 0.9. Scenario S1 is used in this case study.

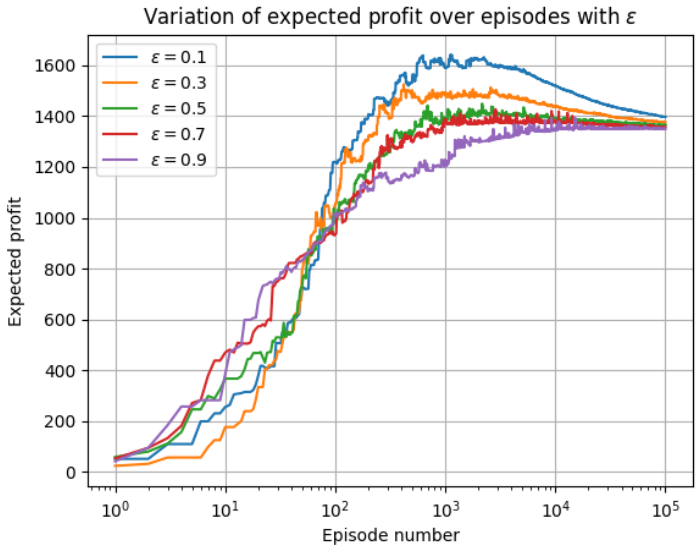

Figure 2.3 Dependence of ϵ on convergence

The best performance in terms of convergence was observed for the ϵ range of 0.5-0.7. The ϵ-values less than 0.5 result in overshoots due to a higher tendency of exploration over exploitation. The ϵ-values greater than 0.7 put more preference for exploitation and thereby, take more episodes to reach the maximum profit. In the subsequent case studies, $\epsilon = 0.6$ is chosen.

2.3.3.2 Stochastic scenarios

The evolution of the expected profit with increase in episodes is depicted in Figure 2.4. This confirms that the policy from Q-learning is improving, and the system is learning the optimal policy over time. It takes about 3000 episodes for the policy in scenario S1 to converge, whereas it takes about 10^5 episodes in the case of scenario S2. The computation time and expected profit on implementing the Q-learning approach are summarized in Table 2.4. As expected, the total

computation time increases with increase in the scenario complexity. Also, there is an increase of computation time per episode (~10 times) due to more state-action pairs.

Table 2.4 Performance of Q-learning on stochastic scenarios

Scenario	Number of episodes simulated	Computation time (secs)	Expected profit
S1	10^4	3.42	1369.81
S2	10^5	356.38	1763.10

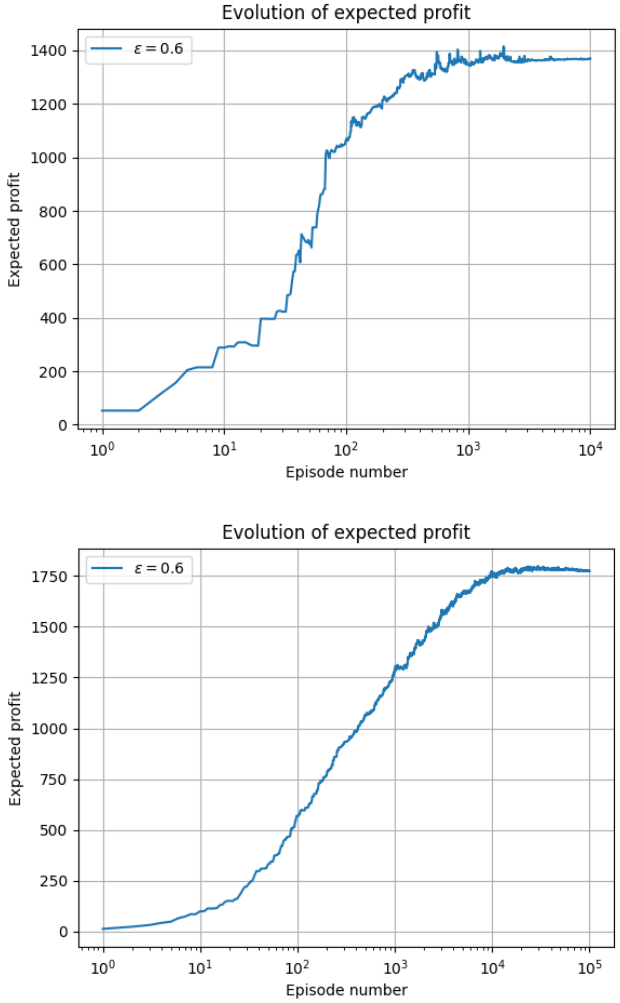

Figure 2.4 Evolution of expected profit with increase in episodes in scenarios 1 (top) and 2 (bottom)

2.3.4 Comparison of Algorithms in Various Scenarios

In this section, the policies derived from Q-learning are compared with dynamic programming on both scenarios (S1, S2). 10000 sets of stochastic data (solar generation, electricity price) were

generated and total profit on implementing the two policies was recorded for each set. The total profits in the first 100 runs for both scenarios are depicted in Figure 2.5. We observe that the profits from Q-learning policy are same or only slightly less than the policy from dynamic programming. This is a promising result since it shows that Q-learning can perform at par with dynamic programming for the aggregated resource management problem, not only in an average sense but also in individual cases or scenarios.

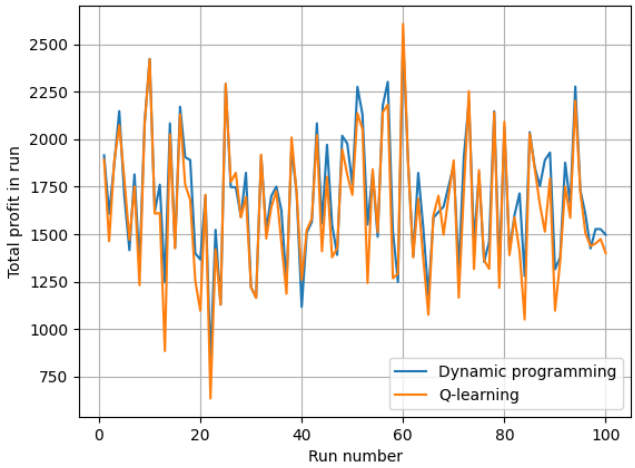

(a) Scenario S1

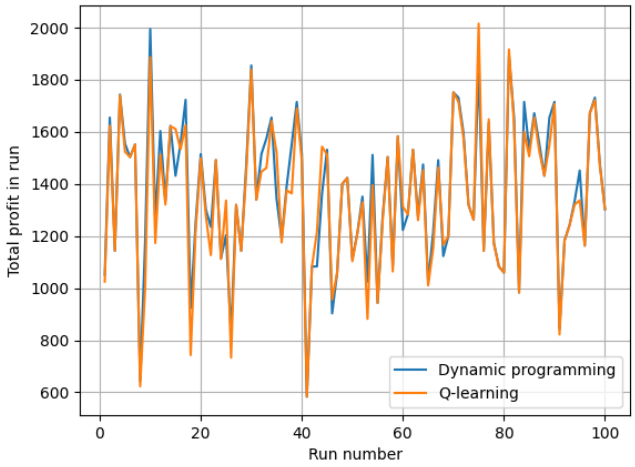

(b) Scenario S2

Figure 2.5 Comparison of policies from dynamic programming and Q-learning for various runs/cases

A metric, optimality %, is defined to assess the performance of Q-learning as compared to dynamic programming. The actual profits from implementing the two policies are used to calculate this metric.

$$\text{Optimality } \% = \frac{\text{Actual profit (average) using Q-learning}}{\text{Actual profit (average) using DP}} \cdot 100$$

The average of total profit across all runs are tabulated in Table 2.5. Similar to the previous result, the average profit from Q-learning policy is quite close to dynamic programming's.

Table 2.5 Comparison of performances of policies from dynamic programming and Q-learning

Scenario	Dynamic Programming		Q-learning		Optimality %
	Expected profit (offline training)	Actual profit (average)	Expected profit (offline training)	Actual profit (average)	
S1	1373.33	1370.32	1369.81	1353.71	98.79
S2	1701.58	1700.74	1763.10	1650.61	97.05

2.4 Conclusion

In this work, two sequential decision-making formulations, namely dynamic programming and Q-learning, were analyzed for the aggregated resource management problem. The observations are summarized below:

- While we know and observe that the dynamic programming approach takes less time to develop a decision-making strategy, we may not have any or have inaccurate transition probability metrics in practical scenarios. Q-learning, a model-free approach, outweighs dynamic programming in such scenarios. Our results show that Q-learning can perform almost as well as dynamic programming in both simple and slightly complicated scenarios. The optimality metric observed for both the scenarios came out to be more than 97%, which shows that the relative accuracy of the Q-learning algorithm compared to dynamic programming for this problem is considerably high.
- An independent analysis of the Q-learning algorithm has also been presented. The variation of expected reward over the number of episodes was depicted. Further analysis showed ϵ's (a user-defined threshold) sensitivity on the number of episodes required to converge to a policy. We observed that ϵ values in the 0.5-0.7 range took 10^3 episodes to converge, whereas $\epsilon = 0.3$ and $\epsilon = 0.9$ took a higher order of episodes ($> 10^5$ and 5×10^4 episodes respectively to converge). Hence, choosing the proper ϵ is essential to reduce the computation time.
- An improved modeling approach over [21] was presented. We observed an improved total profit of the utility with the inclusion of the solar to grid transfer variable, x_{sg}, in the set of actions.

Both dynamic programming and Q-learning have advantages and disadvantages for the aggregated resource management problem. However, given the transition probability requirement in dynamic programming, it is the less preferred approach. Q-learning does well to match the performance in terms of obtaining the optimal policy and profits for the utility. Future work is required to reduce the computation time of the Q-learning approach. Moreover, both approaches use a list of discrete states instead of continuous states, i.e., if the battery energy state space consists of all multiple of 10 from 0 to 100%, the formulations failed to represent the other battery energy values (e.g., 73%). Both these issues of computation and modeling of continuous variables are addressed in the subsequent work.

3. A Sequential Decision-making Framework for Aggregated Energy Resources

3.1 Introduction

In the United States (U.S.), it is projected that solar resource contribution will grow by 75% from 163 million MWh in 2023 to 286 million MWh to 2025. Similarly, wind resources are envisioned to increase by 11% from 430 million MWh to 476 million MWh over the same period [24]. By 2030, DERs could account for up to 30% of total U.S. electricity capacity, driven by solar, wind, and storage integration [25]. Hence, it is apparent that the resource mix in modern electric grids is shifting from conventional resources that are fully controllable and dispatchable to newer resources that are semi/non-dispatchable and semi/non-controllable.

This paradigm shift presents several operational challenges for the stakeholders involved in managing the electric grid. A key challenge is maintaining reliability as the power generation/consumption of DERs is uncertain and intermittent. This can especially be attributed to renewable sources of energy. Resources such as solar and wind are weather dependent, and their generation is influenced by various factors such as time of day, temperature, and cloud cover. Similarly, demand-side management (through load shifting, peak shaving, and other demand response programs) is dependent on consumer preference and/or consumer interference. Another operational challenge associated with DERs is the lack of visibility on the millions of small-scale resources that are integrated into the electric network. Without visibility on individual/behind-the-meter DERs, it is challenging for system operators to ascertain the future generation/consumption capacity of DERs. Similarly, the lack of control for system operators also poses a barrier to the inclusion of DERs in electric grids. All the aforementioned challenges hinder efficient utilization of DERs.

A practical and popular approach to manage multiple DERs is to aggregate the resources and participate in energy markets as a single entity. There are multiple benefits of DERs participating through a "smart aggregator" (entity/company managing the network of resources effectively). First, the concerns of visibility and controllability for system operators is addressed since the aggregator acts as the middleman between the system operator and the network of DERs. The aggregator is further responsible for individual management of resources. Second, aggregation enables leveraging diversity across multiple DERs to improve management of uncertainty. Third, coordinated aggregation of heterogeneous resources can lead to enhanced flexibility and lower curtailments. For example: electric/thermal storage resources can be utilized to compensate for renewable resources (solar PV, wind, etc.) in the network.

While aggregation of DERs can address the problems of visibility and controllability, the effective management of intermittency and uncertainty is still a challenge for an aggregator. Moreover, the challenge is not limited to a single stage. At various time stages during operation, updated information about future consumption/generation profiles will be available and the aggregator will need to make resource management decisions. Figure 3.1 illustrates a temporal progression of uncertainty during the day of operation.

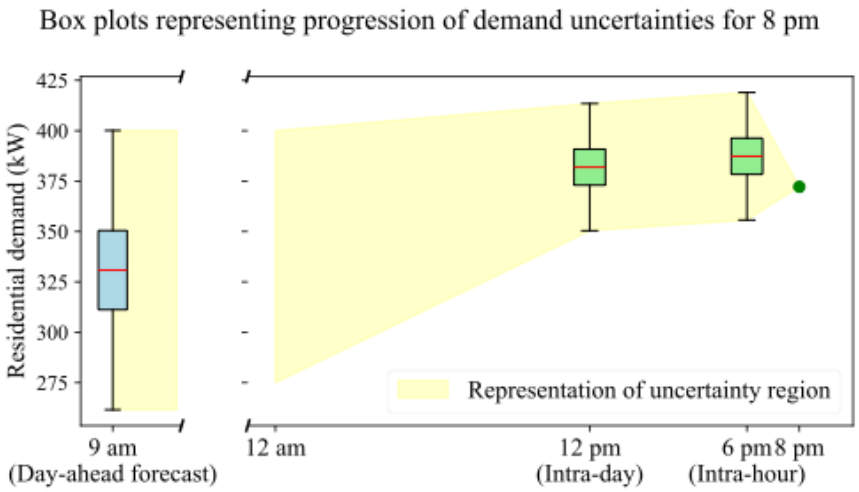

Figure 3.1 Progression of demand uncertainties over different time frames (day-ahead, intra-day, intra-hour) for the operating period starting at 8 pm.

The goal of this chapter is to propose and analyze a sequential decision-making framework for an aggregator managing multiple DERs and participating in energy markets. Furthermore, the emphasis is on the management of intermittency and uncertainty associated to DERs and real-world considerations for an aggregator implementing the decision-making framework.

3.1.1 Literature Survey

The research literature has a plethora of works on bidding and management of DER aggregators, especially over the last decade. The earliest papers on aggregator decision-making were based on deterministic formulations with suitable assumptions about the resource profiles [26], [27], [28]. However, inclusion of weather and consumer behavior introduces uncertainties that need to be considered and modeled by an aggregator for efficient utilization of resources.

To model the uncertainties, multiple stochastic frameworks, namely, dynamic programming [29], [30], alternating direction method of multipliers [31], mixed-integer linear programming [32], [33], [34], machine learning [35], and heuristics [36], have been proposed in literature. Among all proposed frameworks, linear programming (LP) and mixed integer linear programming (MILP) has been the most popular, given its established acceptance in other power systems operations applications like security-constrained unit commitment, transmission expansion planning, and electricity market operations.

Table 3.1 summarizes previous research on LP and MILP formulations for aggregator decision-making. The prior papers are categorized by various modeling considerations and conducted analysis. As observed, most of the previous works (except [37], [38], [39]) focus on a single stage, the day-ahead market (DAM). While most of the schedules are cleared in the DAM, it is important to consider subsequent decision-making stages (i.e., the real-time markets (RTMs)), especially in the context of DERs. As DERs are weather and consumer-dependent, better forecast information is available closer to the actual time of operation. Hence, it is essential to consider additional decision-making stages.

Additionally, an important aspect in real-world aggregator decision-making approaches is the consideration of risks or tradeoffs. Like many decision-making entities, aggregators face tradeoffs between different objectives in their process. For aggregators, the primary tradeoff is between the profitability and the possibility of defaulting on their operational obligation. For example, an aggregator can oversell power if it didn't consider a less probable future scenario of lower net generation. Approaches based on present value-at-risk (VaR) and/or conditional-value-at-risk (CVaR) [33], [40], [41], have been popular to quantify the operational default risks of an aggregator. However, the prior research does not analyze the recourse/reevaluation decisions after the uncertainties are realized.

This chapter proposes an aggregator decision-making framework for participating in energy markets. This chapter includes comprehensive details about the decision-making framework and additional modeling considerations. These details and modeling improvements have been discussed in Sections 3.1.2 and 3.2 of the chapter.

Also, as highlighted in Table 3.1, while there are multiple papers in literature on the management of distributed energy resources using LPs/MILPs, most of them do not analyze the computation needs and none of them delve into the availability of forecast information from a practical perspective. From an aggregator's perspective, it is important to judiciously utilize their decision-making infrastructure. This presents a need for an in-depth analysis of various tradeoffs and factors in the decision-making process.

Table 3.1 Comparison of modeling and analysis insights across papers for aggregator decision-making

Ref.	Modeling/Algorithm				Analysis and Insights		
	Resources considered	Consideration of both day-ahead and real-time markets	Modeling of uncertainty of resources	Modeling of risk levels for aggregators	Effect of different risk parameters	Effect of forecasting variations	Analysis of computational bottlenecks
[37]	Electric vehicles	Yes	Yes	No	-	No	No
[42]	Demand response, wind, fuel cells, diesel generators	No	Yes	Yes	Yes	No	No
[38]	Solar, wind, storage, combined heat and power, load	Yes	Yes	No	-	No	No
[43]	Electric vehicles	No	Yes	No	-	No	Yes
[32]	Wind, battery, load (HVAC)	No	Yes	Yes	Yes	No	No
[44]	EVs	No	No	No	-	No	No

[45]	Electric vehicles, wind	No	Yes	Yes	No	No	No
[46]	Demand flexibility	No	Yes	No	-	No	No
[33], [40]8/12/2025 6:50:00 AM	Electric vehicles, energy storage [33], Renewables (solar PV and wind), diesel generators, battery storage, price-sensitive loads [34]	No	Yes	Yes	Yes	No	No
[47]	Load curtailment, battery, wind, solar	No	Yes	Yes	Yes	No	Yes
[41]	Electric vehicles, distributed generation	No	Yes	Yes	No	No	Yes
[39]	Solar PV, electric storage, and conventional demand	Yes	Yes	Yes	Yes	No	No
This chapter	Solar PV, electric storage, and conventional demand	Yes	Yes	Yes	Yes	Yes	Yes

3.1.2 Key Contributions and Chapter Structure

This chapter intends to complement the previous works on aggregator decision-making and provide additional insights for a real-world aggregator participating in energy markets. The key contributions of this paper are summarized as follows:

- Formulation and demonstration of a sequential decision-making framework for aggregator to efficiently utilize its DER resources and participate in both day-ahead and real-time energy markets.
- Modeling of risk preference for aggregators and inclusion of rolling forecasts with multiple time frames (day-ahead, intra-day, intra-hour) and granularities in decision-making.
- Modeling inclusion of delay between the bidding interval and decision-making time
- Analysis of rolling forecasts from different time frames to understand their impact on profitability.

- Deeper computational analysis of the different components in the real-time stages.

The remaining chapter is organized as follows. The mathematical modeling of the proposed framework is described in Section 3.2. The case studies conducted in this work and the analysis are presented in Section 3.3. Section **Error! Reference source not found.** summarizes the key learnings and provides future directions for this work.

3.2 Mathematical Modeling

This section presents a comprehensive sequential decision-making framework for an aggregator managing multiple solar photovoltaic, electric storage/battery, and residential demand resources. In Section 3.2.1, the timeline considerations and its alignment to energy market operations assumed in this work are summarized. The two key formulations, developed for the day-ahead stage and the real-time stages, are modeled as mixed-integer linear programming (MILP) problems. The day-ahead decision-making is presented in Section 3.2.2, whereas the real-time stage progress is detailed in Section 3.2.3.

3.2.1 Overview of Aggregator and Market Operations Timelines

Similar to existing practices, this work adopts the schedule/timeline of day-ahead and real-time energy markets. The overview of the energy market timelines and corresponding decision-making timeline for the aggregator are summarized in Figure 3.2. As depicted, the bidding deadline for the day-ahead market is set as 10 am, followed by the execution of the day-ahead market by the system operator. At 1:30 pm, the day-ahead schedule for all market participants is released. Hence, the day-ahead decision-making of the aggregator should conclude before 10 am.

During the real-time stages, it is assumed that the market participants can submit until 10 mins before the start of the execution of the real-time market. For example: for the real-time market execution from 12 pm to 12:15 pm, bids can be submitted until 11:50 pm. Then, system operator solves the real-time market formulation to clear the market and determine the real-time schedules of all participants.

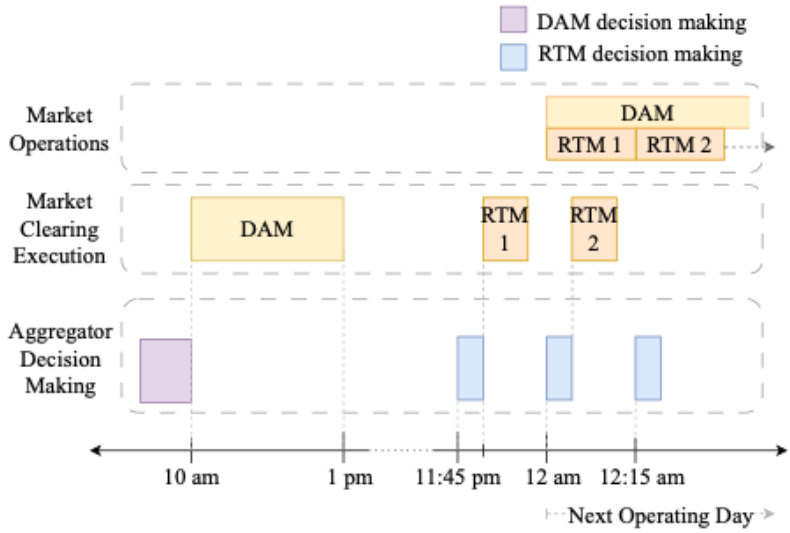

Figure 3.2 Overview of the market clearing and aggregator decision-making timelines

3.2.2 Day-Ahead Decision-making

At this stage, there is a need for a decision-making formulation to use the available day-ahead forecasts to position the aggregator such that it is able to match the net demand efficiently in its network. The following sub-section presents the day-ahead optimization formulation in detail.

3.2.2.1 Optimization Formulation

A mixed-integer linear programming formulation has been presented to determine the battery management decisions ($E^{batt}, P^{ch/dch}$) and day-ahead market bids (P^{DAM}). The optimization formulation is defined by (3.1)–(3.9). The objective function to minimize the cost of operation is defined as:

$$\min \sum_{t \in \mathcal{T}^{\mathrm{DAM}}} \hat{\pi}_t^{\mathrm{DAM}} P_t^{DAM} \tag{3.1}$$

where $\hat{\pi}_t^{\mathrm{DAM}}$ represents the market price forecast at hour t. It is assumed that the aggregator operates at a scale such that it cannot influence the market prices. It acts as a price taker.

To ensure the supply matches the demand within the aggregation at all hours of the day,

$$\sum_{i \in \mathcal{N}_{res}} \hat{P}_{t,i}^{load} - \sum_{i \in \mathcal{N}_{PV,res}} \hat{P}_{t,i}^{PV} = P_t^{\mathrm{DAM}} + P_t^{dch} + P_t^{ch}, \quad \forall t \in \mathcal{T}^{\mathrm{DAM}} \tag{3.2}$$

The constraints associated to the battery decision variables (power and energy levels) are as follows:

$$E_{t+1}^{batt} = E_t^{batt} + \left(\eta^{ch} P_t^{ch} - \frac{P_t^{dch}}{\eta^{dch}}\right) \Delta t^{DAM}, \quad \forall t \in \mathcal{T}^{\mathrm{DAM}} - \{T^{end}\} \tag{3.3}$$

$$E_{min}^{batt} \leq E_t^{batt} \leq E_{max}^{batt}, \quad \forall t \in \mathcal{T}^{\mathrm{DAM}} \tag{3.4}$$

where E_t^{batt}, P_t^{ch}, and P_t^{dch} is the energy level, charging power, and discharging power respectively of the battery at time t. P_{max}^{ch} and P_{max}^{dch} represent the power ratings of the battery. Also, η^{ch} and η^{dch} are the charging and discharging efficiencies respectively of the battery.

To model a set of generalized boundary conditions of the battery, let $\bar{E}_{T_{start}}$ and $\bar{E}_{T_{end}}$ be the input parameters to the formulation. $\bar{E}_{T_{start}}$ can be chosen or derived using a forecasting mechanism to predict the battery level at start of day. Similarly, $\bar{E}_{T_{end}}$ (target energy level at end of day) can be derived based on a policy decision from historical performance. The constraints are:

$$\mathrm{E}_{\mathrm{T^{start}}}^{\mathrm{batt}} = \bar{E}_{T_{start}} \tag{3.5}$$

$$E_{T^{end}}^{batt} + \left(\eta^{ch} P_{T^{end}}^{ch} - \frac{P_{T^{end}}^{dch}}{\eta^{dch}}\right) \Delta t^{DAM} = \bar{E}_{T_{end}} \tag{3.6}$$

Additionally, a binary variable, b_t^{batt}, is introduced to ensure that the battery does not charge and discharge simultaneously. On combining the binary variable with power limits of the battery:

$$0 \leq P_t^{ch} \leq P_{max}^{ch} b_t^{batt}, \quad \forall t \in \mathcal{T}^{\mathrm{DAM}} \tag{3.7}$$

$$0 \leq P_t^{dch} \leq P_{max}^{dch}\left(1 - b_t^{batt}\right), \quad \forall t \in \mathcal{T}^{\mathrm{DAM}} \tag{3.8}$$

$$b_t^{batt} \in \{0,1\}, \quad \forall t \in \mathcal{T}^{\mathrm{DAM}} \tag{3.9}$$

Computationally, the formulated MILP problem is not challenging to solve since only point forecasts are modeled in the problem. In summary, there are 97 constraints and 120 decision variables.

3.2.2.2 Choice of forecast profile

Please note that the focus of this work is on the decision-making framework and not on forecasting algorithms for solar photovoltaic generation and residential demand. Hence, it is assumed that the aggregator has forecast information (i.e., day-ahead forecasts) about the expected solar generation and load profiles across the next day.

The selection of the forecast profile at the day-ahead stage is a crucial choice for the aggregator. Since the solar and load profiles contain uncertainties, there is a varying level of operational default risk for the aggregator based on the profiles it chooses in the previously formulated MILP formulation. To model this, a qualitative risk parameter (*conservative* or *risky*) is utilized to represent the risk preference of the aggregator.

As the name suggests, a risk-avoidance aggregator is modeled through the *conservative* risk preference. This implies that the aggregator considers the lower solar profiles and the higher load profiles in the optimization formulation (illustrated in Figure 3.3). Hence, a higher procurement of power from the grid is expected, thereby, reducing the risk of operational defaults during the next day of operation. Similarly, in the risk-taking/*risky* preference, the aggregator chooses the expected/mean solar and load profiles and follows a more wait-and-observe approach. In the

further sections, case studies are conducted to compare the different risk preferences of aggregators.

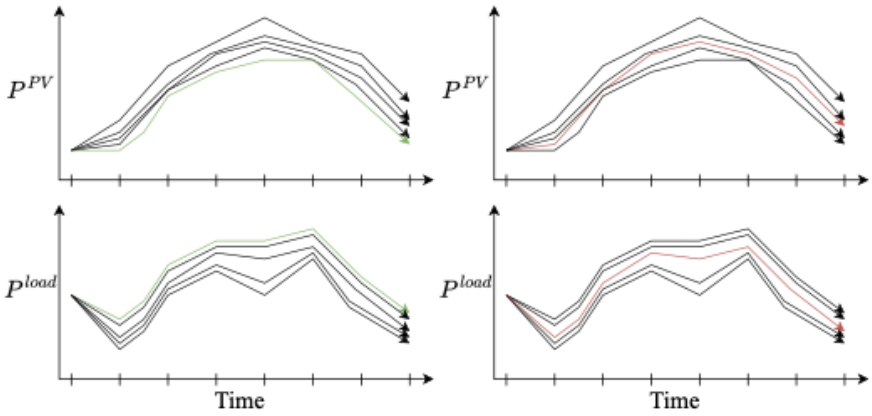

Figure 3.3 Illustration of risk-avoidance/*conservative* (left) and risk-taking/*risky* (right) profiles for solar and load resources

3.2.3 Real-Time Decision-making

As the operation of the aggregator progresses to the real-time stages, the aggregator has better visibility of the resources in its network. This can be attributed to two key characteristics of updated forecasts. First, the updated forecasts have less uncertainties since it is closer to operating time interval. Second, the forecasts are typically more granular (resolution of 15 minutes as opposed to the hourly forecasts during the day-ahead stage). This presents the need of a decision-making framework to incorporate the updated forecasts along with current battery states and cleared DAM bid to compute real-time bids and battery redispatch schedule.

Figure 3.4 summarizes the decision-making process of the aggregator during any real-time stage, which are described in the following sub-sections. As depicted, the process can be divided into four key components: (i) update forecasts, (ii) scenario generation, (iii) estimation of future battery level, and (iv) solving optimization formulation. The mathematical details of these components are presented in the following sub-sections. The remaining relevant details for practical implementation are described and analyzed in the Section 3.3.2.2.

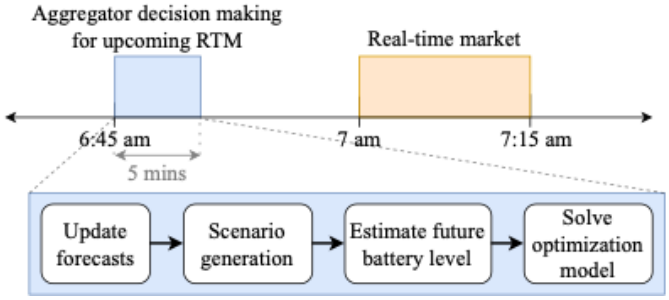

Figure 3.4 Decision-making process for the aggregator during real-time stages

3.2.3.1 Update Forecasts and Scenario Generation

During the real-time stages, lookahead forecasts from various timescales are combined followed by a scenario generation approach to represent future scenarios of net demand in the system. To combine information from various lookahead timescales, the latest available information for every time interval is utilized to create the forecast profile. Figure 3.5 illustrates the different components of the latest solar generation profile.

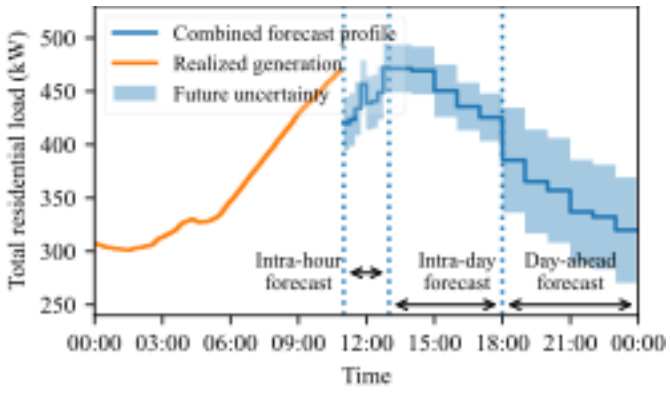

Figure 3.5 Combination of intra-hour, intra-day, and day-ahead forecast information at 11 am

To represent future scenarios, a scenario generation process using Monte-Carlo simulation (MCS) has been leveraged in this work. MCS is a powerful and applicable approach, not limited to power system operations, to represent future uncertainties. In this work, future scenarios are generated from the latest solar generation and demand profiles. Multiple case studies have been analyzed and presented in this work to understand the effect of number of scenarios on profitability and computational burden.

3.2.3.2 Estimation of Future Battery Level

It must be recognized that there is a lead time between the time when the aggregator submits bids for a real-time market interval and the time when the corresponding interval starts. The lead time is illustrated by Figure 3.4, where it can be observed that the decision-making for the 7 am to 7:15 am interval is run at 6:45 am. This causes uncertainty of battery energy level at the start of the upcoming operating interval. Modeling this uncertainty is important from the aggregator's perspective to avoid cases where the actual battery energy level is quite different than the expected level and the battery cannot generate/consume the power that it was expected to.

One approach to quantify the uncertainty of the battery energy level is presented here by generating envelopes or an uncertainty region bounds. The following mathematical equations describe the process in determining the envelope extreme points ($E_{t,low}^{batt}$ and $E_{t,high}^{batt}$). The deviation in system net demand after accounting the cleared DAM bid can be calculated as follows:

$$\Delta P_t = b_1\left(P_t^{load}, P_t^{solar}\right) = P_t^{load} - P_t^{solar} - \bar{P}_t^{DAM} \tag{3.10}$$

Using the calculated net demand, the expected charging and discharging power, as well as the future battery energy level, can be determined.

$$P_t^{dch} = b_2(\Delta P_t) = \min(\max(0, \Delta P_t), P_{max}^{dch}) \tag{3.11}$$

$$P_t^{ch} = b_3(\Delta P_t) = \min(\max(0, -\Delta P_t), P_{max}^{ch}) \tag{3.12}$$

$$E_{t+1}^{batt} = b_4\left(P_t^{ch}, P_t^{dch}\right) = E_t^{batt} + \left(\eta^{ch} P_t^{ch} - \frac{P_t^{dch}}{\eta^{dch}}\right) \Delta t^{RTM} \tag{3.13}$$

Combining b_1, b_2, b_3, and b_4 results in

$$E_{t+1}^{batt} = b_5\left(P_t^{load}, P_t^{solar}\right) \tag{3.14}$$

Hence, the envelope bounds and expected level can be calculated using

$$\hat{E}_{t+1,low}^{batt} = b_5\left(P_{t,high}^{load}, P_{t,low}^{solar}\right) \tag{3.15}$$

$$\hat{E}_{t+1,high}^{batt} = b_5\left(P_{t,low}^{load}, P_{t,high}^{solar}\right) \tag{3.16}$$

$$\hat{E}_{t+1,exp}^{batt} = b_5\left(P_{t,exp}^{load}, P_{t,exp}^{solar}\right) \tag{3.17}$$

3.2.3.3 Optimization Formulation

The mathematical formulation in the real-time stage is similar to the day-ahead strategy with incorporation of different future scenarios. Similar to the day-ahead stage, the objective is to minimize the aggregator's expected costs. Hence, the objective function is defined as:

$$\min \sum_{s\in\mathcal{S}} \sum_{t\in\mathcal{T}} \left(p_s \pi_{s,t}^{RTM} P_{s,t}^{RTM} + M^{SL}\left(SL_{s,t}^{buy} + SL_{s,t}^{sell} + SL_t^{Ebatt}\right)\right) \tag{3.18}$$

where $\mathcal{S}$ and $\mathcal{T} \coloneqq \{T^{start}, \dots, T^{end}\}$ represent the set of future scenarios and time periods respectively. p_s and $\pi_{s,t}^{RTM}$ represent the probability and expected real-time energy market price respectively for scenario s at time t.

The constraints in the real-time stages are as follows:

$$\begin{aligned} &P_{s,t}^{RTM} + P_{s,t}^{dch} - P_{s,t}^{ch} + SL_{s,t}^{buy} - SL_{s,t}^{sell} = \bar{P}_t^{DAM} \\ &+ \sum_{i\in\mathcal{N}_{res}} \hat{P}_{s,t,i}^{load} - \sum_{i\in\mathcal{N}_{PV,res}} \hat{P}_{s,t,i}^{PV}, \forall t \in \mathcal{T}, s \in \mathcal{S} \end{aligned} \tag{3.19}$$

$$E_{s,T^{start}}^{batt} = \widehat{E_0^{batt}}, \qquad \forall s \in \mathcal{S} \tag{3.20}$$

$$E_{s,t}^{batt} + \left(\eta^{ch} P_{s,t}^{ch} - \frac{P_{s,t}^{dch}}{\eta^{dch}}\right) \Delta t^{RTM} - E_{s,t+1}^{batt} = 0, \forall t \in \mathcal{T} - \{T^{end}\}, s \in \mathcal{S} \tag{3.21}$$

$$E_{s,T^{end}}^{batt} - \left(\eta^{ch} P_{s,T^{end}}^{ch} + \frac{P_{s,T^{end}}^{dch}}{\eta^{dch}}\right)\Delta t^{RTM} + SL_t^{Ebatt} \geq \bar{E}_{T_{end}}, \forall s \in \mathcal{S} \quad (3.22)$$

$$E_{min}^{batt} + \left(\hat{E}_{t,exp}^{batt} - \hat{E}_{t,low}^{batt}\right) \leq E_{s,t}^{batt}, \qquad \forall t \in \mathcal{T}, s \in \mathcal{S} \quad (3.23)$$

$$E_{s,t}^{batt} \leq E_{max}^{batt} + \left(\hat{E}_{t,high}^{batt} - \hat{E}_{t,exp}^{batt}\right), \qquad \forall t \in \mathcal{T}, s \in \mathcal{S} \quad (3.24)$$

$$P_{s,t}^{ch}, P_{s,t}^{dch} \geq 0, \qquad \forall t \in \mathcal{T}, s \in \mathcal{S} \quad (3.25)$$

$$P_{s,t}^{ch} \leq P_{max}^{ch} b_{s,t}^{batt}, \qquad \forall t \in \mathcal{T}, s \in \mathcal{S} \quad (3.26)$$

$$P_{s,t}^{dch} \leq P_{max}^{dch}\left(1 - b_{s,t}^{batt}\right), \forall t \in \mathcal{T}, s \in \mathcal{S} \quad (3.27)$$

$$b_{s,t}^{batt} \in \{0,1\}, \qquad \forall t \in \mathcal{T}, s \in \mathcal{S} \quad (3.28)$$

$$-P_{max}^{sell} \leq P_{RTM,s,t} \leq P_{max}^{buy}, \quad \forall t \in \mathcal{T}, s \in \mathcal{S} \quad (3.29)$$

The supply-demand balance across all periods and future scenarios is ensured by (3.19). (3.20)–(3.28) represent the battery constraints (start/end constraints, temporal dependence, energy/power limits, etc.) modeled in the formulation. The bidding limits in the real-time markets are set by (3.29).

3.3 Case Studies and Analysis

This section presents multiple case studies to gain insights about the effect of various parameter choices in the sequential decision-making framework. Details about the dataset and aggregator are summarizes in Section 3.3.1. Section 3.3.2 discusses a sample simulation run of the proposed framework. Sections 3.3.3, 3.3.4, and 3.3.5 present additional case studies to better understand the effect of aggregator risk preferences, forecast information availability, and computational analysis respectively.

3.3.1 Aggregator Details and Dataset Information

The aggregator is assumed to manage a residential network of multiple solar photovoltaic panels, battery storage units, and residential demand. The details and ratings of the resources are summarized in Table 3.2.

Table 3.2 System details

	Capacity of a single unit	Number of units	Total capacity
Solar	0.3 kW	800	240 kW
Demand	1.4 kW	250	350 kW
Battery	5.8 kW, 13.5 kWh	50	290 kW, 675 kWh

The dataset was generated from the NREL dataset provided for the ARPA-E PERFORM program [48]. Without loss of generality, a site on the outskirts of Houston, Texas was chosen to test the proposed framework and conduct a detailed analysis. Hence, ERCOT data was extracted from the NREL dataset. Solar data of site solar 433 was employed to generate the solar PV datasets. Load data of Coast zone was employed to generate the load datasets.

In this work, it is assumed that intra-hour (one-hour ahead) and intra-day (six-hour ahead) forecasts are available to the aggregator. The lead time, horizon, and resolution of forecasts are summarized in Table 3.3.

Table 3.3 Details about lookahead forecasts in real-time stages

	Lead time	**Horizon**	**Resolution**
Day-ahead forecasts	15 hrs	24 hrs	1 hr
Intra-day forecasts	6 hrs	6 hrs	1 hr
Intra-hour forecasts	1 hr	1 hr	15 mins

3.3.2 Sample Simulation

3.3.2.1 Day-Ahead Decision-making

As mentioned before, day-ahead forecasts for solar and residential load resources are utilized to determine the DAM bids and battery schedules. Figure 3.6 and Figure 3.7 depict the key inputs (day-ahead forecasts) and outputs (market bids and battery schedules) respectively of the day-ahead decision-making process. As expected, the aggregator maximizes its profitability by charging the storage resources during lower price hours (for example: hour 14) and discharging when prices are expected to be higher (hour 17).

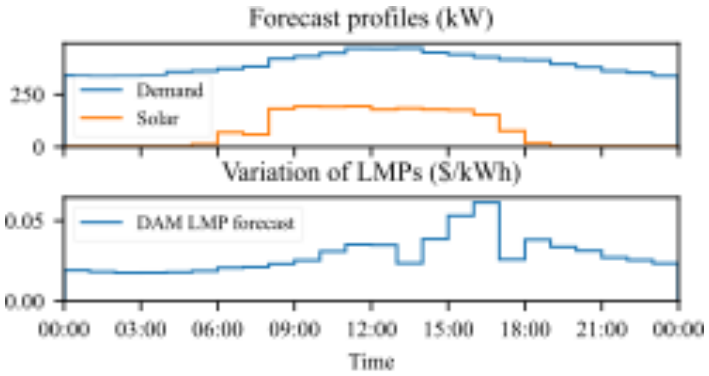

Figure 3.6 Aggregator input data for day-ahead stage decisions

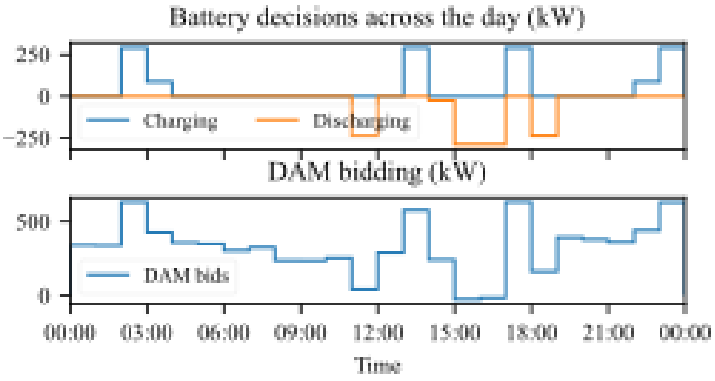

Figure 3.7 Aggregator battery and bid decisions for day-ahead stage

3.3.2.2 Real-time decision-making and actual realization

After implementing the day-ahead stage, the aggregator executes the real-time decision-making formulation (presented in Section 3.2.3) to redispatch storage and participate in the 15-min RTMs.

Simultaneously, a simulation process to emulate actual realization of solar and load values every 5 mins (i.e. for total $24\ \text{hrs} * 12\ \text{intervals/hr} = 288$ time steps). Figure 3.8 summarizes the data loading process, aggregator decision-making every 15 mins, and the resource parameters tracking process.

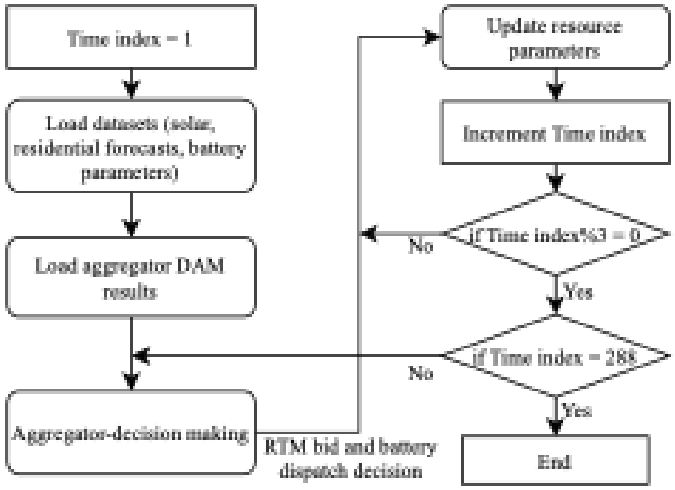

Figure 3.8 Flowchart depicting the sequential process of the simulations

Figures Figure 3.9 and Figure 3.10 depict a snapshot of the various resources during the simulation process. From the former figure, it can be observed that actual solar and load deviate from the day-ahead forecasts, leading to a lower net load in the aggregator's network. This results in a higher battery energy level, as observed in Figure 3.10. The latter figure further shows how the aggregator redispatches battery and bids in the real-time market based on updated forecasts to maximize profitability.

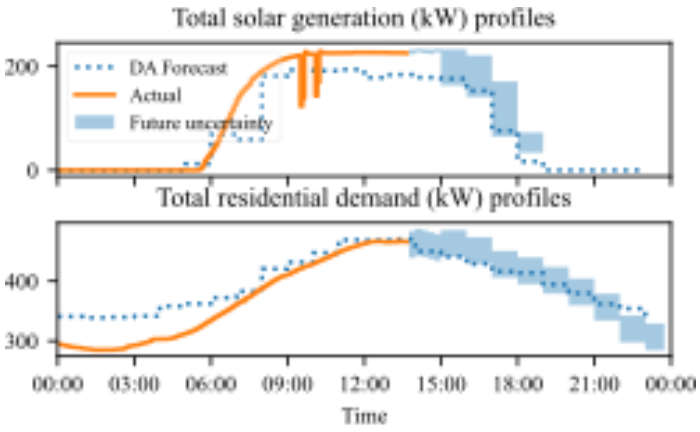

Figure 3.9 Simulation snapshot of the solar and load profiles at 1:45 pm

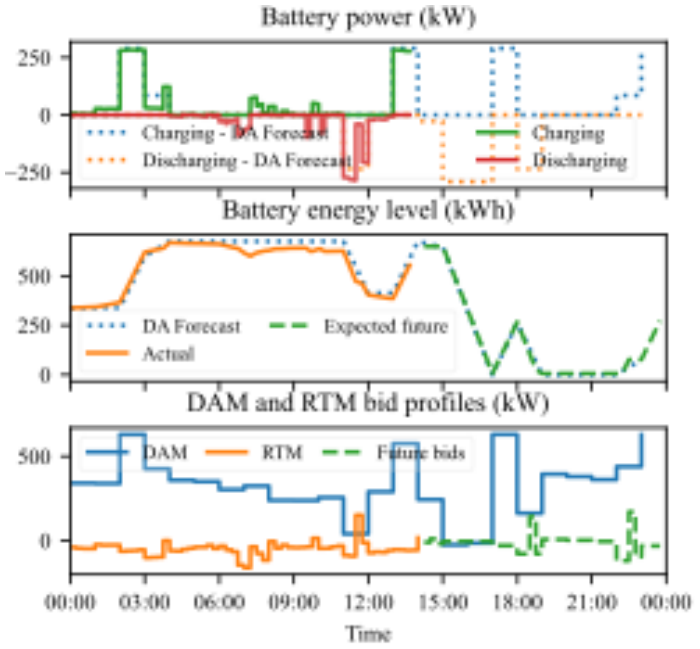

Figure 3.10 Simulation snapshot of battery and bidding decisions at 1:45 pm

3.3.3 Effect of Day-Ahead and Real-Time Risk Preferences

This section summarizes the effect of day-ahead and real-time preferences on the aggregator decision-making. Particularly, the effect on the battery level, bidding profiles, and profitability is analyzed.

First, two day-ahead preferences, *conservative* and *risky* strategies, are compared. In Figure 3.11, it is observed that *conservative* strategy procures more power from the day-ahead market than the *risky* strategy. This is expected due to the *conservative* strategy's higher risk aversion to future defaults. As expected, this translates to a higher DAM settlement (summarized in Table 3.4).

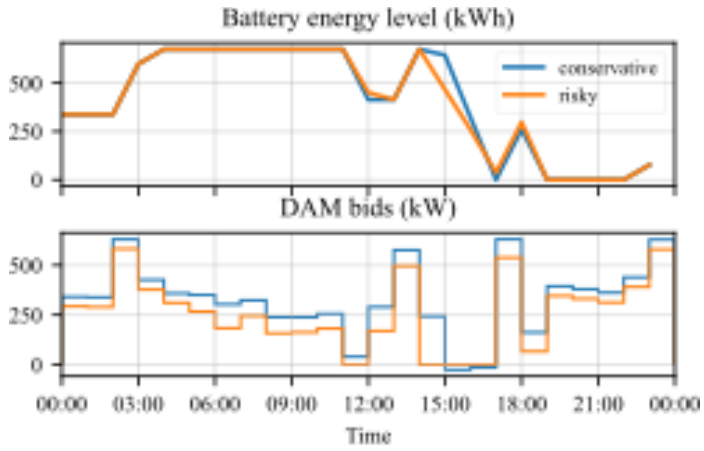

Figure 3.11 Comparison of day-ahead risk preferences in DAM

Figure 3.12 depicts the effect of day-ahead preferences on the actual operating day. Interestingly, the battery level is identical across the two strategies. Moreover, the *conservative* aggregator sells the excess power bought during DAM through the RTMs. This results in a lower RTM settlement for the *conservative* aggregator.

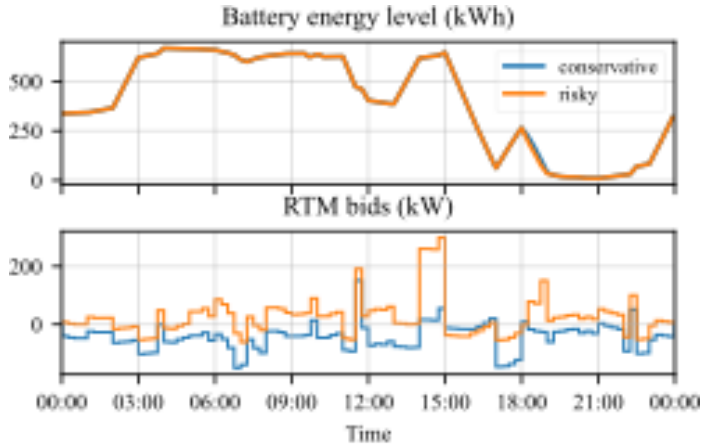

Figure 3.12 Effect of day-ahead risk preferences in real-time stages

Table 3.4 Effect of day-ahead risk preferences on settlement costs

	conservative	*risky*
DAM	$186.38	$143.68
RTM	$(1.32)	$41.38
Total	$185.36	$185.06

Then, the effect of different real-time risk preferences is analyzed. Three simulations with risk levels of *5*, *10*, and *20* are run with the *conservative* strategy. From Figure 3.13, it can be observed that a higher risk level results in a lower procurement from the real-time markets. This is expected since a lower risk level is more averse to potential net load deviations in the future time stages.

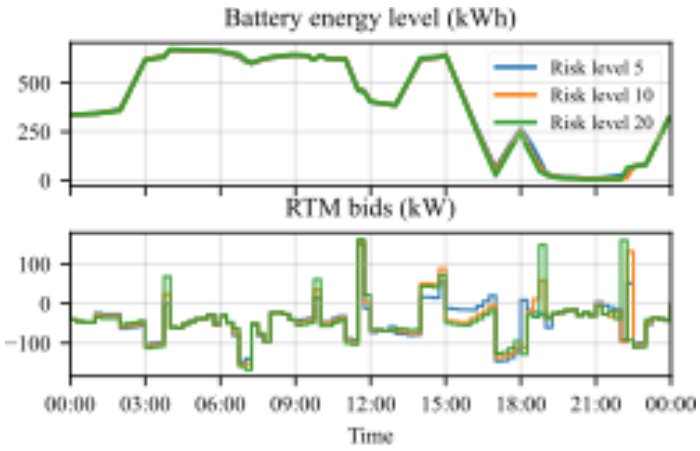

Figure 3.13 Effect of different risk preferences in real-time stages

Table 3.5 Effect of different risk preferences in real-time stages.

Risk Level ->	5	10	20
DAM	$186.38	$186.38	$186.38
RTM	$(1.32)	$11.18	$33.80
Total	$185.06	$197.56	$220.18

3.3.4 Influence of Forecast Information Availability

As mentioned before, it is essential for a sequential decision maker to understand key characteristics (for example: lookahead window, lead time, and granularity) about the future profiles of its resource fleet. A higher lookahead and/or lead time is expected to better prepare the aggregator for future possibilities and perform more effectively. However, procuring more frequent data requires additional forecasting capabilities. This brings the need to compare and quantify the benefits of the availability of forecast information.

In this section, the influence of forecast data is analyzed by utilizing information from different timescales. Three different variations are considered. In the first variation, it is assumed that aggregator has forecast information from day-ahead, six-hour ahead and one-hour ahead for all intervals of the day. In the second variation, forecast information from only the day-ahead and six-hour ahead is available. In the third variation, forecast information from only the day-ahead and one-hour ahead is assumed to be available.

Figures Figure 3.14 and Figure 3.15 depict the effect of the three forecast variations on the real-time market bids and battery states respectively. An interesting observation is that the bidding profiles with using only one-hour ahead information coincides with the bidding profiles with using both one-hour and six-hour ahead profiles. Further analysis showed that this was due to the assumption that the real-time market clearing prices being same as day-ahead clearing prices for every interval.

Also, the bidding profile for the first variation is more abrupt compared to the second variation. This is expected since the latest forecast for the resource is only available one hour prior to the time of operation in the first variation whereas intermediate forecasts are also available for the aggregator to pre-position itself in the second variation.

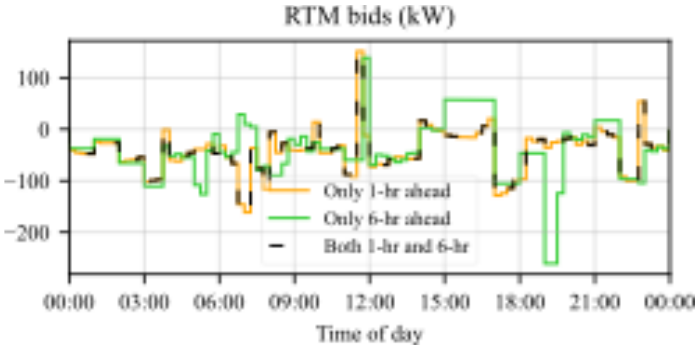

Figure 3.14 Effect of different forecasting variations on RTM bids

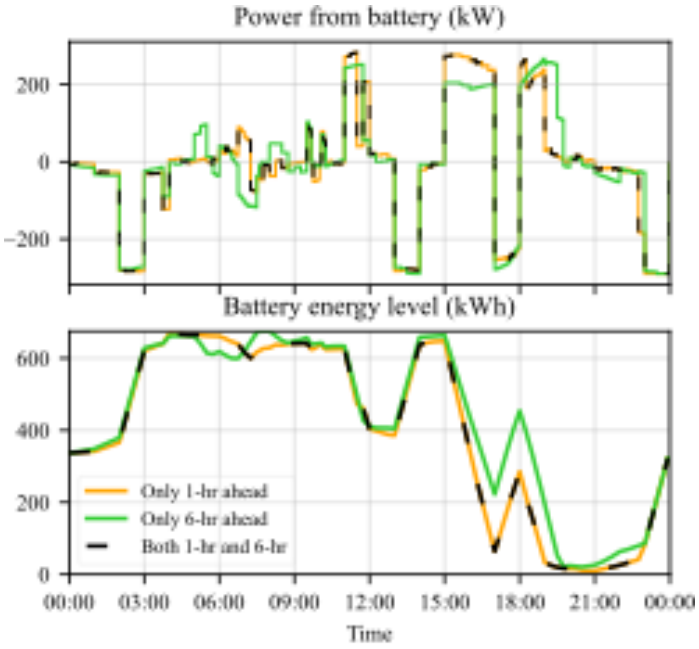

Figure 3.15 Effect of different forecasting variations on battery power and energy level

The above comparisons were simulated for 12 different days to compare the settlement costs of the aggregator with the different forecasting variations. It can be observed from Table 3.6 that in most simulation days, variations 1 and 3 outperform variation 2. This concludes that intra-hour forecasts are more essential than intra-day forecasts to make decision during the real-time stages.

Table 3.6 RTM settlements with different forecasting variations

Simulation	Variation 1 (both)	Variation 2 (only intra-day)	Variation 3 (only intra-hour)

1	-17.92	-13.49	-17.92
2	-34.21	-35.14	-34.21
3	-9.91	-2.61	-9.91
4	-36.01	-40.07	-36.01
5	-18.77	-15.90	-18.77
6	-19.99	-28.44	-19.99
7	15.97	8.66	15.97
8	17.89	336.24	17.89
9	-44.82	-44.87	-44.82
10	-5.10	-11.46	-5.10
11	162.67	180.57	162.67
12	-0.85	-9.01	-0.85

3.3.5 Computational Analysis

From an aggregator's perspective, it is essential to analyze the computation aspects in addition to other factors presented in the previous sections. This analysis is expected to assist aggregators to determine the computation requirements for implementing the proposed decision-making framework.

To better understand the computational requirements, time taken by each decision stage (illustrated in Figure 3.4) is monitored across the base simulation and depicted in Figure 3.16. It is observed that solving the real-time optimization problem takes the most time, followed by the scenario generation process. The estimation of future battery energy and forecast updating processes take negligible time, hence, have been omitted in further analysis. It is also observed that the total computational time decreases over the day. This is expected since the later stages simulate and solve the optimization problem with fewer time stages remaining in the day.

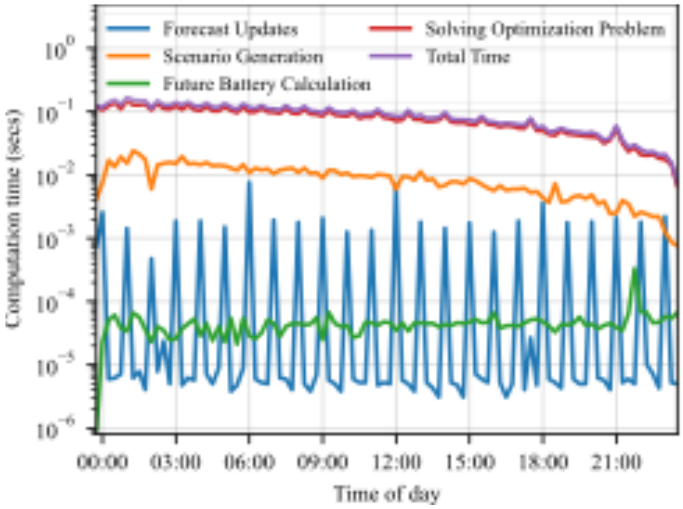

Figure 3.16 Computational time for each of the decision-making stages throughout the day

To understand the effect of day-ahead and real-time risk preferences on the computational time, six case studies (with two day-ahead risk preferences and three real-time risk preferences) are

simulated. Figure 3.17 depicts the different computational times for each of the simulations. It is observed that the computational times are similar irrespective of the day-ahead preference or the real-time risk preference of the aggregator. This observation can be attributed to the argument that the risk preferences do not affect the scenario generation computations or the number of constraints/decision variables of the optimization problem.

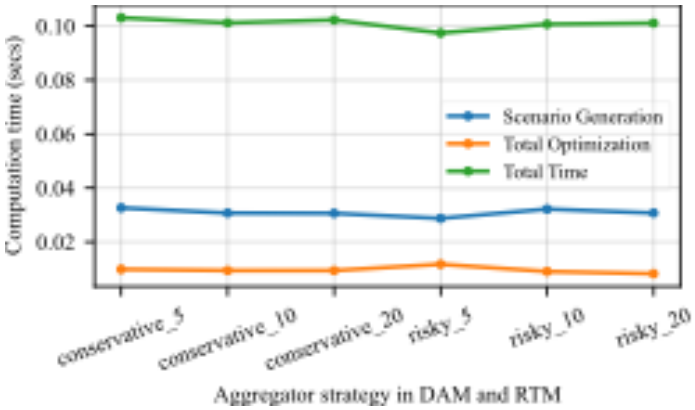

Figure 3.17 Computational time for all decision-making stages with varying risk preferences

Since the time taken in the scenario generation and the optimization problem solving processes are directly dependent on the number of scenarios considered in the real-time decision-making stages, multiple simulations with varying number of scenarios are analyzed for the same risk preferences (*conservative* day-ahead strategy with real-time risk level of *5*). Figure 3.18 depicts the variation of computation times across the different number of scenarios. It is observed that the computational time significantly increases with increase in number of scenarios modeled. Since each real-time decision-making stage is required to be solved within a stipulated time, there is a threshold on the number of scenarios that aggregators can consider to represent the future net load scenarios.

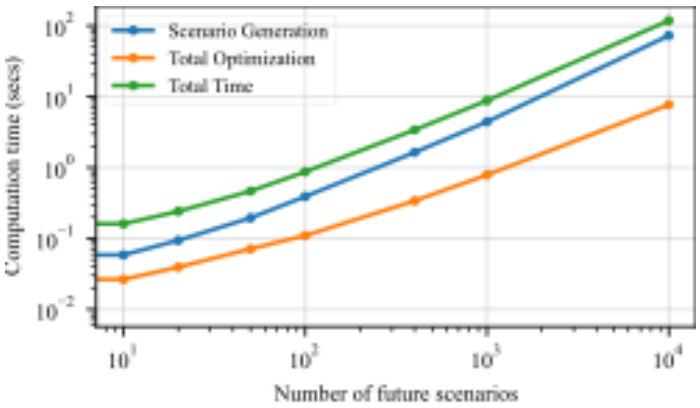

Figure 3.18 Computational time requirement for each real-time stage

3.4 Conclusion

The inclusion of distributed energy resources (DERs) in the modern electric grid brings various challenges that were not present with the conventional resources. This shift in resource mix

introduces operational uncertainties, and lack of visibility and control, and brings the need of an improved decision-making process. While there is rich ongoing research for management of DERs, it still lacks the inclusion of some practical considerations and analysis to assist aggregators.

In this work, a sequential decision-making formulation has been proposed analyzed for an aggregator managing multiple solar photovoltaic and electric storage resources. The formulation included risk preference parameters for an aggregator to represent its choice in the day-ahead and real-time decision-making. It was observed the day-ahead risk preference did not the effect the profitability of the aggregator, whereas the real-time risk preference parameter did play a significant role. Also, the incorporation of rolling horizon forecasts over multiple time frames has been considered and analyzed. It was observed that inclusion of intra-hour forecasts improved the profitability over only including intra-day forecasts. Computational analysis through multiple case studies provided insights on the influence of various steps in the real-time decision-making stages. The key bottleneck for a better representation of future scenarios was the computational time limitation in solving in solving a larger optimization problem.

From the analysis presented here, there are various extensions/improvements that can be done to analyze the decision-making process more practically. First, the incorporation of other market mechanisms, namely reliability unit commitment and ancillary services, are additional mechanisms that can be utilized to increase the profitability of the aggregator. Second, economic studies can be integrated with the analysis in this work to conduct a comprehensive cost analysis of tradeoffs for investments in computational resources.

4. Lookahead Tools for Energy Storage Resources

4.1 Introduction

4.1.1 Background and Motivation

The penetration of renewable energy sources and increasing demand in the electric grid are creating various operational challenges to modern electric systems. The global capacity of renewables is expected to increase by 5,500 GW in the 2024-2030 period, which is a 2.6 times increase compared to the 2017-2023 period [49]. Simultaneously, the peak electricity demand is predicted to increase by 128 GW (almost a 20% increase from 2024) in the next five years - owing to investments in data centers and manufacturing [50]. This rapid growth will exacerbate intermittency and uncertainty in the electric grid, hence, bringing challenges in maintaining reliable and efficient system performance.

Electric storage resources (ESRs) are resources capable of addressing the aforementioned challenges in electric grids. ESRs exhibit two key characteristics that make them a versatile resource. First, since ESRs can store energy, they have both generation and consumption capabilities. This enables them to absorb (or supply) power during periods of surplus (or deficit) generation in the grid. Second, ESRs are fast-ramping resources that be quickly synchronized and dispatched to the grid. Hence, they can be utilized during periods of high up- or down-ramping requirements. In the United States, the capacity of utility-scale ESRs has risen from 800 MW in 2016 to 18,100 MW in 2023 [51] – hence, confirming their potential.

ESRs can be utilized as (i) operating reserves, (ii) arbitrage/load-leveling, (iii) firm capacity and peaking capacity, (iv) black start, (v) transmission and distribution upgrade deferrals [52]. From Figure 4.1, it can be observed that ESRs are utilized most for operating reserves and arbitrage applications.

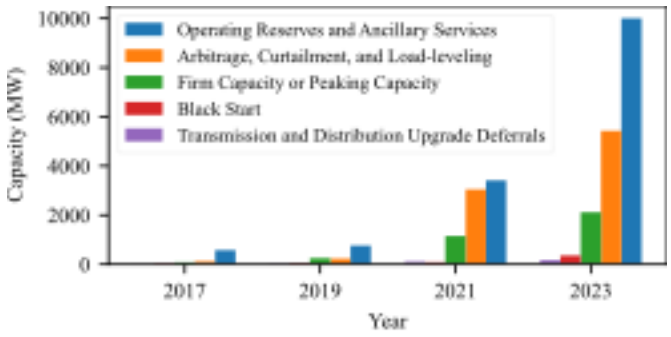

Figure 4.1 Progression of utility-scale ESR capacities by application in the United States [51]

While ESRs are beneficial to the electric grid, system operators (i.e., Independent System Operators or Regional Transmission Operators) face operational challenges in the inclusion of ESRs in their grid operations. A key challenge is limited situational awareness of ESRs in the system. Market participants, including ESRs, participate in day-ahead markets based on day-ahead forecasts of network conditions and energy prices. Closer to real-time, ESRs participate in real-

time markets to adjust their market position based on updated forecasts and their operational objectives. Currently, system operators rely on post-performance penalties and lack lookahead tools to predict the intra-day performance of ESRs. This work aims to provide a lookahead framework to assist system operators to assess the future state of charge and energy availability of ESRs.

4.1.2 Literature Review

In literature, the key focus for ESR applications in grid operations has been on scheduling and dispatch problems. From an ESR owner's perspective, [39], [53], [54], [55] propose bidding and battery management frameworks for participation in electricity markets. For distribution or transmission grid operators, [56], [57], [58] propose market clearing or coordinated operation strategies for electric networks with multiple participants with storage resources.

However, there are no guarantees that the market participants will fulfill their obligations. There are only a handful works that tackle the problem of situational awareness from the system operator's perspective. The current market regulations are post-performance-based penalties. The Dynamic Assessment and Determination of Operating Reserve (DynADOR) tool, developed by Electric Power Research Institute (EPRI), is used by balancing area authorities and system operators to determine the operating reserve requirements [59]. The tool assesses the variability and uncertainty from load and renewable energy sources to quantify the operating reserve requirements. Similarly, E3 has developed the RESERVE tool for determining ancillary services needs of highly renewable electricity grids. The Resource Forecast and Ramp Visualization for Situational Awareness (RAVIS), developed by National Renewable Energy Laboratory (NREL), is an open-source tool for assessing and visualizing resource forecasts and ramp alerts for significant up/down ramps associated to variable renewable resources [60]. It utilizes market results, probabilistic forecasts of renewables and load, site/regional-level data parameters, etc. to help operational control centers to mitigate upcoming operational challenges.

There are various other works, including [61], [62], [63], that propose similar methodologies to assess reserve requirements associated to variable renewable energy resources. However, the previous works focus on the application of operating reserve requirement associated to renewable resources only.

This work presents a similar methodology with the primary focus on ESRs and hybrid (renewables with ESRs) aggregations. The focus is on quantifying future ESR levels and categorizing them into three energy levels (high, medium, and low). Like the tools and papers presented earlier, the intra-day time frame (1 to 12 hours ahead) is analyzed in this work. The use cases of this tool include (i) comparison of future capability with its market position, (ii) assessing the overall resource adequacy of the storage resources in the system operator's network.

The literature on time series prediction models is extensive. Such models have been widely applied in various power system forecasting applications, including load and renewable energy prediction. One of the earliest works on load forecasting was based on ARIMA modeling was conducted in [64]. Since then, various time series prediction frameworks like semi-parametric additive model [65], extreme machine learning-based probabilistic forecasting [66], XGBoost [67], [68],

convolutional neural networks [69], temporal convolutional network [70], etc. have also been applied for short-term load forecasting. Similarly, machine learning approaches have been applied for forecasting renewable profiles in [71], [72], [73]. More recently, long short-term memory (LSTM) models for diverse applications like weather prediction [74] and the prognosis of wind turbine blades [75].

This chapter aims to leverage the existing time series prediction models for the application of intra-day situational awareness tool for ESRs. Specifically, three well-known models, seasonal ARIMA with exogenous variables, extreme gradient boosting, and long short-term memory, are explored in this work. As mentioned previously, ESRs have a higher potential for operating reserves and arbitrage applications. This work focuses on ESRs suitable for the latter application of arbitrage, curtailment and load leveling.

4.1.3 Key Contributions and Chapter Structure

This work addresses a novel need for improving the situational awareness of modern electric grids, especially in the context of electric storages resources (ESRs). The key contributions of the work are highlighted below:

- Well-known time series prediction models are applied to predict intra-day energy availability of ESRs. Detailed analysis is conducted to understand the behavior of the prediction models under various lookahead time frames ranging from 1 hour to 12 hours.
- A dataset containing one year of time series data containing ESR bidding and SOC levels is created using existing works in the literature.

Section 4.2 briefly summarizes the modeling preliminaries and proposed framework for the prediction tool. Section 4.3 presents a detailed case study of a profit-maximizing aggregator with electric storage resources. Section 4.4 summarizes the key learnings and insights of the proposed methodology.

4.2 Mathematical Modeling Preliminaries

This section summarizes the methodology proposed to develop a lookahead tool to predict future battery level of energy storage resources.

4.2.1 SARIMAX

The ARIMA model is a widely used statistical method for modeling and forecasting time series data. It consists of three components: autoregressive (AR), differencing/integrated (I), and moving average (MA). As the names suggest, autoregressive term models the relation of current value with its past values or lags, and moving average term models the current value as a linear combination of past forecast errors. The remaining term, differencing/integrated, removes the non-stationarity component by differencing the current value with the preceding value to stabilize the mean of the process. Mathematically, an ARIMA model is characterized by three parameters, p, d, and q, to represent the orders of the autoregressive, differencing, and moving average terms respectively. The model is as follows:

$$y_t = c + \sum_{n=1}^{p} \alpha_n y_{t-n} + \sum_{n=1}^{q} \theta_n \epsilon_{t-n} + \epsilon_t \quad (4.1)$$

where y_t and ϵ_t represent the output variable and forecast error at instant t. α and θ represent the linear coefficients in the model.

The Seasonal ARIMA with eXogenous variables (SARIMAX) model is an extension of the ARIMA model to include seasonal behavior and exogenous variables. Both these characteristics are relevant for ESR time series data due to inherent daily and yearly trends in resource profiles. Moreover, operation of ESRs is heavily dependent on exogenous parameters like time of day, electricity prices, weather parameters, etc.

The general mathematical formulation of SARIMAX(p,d,q)(P,D,Q,s) is given by:

$$y_t = c + \sum_{n=1}^{p} \alpha_n y_{t-n} + \sum_{n=1}^{q} \theta_n \epsilon_{t-n} + \sum_{n=1}^{r} \beta_n x_{n_t} + \sum_{n=1}^{P} \theta_n y_{t-sn} + \sum_{n=1}^{Q} \eta_n \epsilon_{t-sn} + \epsilon_t \quad (4.2)$$

where y represents the output variable, x represents the exogenous variables, ϵ represents the white-noise in the model, c represents the constant term. Also, P, D, Q represent the p, d, q counterparts respectively of the seasonal model.

4.2.2 XGBoost

Extreme Gradient Boosting (XGBoost) is a supervised machine learning based on decision trees [76]. It offers both classification and regression capabilities, thereby, making it suitable for the lookahead assessment of battery SOC levels. Technically, XGBoost builds an ensemble of weak learners (typically, decision trees), where each successive model utilizes errors from previous iterations to improve the ensemble model.

$$\hat{y}_i = \phi(\mathbf{x_i}) = \sum_{k=1}^{K} f_k(\mathbf{x_i}), \qquad f_k \in \mathcal{F} \quad (4.3)$$

where $\hat{y}_i$ is the predicted value, x_i is the input vector, f_k is the k-th regression tree from the space of functions $\mathcal{F}$, and K is the number of boosting rounds. The model is trained by minimizing a regularized objective function:

$$\mathcal{L}(\phi) = \sum_{i=1}^{n} l(y_i, \hat{y}_i) + \sum_{k=1}^{K} \Omega(f_k) \quad (4.4)$$

where $\Omega(f) = \gamma T + \frac{1}{2}\lambda\left||w|\right|^2$, l is a differentiable convex loss function, T is the number of leaves in a tree, and w is the vector of leaf weights.

Unlike linear models like ARIMA or SARIMAX, XGBoost does not rely on linear relationships. This makes it particularly useful for capturing non-linear relationships and complex dynamics between exogenous features and output variables.

4.2.3 LSTM-based Models

As discussed in Section 4.1.2, Long Short-Term Memory (LSTM) frameworks show immense potential in learning sequential patterns and long-term dependencies [77]. Structurally, it consists of three gates: forget gate, input gate, and output gate.

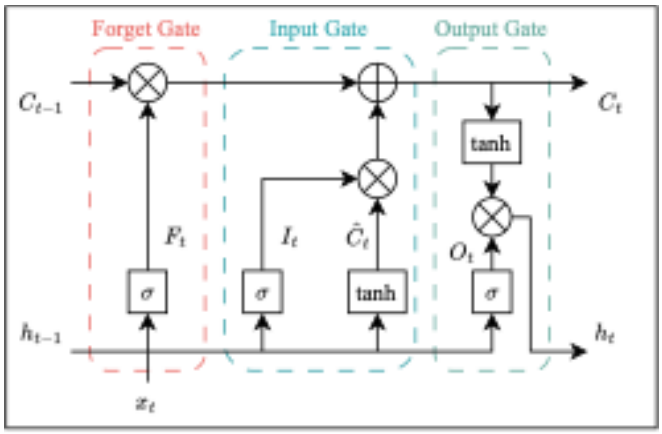

Figure 4.2 Structure of an LSTM cell [77]

As the name suggests, the forget gate determines whether to keep the current value of the memory or to forget it. Intuitively, the input gate determines how much of the input node's value should be added to the current cell internal state. Lastly, the output gate determines whether the memory cell should influence the output at the current time step. The mathematical process is represented below:

$$F_t = \sigma\left(x_t W_{xf} + h_{t-1} W_{hf} + b_f\right) \tag{4.5}$$

$$I_t = \sigma(x_t W_{xi} + h_{t-1} W_{hi} + b_i) \tag{4.6}$$

$$O_t = \sigma(x_t W_{xo} + h_{t-1} W_{ho} + b_o) \tag{4.7}$$

where F_t, I_t, and O_t represents the forget, input, and output state in the LSTM cell. The W's and b's represent the appropriate weight and bias parameters.

4.3 Case Study: Aggregator with only ESR Resources

An aggregator system with multiple ESR resources has been considered in this study. Without loss of generality, a utility-scale aggregator with 700 Tesla Powerwalls of 13.5 kWh and 5.8 kW each. Hence, the rated power and energy of the aggregation is 4.06 MW and 9.45 MWh respectively.

To note, a MacBook Pro with an M2 chip and 16 GB unified memory was utilized for implementing and executing the proposed case study.

4.3.1 Dataset Generation and Preprocessing

Methodologies from existing works like [39] were utilized to emulate an ESR aggregator participating in wholesale markets. A sequential framework was implemented to generate bidding decisions in the ERCOT day-ahead and real-time markets. Using this framework, one year (2018) of decision-making was implemented for the aggregator to create a dataset containing hourly battery level, charging power and discharging power. For the same time period, LMPs in the ERCOT region are also extracted.

The extracted time series of hourly battery level, LMPs, and hour of day was utilized dataset for the SARIMAX model. This dataset was split in the 80:20 ratio to generate the training and testing dataset.

On the other hand, XGBoost and LSTMs require input and output sequences for training and testing the models. Hence, a common approach, i.e. rolling horizon, is followed to convert the time series data into input features and output. Figure 4.3 depicts the time series to dataset conversion process. The lengths of past horizon for SOC levels and future horizon for prices is set to as 3 hours and 24 hours respectively. Since the forecasting timeframe is 12 hours, the future horizon is set accordingly to 12 hours.

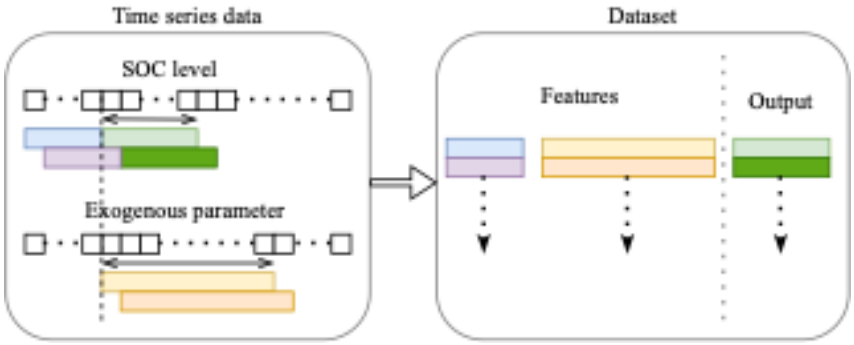

Figure 4.3 Rolling horizon approach to create the dataset from time series data

4.3.2 Model Training

All the models were trained and assessed using the *scikit-learn* library in Python [78]. Standard error metrics like mean absolute error (MAE) and root mean square error (RMSE) is utilized during the training process.

$$MAE = \frac{1}{N}\sum_{i=1}^{N}|y_i - \hat{y}(x_i)| \tag{4.5}$$

$$MAE = \sqrt{\frac{1}{N}\sum_{i=1}^{N}\left(y_i - \hat{y}(x_i)\right)^2} \tag{4.6}$$

where N represents the number of samples, y_i represents the actual value, and $\hat{y}(x\_i)$ represents the predicted value from the model.

4.3.2.1 SARIMAX

Before training the SARIMAX model, a key step is the determination of the parameters p, d, q, P, D, Q, and s. The first step is to check the stationarity of the time series using the Augmented Dickey-Fuller (ADF) Test. First, The first differencing terms are calculated. Then, from partial autocorrelation (PACF) and autocorrelation (ACF) plots depicted in Figure 4.4, it can be observed that there is a seasonal trend with a period of 24 (i.e., $s = 24$). Also, it can be observed that lag 1 terms in both PACF and ACF plots are significant. Hence, $p = q = 1$. Similarly, by observing the ACF and PACF plots at lags equal to 24 and 48, P = Q = 1.

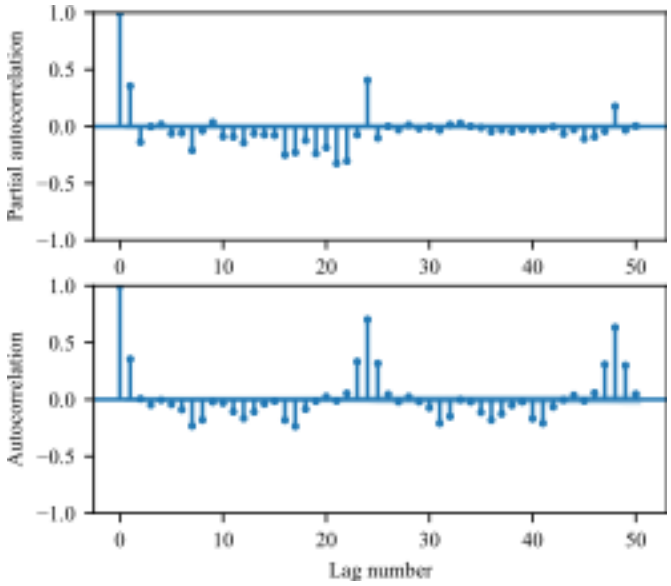

Figure 4.4 PACF and ACF plots for the SOC level time series

To affirm the model parameters, a grid search algorithm with (1,1,1)(1,1,1,24) as the base parameter combination is implemented. It is assumed that all parameters except s can change by 1 unit. The models are compared using Akaike Information Criterion (AIC) and Bayesian Information Criterion (BIC) statistical measures. On implementation, the base parameter resulted in the lowest AIC and BIC values. Hence, SARIMAX(1,1,1)(1,1,1,24) model was chosen for further analysis.

4.3.2.2 XGBoost

An open-source hyperparameter optimization framework, *Optuna*, is utilized to determine the number of estimators, depth, and learning rate of the XGBoost model [79]. For every trial consisting of a set of hyperparameters, the training set was used to train the model, followed by assessing the RMSE on the testing set.

An *Optuna* study of 200 trials with the parameters summarized in Table 4.1 was executed to determine the hyperparameters in the XGBoost model. The least error metric was observed for the estimator, depth, and learning rate values of 650, 5, and 0.05 respectively.

Table 4.1 Range and nature of sampling process for the *Optuna* study

	Minimum	Maximum	Sampling Nature
Number of estimators	10	10000	Logarithm
Max depth	3	10	Linear
Learning rate	10^{-3}	0.5	Logarithm

4.3.2.3 LSTM-based model

The LSTM model considered in this work consists of various encoders to extract useful information from input features, followed by a decoder network and a dense network to predict the future SOC levels of the battery. The final architecture (depicted in Figure 4.5) and hyperparameters were determined through an analysis of hit-and-trial cases and *Optuna* studies.

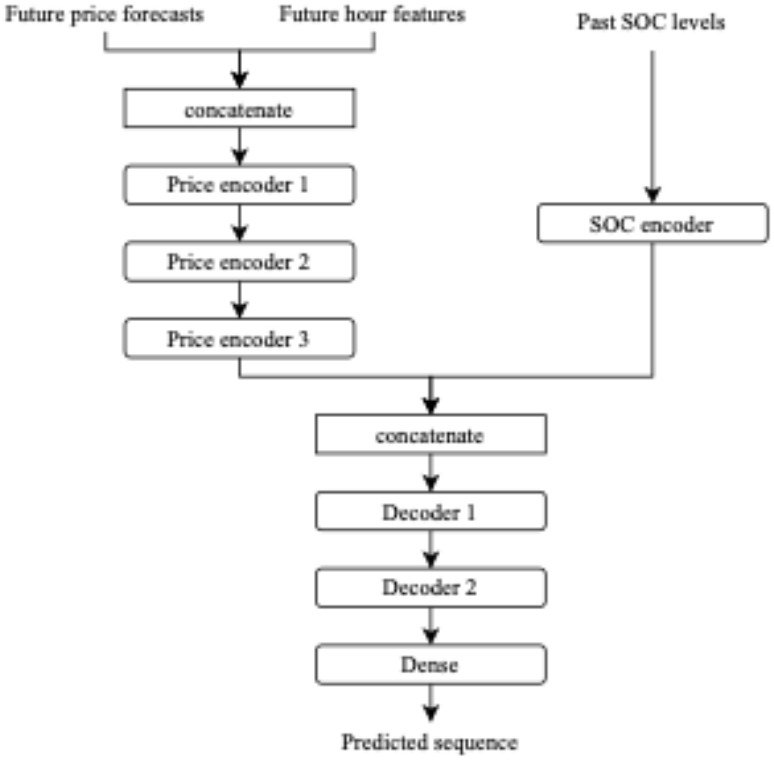

Figure 4.5 LSTM model architecture

Table 4.2 presents a sample of tested hyperparameters combinations consisting of various number of states, dropout rates and batch sizes, and the resultant error metric on the validation set. It can be observed that trial number 8 resulted in the least value of the error metric. Henceforth, further

analysis presented on LSTM models was conducted using the hyperparameters obtained in the best trial.

Table 4.2 A sample of hyperparameter combinations tested using *Optuna* for LSTM model tuning

Trial number	Number of states			Dropout rate			Batch size	RMSE on validation set
	SOC encoder	Price encoder	Decoder	SOC encoder	Price encoder	Decoder		
1	64	64	64	0.2	0.2	0.2	64	1.3403
2	64	8	32	0.1	0.3	0.2	16	2.1284
3	32	8	8	0.05	0.05	0	256	1.8919
4	16	8	64	0	0.3	0.05	16	2.1799
5	32	8	8	0	0.3	0.05	128	3.0875
6	32	8	16	0.3	0.2	0.05	16	1.8622
7	8	64	32	0.2	0.2	0.3	64	1.2337
8	8	64	64	0.2	0.2	0.3	64	1.1533
9	8	64	64	0.3	0.1	0.3	32	1.4283
10	16	32	64	0.05	0	0.1	64	1.9630

The training process with the obtained hyperparameters are depicted in Figure 4.6. It can be observed that the validation loss reduces until about 650 epochs and then plateaus. On the other hand, the training loss decreases as number of epochs increase. Since the validation loss does not decrease further, the training is concluded, and the parameters of the best model is saved. An interesting observation is that the validation loss is lower than the training loss during the process. This is possible due to the inclusion of dropout hyperparameters in the model. This implies the training process does not consider the LSTM complete model together at any stage and calculates the training loss based on the reduced model. In contrast, the validation loss calculation does utilize the complete model and thereby, results in a better prediction.

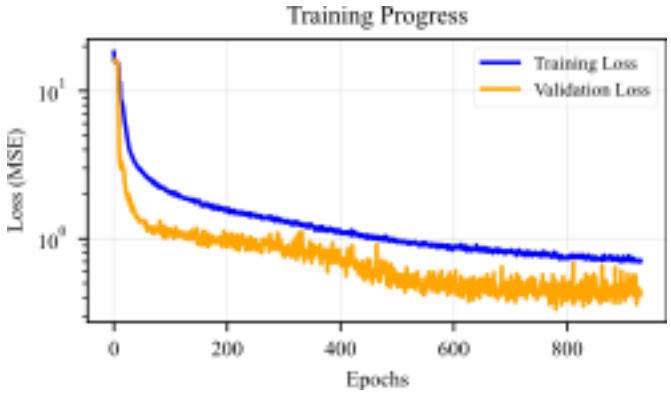

Figure 4.6 Training and validation losses during LSTM model training

4.3.3 Performance Comparison

Section 4.3.3.1 presents a preliminary comparison of the three trained models by depicting the prediction trajectories for a single test sample. In the remaining sections, the complete testing dataset is utilized to compare the performance of the models.

4.3.3.1 Depiction of prediction trajectories

Figure 4.7 depicts the forecasts of the trained models on a common test sample. As observed, all three models adequately capture the future SOC level pattern, especially, until 4-hour lookahead. After four hours, the SARIMAX prediction deviates the most from the actual sample, followed by the prediction from the XGBoost model. The prediction LSTM model most closely aligns the future SOC level time series information.

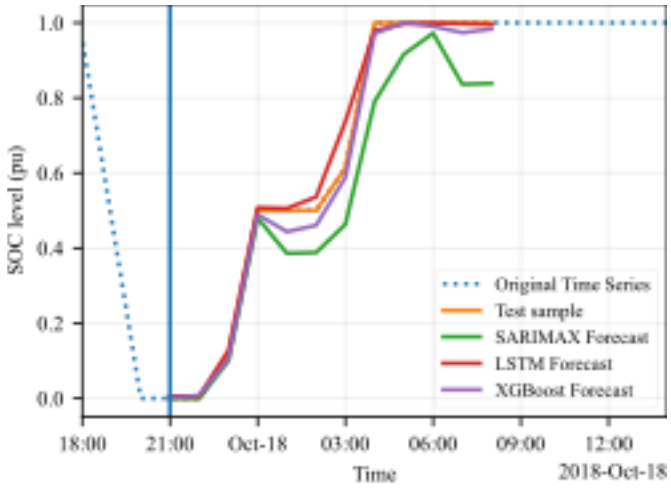

Figure 4.7 Comparison of predictions from different models for a common test sample

4.3.3.2 Analysis of continuous parameters

As mentioned earlier, the performance is assessed using standard metrics like root mean square error (RMSE) and mean absolute error (MAE) for continuous parameters. For categorical parameters, accuracy and confusion matrices are utilized.

Figure 4.8 depicts the MAE and RMSE metrics for the three developed models. It can be SARIMAX performs the worst among the three models. Interestingly, XGBoost and LSTMs have similar error metrics for the one-hour lookahead prediction. However, after the first hour, LSTM performs better. An interesting observation is that the error metrics depict a plateau-like shape. The SARIMAX, XGBoost, and LSTM models' error stagnate after a lookahead horizon of 8 hours, 4 hours, and 2 hours respectively.

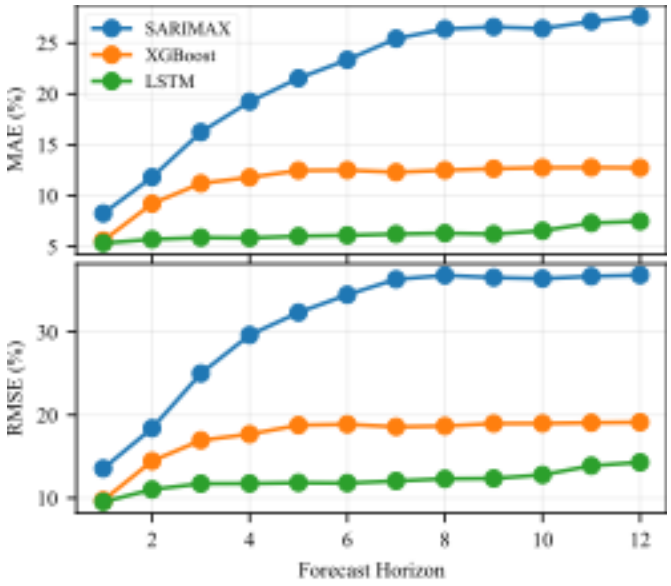

Figure 4.8 Error metrics for the three models across the forecasting horizon

Overall, the error metrics for the XGBoost and LSTM models are reasonable considering that the ESRs considered in this case study have a high charge/discharge rating compared to the energy rating. Mathematically, the battery is capable of charging or discharging by 5.8/13.5 *100 = 42.96% of its SOC level in an hour.

4.3.3.3 Analysis of categorical predictions

In certain applications of situational awareness frameworks, the objective is not to quantify future risks with high precision, but rather them into predefined levels to support quick and timely decision making. In this section, the models are analyzed and compared based on their ability to predict the appropriate SOC range instead of a specific SOC level. Three SOC ranges: *low*, *medium*, and *high* are considered based on the expected depletion of the battery. If the expected depletion is less than a certain threshold (for example: 30% in this analysis), the ESR will likely not have sufficient energy for obliging with its generation requirements in the market. On the other side, if the expected SOC level is more than a predefined threshold (for example: 70%), the ESR will likely be limited in charging.

The categorical predictions are envisioned to provide system operators with a quick illustration of the capabilities of the ESRs in the electric network a few hours in advance so that operators can make suitable downstream decisions associated to reserve procurement and resource dispatch.

Table 4.3 summarizes the classification accuracies of the three models across the key timeframes: 1-hour, 3-hours, 6-hours, and 12-hours. Two general trends can be observed from the table. First, for all models, the accuracies decrease with increase in lookahead time frames. Overall, LSTMs significantly outperforms the other models and SARIMAX does not produce acceptable results.

Table 4.3 Comparison of various models based on classification accuracies across various timeframes

	1-hour lookahead	3-hours lookahead	6-hours lookahead	12-hours lookahead
SARIMAX	84.17%	69.94%	59.90%	49.45%
XGBoost	91.34%	83.50%	80.61%	80.84%
LSTM	92.67%	90.21%	90.27%	88.34%

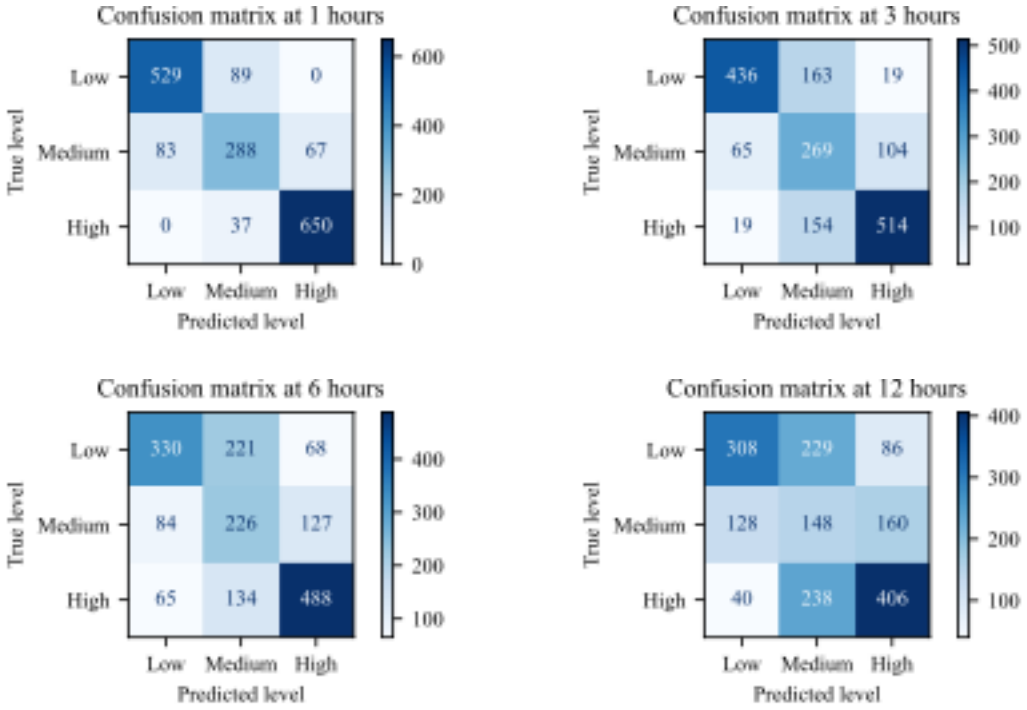

Figure 4.9, Figure 4.10, and Figure 4.11 expand the classification accuracies of the SARIMAX, XGBoost, and LSTM models respectively using confusion matrices. The number on the diagonal elements represent the cases where the prediction matched the true labels. As expected, it can be observed that the LSTM model performs the best, followed by the XGBoost model. Also, it can be observed that as the lookahead timeframe increases, the predictions worsen, and the confusion matrices become less sparse.

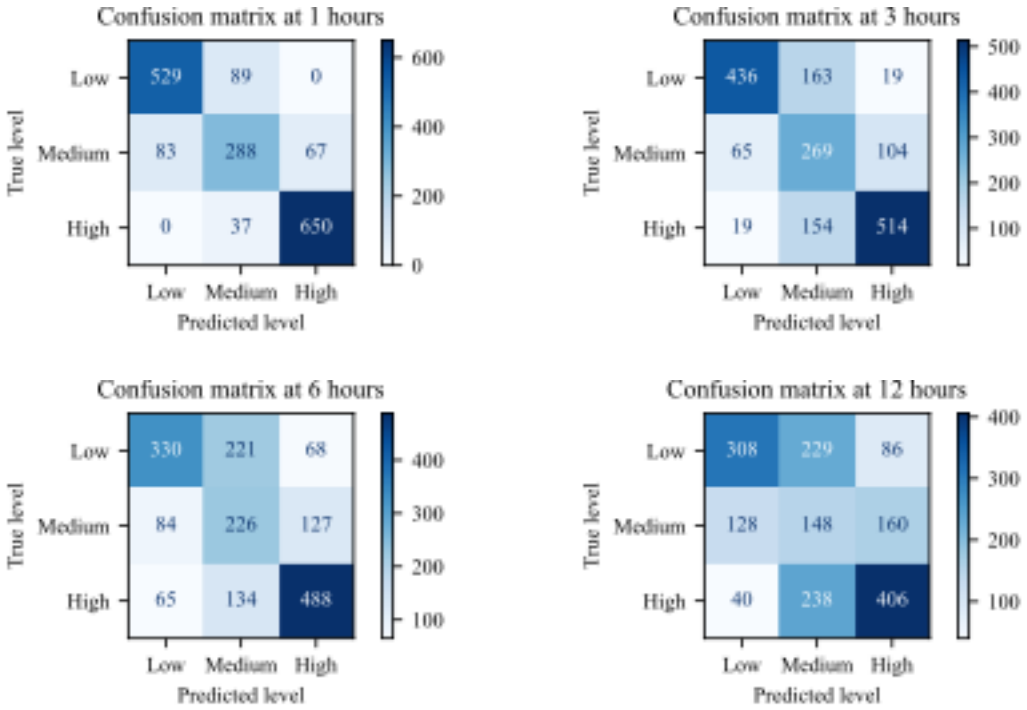

Figure 4.9 Performance of the SARIMAX model for category prediction across various time stages

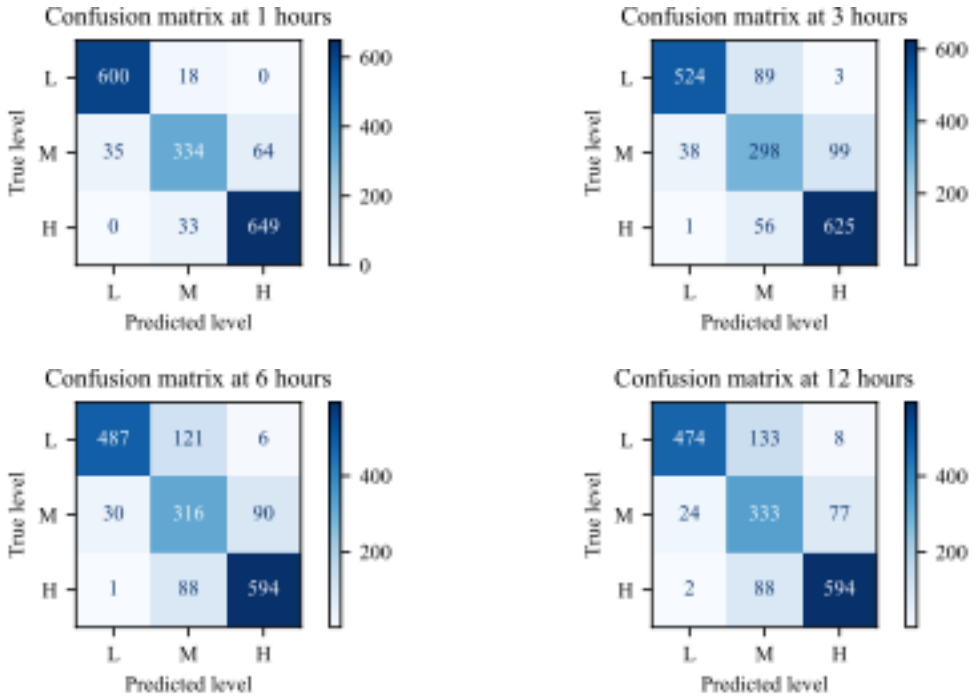

Figure 4.10 Performance of the XGBoost model for category prediction across various time stages

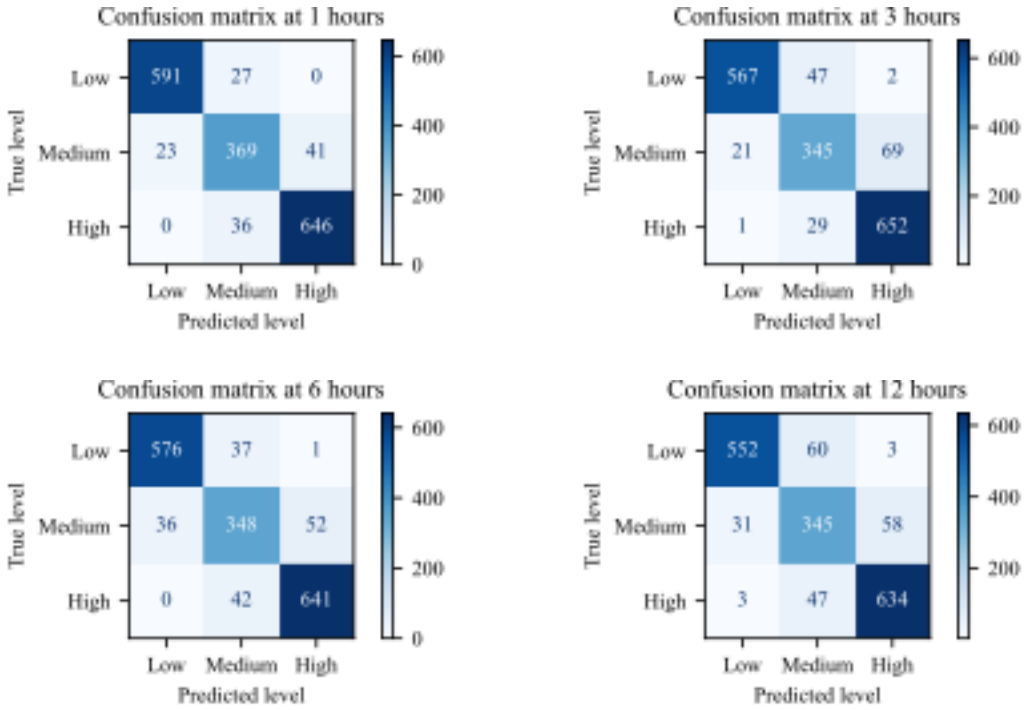

Figure 4.11 Performance of the LSTM model for category prediction across various time stages

4.3.3.4 Computational comparison

To better understand the computational burden associated to each of the proposed frameworks, the training time and inference time (i.e., the time required to compute a prediction) to generate a forecast is reported. From Table 4.4, it can be observed that the LSTM is computationally most burdensome. This is expected since LSTMs have the highest number of trainable parameters in its framework. However, for practical applications, all three models can be implemented since the models are trained through offline studies. During online/real-time operations, the models can be utilized for prediction since the inference time is close or less than 1 milliseconds.

Table 4.4 Computational time requirements for each framework

Model	Training time	Inference time
SARIMAX	117.72 secs	< 1 ms
XGBoost	11.38 secs	< 1 ms
LSTM	55.2 mins	~ 1 ms

4.4 Conclusion

In this chapter, an intra-day lookahead framework has been proposed to predict future energy availability of electric storage resources (ESRs). The main motivation of this framework is to provide situational awareness of the ESRs to system operators and ensure reliability in the electric grid.

Three popular time series prediction models, namely, seasonal ARIMA with exogenous variables (SARIMAX), extreme gradient boosting (XGBoost), and long short-term memory (LSTM), were explored. The models were compared using standard error metrics including mean absolute error and root mean square error. It was found that the LSTM model results in lowest errors, followed by XGBoost. This was expected since LSTM models are known to recognize complex patterns from time series data.

The state-of-charge (SOC) prediction analysis was extended to categorical predictions of *low*, *medium*, and *high* categories to provide system operators a quick depiction of the ESRs. The models were assessed using accuracy scores and confusion matrices. Similar to the continuous time series analysis, LSTMs outperformed the other models here as well.

However, the main downside of LSTMs is the black box nature of the model, hence, limiting access to relevant insights associated to individual features. Another downside from a realistic implementation was the computational requirement in training and storing the model. While the training time of about one hour is within acceptable limits, additional analysis is required while scaling to a network of ESRs.

5. Summary

From the rise of sustainable sources of energy and upcoming technologies like electric storage, electric vehicles, and demand-side management, it is evident that the modern electric grid is undergoing a transition. The characteristics associated to the newer resources present operational challenges to multiple stakeholders in the process. This chapter summarizes the key learnings and insights derived the various approaches associated to DER participation in wholesale energy markets. Overall, chapters 2 and 3 addressed the challenges associated to aggregator decision-making. Two modeling frameworks, namely, Markov Decision Processes and Optimization using Mixed-Integer Linear Programming, are explored. On the other hand, chapter 4 presented an intra-day tool to assess future capabilities of energy storage resources.

In the approach using Markov Decision Processes, the problem is formulated using appropriate state variables, action variables, and transition probabilities. Two algorithms, dynamic programming and Q-learning, were implemented to analyze the associated intricacies. As expected, dynamic programming resulted in optimal decisions, but the computational time requirements became intractable for larger systems. On the other hand, Q-learning was observed to be relatively scalable and produced a decision with an average optimality gap of 97%.

In Chapter 3, a sequential decision-making framework is presented for an aggregator or Virtual Power Plant participating in both day-ahead and real-time energy markets. The risk preference of aggregators, and future uncertainty of solar and load resources is modeled in a mixed-integer linear programming framework to determine market bidding and battery management decisions. It was observed that the proposed framework appropriately handled the resource uncertainties using storage resources to fulfill the market obligations. A detailed analysis has been conducted to understand the effect of aggregator risk preferences, effect of various forecasting timeframes, and computational bottlenecks in the process.

Chapter 4 presented a situational assessment framework to assess electric storage resources (ESR) during the intra-day stages (i.e., ranging from 1 hour to 12 hours lookahead). Motivated by existing tools in industry to assess future profiles of renewables and quantify reserve procurement criteria, the proposed framework also aims to assist system operators to ensure reliability in the electric grid. To quantify/predict future battery state-of-charge (SOC) levels, time series prediction models have been applied on historical market prices and aggregator data. Three models, namely, seasonal ARIMA with exogenous variables (SARIMAX), extreme gradient boosting (XGBoost), and long short-term memory (LSTM), have been explored. The models were trained and analyzed for an aggregator following the decision-making presented in Chapter 3. Multiple insights about the merits and demerits of the three models have been derived and presented. In summary, it was SARIMAX was not suitable due to its limitation of failing to recognize/model complex patterns from the time series data. On the other hand, the LSTM model outperformed the other models based on various standard error metrics.

References

[1] X. Yu and Y. Xue, "Smart Grids: A Cyber–Physical Systems Perspective," *Proc. IEEE*, vol. 104, no. 5, pp. 1058–1070, May 2016, doi: 10.1109/JPROC.2015.2503119.

[2] \relax International Energy Agency (IEA), "Renewables 2021." 2021. Accessed: Mar. 14, 2023. [Online]. Available: https://www.iea.org/reports/renewables-2021

[3] E. J. Vaughan, *Risk management*. John Wiley and Sons, 1997.

[4] P. L. Bernstein, *Against the gods : the remarkable story of risk*. John Wiley and Sons, 1996.

[5] L. N. Shama, "The mean and variance of climate change in the oceans: hidden evolutionary potential under stochastic environmental variability in marine sticklebacks," *Sci. Rep.*, vol. 7, no. 1, pp. 1–14, 2017.

[6] J. B. Chakole, M. S. Kolhe, G. D. Mahapurush, A. Yadav, and M. P. Kurhekar, "A Q-learning agent for automated trading in equity stock markets," *Expert Syst. Appl.*, vol. 163, p. 113761, 2021, doi: https://doi.org/10.1016/j.eswa.2020.113761.

[7] H. Yu and D. P. Bertsekas, "Q-learning and policy iteration algorithms for stochastic shortest path problems," *Ann. Oper. Res.*, vol. 208, no. 1, pp. 95–132, 2013.

[8] C. Guan, Y. Wang, X. Lin, S. Nazarian, and M. Pedram, "Reinforcement learning-based control of residential energy storage systems for electric bill minimization," in *2015 12th Annual IEEE Consumer Communications and Networking Conference (CCNC)*, 2015, pp. 637–642. doi: 10.1109/CCNC.2015.7158054.

[9] R. Sioshansi, S. H. Madaeni, and P. Denholm, "A Dynamic Programming Approach to Estimate the Capacity Value of Energy Storage," *IEEE Trans. Power Syst.*, vol. 29, no. 1, pp. 395–403, 2014, doi: 10.1109/TPWRS.2013.2279839.

[10] N. Secomandi, "Optimal commodity trading with a capacitated storage asset," *Manag. Sci.*, vol. 56, no. 3, pp. 449–467, 2010.

[11] J. M. Nascimento and W. B. Powell, "An optimal approximate dynamic programming algorithm for the lagged asset acquisition problem," *Math. Oper. Res.*, vol. 34, no. 1, pp. 210–237, 2009.

[12] L. Hannah and D. B. Dunson, "Approximate dynamic programming for storage problems," in *ICML*, 2011.

[13] J. Nascimento and W. B. Powell, "An optimal approximate dynamic programming algorithm for concave, scalar storage problems with vector-valued controls," *IEEE Trans. Autom. Control*, vol. 58, no. 12, pp. 2995–3010, 2013.

[14] D. F. Salas and W. B. Powell, "Benchmarking a Scalable Approximate Dynamic Programming Algorithm for Stochastic Control of Grid-Level Energy Storage," *Inf. J. Comput.*, vol. 30, no. 1, pp. 106–123, 2018, doi: 10.1287/ijoc.2017.0768.

[15] R. S. Sutton and A. G. Barto, *Reinforcement learning: An introduction*. MIT press, 2018.

[16] M. L. Puterman, *Markov decision processes: discrete stochastic dynamic programming*. John Wiley & Sons, 2014.

[17] D. Bertsekas, *Dynamic programming and optimal control: Volume I*, vol. 1. Athena scientific, 2012.

[18] J. Clifton and E. Laber, "Q-learning: theory and applications," *Annu. Rev. Stat. Its Appl.*, vol. 7, pp. 279–301, 2020.

[19] F. S. Melo, "Convergence of Q-learning: A simple proof," *Inst. Syst. Robot. Tech Rep*, pp. 1–4, 2001.

[20] J. R. Vázquez-Canteli and Z. Nagy, “Reinforcement learning for demand response: A review of algorithms and modeling techniques,” *Appl. Energy*, 2019.
[21] D. R. Jiang, T. V. Pham, W. B. Powell, D. F. Salas, and W. R. Scott, “A comparison of approximate dynamic programming techniques on benchmark energy storage problems: Does anything work?,” in *2014 IEEE Symposium on Adaptive Dynamic Programming and Reinforcement Learning (ADPRL)*, 2014, pp. 1–8. doi: 10.1109/ADPRL.2014.7010626.
[22] R. Bellman, “Dynamic programming,” *Science*, vol. 153, no. 3731, pp. 34–37, 1966.
[23] M. Sewak, “Q-Learning in Code,” in *Deep Reinforcement Learning*, Springer, 2019, pp. 65–74.
[24] Solar and wind to lead growth of U.S. power generation for the next two years - U.S. Energy Information Administration (EIA). [Online]. Available: https://www.eia.gov/todayinenergy/detail.php?id=61242
[25] Solar, battery storage to lead new U.S. generating capacity additions in 2025. [Online]. Available: https://www.eia.gov/todayinenergy/detail.php?id=64586
[26] A. Agnetis, G. Dellino, G. De Pascale, G. Innocenti, M. Pranzo, and A. Vicino, “Optimization models for consumer flexibility aggregation in smart grids: The ADDRESS approach,” in *2011 IEEE First International Workshop on Smart Grid Modeling and Simulation (SGMS)*, 2011, pp. 96–101. doi: 10.1109/SGMS.2011.6089206.
[27] R. J. Bessa and M. A. Matos, “Global against divided optimization for the participation of an EV aggregator in the day-ahead electricity market. Part II: Numerical analysis,” *Electr. Power Syst. Res.*, vol. 95, pp. 319–329, 2013, doi: https://doi.org/10.1016/j.epsr.2012.08.013.
[28] M. Heleno, M. A. Matos, and J. A. P. Lopes, “Availability and Flexibility of Loads for the Provision of Reserve,” *IEEE Trans. Smart Grid*, vol. 6, no. 2, pp. 667–674, 2015, doi: 10.1109/TSG.2014.2368360.
[29] T. Roy, A. K. Jana, and K. W. Hedman, “Optimization of Aggregated Energy Resources using Sequential Decision Making,” in *2022 North American Power Symposium (NAPS)*, 2022, pp. 1–6. doi: 10.1109/NAPS56150.2022.10012186.
[30] S. Vandael, B. Claessens, M. Hommelberg, T. Holvoet, and G. Deconinck, “A Scalable Three-Step Approach for Demand Side Management of Plug-in Hybrid Vehicles,” *IEEE Trans. Smart Grid*, vol. 4, no. 2, pp. 720–728, 2013, doi: 10.1109/TSG.2012.2213847.
[31] J. Iria, P. Scott, A. Attarha, D. Gordon, and E. Franklin, “MV-LV network-secure bidding optimisation of an aggregator of prosumers in real-time energy and reserve markets,” *Energy*, vol. 242, p. 122962, 2022, doi: https://doi.org/10.1016/j.energy.2021.122962.
[32] E. G. Kardakos, C. K. Simoglou, and A. G. Bakirtzis, “Optimal Offering Strategy of a Virtual Power Plant: A Stochastic Bi-Level Approach,” *IEEE Trans. Smart Grid*, vol. 7, no. 2, pp. 794–806, 2016, doi: 10.1109/TSG.2015.2419714.
[33] B. Vatandoust, A. Ahmadian, M. A. Golkar, A. Elkamel, A. Almansoori, and M. Ghaljehei, “Risk-Averse Optimal Bidding of Electric Vehicles and Energy Storage Aggregator in Day-Ahead Frequency Regulation Market,” *IEEE Trans. Power Syst.*, vol. 34, no. 3, pp. 2036–2047, 2019, doi: 10.1109/TPWRS.2018.2888942.
[34] J. M. Kemp, M. Heleno, and A. D. Mills, “Hybrid Power Plant Bidding in Models of Future Electricity Systems,” in *2023 IEEE Power & Energy Society General Meeting (PESGM)*, 2023, pp. 1–5. doi: 10.1109/PESGM52003.2023.10252335.
[35] G. Tsaousoglou, K. Mitropoulou, K. Steriotis, N. G. Paterakis, P. Pinson, and E. Varvarigos, “Managing Distributed Flexibility Under Uncertainty by Combining Deep Learning With

Duality," *IEEE Trans. Sustain. Energy*, vol. 12, no. 4, pp. 2195–2204, 2021, doi: 10.1109/TSTE.2021.3086846.
[36] J. Qiu, K. Meng, Y. Zheng, and Z. Y. Dong, "Optimal scheduling of distributed energy resources as a virtual power plant in a transactive energy framework," *IET Gener. Transm. Distrib.*, vol. 11, no. 13, pp. 3417–3427, 2017, doi: https://doi.org/10.1049/iet-gtd.2017.0268.
[37] S. I. Vagropoulos and A. G. Bakirtzis, "Optimal Bidding Strategy for Electric Vehicle Aggregators in Electricity Markets," *IEEE Trans. Power Syst.*, vol. 28, no. 4, pp. 4031–4041, 2013, doi: 10.1109/TPWRS.2013.2274673.
[38] D. Koraki and K. Strunz, "Wind and Solar Power Integration in Electricity Markets and Distribution Networks Through Service-Centric Virtual Power Plants," *IEEE Trans. Power Syst.*, vol. 33, no. 1, pp. 473–485, 2018, doi: 10.1109/TPWRS.2017.2710481.
[39] T. Roy and K. W. Hedman, "Risk Quantification with Management of Aggregated Energy Resources," in *2024 IEEE Power & Energy Society General Meeting (PESGM)*, 2024, pp. 1–5. doi: 10.1109/PESGM51994.2024.10689045.
[40] J. Shen, C. Jiang, Y. Liu, and X. Wang, "A Microgrid Energy Management System and Risk Management Under an Electricity Market Environment," *IEEE Access*, vol. 4, pp. 2349–2356, 2016, doi: 10.1109/ACCESS.2016.2555926.
[41] Z. Xu, Z. Hu, Y. Song, and J. Wang, "Risk-Averse Optimal Bidding Strategy for Demand-Side Resource Aggregators in Day-Ahead Electricity Markets Under Uncertainty," *IEEE Trans. Smart Grid*, vol. 8, no. 1, pp. 96–105, 2017, doi: 10.1109/TSG.2015.2477101.
[42] D. T. Nguyen and L. B. Le, "Risk-Constrained Profit Maximization for Microgrid Aggregators With Demand Response," *IEEE Trans. Smart Grid*, vol. 6, no. 1, pp. 135–146, 2015, doi: 10.1109/TSG.2014.2346024.
[43] M. González Vayá and G. Andersson, "Optimal Bidding Strategy of a Plug-In Electric Vehicle Aggregator in Day-Ahead Electricity Markets Under Uncertainty," *IEEE Trans. Power Syst.*, vol. 30, no. 5, pp. 2375–2385, 2015, doi: 10.1109/TPWRS.2014.2363159.
[44] E. Sortomme and M. A. El-Sharkawi, "Optimal Combined Bidding of Vehicle-to-Grid Ancillary Services," *IEEE Trans. Smart Grid*, vol. 3, no. 1, pp. 70–79, 2012, doi: 10.1109/TSG.2011.2170099.
[45] H. Wu, M. Shahidehpour, A. Alabdulwahab, and A. Abusorrah, "A Game Theoretic Approach to Risk-Based Optimal Bidding Strategies for Electric Vehicle Aggregators in Electricity Markets With Variable Wind Energy Resources," *IEEE Trans. Sustain. Energy*, vol. 7, no. 1, pp. 374–385, 2016, doi: 10.1109/TSTE.2015.2498200.
[46] M. Di Somma, G. Graditi, and P. Siano, "Optimal Bidding Strategy for a DER Aggregator in the Day-Ahead Market in the Presence of Demand Flexibility," *IEEE Trans. Ind. Electron.*, vol. 66, no. 2, pp. 1509–1519, 2019, doi: 10.1109/TIE.2018.2829677.
[47] W. Pei, Y. Du, W. Deng, K. Sheng, H. Xiao, and H. Qu, "Optimal Bidding Strategy and Intramarket Mechanism of Microgrid Aggregator in Real-Time Balancing Market," *IEEE Trans. Ind. Inform.*, vol. 12, no. 2, pp. 587–596, 2016, doi: 10.1109/TII.2016.2522641.
[48] B. Sergi *et al.*, "ARPA-E PERFORM datasets." National Renewable Energy Laboratory (NREL), Aug. 18, 2022. doi: 10.25984/1891136.
[49] International Energy Agency, "Renewables 2024." International Energy Agency, 2024. [Online]. Available: https://www.iea.org/reports/renewables-2024

[50] J. D. Wilson, Z. Zimmerman, and R. Gramlich, “Strategic Industries Surging: Driving US Power Demand.” Grid Strategies LLC, Dec. 2024. [Online]. Available: https://gridstrategiesllc.com/wp-content/uploads/National-Load-Growth-Report-2024.pdf
[51] EIA-860 detailed data with previous form data (EIA-860A/860B). [Online]. Available: https://www.eia.gov/electricity/data/eia860/
[52] T. Bowen, I. Chernyakhovskiy, and P. L. Denholm, “Grid-Scale Battery Storage: Frequently Asked Questions,” National Renewable Energy Laboratory (NREL), Golden, CO (United States), Sept. 2019. doi: 10.2172/1561843.
[53] H. Akhavan-Hejazi and H. Mohsenian-Rad, “Optimal Operation of Independent Storage Systems in Energy and Reserve Markets With High Wind Penetration,” *IEEE Trans. Smart Grid*, vol. 5, no. 2, pp. 1088–1097, 2014, doi: 10.1109/TSG.2013.2273800.
[54] G. Liu, Y. Xu, and K. Tomsovic, “Bidding Strategy for Microgrid in Day-Ahead Market Based on Hybrid Stochastic/Robust Optimization,” *IEEE Trans. Smart Grid*, vol. 7, no. 1, pp. 227–237, 2016, doi: 10.1109/TSG.2015.2476669.
[55] D. Krishnamurthy, C. Uckun, Z. Zhou, P. R. Thimmapuram, and A. Botterud, “Energy Storage Arbitrage Under Day-Ahead and Real-Time Price Uncertainty,” *IEEE Trans. Power Syst.*, vol. 33, no. 1, pp. 84–93, 2018, doi: 10.1109/TPWRS.2017.2685347.
[56] Z. Yi, Y. Xu, H. Wang, and L. Sang, “Coordinated Operation Strategy for a Virtual Power Plant With Multiple DER Aggregators,” *IEEE Trans. Sustain. Energy*, vol. 12, no. 4, pp. 2445–2458, 2021, doi: 10.1109/TSTE.2021.3100088.
[57] Z. Tang, Y. Liu, L. Wu, J. Liu, and H. Gao, “Reserve Model of Energy Storage in Day-Ahead Joint Energy and Reserve Markets: A Stochastic UC Solution,” *IEEE Trans. Smart Grid*, vol. 12, no. 1, pp. 372–382, 2021, doi: 10.1109/TSG.2020.3009114.
[58] D. Li, J. Sun, Q. Zhao, H. Guo, Y. Feng, and B. Wang, “Optimization strategies for clearing the electric energy and FM market with combined thermal energy and storage,” in *2024 36th Chinese Control and Decision Conference (CCDC)*, 2024, pp. 5727–5732. doi: 10.1109/CCDC62350.2024.10587962.
[59] \relax Electric Power Research Institute, “Dynamic Reserve Determination Tool,” *EPRI Home*. [Online]. Available: https://www.epri.com/research/programs/067417/
[60] V. Krishnan, H. Sky, B. Roberts, P. Edwards, A. Weissman, and J. Smith, “Resource Forecast and Ramp Visualization for Situational Awareness (RAVIS).” Mar. 2021. doi: 10.11578/dc.20210418.3.
[61] C. Zhao, C. Wan, and Y. Song, “Operating Reserve Quantification Using Prediction Intervals of Wind Power: An Integrated Probabilistic Forecasting and Decision Methodology,” *IEEE Trans. Power Syst.*, vol. 36, pp. 3701–3714, 2021.
[62] Q. Wang *et al.*, “Assessing Dynamic Reserves vs. Stochastic Optimization for Effective Integration of Operating Probabilistic Forecasts,” *IEEE Trans. Sustain. Energy*, vol. 16, no. 3, pp. 2132–2143, 2025, doi: 10.1109/TSTE.2025.3547561.
[63] S. Garg, A. K. Nayak, R. Bhakar, and H. Tiwari, “Online Interval Forecast Based Operating Reserve Quantification Considering Net-Load Uncertainties,” in *2025 21st International Conference on the European Energy Market (EEM)*, 2025, pp. 1–6. doi: 10.1109/EEM64765.2025.11050254.
[64] N. Amjady, “Short-term hourly load forecasting using time-series modeling with peak load estimation capability,” *IEEE Trans. Power Syst.*, vol. 16, no. 3, pp. 498–505, 2001, doi: 10.1109/59.932287.

[65] S. Fan and R. J. Hyndman, "Short-Term Load Forecasting Based on a Semi-Parametric Additive Model," *IEEE Trans. Power Syst.*, vol. 27, no. 1, pp. 134–141, 2012, doi: 10.1109/TPWRS.2011.2162082.
[66] C. Wan, Z. Xu, P. Pinson, Z. Y. Dong, and K. P. Wong, "Probabilistic Forecasting of Wind Power Generation Using Extreme Learning Machine," *IEEE Trans. Power Syst.*, vol. 29, no. 3, pp. 1033–1044, 2014, doi: 10.1109/TPWRS.2013.2287871.
[67] J. Song, L. Jin, Y. Xie, and C. Wei, "Optimized XGBoost based sparrow search algorithm for short-term load forecasting," in *2021 IEEE International Conference on Computer Science, Artificial Intelligence and Electronic Engineering (CSAIEE)*, 2021, pp. 213–217. doi: 10.1109/CSAIEE54046.2021.9543453.
[68] X. Yao, X. Fu, and C. Zong, "Short-Term Load Forecasting Method Based on Feature Preference Strategy and LightGBM-XGboost," *IEEE Access*, vol. 10, pp. 75257–75268, 2022, doi: 10.1109/ACCESS.2022.3192011.
[69] S. H. Rafi, Nahid-Al-Masood, S. R. Deeba, and E. Hossain, "A Short-Term Load Forecasting Method Using Integrated CNN and LSTM Network," *IEEE Access*, vol. 9, pp. 32436–32448, 2021, doi: 10.1109/ACCESS.2021.3060654.
[70] Y. Wang *et al.*, "Short-Term Load Forecasting for Industrial Customers Based on TCN-LightGBM," *IEEE Trans. Power Syst.*, vol. 36, no. 3, pp. 1984–1997, 2021, doi: 10.1109/TPWRS.2020.3028133.
[71] F. Golestaneh, P. Pinson, and H. B. Gooi, "Very Short-Term Nonparametric Probabilistic Forecasting of Renewable Energy Generation— With Application to Solar Energy," *IEEE Trans. Power Syst.*, vol. 31, no. 5, pp. 3850–3863, 2016, doi: 10.1109/TPWRS.2015.2502423.
[72] A. Gensler, J. Henze, B. Sick, and N. Raabe, "Deep Learning for solar power forecasting — An approach using AutoEncoder and LSTM Neural Networks," in *2016 IEEE International Conference on Systems, Man, and Cybernetics (SMC)*, 2016, pp. 002858–002865. doi: 10.1109/SMC.2016.7844673.
[73] Y. Chen, Y. Wang, D. Kirschen, and B. Zhang, "Model-Free Renewable Scenario Generation Using Generative Adversarial Networks," *IEEE Trans. Power Syst.*, vol. 33, no. 3, pp. 3265–3275, 2018, doi: 10.1109/TPWRS.2018.2794541.
[74] A. B. Mohideen, M. A. K. Reddy, T. C. Dinesh, I. S. Reddy, and M. P. Kumar, "A Hybrid Approach of LSTM and ARIMA for Enhancing Numerical Weather Prediction Accuracy Using Deep Learning," in *2025 6th International Conference on Inventive Research in Computing Applications (ICIRCA)*, 2025, pp. 1064–1071. doi: 10.1109/ICIRCA65293.2025.11089776.
[75] L. Li and Q. Jian, "Health Assessment and Prognosis of Offshore Wind Turbine Blades Under Variable Operating Conditions via Optimized Bi-LSTM," *IEEE Sens. J.*, vol. 25, no. 10, pp. 18223–18235, 2025, doi: 10.1109/JSEN.2025.3554645.
[76] T. Chen and C. Guestrin, "XGBoost: A Scalable Tree Boosting System," in *Proceedings of the 22nd ACM SIGKDD International Conference on Knowledge Discovery and Data Mining*, in KDD '16. New York, NY, USA: Association for Computing Machinery, 2016, pp. 785–794. doi: 10.1145/2939672.2939785.
[77] S. Hochreiter and J. Schmidhuber, "Long Short-Term Memory," *Neural Comput.*, vol. 9, no. 8, pp. 1735–1780, 1997, doi: 10.1162/neco.1997.9.8.1735.
[78] F. Pedregosa *et al.*, "Scikit-learn: Machine Learning in Python," *J. Mach. Learn. Res.*, vol. 12, pp. 2825–2830, 2011.

[79] T. Akiba, S. Sano, T. Yanase, T. Ohta, and M. Koyama, “Optuna: A Next-generation Hyperparameter Optimization Framework,” in *Proceedings of the 25th ACM SIGKDD International Conference on Knowledge Discovery and Data Mining*, 2019.

Part II

DER and Smart Inverter Management for Coordinating Transmission - Distribution Services and Enhancing Distribution System Flexibility

Mojdeh Khorsand
Hari Krishna Achuthan Parthasarathy, Graduate Student

Arizona State University

For information about this project, contact

Mojdeh Khorsand
Arizona State University
School of Electrical. Computer, and Energy Engineering
P.O. Box 875706
Tempe, AZ 85287-5706
Phone: (480) 965-0787
Email: mojdeh.khorsand@asu.edu

Power Systems Engineering Research Center

The Power Systems Engineering Research Center (PSERC) is a multi-university Center conducting research on challenges facing the electric power industry and educating the next generation of power engineers. More information about PSERC can be found at the Center's website: http://www.pserc.org.

For additional information, contact:

Power Systems Engineering Research Center
Arizona State University
527 Engineering Research Center
Tempe, Arizona 85287-5706
Phone: 480-965-1643
Fax: 480-727-2052

Notice Concerning Copyright Material

Table of Contents

List of Figures

List of Tables

1. Unified Mode Selection Framework for DER Scheduling Applications Considering Unbalanced Distribution Systems

1.1 Introduction

The modern-day distribution system is constantly evolving due to the increasing push behind the adoption of renewable energy resources. Installation of residential PV rooftop units are leading the wave in this drive behind the adoption. According to [1], as shown in Figure 1.1, the United States observed a growth in the installation of small-scale solar capacity from 7.3 GW in 2014 to 39.5 GW in 2022. This growth is due to several social and economic factors, including the conscious decision to reduce the impact on the environment by utilizing more sustainable forms of energy.

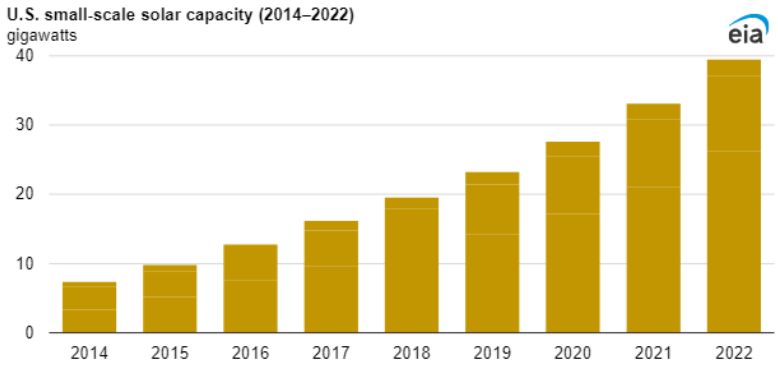

Figure 1.1 Installed Small-Scale PV Capacity in the US between the Years 2014-2022 [1]

From a financial standpoint, [2] presents an economic analysis of residential rooftop PV installation in the state of Texas for a generic system. Comprehensively considering factors such as, but not limited to the Net Present Value (NPV) and the Payback Period (PP), a Profitability Index (PI) of 1.31 was projected, which implies that investing in such a system is a prudent and a profitable venture. Coupled with the present-day incentives from the government and the net metering policies of utilities across the United States, this growth is inevitable. The accelerated growth is also having a severe impact on the distribution system operation due to several issues. High amounts of penetration present a challenging phenomenon, known as "Reverse power flow", where the excess power generated flows back through the substation, to the power grid. This phenomenon occurs during discrete time periods over the course of 24 hours, where the PV active power generated exceeds the residential load demand in the distribution feeder.

Due to this phenomenon, bus voltages at the end nodes of the feeder are usually higher than bus voltages, situated closer to the substation. Excess power flow could also cause thermal line limit violation issues in the feeders due to high amounts of current being fed back to the grid. During seasons such as spring, low demand and high solar irradiance are observed. Owing to nominal ambient temperatures, residential cooling loads are reduced, which account for a significant portion of residential loads during the daytime. Linking these factors together, distribution feeders experience severe overvoltage issues. According to ANSI C84.1-1995, voltage magnitude within the feeder are to be maintained between 0.95 pu and 1.05 pu. Excessive overvoltage issues can

cause severe problems including insulation damage to equipment connected to the feeder, and reduction in the lifetime of the equipment. Higher no-load losses in transformers are also observed considering how magnetizing currents are higher at higher voltages [3].

The growth of renewable resources has also positively impacted the increasing adoption of EVs. Residential customers install charging resources within their own homes for ease of access. Characterized by high power inverter-based energy storage and drive trains, the charging process of EVs also accounts for a significant portion of residential demand. As the charging time itself is a consumer choice, accurately predicting changes in demand is a difficult task. At secondary sections, feeders majorly consist of single-phase lines which implies specific neighborhoods have a specific phase connection. Affluent neighborhoods would tend to adopt EVs at a much higher rate due to high price points. This dynamic causes an imbalance in the amount of EV loads being charged in a specific phase, causing voltage unbalance in the primary sections of the feeder. Voltage unbalance is also caused due to other reasons, but primarily due to unbalanced loading conditions on a specific phase. Three-phase equipment connected to the primary sections including power distribution equipment are less efficient due to increased negative-sequence voltages causing overheating. These thermal issues also cause lifetime reductions for the equipment causing monetary loss to the utility and the consumers within the feeder [3].

High penetration levels of PV units also cause protection scheme malfunction and protection "desensitization" due to the reverse power flow phenomenon [4]. A rapid imbalance in adoption of PV units within the feeder also creates potential scenarios for miscoordination among protection schemes [5]. With the active power transfer potentially being bi-directional at the substation with the increasing penetration, solutions such as increased short circuit capacity, harmonic mitigation and grid islanding protection are required [6]. Reference [6] also mentions the potential rise in flicker and stress issues on distribution transformers which effectively increases the likelihood of failure in these equipment. Conventional issues such as overvoltage and voltage unbalance were typically solved using legacy VAr support devices such as On Load Tap Changers (OLTCs), switched capacitor banks, and voltage regulators. But the introduction of Inverter Based Resources (IBRs) has introduced a new challenge which is to be handled. Inverters operate at time scales different from conventional rotating machines (due to the high frequency switching nature). Considering the highly intermittent nature of PV resources, the coupled phenomenon causes dynamic fast voltage fluctuations in the grid, that adversely affect the loads connected within the distribution feeder.

Considering the above factors, the operation of the modern distribution system has evolved beyond the existing control and operational infrastructure and strategy. Coupled with new developments on maximizing resources, a significant overhaul of the primitive infrastructure and strategy is required.

1.1.1 Background and Motivation

Based on FERC order 2222 [7], DER aggregators are encouraged to participate in the wholesale market, based on Independent System Operators (ISOs) proposed coordination and participation rules. This order enables maximizing the potential of the excess power generated by DERs in the distribution system. However, in the pursuit of fulfilling aggregator bids, distribution system operational limits should not be violated. Reference [8] simulated 10% increments of system PV

penetration, to show that the number of voltage violation and unbalance occurrences in half-hourly time steps, exponentially increased with increase in penetration. Inverters shutting off due to voltage issues also caused severe monetary loss, as cheaper retail price resources were lost.

Typically, voltage issues were handled by legacy VAr support devices such as OLTCs, switched capacitor banks and voltage regulators. These devices do not serve as an effective solution due to multiple reasons. Reference [9] describes how intermittent PV output and fast control actions of inverters cause voltage fluctuations to occur rapidly, that traditional OLTCs and switched capacitors cannot regulate these fluctuations. Lowering the set-point of OLTCs at the substation could help with meeting voltage limits but might not ensure this thought the feeder [9]. In a study conducted in [10], the fast voltage fluctuations caused excessive OLTC operations, which can reduce the lifetime of distribution equipment, and cause increased maintenance costs. With the introduction of the IEEE 1547-2018 standards [11], DERs are allowed to provide reactive power support for voltage regulation issues in distribution feeders. Due to the fast control actions of SIs, fast voltage fluctuations are effectively handled. The standards specify four distinct reactive power operational modes including constant power factor mode, constant reactive power mode, voltage-reactive power mode (Volt-VAr) and active power-reactive power mode (Watt-VAr), of which the latter two are popular operational modes (Table 1.1). Apart from this, a voltage-active power (Volt-Watt) mode of operation is also specified, which is meant to be enabled along with any one of the reactive power operational modes. The inclusion of these modes under standard operation depend upon the category of standard. Category A corresponds to minimum performance capabilities for voltage regulation attained by current DERs [11]. Category B corresponds to all the capabilities included in category A and supplemental requirements where DER penetrations are higher [11].

Table 1.1 Reactive and Active Power Operational Modes Following IEEE 1547-2018 [11]

DER Category	Category A	Category B
Reactive Power Operational Mode		
Constant Power Factor Mode	Mandatory	Mandatory
Constant Reactive Power Mode	Mandatory	Mandatory
Voltage-Reactive Power Mode	Mandatory	Mandatory
Active Power-Reactive Power Mode	Not required	Mandatory
Active Power Operational Mode		
Voltage-Active Power Mode	Not required	Mandatory

The proper utilization of these reactive power capabilities can improve voltage issues at local buses. To maximize the effect of sparsely populated smart inverters, a robust optimal power flow model is required. Modeling the distribution system is a difficult task considering the high R/X ratio. An effective model considers the unbalanced nature of distribution systems as well as the single phase and three phase lines, the mutual impedance, and the shunt admittances. Including all these features increases model complexity and excluding them affects accuracy. Finally, considering all the above-mentioned factors, a DER scheduling tool must also be computationally efficient.

1.1.2 Contributions

Taking into account the above-mentioned issues, the goals and contributions of this work include:

- Formulation of a piece-wise Watt-VAr operational mode, compliant to the IEEE 1547-2018 standards, for smart inverters, capable of injecting reactive power to the feeder as a function of active power output.
- Inducting the Watt-VAr curve into a robust DOPF (Distribution Optimal Power Flow) to create a DER scheduling tool capable of dispatching individual inverters in the feeder.
- Developing a model which co-optimizes the Watt-VAr operational curve according to the IEEE 1547-2018 standards, based on system operational conditions to schedule the optimal amount of active and reactive power.
- Formulation and induction of the Volt-Watt operational mode, compliant to the IEEE 1547-2018 standard, into a robust DOPF to create a DER scheduling tool.
- Presenting different approaches to minimize voltage unbalance in a distribution feeder within the optimization framework, including a constraint-based approach and an objective-based approach.
- Formulation and development of a UMS (Unified Mode Selection) operational framework, capable of optimally selecting the operational mode, within the DER scheduling tool.
- Formulating additional constraints to develop a Co-optimized UMS operational framework capable of optimally selecting the operational mode and zone, within the DER scheduling tool.

1.2 Literature Survey

1.2.1 Issues Faced by the Modern Distribution System

Due to the accelerated adoption of roof-top residential PV units, several power quality issues have risen, including voltage issues such as voltage unbalance and voltage violation. Historically, voltage regulation devices such as OLTCs, switched capacitors and voltage regulators efficiently mitigated these issues. Due to the highly intermittent nature of PV units and the fast control actions of SIs, the power grid is subject to excess fast voltage fluctuations. Reference [9] describes how the rapid nature of the fluctuations cannot be efficiently mitigated by legacy VAr devices such as OLTCs and switched capacitors. Tap changes are performed over set time scales which are orders of magnitude larger than that of voltage fluctuations. Apart from the speed of operations, legacy VAr devices are inhibited by the frequency of corrective operations. In a study conducted in [10], a co-simulation of transmission and distribution system under DER penetration was performed, which exhibited excessive operations of OLTCs to handle the issue of intermittency. Reference [10] also mentions the ineffectiveness of OLTCs in terms of its sparse nature to handle voltage issues. The fast control actions of SIs also have the possibility of causing equipment malfunction among legacy VAr devices [4]. Continuous operation of these devices in high voltages also affects insulation strength and causes lifetime reduction [3]. Coupled with the cost of maintenance and replacement, a comprehensive solution is required to augment the operation of legacy VAr devices.

Reference [8] describes how increasing penetration of PV units in low voltage distribution systems is causing increasing voltage violation issues. Based on a simulation performed on a pi-modeled

balanced circuit with shunt admittance, a linear increase in penetration caused an exponential increase in the overvoltage instances observed. As mentioned in [3], continuous operation in abnormal voltages causes insulation degradation and equipment to be replaced more often. Intermittency of PV also causes undervoltage scenarios which reduce the efficiency of the equipment as increased losses are observed due to more current being drawn [3]. Voltage unbalance is also another issue faced due to an imbalance in penetration levels among different phases and the increasing adoption of EVs. The work presented in [12], describes how distribution feeders experience severe unbalance due to EVs, especially at the secondary sections. A test conducted on the effect of charging and discharging operations on a generic radial distribution feeder, showed that the system voltage unbalance exceeded 2% in 34% of the testing scenarios [12]. Another cause of the problem might be due to the large single-phase laterals, due to heavily loaded phases [3].

The main effects of voltage unbalance are observed in loads and distribution feeder equipment connected to the primary sections of the feeder which are majorly three phase. Any three-phase equipment in operation requires a nominal supply voltage, without which equipment efficiency and lifetime is affected. Extended operations in unbalanced conditions causes thermal issues and lifetime reduction in motor loads connected to the feeder [4]. This reduction can be attributed to increasing current unbalance and magnitude in a single phase which increases losses in the winding [13]. Significant torque oscillations are also observed due to amplified harmonics in the current and voltage [13].There are several solutions mentioned among literature in solving the issue of voltage unbalance. Historically, as the root cause of voltage unbalance was due to imbalance in loading conditions, load reduction was performed by equally redistributing the loads [3]. The single-phase laterals connected to heavy loads were connected to different phases to redistribute the load. Reference [3] also describes how loads were transferred to another circuit through reconnection to solve this issue. Due to the rapid nature of the EV charging and discharging process, load imbalance is more frequent with a greater magnitude of change [12]. Therefore, reconnection to solve the issue of voltage unbalance is not a practical solution. References [14] and [15] present strategies in limiting voltage unbalance caused by increasing charging operations of EVs with charging management. Reference [14] mentions two approaches to solving the unbalance issue. The first approach involves optimal phase switching of the EV charger connections to balance load in the feeder. Even with the presence of automated switches with control, the sparse nature of this equipment makes this solution impractical. The second approach involves active power charging and reactive power discharging from the inverters within the EVs [14]. Reactive power discharge can help alleviate voltage issues, but also impede charging capacity due to inverter apparent power limits. The solution as presented in [15], involves limiting unbalance by controlling the EV charging rate as a function of voltage unbalance and a fixed active power set-point. Both the above-mentioned solutions from [14] and [15] involve charging rate curtailment which impedes consumer experience. Therefore, these solutions may not be practical.

1.2.2 Distribution System Modeling

Considering the above-mentioned facts and the objective of FERC order 2222 [7], a comprehensive solution is to be developed. This solution should be capable of mitigating voltage issues within the distribution feeder, without impeding consumer experience, while still maximizing the potential of roof-top PV units as directed by [7]. The appropriate solution as

enabled by the IEEE 1547-2018 standards [11] would be a scheduling mechanism which takes network conditions into account and optimally dispatches SIs in the feeder. Such a mechanism involves complex components, including a robust distribution system model, accurate development of SI reactive power capability according to the IEEE 1547 standards [11], and a computationally efficient formulation. Traditionally, distribution systems have been a passive fragment of the bulk power system with transmission system modeling and dispatch taking precedence. With the increasing active nature of distribution systems, modeling and dispatch are being more vigorously investigated. Transmission systems consist of low R/X ratio and balanced circuits, which enable them to have a simpler model by utilizing assumptions [3]. These assumptions also include the strong coupling between voltage-reactive power and angle-active power. The same assumptions cannot be applied to distribution systems due to several reasons.

Distribution systems generally have high R/X ratios which implies the resistive nature of the circuit dominates the reactive nature. This fact reverses the strong coupling effect, where distribution systems have a strong coupling phenomenon between voltage-active power and angle-reactive power [3]. Apart from this effect, distribution systems cannot be assumed to be balanced systems. This is due to characteristics such as the multiphase (distribution systems consist of three phase lines, single phase laterals) and the untransposed nature. The mutual impedance and shunt admittance cannot be ignored due to the fact that lines are not transposed. References [8], [16], [17], [18], [19], [20], [21], [22] all present VAr control strategies for feeders with high PV penetration based on balanced distribution system models. There are a few drawbacks with regard to utilizing a balanced distribution system model. One such drawback is the reduction in dispatch accuracy, which is caused by the inability to capture the virtual paths between the phases. This affects the accuracy of current estimation in a specific phase. Moreover, a significant portion of the rooftop PV units installed are single phase units, which implies a more comprehensive model is required to dispatch such units. Issues such as voltage unbalance cannot be mitigated without having a multi-phase representation of the distribution system. Therefore, modeling the distribution system accurately is a significant requirement.

A substantial portion of a dispatch mechanism involves a robust DOPF (Distribution Optimal Power Flow) model which is capable of efficiently computing dispatch metrics and also modeling the distribution system accurately. As the distribution power flow model is inherently non-linear, it is pertinent to balance solution accuracy and solution quality. The literature reviewed in this section, present distinct formulations to represent such a tool, including Mixed Integer Non-Linear Programming (MINLP) models, Mixed Integer Second Order Cone Programming (MISOCP) models, and Mixed Integer Linear Programming (MILP) models. These models are solved using commercial solvers specified for LP, MILP and NLP. References [22], [23], [24], [25], and [26] all present either NLP or MINLP based DOPF models which rely on a nonlinear power flow model. In all instances, generic solver were used to solve these problems, with the test systems being limited to 123 bus systems. The interior point method, or variations of it were used to solve these models, which traverses the interior portions of the feasible region which aids in large scale problems, but this property is specific to problem types.

Reference [27] benchmarks different formulations for a DOPF application using commercial solvers and well-known distribution system models. The main observation of this study points to the fact that NLP models are hindered by the issue of scalability, with large test cases not converging. From this observation, it is concluded that for the DOPF application, two issues plague

NLP models, including the issues of model scalability and solution quality (due to the solver converging to local optimal solutions) [27]. Therefore, ensuring model convexity can aid in the quality of solution obtained. Due to the increasing robustness of MILP solvers in recent times, mixed integer convex models are more popular as they solve the issue of solution quality and exhibit good scalability. Convex relaxations provide good alternatives to non-convex models due to solution guarantees. References [16], [17], [18], and [19], present convex relaxations to the non-linear non-convex DOPF models using techniques such as Second Order Cone Programming (SOCP) and Semi Definite Programming (SDP). Convex relaxations work by fitting the non-convex regions of the feasible space with a convex estimator. One main drawback of these relaxation techniques is that they lead to expanded feasible regions. This expansion leads to a possibility where the converged solution might not be a feasible to the original problem, leading to "inexactness" [28].

Linear formulations of power flow in distribution systems often involve an approximation technique which effectively transforms the non-linear non-convex portion of the formulation into linear versions. Taylor series approximation, McCormick linearization, polyhedral linearization are a few examples of approximation techniques. References [29] and [30] present DOPF models based on polyhedral linearization. This linearization involves the calculation of derivatives to form a tight convex hull at specific points to form a piecewise approximation. Techniques such as polyhedral linearization often involve a large number of linear constraints to approximate the true feasible region which might make them computationally expensive [31]. References [21], [29], [30], and [32] present linearized DOPF formulations such as LinDistFlow and LinDist3Flow which make assumptions on system conditions to approximate the non-linearities and complexities in the model. As mentioned in [32] which presents a multiphase unbalanced formulation of the LinDistFlow model, terms associated with the loss are neglected, and ratio of voltage phasors are considered to be constant. Apart from the reduction in accuracy due to the ignoring of losses, the assumption regarding the ratio of voltage phasors to be constant, affects the model from being used in voltage balancing applications [32].

1.2.3 Volt-VAr and Volt-Watt Operational Mode in Literature

According to the IEEE 1547-2018 standards, SIs are allowed to provide VAr support according to four distinct modes of operations. Volt-VAr and Watt-VAr operational modes are two popular solutions widely discussed among literature. References [18], [24], [25], [26], [29], [30], and [33] model reactive power operational modes controlled by bus voltages. Both [29] and [30] present an unbalanced DOPF based on the LinDist3Flow model, where the constraints related to smart inverters are linearized with polyhedral linearization. Reference [29] formulates Volt-Watt and Volt-VAr curves utilizing the lambda method with the objective of minimizing net load curve. The set-points of the Volt-Watt curve chosen exceed the range of limits as prescribed by the IEEE 1547-2018 standards. This issue leads to real time unavailability of scheduled reactive power as the SI follows the curve according to the IEEE 1547-2018 standards. A two-stage solution is presented in [30], where the first stage is a centralized DOPF optimization process where active power dispatch and LTC status is decided. A fixed Volt-VAr curve is modeled with a combination of the Big-M method and Bilinear constraints. The second stage presents an adaptive delta Volt-VAr curve where the slope is modified using a controller. The work presented in [33], describes a two-stage implementation, where the Volt-VAr curve is accurately modeled according to the IEEE

1547-2018 standards, within an unbalanced DOPF in the first stage. From the active power dispatch obtained in the first stage, the second stage models the Volt-Watt curve according to the IEEE 1547-2018 standards and obtains the voltages, active power, and reactive power values. As Volt-Watt operates beyond 1.05 pu, modeling the curve within a framework with the objective of limiting the voltage violation below 1.05 pu is retroactive.

Reference [18] presents a DOPF based on a balanced BFM (Branch Flow Model) which is relaxed using SOCP. The piecewise Volt-VAr curve according to the IEEE 1547-2018 standards, is modeled using bilinear terms which is relaxed using different linearization techniques such as Taylor series, McCormick relaxation, quadratic relaxation, and piecewise quadratic relaxation. The objective of the tool was to minimize system loss. As mentioned previously, SOCP leads to expanded feasible regions, where the solution obtained may not be feasible to the original problem [28].References [24], [25] and [26] present unbalanced DOPFs based on an NLP formulation. Both [24] and [25] perform the same task of performing mode selection on 4 modes including Volt-Watt, Volt-VAr (P-priority), and Volt-VAr (Q-Priority). The main drawback of this approach is that the mode selection includes Volt-Watt, which is an active power curtailment operational mode which works on top of the other modes listed above [11]. Considering the overall objective of DER scheduling to maximize PV utilization, Volt-VAr should by default be operated with P-priority.

Apart from this, the oversized inverters have rated reactive power ratings of 0.6 pu, which, even considering the oversizing factor, according to the IEEE 1547-2018 standards, should not exceed 0.55 pu. Reference [26] presents a nonlinear DOPF formulation which models a similar set of control modes as mentioned above with the exception of the action of mode selection. This system is solved using Particle Swarm Optimization (PSO) which is a meta-heuristic algorithm, affected by slow convergence and solution quality [34]. One common observation among [24], [25] and [26] is the fact that the test systems never exceeded a 123-bus system. This further explains the issue of solution quality and scalability for DOPF applications using MINLP and NLP formulations [27].

1.2.4 Watt-VAr Operational Mode in Literature

High R/X ratio of distribution systems imply a greater sensitivity of voltage to active power change. Utilizing this property, active power generation curtailment strategy can serve as a good solution to mitigate voltage issues across distribution feeders. The adverse effect of utilizing this strategy is the cost penalty associated with the increased cost of operation. This penalty is due to the reduction in the utilization of cheap renewable resources. The literature survey presented in this section covers [16], [19], [21], [22], [35], and [36] which present an active power-reactive power operational scheme for VAr dispatch. References [35] and [36] present active power-reactive power operational schemes, with modified slope factors computed based on the voltage difference and the reactive power injected, with respect to a threshold. This implementation is performed system wide using voltage sensitivity matrices, based on a power flow model. The usage of voltage sensitivity matrices imply that the solution obtained yields a feasible solution but does not guarantee an optimal solution. Apart from this, a power flow model is used, instead of an optimal power flow model which suggests that active power dispatch is not controlled. Reference [21] presents a LinDistFlow model based OPF assuming a balanced distribution system. The Watt-VAr curve is formulated using a set of bilinear constraints according to the IEEE 1547-2018 standard, which are linearized using McCormick relaxation. A mixed integer formulation is

presented where optimal setting selection is also performed. Due to the balanced representation of the distribution system model, the formulation possibly suffers from accuracy issues.

Reference [16] and [19] present balanced DOPF models based on convex relaxations. The work presented in [16] involves a balanced DistFlow model which is relaxed using SOCP. A two-stage solution is proposed with a centralized optimization process (Day-Ahead) for dispatch points in the feeder considering the objective of minimizing losses and voltage violations. A secondary stage (hourly time step) is presented for local VAr control using Convolution Neural Networks (CNNs). The dispatch of OLTCs and capacitor banks are considered in the primary stage. The assumption of a balanced system also adds to the inability to model voltage unbalance mitigation. The formulation presented in [19], considers a pi-model, which includes the complete representation of circuit including shunt admittances, relaxed utilizing SDP. However, the assumption of a balanced system affects the ability to consider the effect of mutual impedance and admittances within the formulation. This assumption affects the solution accuracy. Moreover, both [16] and [19] model the Watt-VAr curves in an approach which is not compliant to the IEEE 1547-2018 standard [11].

Reference [22] presents an NLP based probabilistic approach of hosting high PV penetration, considering the stochastic nature of PVs and the loads. With the assumption of a balanced distribution system, the work minimizes the total voltage deviation and the PV power output for a 33-bus distribution system. Optimal PV placement is also performed within this formulation. Apart from the assumption of balanced system, the Watt-VAr mode of operation does not contain a piece-wise curve as prescribed by the IEEE 1547-2018 standard, with the reactive power only constrained by capacity and a function of active power.

1.2.5 Operational Mode Selection in Literature

Mode selection has not been widely presented in literature considering the complexities involved in modeling such a framework. To the best of the author's knowledge, [24] and [25] (which is an extension of [24]) are the only two works, to present a mode selection framework, wherein different reactive power operational modes are modeled. As mentioned previously, both the works contain an MINLP based unbalanced distribution system model where four different operation modes such as Volt-Watt, Volt-VAr (P-Priority), Volt-VAr (Q-Priority) and constant power factor mode are modeled and whose set-points are optimized. This two-stage implementation is tested on an IEEE 123 bus system with the objective of minimizing total voltage deviation. The piece-wise curves are modeled using Heavyside functions.

The rated reactive power limits for inverters are calculated on the basis of an oversizing factor of 1.25 pu, to be 0.6 pu [24]-[25]. According to the IEEE 1547-2018 standards [11], the rated value of reactive power dispatch cannot be more than 44% of rated apparent power limits, which imply that the reactive power limits considered should not exceed 0.55 pu. Apart from this, Volt-Watt, which is an active power reactive power capability mode, according to the standard [11], is to be enabled in conjunction with one of the reactive power capability modes. Having a mode selection framework optimally selecting between Volt-Watt and the other three modes is counterintuitive considering the nature of the operational modes. In the case of minimizing an objective function which involves active power curtailment of PVs, operational costs and so on, active power from PVs should be prioritized, as presented in this thesis. So, the Volt-VAr mode of operation

inherently assumes active power priority (P-Priority) even though it is not comprehensively specified by the standards. The largest test system utilized in [24] and [25] is the IEEE 123 bus system. Scalability is one issue that can potentially affect this approach due to the MINLP formulation [27].

1.3 Active Power-Reactive Power Operational Mode

1.3.1 Watt VAr Mode

According to the IEEE 1547-2018 standards, Watt-VAr operational mode involves the control of reactive power dispatch as a function of active power dispatch of the inverter. The participation of DERs in any specified reactive power operational mode for voltage regulation requires the approval of the area Electric Power System (EPS) operator [11]. The specified characteristic is a piecewise linear active power-reactive power function. Figure 1.1 exhibits the Watt-VAr curve as specified by the IEEE 1547-2018 standard. The characteristic curve has 7 different zones of operation including 6 operating set-points for both active power and reactive power. As defined by the default values of the curve settings, each zone represents reactive power dispatch values to be followed as a linear function of active power dispatch.

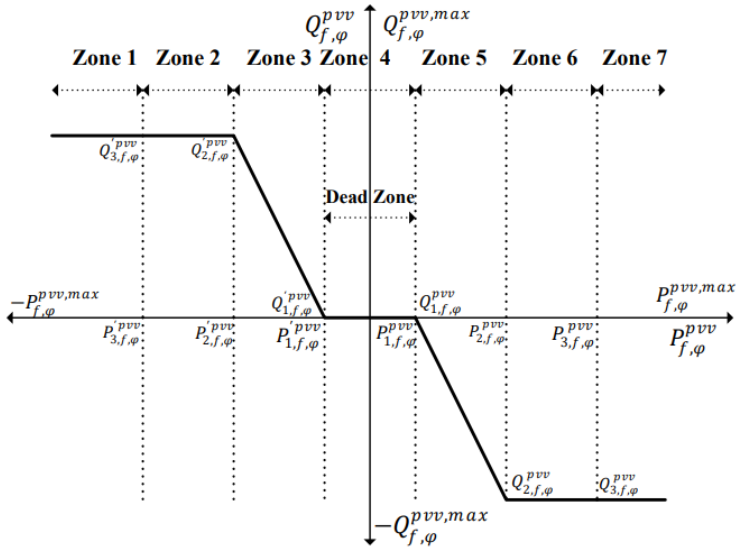

Figure 1.2 The Watt-VAr Piecewise Linear Function According to the IEEE 1547-2018 Standard [11]

Zone 1 represents the zone of operation, where beyond active power set-point $P_{3,\varphi}^{'pvv}$, the inverter injects constant reactive power into the grid, as defined by $Q_{3,\varphi}^{'pvv}$. Zone 2 represents the zone of operation, where between $P_{3,\varphi}^{'pvv}$ and $P_{2,\varphi}^{'pvv}$, the inverter injects reactive power according to a linear relationship with the active power dispatch as defined by the slope between $(P_{3,\varphi}^{'pvv}, Q_{3,\varphi}^{'pvv})$ and $(P_{2,\varphi}^{'pvv}, Q_{2,\varphi}^{'pvv})$. Zone 3 represents the zone of operation, where between $P_{2,\varphi}^{'pvv}$ and $P_{1,\varphi}^{'pvv}$, the inverter injects reactive power according to a linear relationship with the active power dispatch as defined by the slope between $(P_{2,\varphi}^{'pvv}, Q_{2,\varphi}^{'pvv})$ and $(P_{1,\varphi}^{'pvv}, Q_{1,\varphi}^{'pvv})$. Zone 4 represents the zone of

operation, where between $P_{1,\varphi}^{'pvv}$ and $P_{1,\varphi}^{pvv}$, the inverter injects or absorbs reactive power according to a linear relationship with the active power dispatch as defined by the slope between $(P_{1,\varphi}^{'pvv}, Q_{1,\varphi}^{'pvv})$ and $\left(P_{1,\varphi}^{pvv}, Q_{1,\varphi}^{pvv}\right)$. Zone 4 is usually modeled as a dead zone, by considering the values of $(P_{1,\varphi}^{'pvv}, Q_{1,\varphi}^{'pvv})$ and $\left(P_{1,\varphi}^{pvv}, Q_{1,\varphi}^{pvv}\right)$ such that, reactive power is neither injected nor absorbed by the SI.

Zone 5 represents the zone of operation, where between $P_{1,\varphi}^{pvv}$ and $P_{2,\varphi}^{pvv}$, the inverter absorbs reactive power according to a linear relationship with the active power dispatch as defined by the slope between $(P_{1,\varphi}^{pvv}, Q_{1,\varphi}^{pvv})$ and $\left(P_{2,\varphi}^{pvv}, Q_{2,\varphi}^{pvv}\right)$. Zone 6 represents the zone of operation, where between $P_{2,\varphi}^{pvv}$ and $P_{3,\varphi}^{pvv}$, the inverter absorbs reactive power according to a linear relationship with the active power dispatch as defined by the slope between $(P_{2,\varphi}^{pvv}, Q_{2,\varphi}^{pvv})$ and $\left(P_{3,\varphi}^{pvv}, Q_{3,\varphi}^{pvv}\right)$. Zone 7 represents the zone of operation, where beyond $P_{3,\varphi}^{pvv}$, the inverter absorbs reactive power according to the reactive power set-point $Q_{3,\varphi}^{pvv}$. The IEEE 1547-2018 standard has enabled SIs to modify these set-points within an allowable range which are to be immediately implemented by the DER operator [11]. Table 1.2 and Table 1.3 describes the default settings utilized and the allowable range of modifications for the set-points as described by the IEEE 1547-2018 standard. $P_{f,\varphi}^{'max,pvv}$ and $P_{f,\varphi}^{max,pvv}$ correspond to the respective rated active power absorption and injection limit for each Inverter f at Phase φ. Active power absorption is enabled only when the inverter is interfaced to a Battery Energy Storage (BES) device, and therefore $P_{f,\varphi}^{'max,pvv}$ is constrained by the device capacity.

Table 1.2 Active Power Set-Points for the Watt-VAr Operational Mode Curve Following the IEEE 1547-2018 Standard [11]

Active Power Set-Points	Default Settings	Modification Range	
		Minimum	Maximum
$P_{3,\varphi}^{'pvv}$	100 % $P_{f,\varphi}^{'max,pvv}$	$P_{f,\varphi}^{'max,pvv}$	$P_{2,\varphi}^{'pvv}$+10% $P_{f,\varphi}^{'max,pvv}$
$P_{2,\varphi}^{'pvv}$	40 % $P_{f,\varphi}^{'max,pvv}$	80% $P_{f,\varphi}^{'max,pvv}$	40% $P_{f,\varphi}^{'max,pvv}$
$P_{1,\varphi}^{'pvv}$	20 % $P_{f,\varphi}^{'max,pvv}$	$P_{2,\varphi}^{'pvv}$-10% $P_{f,\varphi}^{'max,pvv}$	0
$P_{1,\varphi}^{pvv}$	20 % $P_{f,\varphi}^{max,pvv}$	0	$P_{2,\varphi}^{pvv}$-10% $P_{f,\varphi}^{max,pvv}$
$P_{2,\varphi}^{pvv}$	40 % $P_{f,\varphi}^{max,pvv}$	40% $P_{f,\varphi}^{max,pvv}$	80% $P_{f,\varphi}^{max,pvv}$
$P_{3,\varphi}^{pvv}$	100 % $P_{f,\varphi}^{max,pvv}$	$P_{2,\varphi}^{pvv}$+10% $P_{f,\varphi}^{max,pvv}$	$P_{f,\varphi}^{max,pvv}$

Table 1.3 Reactive Power Set-Points for the Watt-VAr Operational Mode Curve Following the IEEE 1547-2018 Standard [11]

Reactive Power Set-Points	Default Settings	Modification Range	
		Minimum	Maximum
$Q_{3,\varphi}^{'pvv}$	100 % $Q_{f,\varphi}^{max,pvv}$	-$Q_{f,\varphi}^{max,pvv}$	+$Q_{f,\varphi}^{max,pvv}$
$Q_{2,\varphi}^{'pvv}$	100 % $Q_{f,\varphi}^{max,pvv}$	-$Q_{f,\varphi}^{max,pvv}$	+$Q_{f,\varphi}^{max,pvv}$
$Q_{1,\varphi}^{'pvv}$	0 % $Q_{f,\varphi}^{max,pvv}$	-$Q_{f,\varphi}^{max,pvv}$	+$Q_{f,\varphi}^{max,pvv}$
$Q_{1,\varphi}^{pvv}$	0 % -$Q_{f,\varphi}^{max,pvv}$	-$Q_{f,\varphi}^{max,pvv}$	+$Q_{f,\varphi}^{max,pvv}$

$Q_{2,\varphi}^{pvv}$	100 % -$Q_{f,\varphi}^{max,pvv}$	-$Q_{f,\varphi}^{max,pvv}$	+$Q_{f,\varphi}^{max,pvv}$
$Q_{3,\varphi}^{pvv}$	100 % -$Q_{f,\varphi}^{max,pvv}$	-$Q_{f,\varphi}^{max,pvv}$	+$Q_{f,\varphi}^{max,pvv}$

$Q_{f,\varphi}^{max,pvv}$ corresponds to the rated reactive power capacity which is constrained at 44% of the rate apparent power limits according to the IEEE 1547-2018 standard [11]. According to the standard, each reactive power set-point can be modified from the rated reactive power absorption limit to the rate reactive power injection limit. Considering an oversizing factor for the inverter, changes the 44% limit based on the factor itself according to (1.1).

$$Q_{f,\varphi}^{max,pvv}(p.u.) = S_{f,\varphi}^{max,pvv}(p.u.) \times Oversizing\ Factor \times 0.44 \quad (1.1)$$

As shown in Figure 1.1, the left half of the plane, where the inverter absorbs active power, is only active when a BES device is interfaced with the inverter. As the set-points are modifiable, it is not necessary that reactive power can only be injected when active power is being absorbed.

1.3.2 Problem Formulation

To study the effectiveness of the Watt-VAr mode in mitigating voltage issues and maximizing the potential of SIs within distribution feeders, a robust DOPF model is required. The DOPF model should be capable of creating an accurate representation of the distribution system, considering all the complexities to efficiently schedule the SIs. The IVACOPF [37][38], is one such model, which accurately models the unbalanced distribution system. Considering a pi-modeled unbalanced distribution system with the mutual impedance and shunt admittance effect, the model is a comprehensive representation of the distribution system, leading to increased accuracy for DOPF applications. Considering Node i and Node j, the voltage drop across the two nodes connected by Line ℓ at Phase φ is given by (1.2).

$$V_i^{\varphi} - V_j^{\varphi} = \sum_{\varphi' \in \phi} Z_{\ell}^{\varphi,\varphi'} I_{\ell}^{\varphi'} - \frac{1}{2} \sum_{\varphi' \in \phi} Z_{\ell}^{\varphi,\varphi'} \left(\sum_{\varphi'' \in \phi} y_{\ell}^{\varphi',\varphi''} V_i^{\varphi''} \right), \forall \varphi \in \phi, \ell \in K \quad (1.2)$$

Equation (1.2) can also be reformulated to represent the current flowing through a Line ℓ, between Nodes i and j, at Phase φ, as shown in (1.3).

$$I_{\ell}^{\varphi} = \left(Z_{\ell}^{\varphi,\varphi}\right)^{-1} \left[V_i^{\varphi} - V_j^{\varphi} - \sum_{\varphi' \in \phi, \varphi' \neq \varphi} Z_{\ell}^{\varphi,\varphi'} I_{\ell}^{\varphi'} + \frac{1}{2} \sum_{\varphi' \in \phi} Z_{\ell}^{\varphi,\varphi'} \left(\sum_{\varphi'' \in \phi} y_{\ell}^{\varphi',\varphi''} V_i^{\varphi''} \right) \right], \forall \varphi \in \phi, \ell \in K \quad (1.3)$$

Equations (1.2) and (1.3) represent how the current flowing through a line across two nodes or the voltage drop across the two nodes, not just depend on the voltage and currents of that phase φ, but also the other two phases φ' and φ'', in an unbalanced distribution system. Both (1.2) and (1.3) are both linear and completely capture the characteristics of the unbalanced distribution system. Equation (1.3) can be resolved into the real and imaginary parts of the current across Line ℓ, in rectangular coordinates as shown in (1.4) and (1.5).

$$I_{\ell}^{r,\varphi} = \left(R_{\ell}^{\varphi,\varphi}\right)^{-1}\left[V_i^{r,\varphi} - V_j^{r,\varphi} - \sum_{\varphi'\in\phi,\varphi'\neq\varphi} R_{\ell}^{\varphi,\varphi'} I_{\ell}^{r,\varphi'} + \sum_{\varphi'\in\phi,\varphi'\neq\varphi} X_{\ell}^{\varphi,\varphi'}\left(I_{\ell}^{im,\varphi'} - \frac{1}{2}\sum_{\varphi''\in\phi} y_{\ell}^{\varphi',\varphi''} V_i^{r,\varphi''}\right) - \frac{1}{2}\sum_{\varphi'\in\phi} R_{\ell}^{\varphi,\varphi'}\left(\sum_{\varphi''\in\phi} y_{\ell}^{\varphi',\varphi''} V_i^{im,\varphi''}\right)\right], \forall\varphi\in\phi, \ell\in K \quad (1.4)$$

$$I_{\ell}^{im,\varphi} = \left(R_{\ell}^{\varphi,\varphi}\right)^{-1}\left[V_i^{im,\varphi} - V_j^{im,\varphi} - \sum_{\varphi'\in\phi,\varphi'\neq\varphi} R_{\ell}^{\varphi,\varphi'} I_{\ell}^{im,\varphi'} - \sum_{\varphi'\in\phi,\varphi'\neq\varphi} X_{\ell}^{\varphi,\varphi'}\left(I_{\ell}^{r,\varphi'} + \frac{1}{2}\sum_{\varphi''\in\phi} y_{\ell}^{\varphi',\varphi''} V_i^{im,\varphi''}\right) + \frac{1}{2}\sum_{\varphi'\in\phi} R_{\ell}^{\varphi,\varphi'}\left(\sum_{\varphi''\in\phi} y_{\ell}^{\varphi',\varphi''} V_i^{r,\varphi''}\right)\right], \forall\varphi\in\phi, \ell\in K \quad (1.5)$$

Considering Node i, the set of all lines connected to it is Set $h(i)$. According to the Kirchoff Current Laws (KCL), the net injection at Node i is given by the sum of all current flowing in and out of the node as shown in (1.6) and (1.7), represented in rectangular coordinates.

$$I_i^{r,\varphi} = \sum_{\ell\in h(i)} I_l^{r,\varphi}, \forall\varphi\in\phi, i\in P \quad (1.6)$$

$$I_i^{im,\varphi} = \sum_{\ell\in h(i)} I_l^{im,\varphi}, \forall\varphi\in\phi, i\in P \quad (1.7)$$

The power balance constraints are also formulated based on rectangular coordinates, giving rise to active power balance and reactive power balance constraints as shown in (1.8) and (1.9) respectively. The set of all buses which correspond to the substation is given by the Set $s(i)$. The set of all capacitor banks connected to a Node i, is given by the Set $k(i)$. The set of all the demand buses is given by the Set $d(i)$. The set of all PVs with controller enabled is given by $F_1(i)$. The set of PVs with controllers not enabled operation at unity power factor is given by $F_2(i)$. The set of all transformers connected to a Node i is given by Set $o(i)$.

$$\sum_{\forall s(i)} P_{s,\varphi}^{B} + \sum_{\forall f\in F1(i)} P_{f,\varphi}^{pvv} + \sum_{\forall e\in F2(i)} P_{e,\varphi}^{pv} - \sum_{\forall d\in d(i)} D_{i,\varphi}^{P} - \sum_{\forall o\in o(i)} L_{o,\varphi}^{T} = P_{i,\varphi} \quad (1.8)$$

$$\sum_{\forall s(i)} Q_{s,\varphi}^{B} + \sum_{\forall f\in F1(i)} Q_{f,\varphi}^{pvv} - \sum_{\forall d\in d(i)} D_{i,\varphi}^{Q} - \sum_{\forall k\in k(i)} Q_{k,\varphi}^{C} = Q_{i,\varphi} \quad (1.9)$$

Equations (1.8) and (1.9) are linear. However, the net active power and reactive power injection/absorption at a given Node i, as shown in (1.10) and (1.11) are non-convex and nonlinear.

$$P_{i,\varphi} = V_i^{r,\varphi} I_i^{r,\varphi} + V_i^{im,\varphi} I_i^{im,\varphi}, \forall\varphi\in\phi, i\in P \quad (1.10)$$

$$Q_{i,\varphi} = V_i^{im,\varphi} I_i^{r,\varphi} + V_i^{r,\varphi} I_i^{im,\varphi}, \forall\varphi\in\phi, i\in P \quad (1.11)$$

To preserve model convexity and improve accuracy, (1.10) and (1.11) are reformulated with linearized constraints using first order Taylor's series approximation. This model is then iteratively solved, wherein the Taylor's series parameters, indicated by the superscript (t), are updated each iteration with the previous iteration's solution. This iterative process improves accuracy without increasing computational complexity. The reformulated constraints are presented in (1.12) and (1.13).

$$P_{i,\varphi} = V_i^{r,\varphi^{(t)}} I_i^{r,\varphi} + V_i^{im,\varphi^{(t)}} I_i^{im,\varphi} + V_i^{r,\varphi} I_i^{r,\varphi^{(t)}} + V_i^{im,\varphi} I_i^{im,\varphi^{(t)}} - V_i^{r,\varphi^{(t)}} I_i^{r,\varphi^{(t)}} - V_i^{im,\varphi^{(t)}} I_i^{im,\varphi^{(t)}}, \forall\varphi\in\phi, i\in P \quad (1.12)$$

$$Q_{i,\varphi} = V_i^{im,\varphi^{(t)}} I_i^{r,\varphi} - V_i^{r,\varphi^{(t)}} I_i^{im,\varphi} + V_i^{im,\varphi} I_i^{r,\varphi^{(t)}} - V_i^{r,\varphi} I_i^{im,\varphi^{(t)}} - V_i^{im,\varphi^{(t)}} I_i^{r,\varphi^{(t)}} + V_i^{r,\varphi^{(t)}} I_i^{im,\varphi^{(t)}}, \forall \varphi \in \phi, i \in P \quad (1.13)$$

One of the main goals of the DER scheduling tool is to mitigate voltage violations across the distribution feeders with reactive power support from SIs. Having mentioned the objective, the voltage at all the buses across the distribution feeder is constrained to the ANSI standard specified limits. The voltage magnitude is calculated as shown in (1.14).

$$V_i^{\varphi} = \sqrt[2]{V_i^{r,\varphi^2} + V_i^{im,\varphi^2}}, \forall \varphi \in \phi, i \in P \quad (1.14)$$

Equation (1.14) is also a non-linear, non-convex constraint as it is represented in rectangular coordinates and is reformulated linearly using Taylor's series approximation as shown in (1.15).

$$V_i^{\varphi} = \frac{V_i^{r,\varphi^{(t)}} V_i^{r,\varphi}}{\sqrt[2]{V_i^{r,\varphi^{2(t)}} + V_i^{im,\varphi^{2(t)}}}} + \frac{V_i^{im,\varphi^{(t)}} V_i^{im,\varphi}}{\sqrt[2]{V_i^{r,\varphi^{2(t)}} + V_i^{im,\varphi^{2(t)}}}} \quad (1.15)$$

The voltage magnitude at each Node i at Phase φ, is limited to the ANSI standard specified limit as shown in (1.16).

$$0.95 \leq V_i^{\varphi} \leq 1.05, \forall \varphi \in \phi, i \in P \quad (1.16)$$

Lines cannot operate beyond a certain rated current value due to excessive thermal issues. The thermal line limit rating is constrained by (1.17). The constraint is convex as the function space is convex (a filled circle). These types of constraints can be handled by any generic solver.

$$I_i^{r,\varphi^2} + I_i^{im,\varphi^2} \leq I_{\ell}^{max,\varphi^2}, \forall \varphi \in \phi, \ell \in K \quad (1.17)$$

The capacitor banks are limited by rate reactive power injection or absorption capacities which cannot be exceeded. These limitations are formulated as (1.18).

$$Q_{k,\varphi}^{C} \leq Q_{k,\varphi}^{C,max}, \forall \varphi \in \phi, k \in k(i) \quad (1.18)$$

Apart from the network constraints, Inverters interfaced with PV units are also constrained by apparent power ratings. SIs with PV controllers not enabled, inject available active power generation at unity power factor, with neither reactive power injection nor absorption as shown in (1.19).

$$P_{e,\varphi}^{pv} = P_{e,\varphi}^{pv,av}, \forall \varphi \in \phi, e \in F2 \quad (1.19)$$

SIs enabled with PV controllers, have the ability to inject or absorb reactive power. The inverter apparent power injection or absorption is constrained by (1.20).

$$P_{f,\varphi}^{pvv^2} + Q_{f,\varphi}^{pvv^2} \leq S_{f,\varphi}^{pvv,max^2}, \forall \varphi \in \phi, f \in F1 \quad (1.20)$$

With PV controllers enabled, active power curtailment is also enabled which implies that active power injection is constrained by (1.21).

$$P_{f,\varphi}^{pvv} \leq P_{f,\varphi}^{pvv,av}, \forall \varphi \in \phi, f \in F1 \tag{1.21}$$

Reactive power limits as specified by the IEEE 1547-2018 standard [11], is used to constrain reactive power injection or absorption as shown in (1.22).

$$-Q_{f,\varphi}^{pvv,max} \leq Q_{f,\varphi}^{pvv} \leq Q_{f,\varphi}^{pvv,max}, \forall \varphi \in \phi, f \in F1 \tag{1.22}$$

As mentioned previously, the Watt-VAr curve is a piece-wise linear function, based on discrete set-points and clear operational bounds which are modifiable within an allowable range [11]. The default settings as mentioned above in Tables 1.2 and 1.3, are utilized to create a curve capable of dispatching reactive power with fixed operational bounds. Figure 1.1 represents the piece-wise function which is shown in (1.23).

$$Q_{f,\varphi}^{pvv} = \begin{cases} Q_{f,\varphi}^{pvv,max} & , P_{f,\varphi}^{pvv} < P_{3,\varphi}^{\prime pvv} \\ Q_{2,\varphi}^{\prime pvv} + \frac{\left(P_{2,\varphi}^{\prime pvv} - P_{f,\varphi}^{pvv}\right)\left(Q_{3,\varphi}^{\prime pvv} - Q_{2,\varphi}^{\prime pvv}\right)}{P_{2,\varphi}^{\prime pvv} - P_{3,\varphi}^{\prime pvv}} & , P_{3,\varphi}^{\prime pvv} \leq P_{f,\varphi}^{pvv} < P_{2,\varphi}^{\prime pvv} \\ Q_{1,\varphi}^{\prime pvv} + \frac{\left(P_{1,\varphi}^{\prime pvv} - P_{f,\varphi}^{pvv}\right)\left(Q_{2,\varphi}^{\prime pvv} - Q_{1,\varphi}^{\prime pvv}\right)}{P_{1,\varphi}^{\prime pvv} - P_{2,\varphi}^{\prime pvv}} & , P_{2,\varphi}^{\prime pvv} \leq P_{f,\varphi}^{pvv} < P_{1,\varphi}^{\prime pvv} \\ Q_{1,\varphi}^{pvv} + \frac{\left(P_{1,\varphi}^{pvv} - P_{f,\varphi}^{pvv}\right)\left(Q_{1,\varphi}^{\prime pvv} - Q_{1,\varphi}^{pvv}\right)}{P_{1,\varphi}^{pvv} - P_{1,\varphi}^{\prime pvv}} & , P_{1,\varphi}^{\prime pvv} \leq P_{f,\varphi}^{pvv} < P_{1,\varphi}^{pvv} \\ Q_{2,\varphi}^{pvv} + \frac{\left(P_{2,\varphi}^{pvv} - P_{f,\varphi}^{pvv}\right)\left(Q_{1,\varphi}^{pvv} - Q_{2,\varphi}^{pvv}\right)}{P_{2,\varphi}^{pvv} - P_{1,\varphi}^{pvv}} & , P_{1,\varphi}^{pvv} \leq P_{f,\varphi}^{pvv} < P_{2,\varphi}^{pvv} \\ Q_{3,\varphi}^{pvv} + \frac{\left(P_{3,\varphi}^{pvv} - P_{f,\varphi}^{pvv}\right)\left(Q_{2,\varphi}^{pvv} - Q_{3,\varphi}^{pvv}\right)}{P_{3,\varphi}^{pvv} - P_{2,\varphi}^{pvv}} & , P_{2,\varphi}^{pvv} \leq P_{f,\varphi}^{pvv} < P_{3,\varphi}^{pvv} \\ -Q_{f,\varphi}^{pvv,max} & , P_{f,\varphi}^{pvv} \geq P_{3,\varphi}^{pvv} \end{cases} \tag{1.23}$$

The above described piece-wise function is formulated in a mixed-integer linear fashion using the Big-M method. Each piecewise section represents a zone of operation, wherein the reactive power dispatch in Zones 2-6 depend on the respective slopes of the linear sections. Zone 1, where the reactive power is injected with respect to set-point $Q_{f,\varphi}^{pvv,max}$, operates beyond set-point $P_{3,\varphi}^{\prime pvv}$. The aforementioned zone is formulated as shown in (1.24) and (1.25).

$$M_1 u_{1,f,\varphi}^{pq} + P_{3,\varphi}^{\prime pvv} \geq P_{f,\varphi}^{pvv} \tag{1.24}$$

$$-M_1 u_{1,f,\varphi}^{pq} \leq Q_{f,\varphi}^{pvv} - Q_{f,\varphi}^{pvv,max} \leq M_1 u_{1,f,\varphi}^{pq} \tag{1.25}$$

The zone is activated or selected, when the binary variable associated with the zone of operation, $u_{1,f,\varphi}^{pq}$, is set to zero, which tightens the constraint bounds, thereby "enabling" that specific constraint. Zone 2 where the reactive power is injected with respect to the slope of the linear section

as shown in (1.26), operates between the set-points $P_{3,\varphi}^{\prime pvv}$ and $P_{2,\varphi}^{\prime pvv}$. The aforementioned zone is formulated as shown in (1.27) and (1.28).

$$Slope_{zone\ 2} = \frac{Q_{3,\varphi}^{\prime pvv} - Q_{2,\varphi}^{\prime pvv}}{P_{3,\varphi}^{\prime pvv} - P_{2,\varphi}^{\prime pvv}} \tag{1.26}$$

$$-M_1 u_{2,f,\varphi}^{pq} + P_{3,\varphi}^{\prime pvv} \leq P_{f,\varphi}^{pvv} \leq M_1 u_{2,f,\varphi}^{pq} + P_{2,\varphi}^{\prime pvv} \tag{1.27}$$

$$-M_1 u_{2,f,\varphi}^{pq} \leq Q_{f,\varphi}^{pvv} - Q_{2,\varphi}^{\prime pvv} + \frac{\left(P_{2,\varphi}^{\prime pvv} - P_{f,\varphi}^{pvv}\right)\left(Q_{3,\varphi}^{\prime pvv} - Q_{2,\varphi}^{\prime pvv}\right)}{P_{2,\varphi}^{\prime pvv} - P_{3,\varphi}^{\prime pvv}} \leq M_1 u_{2,f,\varphi}^{pq} \tag{1.28}$$

The zone is activated, when the binary variable associated with the zone of operation, $u_{2,f,\varphi}^{pq}$, is set to zero. Zone 3 where the reactive power is injected with respect to the slope of the linear section as shown in (1.29), operates between the set-points $P_{2,\varphi}^{\prime pvv}$ and $P_{1,\varphi}^{\prime pvv}$. The aforementioned zone is formulated as shown in (1.30) and (1.31).

$$Slope_{zone\ 3} = \frac{Q_{2,\varphi}^{\prime pvv} - Q_{1,\varphi}^{\prime pvv}}{P_{2,\varphi}^{\prime pvv} - P_{1,\varphi}^{\prime pvv}} \tag{1.29}$$

$$-M_1 u_{3,f,\varphi}^{pq} + P_{2,\varphi}^{\prime pvv} \leq P_{f,\varphi}^{pvv} \leq M_1 u_{3,f,\varphi}^{pq} + P_{1,\varphi}^{\prime pvv} \tag{1.30}$$

$$-M_1 u_{3,f,\varphi}^{pq} \leq Q_{f,\varphi}^{pvv} - Q_{1,\varphi}^{\prime pvv} - \frac{\left(P_{1,\varphi}^{\prime pvv} - P_{f,\varphi}^{pvv}\right)\left(Q_{2,\varphi}^{\prime pvv} - Q_{1,\varphi}^{\prime pvv}\right)}{P_{1,\varphi}^{\prime pvv} - P_{2,\varphi}^{\prime pvv}} \leq M_1 u_{3,f,\varphi}^{pq} \tag{1.31}$$

The zone is activated, when the binary variable associated with the zone of operation, $u_{3,f,\varphi}^{pq}$, is set to zero. Zone 4 is generally, and in this case, modeled as a dead zone where the inverter neither injects nor absorbs reactive power. Therefore, the general constraint is formulated as shown in (1.32) and (1.33), but the set points, $Q_{1,\varphi}^{\prime pvv}$ and $Q_{1,\varphi}^{pvv}$ are set to zero.

$$-M_1 u_{4,f,\varphi}^{pq} + P_{1,\varphi}^{\prime pvv} \leq P_{f,\varphi}^{pvv} \leq M_1 u_{4,f,\varphi}^{pq} + P_{1,\varphi}^{pvv} \tag{1.32}$$

$$-M_1 u_{4,f,\varphi}^{pq} \leq Q_{f,\varphi}^{pvv} - Q_{1,\varphi}^{pvv} - \frac{\left(P_{1,\varphi}^{pvv} - P_{f,\varphi}^{pvv}\right)\left(Q_{1,\varphi}^{\prime pvv} - Q_{1,\varphi}^{pvv}\right)}{P_{1,\varphi}^{pvv} - P_{1,\varphi}^{\prime pvv}} \leq M_1 u_{4,f,\varphi}^{pq} \tag{1.33}$$

The dead zone is activated, when the binary variable associated with the zone of operation, $u_{4,f,\varphi}^{pq}$, is set to zero. Zone 5 is the zone of operation, where reactive power is absorbed with respect to the slope of the linear section as shown (1.34). This zone operates between the set-points $P_{1,\varphi}^{pvv}$ and $P_{2,\varphi}^{pvv}$, and is formulated as shown in (1.35) and (1.36).

$$Slope_{zone\ 5} = \frac{Q_{1,\varphi}^{pvv} - Q_{2,\varphi}^{pvv}}{P_{1,\varphi}^{pvv} - P_{2,\varphi}^{pvv}} \tag{1.34}$$

$$-M_1 u_{5,f,\varphi}^{pq} + P_{1,\varphi}^{pvv} \leq P_{f,\varphi}^{pvv} \leq M_1 u_{5,f,\varphi}^{pq} + P_{2,\varphi}^{pvv} \tag{1.35}$$

$$-M_1 u_{5,f,\varphi}^{pq} \leq Q_{f,\varphi}^{pvv} - Q_{2,\varphi}^{pvv} - \frac{\left(P_{2,\varphi}^{pvv} - P_{f,\varphi}^{pvv}\right)\left(Q_{1,\varphi}^{pvv} - Q_{2,\varphi}^{pvv}\right)}{P_{2,\varphi}^{pvv} - P_{1,\varphi}^{pvv}} \leq M_1 u_{5,f,\varphi}^{pq} \tag{1.36}$$

The zone is activated, when the binary variable associated with the zone of operation, $u_{5,f,\varphi}^{pq}$, is set to zero. Zone 6 is the zone of operation, where reactive power is absorbed with respect to the slope of the linear section as shown (1.37). This zone operates between the set-points $P_{2,\varphi}^{pvv}$ and $P_{3,\varphi}^{pvv}$, and is formulated as shown in (1.38) and (1.39).

$$Slope_{zone\ 6} = \frac{Q_{2,\varphi}^{pvv} - Q_{3,\varphi}^{pvv}}{P_{2,\varphi}^{pvv} - P_{3,\varphi}^{pvv}} \tag{1.37}$$

$$-M_1 u_{6,f,\varphi}^{pq} + P_{2,\varphi}^{pvv} \leq P_{f,\varphi}^{pvv} \leq M_1 u_{6,f,\varphi}^{pq} + P_{3,\varphi}^{pvv} \tag{1.38}$$

$$-M_1 u_{6,f,\varphi}^{pq} \leq Q_{f,\varphi}^{pvv} - Q_{3,\varphi}^{pvv} - \frac{\left(P_{3,\varphi}^{pvv} - P_{f,\varphi}^{pvv}\right)\left(Q_{2,\varphi}^{pvv} - Q_{3,\varphi}^{pvv}\right)}{P_{3,\varphi}^{pvv} - P_{2,\varphi}^{pvv}} \leq M_1 u_{6,f,\varphi}^{pq} \tag{1.39}$$

The zone is activated, when the binary variable associated with the zone of operation, $u_{6,f,\varphi}^{pq}$, is set to zero. Zone 7, where the reactive power is absorbed with respect to set-point $-Q_{f,\varphi}^{pvv,max}$, operates beyond set-point $P_{3,\varphi}^{pvv}$. The aforementioned zone is formulated as shown in (1.40) and (1.41).

$$-M_1 u_{7,f,\varphi}^{pq} + P_{3,\varphi}^{pvv} \leq P_{f,\varphi}^{pvv} \tag{1.40}$$

$$-M_1 u_{7,f,\varphi}^{pq} \leq Q_{f,\varphi}^{pvv} + Q_{f,\varphi}^{pvv,max} \leq M_1 u_{7,f,\varphi}^{pq} \tag{1.41}$$

This zone is activated, when the binary variable associated with the zone of operation, $u_{7,f,\varphi}^{pq}$, is set to zero. Equations (1.24) - (1.41) represent the distinct piecewise sections of the curve and are bound together by (1.42). Equation (1.42) is a mutual exclusivity constraint, which ensures that only one zone of operation is chosen at any given time step within the DER scheduling tool.

$$u_{1,f,\varphi}^{pq} + u_{2,f,\varphi}^{pq} + u_{3,f,\varphi}^{pq} + u_{4,f,\varphi}^{pq} + u_{5,f,\varphi}^{pq} + u_{6,f,\varphi}^{pq} + u_{7,f,\varphi}^{pq} \leq 6, \forall f \in F1 \tag{1.42}$$

Co-optimizing the set-points in the Watt-VAr scheme, yields flexibility to the DER operator, as optimal curves are designed for each individual SI, to mitigate voltage issues feeder-wide, while still maximizing the potential of the excess PV generation in reducing operational cost. Given fixed set-points, (1.28), (1.31), (1.33), (1.36), and (1.39), are mixed-integer and linear. Co-optimizing the set-points, converts the aforementioned constraints into non-linear, non-convex constraints. Therefore, they are linearly approximated using Taylor's series approximation, as mentioned in (1.43)-(1.47). The rest of the equations remain the same due to their convexity being preserved. Terms specified with the superscript (t), correspond to a Taylor's series parameter which are updated every iteration with the previous iteration's solution. Equation (1.28) is approximated and linear formulated as shown in (1.43), where $u_{2,f,\varphi}^{pq}$ corresponds to the binary variable, associated with the operation of zone two.

$$-M_1 u_{2,f,\varphi}^{pq} \le Q_{f,\varphi}^{pvv} - Q_{2,\varphi}^{\prime pvv^{(t)}} - \frac{\left(Q_{3,\varphi}^{\prime pvv^{(t)}} - Q_{2,\varphi}^{\prime pvv^{(t)}}\right)\left(P_{2,\varphi}^{\prime pvv^{(t)}} - P_{f,\varphi}^{pvv^{(t)}}\right)}{P_{2,\varphi}^{\prime pvv^{(t)}} - P_{3,\varphi}^{\prime pvv^{(t)}}} - \frac{\left(P_{f,\varphi}^{pvv^{(t)}} - P_{3,\varphi}^{\prime pvv^{(t)}}\right)\left(Q_{2,\varphi}^{\prime pvv} - Q_{2,\varphi}^{\prime pvv^{(t)}}\right)}{P_{2,\varphi}^{\prime pvv^{(t)}} - P_{3,\varphi}^{\prime pvv^{(t)}}} - \frac{\left(Q_{3,\varphi}^{\prime pvv^{(t)}} - Q_{2,\varphi}^{\prime pvv^{(t)}}\right)\left(P_{f,\varphi}^{pvv^{(t)}} - P_{3,\varphi}^{\prime pvv^{(t)}}\right)\left(P_{2,\varphi}^{\prime pvv} - P_{2,\varphi}^{\prime pvv^{(t)}}\right)}{\left(P_{2,\varphi}^{\prime pvv^{(t)}} - P_{3,\varphi}^{\prime pvv^{(t)}}\right)^2} - \frac{\left(Q_{3,\varphi}^{\prime pvv^{(t)}} - Q_{2,\varphi}^{\prime pvv^{(t)}}\right)\left(P_{2,\varphi}^{\prime pvv^{(t)}} - P_{f,\varphi}^{pvv^{(t)}}\right)\left(P_{3,\varphi}^{\prime pvv} - P_{3,\varphi}^{\prime pvv^{(t)}}\right)}{\left(P_{2,\varphi}^{\prime pvv^{(t)}} - P_{3,\varphi}^{\prime pvv^{(t)}}\right)^2} + \frac{\left(Q_{3,\varphi}^{\prime pvv^{(t)}} - Q_{2,\varphi}^{\prime pvv^{(t)}}\right)\left(P_{f,\varphi}^{pvv} - P_{f,\varphi}^{pvv^{(t)}}\right)}{P_{2,\varphi}^{\prime pvv^{(t)}} - P_{3,\varphi}^{\prime pvv^{(t)}}} \le M_1 u_{2,f,\varphi}^{pq} \tag{1.43}$$

Equation (1.31) is approximated and linear formulated as shown in (1.44), where $u_{3,f,\varphi}^{pq}$ corresponds to the binary variable, associated with the operation of Zone 3.

$$-M_1 u_{3,f,\varphi}^{pq} \le Q_{f,\varphi}^{pvv} - Q_{1,\varphi}^{\prime pvv^{(t)}} - \frac{\left(Q_{2,\varphi}^{\prime pvv^{(t)}} - Q_{1,\varphi}^{\prime pvv^{(t)}}\right)\left(P_{1,\varphi}^{\prime pvv^{(t)}} - P_{f,\varphi}^{pvv^{(t)}}\right)}{P_{1,\varphi}^{\prime pvv^{(t)}} - P_{2,\varphi}^{\prime pvv^{(t)}}} - \frac{\left(P_{f,\varphi}^{pvv^{(t)}} - P_{2,\varphi}^{\prime pvv^{(t)}}\right)\left(Q_{1,\varphi}^{\prime pvv} - Q_{1,\varphi}^{\prime pvv^{(t)}}\right)}{P_{1,\varphi}^{\prime pvv^{(t)}} - P_{2,\varphi}^{\prime pvv^{(t)}}} - \frac{\left(Q_{2,\varphi}^{\prime pvv^{(t)}} - Q_{1,\varphi}^{\prime pvv^{(t)}}\right)\left(P_{f,\varphi}^{pvv^{(t)}} - P_{2,\varphi}^{\prime pvv^{(t)}}\right)\left(P_{1,\varphi}^{\prime pvv} - P_{1,\varphi}^{\prime pvv^{(t)}}\right)}{\left(P_{1,\varphi}^{\prime pvv^{(t)}} - P_{2,\varphi}^{\prime pvv^{(t)}}\right)^2} - \frac{\left(Q_{2,\varphi}^{\prime pvv^{(t)}} - Q_{1,\varphi}^{\prime pvv^{(t)}}\right)\left(P_{1,\varphi}^{\prime pvv^{(t)}} - P_{f,\varphi}^{pvv^{(t)}}\right)\left(P_{2,\varphi}^{\prime pvv} - P_{2,\varphi}^{\prime pvv^{(t)}}\right)}{\left(P_{1,\varphi}^{\prime pvv^{(t)}} - P_{2,\varphi}^{\prime pvv^{(t)}}\right)^2} + \frac{\left(Q_{2,\varphi}^{\prime pvv^{(t)}} - Q_{1,\varphi}^{\prime pvv^{(t)}}\right)\left(P_{f,\varphi}^{pvv} - P_{f,\varphi}^{pvv^{(t)}}\right)}{P_{1,\varphi}^{\prime pvv^{(t)}} - P_{2,\varphi}^{\prime pvv^{(t)}}} \le M_1 u_{3,f,\varphi}^{pq} \tag{1.44}$$

Equation (1.33) is approximated and linear formulated as shown in (1.45), where $u_{4,f,\varphi}^{pq}$ corresponds to the binary variable, associated with the operation of Zone 4.

$$-M_1 u_{4,f,\varphi}^{pq} \le Q_{f,\varphi}^{pvv} - Q_{1,\varphi}^{pvv^{(t)}} - \frac{\left(Q_{1,\varphi}^{\prime pvv^{(t)}} - Q_{1,\varphi}^{pvv^{(t)}}\right)\left(P_{1,\varphi}^{pvv^{(t)}} - P_{f,\varphi}^{pvv^{(t)}}\right)}{P_{1,\varphi}^{pvv^{(t)}} - P_{1,\varphi}^{\prime pvv^{(t)}}} - \frac{\left(P_{f,\varphi}^{pvv^{(t)}} - P_{1,\varphi}^{\prime pvv^{(t)}}\right)\left(Q_{1,\varphi}^{pvv} - Q_{1,\varphi}^{pvv^{(t)}}\right)}{P_{1,\varphi}^{pvv^{(t)}} - P_{1,\varphi}^{\prime pvv^{(t)}}} - \frac{\left(Q_{1,\varphi}^{\prime pvv^{(t)}} - Q_{1,\varphi}^{pvv^{(t)}}\right)\left(P_{f,\varphi}^{pvv^{(t)}} - P_{1,\varphi}^{\prime pvv^{(t)}}\right)\left(P_{1,\varphi}^{pvv} - P_{1,\varphi}^{pvv^{(t)}}\right)}{\left(P_{1,\varphi}^{pvv^{(t)}} - P_{1,\varphi}^{\prime pvv^{(t)}}\right)^2} - \frac{\left(Q_{1,\varphi}^{\prime pvv^{(t)}} - Q_{1,\varphi}^{pvv^{(t)}}\right)\left(P_{1,\varphi}^{pvv^{(t)}} - P_{f,\varphi}^{pvv^{(t)}}\right)\left(P_{1,\varphi}^{\prime pvv} - P_{1,\varphi}^{\prime pvv^{(t)}}\right)}{\left(P_{1,\varphi}^{pvv^{(t)}} - P_{1,\varphi}^{\prime pvv^{(t)}}\right)^2} + \frac{\left(Q_{1,\varphi}^{\prime pvv^{(t)}} - Q_{1,\varphi}^{pvv^{(t)}}\right)\left(P_{f,\varphi}^{pvv} - P_{f,\varphi}^{pvv^{(t)}}\right)}{P_{1,\varphi}^{pvv^{(t)}} - P_{1,\varphi}^{\prime pvv^{(t)}}} \le M_1 u_{4,f,\varphi}^{pq} \tag{1.45}$$

Equation (1.36) is approximated and linear formulated as shown in (1.46), where $u_{5,f,\varphi}^{pq}$ corresponds to the binary variable, associated with the operation of Zone 5.

$$-M_1 u_{5,f,\varphi}^{pq} \leq Q_{f,\varphi}^{pvv} - Q_{2,\varphi}^{pvv^{(t)}} - \frac{\left(Q_{1,\varphi}^{pvv^{(t)}} - Q_{2,\varphi}^{pvv^{(t)}}\right)\left(P_{2,\varphi}^{pvv^{(t)}} - P_{f,\varphi}^{pvv^{(t)}}\right)}{P_{2,\varphi}^{pvv^{(t)}} - P_{1,\varphi}^{pvv^{(t)}}} - \frac{\left(P_{f,\varphi}^{pvv^{(t)}} - P_{1,\varphi}^{pvv^{(t)}}\right)\left(Q_{2,\varphi}^{pvv} - Q_{2,\varphi}^{pvv^{(t)}}\right)}{P_{2,\varphi}^{pvv^{(t)}} - P_{1,\varphi}^{pvv^{(t)}}} - \frac{\left(Q_{1,\varphi}^{pvv^{(t)}} - Q_{2,\varphi}^{pvv^{(t)}}\right)\left(P_{f,\varphi}^{pvv^{(t)}} - P_{1,\varphi}^{pvv^{(t)}}\right)\left(P_{2,\varphi}^{pvv} - P_{2,\varphi}^{pvv^{(t)}}\right)}{\left(P_{2,\varphi}^{pvv^{(t)}} - P_{1,\varphi}^{pvv^{(t)}}\right)^2} - \frac{\left(Q_{1,\varphi}^{pvv^{(t)}} - Q_{2,\varphi}^{pvv^{(t)}}\right)\left(P_{2,\varphi}^{pvv^{(t)}} - P_{f,\varphi}^{pvv^{(t)}}\right)\left(P_{1,\varphi}^{pvv} - P_{1,\varphi}^{pvv^{(t)}}\right)}{\left(P_{2,\varphi}^{pvv^{(t)}} - P_{1,\varphi}^{pvv^{(t)}}\right)^2} + \frac{\left(Q_{1,\varphi}^{pvv^{(t)}} - Q_{2,\varphi}^{pvv^{(t)}}\right)\left(P_{f,\varphi}^{pvv} - P_{f,\varphi}^{pvv^{(t)}}\right)}{P_{2,\varphi}^{pvv^{(t)}} - P_{1,\varphi}^{pvv^{(t)}}} \leq M_1 u_{5,f,\varphi}^{pq} \quad (1.46)$$

Equation (1.39) is approximated and linear formulated as shown in (1.47), where $u_{6,f,\varphi}^{pq}$ corresponds to the binary variable, associated with the operation of Zone 6.

$$-M_1 u_{6,f,\varphi}^{pq} \leq Q_{f,\varphi}^{pvv} - Q_{3,\varphi}^{pvv^{(t)}} - \frac{\left(Q_{2,\varphi}^{pvv^{(t)}} - Q_{3,\varphi}^{pvv^{(t)}}\right)\left(P_{3,\varphi}^{pvv^{(t)}} - P_{f,\varphi}^{pvv^{(t)}}\right)}{P_{3,\varphi}^{pvv^{(t)}} - P_{2,\varphi}^{pvv^{(t)}}} - \frac{\left(P_{f,\varphi}^{pvv^{(t)}} - P_{2,\varphi}^{pvv^{(t)}}\right)\left(Q_{3,\varphi}^{pvv} - Q_{3,\varphi}^{pvv^{(t)}}\right)}{P_{3,\varphi}^{pvv^{(t)}} - P_{2,\varphi}^{pvv^{(t)}}} - \frac{\left(Q_{2,\varphi}^{pvv^{(t)}} - Q_{3,\varphi}^{pvv^{(t)}}\right)\left(P_{f,\varphi}^{pvv^{(t)}} - P_{2,\varphi}^{pvv^{(t)}}\right)\left(P_{3,\varphi}^{pvv} - P_{3,\varphi}^{pvv^{(t)}}\right)}{\left(P_{3,\varphi}^{pvv^{(t)}} - P_{2,\varphi}^{pvv^{(t)}}\right)^2} - \frac{\left(Q_{2,\varphi}^{pvv^{(t)}} - Q_{3,\varphi}^{pvv^{(t)}}\right)\left(P_{3,\varphi}^{pvv^{(t)}} - P_{f,\varphi}^{pvv^{(t)}}\right)\left(P_{2,\varphi}^{pvv} - P_{2,\varphi}^{pvv^{(t)}}\right)}{\left(P_{3,\varphi}^{pvv^{(t)}} - P_{2,\varphi}^{pvv^{(t)}}\right)^2} + \frac{\left(Q_{2,\varphi}^{pvv^{(t)}} - Q_{3,\varphi}^{pvv^{(t)}}\right)\left(P_{f,\varphi}^{pvv} - P_{f,\varphi}^{pvv^{(t)}}\right)}{P_{3,\varphi}^{pvv^{(t)}} - P_{2,\varphi}^{pvv^{(t)}}} \leq M_1 u_{6,f,\varphi}^{pq} \quad (1.47)$$

The Taylor's series parameters for all the set-points in the first iteration are initialized with the respective default-set-points. The variable set-points are optimized within the permissible ranges as specified by the IEEE 1547-2018 standard [11]. Accordingly, these ranges are formulated as constraints in a linear fashion. Equations (1.48) – (1.53), present the constraints indicating the permissible limits for the active power set-points.

$$P_{f,\varphi}^{\prime pvv,max} \leq P_{3,\varphi}^{\prime pvv} \leq P_{2,\varphi}^{\prime pvv} + 0.1 \times P_{f,\varphi}^{\prime pvv,max} \quad (1.48)$$

$$0.8 \times P_{f,\varphi}^{\prime pvv,max} \leq P_{2,\varphi}^{\prime pvv} \leq 0.4 \times P_{f,\varphi}^{\prime pvv,max} \quad (1.49)$$

$$P_{2,\varphi}^{\prime pvv} - 0.1 \times P_{f,\varphi}^{\prime pvv,max} \leq P_{1,\varphi}^{\prime pvv} < 0 \quad (1.50)$$

$$0 < P_{1,\varphi}^{pvv} \leq P_{2,\varphi}^{pvv} - 0.1 \times P_{f,\varphi}^{pvv,max} \quad (1.51)$$

$$0.4 \times P_{f,\varphi}^{pvv,max} \leq P_{2,\varphi}^{pvv} \leq 0.8 \times P_{f,\varphi}^{pvv,max} \quad (1.52)$$

$$P_{2,\varphi}^{pvv} + 0.1 \times P_{f,\varphi}^{pvv,max} \leq P_{3,\varphi}^{pvv} \leq P_{f,\varphi}^{pvv,max} \quad (1.53)$$

Equations (1.54) – (1.59), present the constraints indicating the permissible limits for the reactive power set-points as specified by the IEEE 1547-2018 standard [11].

$$-Q_{f,\varphi}^{pvv,max} \leq Q_{3,\varphi}^{\prime pvv} \leq Q_{f,\varphi}^{pvv,max} \quad (1.54)$$

$$-Q_{f,\varphi}^{pvv,max} \leq Q_{2,\varphi}^{'pvv} \leq Q_{f,\varphi}^{pvv,max} \tag{1.55}$$

$$-Q_{f,\varphi}^{pvv,max} \leq Q_{1,\varphi}^{'pvv} \leq Q_{f,\varphi}^{pvv,max} \tag{1.56}$$

$$-Q_{f,\varphi}^{pvv,max} \leq Q_{1,\varphi}^{pvv} \leq Q_{f,\varphi}^{pvv,max} \tag{1.57}$$

$$-Q_{f,\varphi}^{pvv,max} \leq Q_{2,\varphi}^{pvv} \leq Q_{f,\varphi}^{pvv,max} \tag{1.58}$$

$$-Q_{f,\varphi}^{pvv,max} \leq Q_{3,\varphi}^{pvv} \leq Q_{f,\varphi}^{pvv,max} \tag{1.59}$$

Equation (1.60) is also presented in the formulation to change the rated reactive power set-point to lower limits if system conditions are nominal, without any reactive power injection or absorption. The Taylor's series parameters for rated reactive power, $-Q_{f,\varphi}^{pvv,max(t)}$ are initialized with the 44% apparent power rating and are down-rated in the above scenario mentioned in each iteration until an optimal set-point is reached.

$$-Q_{f,\varphi}^{pvv,max(t)} \leq Q_{f,\varphi}^{pvv,max} \leq Q_{f,\varphi}^{pvv,max(t)} \tag{1.60}$$

DER scheduling tools are utilized for a host of applications including minimizing voltage issues within the distribution feeder, operational cost, active power generation curtailment from PV and, maximizing profit, PV power utilization, etc. For the purposes of this work, managing voltage issues distribution feeder wide and minimizing the cost of operation from the standpoint of purchasing power from the substation are considered. Since satisfying the ANSI standards for the voltage violation issues are acceptable, mitigation is achieved through formulating constraints. Therefore, the main objective of the work presented here, is to minimize the operational cost as defined by purchasing power from the substation, as opposed to utilizing the cheaper renewable resources, i.e., roof-top PV units within the distribution feeder. As such, (1.61) presents the objective function utilized in this section.

$$\min_{\substack{V_i^{r,\varphi}, V_i^{im,\varphi}, I_i^{r,\varphi}, I_i^{im,\varphi} \\ I_\ell^{r,\varphi}, I_\ell^{im,\varphi}, P_{f,\varphi}^{pvv}, Q_{f,\varphi}^{pvv}}} \sum_{\varphi \in \phi} \begin{pmatrix} \sum_{\forall s(i)} \pi_{s,\varphi}^{B} P_{s,\varphi}^{B} + \sum_{\forall f \in F1(i)} \pi_{f,\varphi}^{pvv} P_{f,\varphi}^{pvv} \\ + \sum_{\forall e \in F2(i)} \pi_{e,\varphi}^{pv} P_{e,\varphi}^{pv} \end{pmatrix} \tag{1.61}$$

1.3.3 Results and Analysis

Two DER scheduling models are presented and analyzed including the Watt-VAr (default settings) and Watt-VAr (co-optimized settings). The first section presents the description of the test system. The second section presents the results obtained using a DER scheduling model with Watt-VAr (default settings), compared against a prior work [39], where a DER scheduling model is presented with Volt-VAr (default settings). The third section presents the results obtained using a DER scheduling model with Watt-VAr (co-optimized settings) and compares it with the results obtained in the previous sections.

a) Test System

The test system utilized is a large distribution feeder from a utility in Arizona which serves residential prosumers and has one of the largest PV penetration levels among the utility's active feeders. The distribution feeder is 9 km long, with both primary and secondary sections presented to create a comprehensive model. The service voltage is rated at 12.5 kV, with an installed roof-top PV capacity of 3800 kW. The optimization is performed on a snapshot of the distribution feeder, where it experienced severe over-voltage conditions on March 15, 2019. This typically occurs during spring, where the active power generation potential is high for PV resources and the residential cooling load is low due to nominal ambient temperatures. An instantaneous PV penetration level of 232% was observed with 3.625 MW of active power injected, with respect to only 1.563 MW of active power demand. The extensive model used to perform the simulation serves as an evidence to the scalability of the model proposed in the below sections. The model includes 8095 buses, 7943 lines and 742 PV units, out of which varying amounts of PV units are equipped with controllers to observe the effects of sparsity. More information about this feeder is presented in [40].

b) Watt-VAr: Default Settings

This subsection presents the DER scheduling model, which includes a Watt-VAr operational mode (default settings), to optimally dispatch active power and reactive power within the distribution feeder, to mitigate voltage issues throughout the system. The results are compared against a previous work which involves modeling a similar DER scheduling tool, with a Volt-VAr operational mode (default settings). The optimization is performed over three iterations, for the linearization error to converge and is performed on different sets of PV controllers including 110, 85, 75 and 70 controllers.

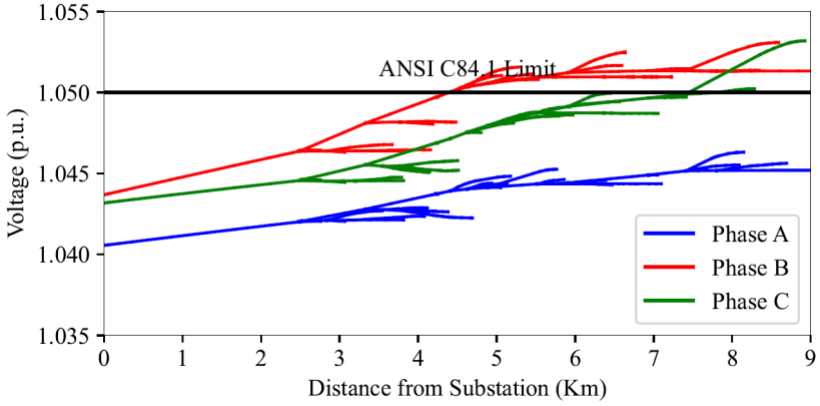

Figure 1.3 Voltage Profile with respect to Distance from Substation in the Primary Sections of the Distribution Feeder prior to VAr Optimization.

Figure 1.3 presents the voltage profile in the primary sections of the feeder with respect to the distance from the substation in kilometers prior to being optimized by the DER scheduling tool. Voltages at the secondary sections were higher than what was observed in the primary sections, with the highest voltage leading up to 1.06 pu. Due to no PV controllers being enabled in this snapshot, the SIs continued to inject available active power at unity power factor in an uncontrolled fashion, leading to severe over voltage situations. The DER Scheduling tool presented in this section, has the ability to absorb reactive power due to the Watt-VAr operational mode, as specified by the IEEE 1547-2018 standard [11]. After optimal dispatch of reactive power and

active power are performed, the voltage at the primary sections of the feeder are limited to below the prescribed ANSI standards as shown in Figure 1.4. Phase B and Phase C, which had significantly elevated voltage levels due to increased concentrations of PV units in the distribution feeder, in Figure 1.3, exhibit a drastic change in Figure 1.4 due to reactive power absorption.

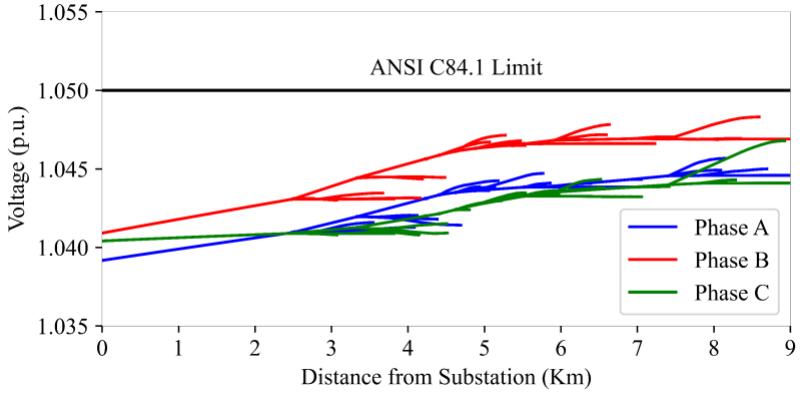

Figure 1.4 Voltage Profile with respect to Distance from Substation in the Primary Sections of the Distribution Feeder Post VAr Optimization.

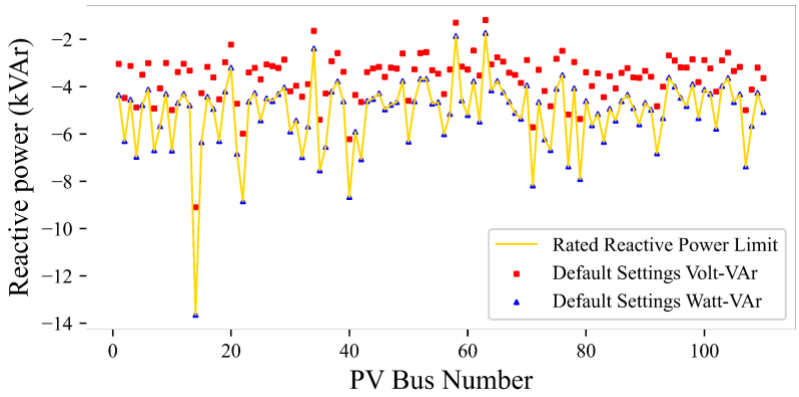

Figure 1.5 Reactive Power Absorption among PVs with 110 Controllers Enabled

Considering a popular operational mode such as Volt-VAr, the performance of the Watt-VAr operational mode is compared against it. Figure 1.5 exhibits the reactive power absorbed by Volt-VAr and Watt-VAr for the same system conditions and for the same number of PV controllers (110). The thin region of Volt-VAr reactive power dispatch points clearly lie below the reactive power dispatch points of Watt-VAr. At the same time, it is clearly observed that Watt-VAr operational mode, in a majority of instances, absorbs the rated reactive power. This absorption metric is clearly reflected in the reduction in over-voltage conditions as shown in Figure 1.6 for local bus voltages. Figure 1.7 also clearly reflects how the DER scheduling tool dispatches reactive power and active power among SIs, to resolve voltage issues not only in the local buses, but also distribution feeder wide.

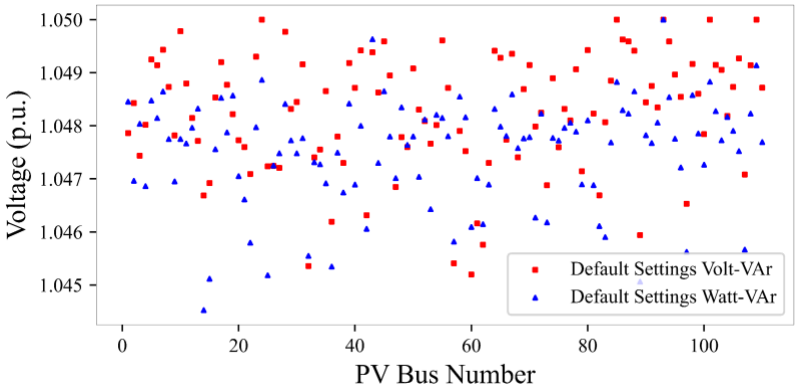

Figure 1.6 Local Bus Voltages at SIs with PV controllers Enabled

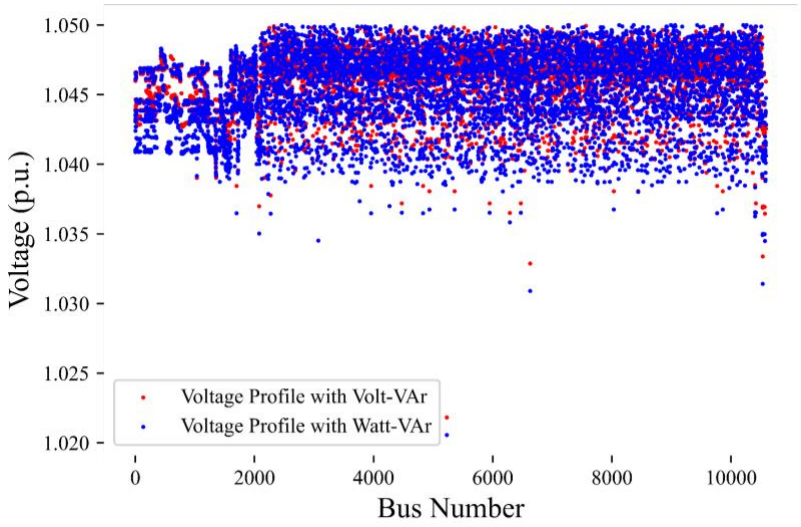

Figure 1.7 Distribution Feeder-Wide Voltage Profile

Assuming the fact that the inverter is not at its rated apparent power limit, absorbing reactive power reduces local bus voltage, which enables the inverter to inject more active power, without violating ANSI standards. The effect of reactive power absorption is observed in the active power injection metrics as shown in Figure 1.8, where at instances where Volt-VAr operational mode cannot inject the maximum active power available, Watt-VAr successfully does so. This effect is due to the fact that Volt-VAr operational mode does not absorb enough reactive power at specific buses as shown in Figure 1.5, which increases bus voltages to a greater extent. The curtailment of active power at these specific buses aids in mitigating the over-voltage issue due to the high R/X ratio of distribution systems, which cause a greater sensitivity of bus voltages to active power than reactive power.

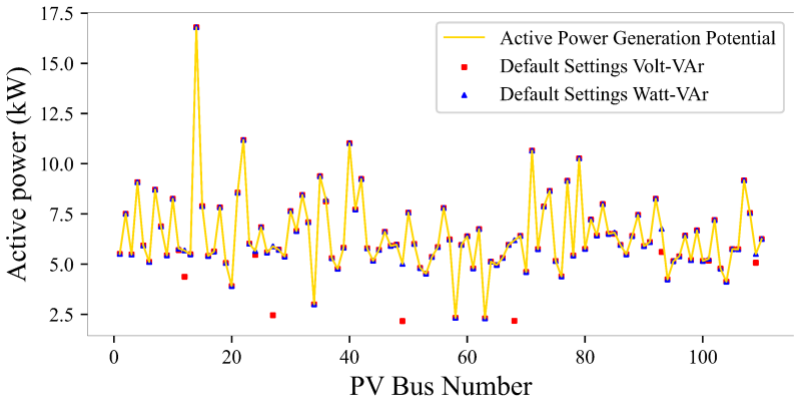

Figure 1.8 Active Power Injection among SIs Enabled with PV Controllers

Reactive power absorption aids in the increased injection of active power. The curtailment observed in the above Figure 1.8, with the Volt-VAr operational mode, causes increased cost of operation due to reduced utilization of cheap PV resources. But at the same time over-absorption of reactive power can be an issue pertaining to Watt-VAr mode of operation. Figure 1.9 exhibits the reactive power dispatch in pu with respect to bus voltage. Even with instances observed with lower bus voltages, increased reactive power absorption is observed, which is not the case with Volt-VAr. This observation is mainly due to the fact that reactive power absorption is a function of active power injection and not bus voltage with respect to Watt-VAr operational mode. This is not the case with Volt-VAr operational mode as it is constrained as a function of bus voltage, which regulates reactive power absorption.

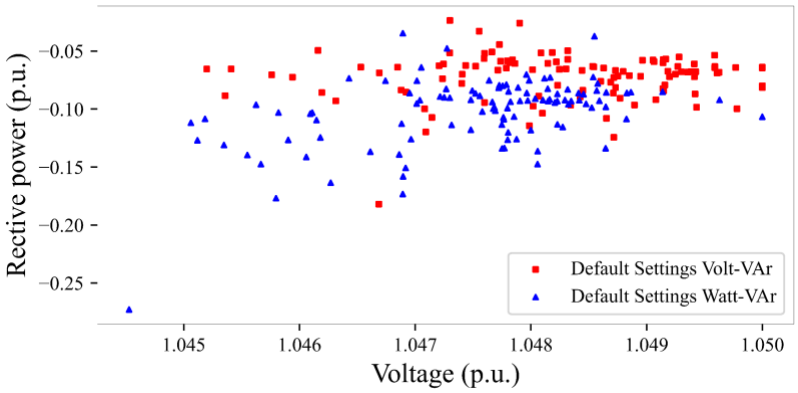

Figure 1.9 Reactive Power Dispatch of SIs with respect to Local Bus Voltages

Apart from the power quality issues observed with low power factors, over-absorption of reactive power can also lead to high bus voltage deviations as the reactive power absorbed at a bus is injected at another bus, which causes a concentrated “rise” and “dip” in bus voltages among different sections of the feeder. This phenomenon is observed when analyzing the difference in bus voltages for the same system conditions among DER scheduling tools equipped with Watt-VAr operational mode and Volt-VAr operational mode as shown in Figure 1.10. Figure 1.10 clearly shows concentrated regions of positive and negative voltage delta, which implies that Watt-

VAr operational mode is successful in reducing bus voltages to a greater extent than Volt-VAr operational mode in certain buses, while Volt-VAr is successful in reducing the voltage in other buses.

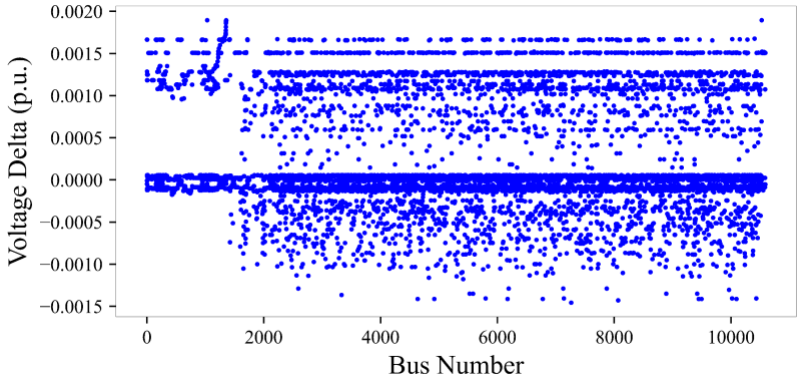

Figure 1.10 System-Wide Bus Voltage Difference among DER Scheduling tools equipped with Volt-VAr and Watt-VAr operational modes

Active power curtailment is still a big factor considering the cost implications associated with it. Along with the test of sparsity, an elevated substation voltage is also simulated to test the ability of the operational modes to prevent curtailment and mitigate voltage issues. For a distribution feeder with reverse power flow back to the substation from the end nodes of the feeder, voltage at the end nodes are considerably higher than the substation voltage. Increasing the substation voltage causes a ripple effect where the entire feeder experiences an increase in voltage. Tables 1.4, 1.5 and 1.6 present the different metrics for different sets of PV controllers enabled and different substation voltages. At every scenario and sparsity level, Watt-VAr operational mode performs better than Volt-VAr operational mode. The test of sparsity proves that with a reduction in the number of PV controllers enabled, Watt-VAr operational mode better mitigates the over-voltage by reducing the amount of curtailment, while still maintaining bus voltages within the ANSI standards. With the increased substation voltage, and the bus voltage, Watt-VAr operational mode still manages to absorb sufficient reactive power, even though active power curtailment is increased, which affects the absorption capability due to active power dependence. This effectively concludes that Watt-VAr operational mode performs better under tested conditions.

Table 1.4 SI Output Metrics over Different Sets of PV Controllers for Substation Phase 1 Voltage at 1.035 pu

Substation Phase 1 Voltage (pu)		1.035			
No. of PV Controllers		110	85	75	70
Active Power (kW)	Volt-VAr	707.6	589.0	534.3	506.8
	Watt-VAr	707.6	589.0	534.3	506.8
Reactive Power (kVAr)	Volt-VAr	-334.5	-282.0	-257.1	-244.5
	Watt-VAr	-563.0	-468.8	-426.1	-404.2
Curtailment (kW)	Volt-VAr	0	0	0	0
	Watt-VAr	0	0	0	0

Table 1.5 SI Output Metrics over Different Sets of PV Controllers for Substation Phase 1 Voltage at 1.039 pu

Substation Phase 1 Voltage (pu)		1.039			
No. of PV Controllers		110	85	75	70
Active Power (kW)	Volt-VAr	707.6	516.8	329.4	280.3
	Watt-VAr	707.6	556.7	412.4	364.6
Reactive Power (kVAr)	Volt-VAr	-387.4	-314.3	-265.8	-249.8
	Watt-VAr	-563.0	-468.8	-426.1	-404.2
Curtailment (kW)	Volt-VAr	0	72.7	204.9	226.4
	Watt-VAr	0	32.3	121.8	142.2

Table 1.6 SI Output Metrics over Different Sets of PV Controllers for Substation Phase 1 Voltage at 1.040 pu

Substation Phase 1 Voltage (pu)		1.040			
No. of PV Controllers		110	85	75	70
Active Power (kW)	Volt-VAr	706.3	478.9	236.2	175.6
	Watt-VAr	707.6	531.3	345.9	282.3
Reactive Power (kVAr)	Volt-VAr	-391.3	-313.4	-260.3	-242.8
	Watt-VAr	-563.0	-468.8	-426.1	-404.2
Curtailment (kW)	Volt-VAr	1.3	110.1	298.1	331.2
	Watt-VAr	0	57.6	188.4	224.5

c) Watt-VAr: Co-Optimized Settings

The flexibility offered by reactive power operational modes, with default settings, not only reduced active power curtailment due to overvoltage situations, but also mitigated overvoltage violations with reactive power support. This flexibility is further extended in this section by co-optimizing the set-points of the Watt-VAr operational mode to observe if the potential for operational efficiency can be maximized. As such the results of this section are compared against the metrics, as posted by Watt-VAr operational mode with default settings, to observe the gains obtained by enhancing flexibility. Figure 1.11 presents the voltage profile with respect to distance from substation in primary sections of the distribution feeder, post VAr optimization. Compared to Figure 1.3, a drastic improvement in the voltage profile is observed.

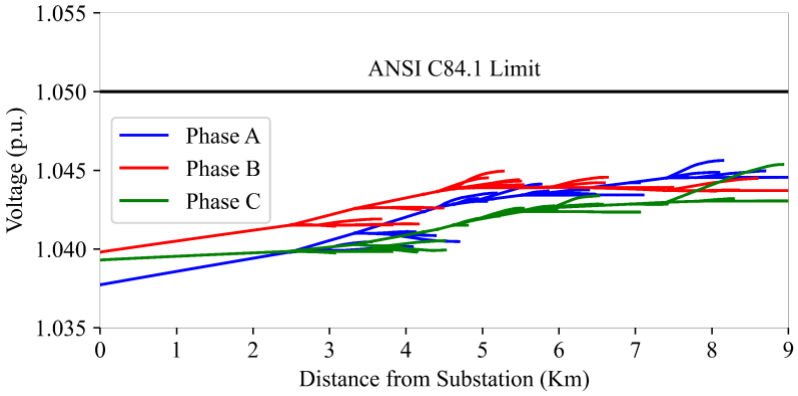

Figure 1.11 Voltage Profile with respect to Distance from Substation in the Primary Sections of the Distribution Feeder Post VAr Optimization.

Phases B and C show elevated levels of voltage in the primary sections of the feeder due to high concentrations of PV units in the secondary sections. The secondary sections face higher voltages than primary sections due to the reverse power flow phenomenon. Figure 1.11 exhibits how providing VAr support mitigates the overvoltage violation issues faced in phases B and C of the distribution feeder. Reactive power dispatch is observed in Watt-VAr operational mode with default settings, where due to high instantaneous PV penetration levels, high amounts of reactive power were absorbed. Figure 1.12 exhibits the reactive power dispatch levels of PV SIs for a case of 70 controllers enabled. Dispatch points observed in Figure 1.12 exhibit the case where, due to reduced number of controllers, reactive power absorption capability is reduced. Considering such a case, active power curtailment is the only option, in scenario where reactive power support alone cannot reduce the voltages within the ANSI standards. Active power curtailment is therefore utilized to limit the voltages to within the ANSI standards.

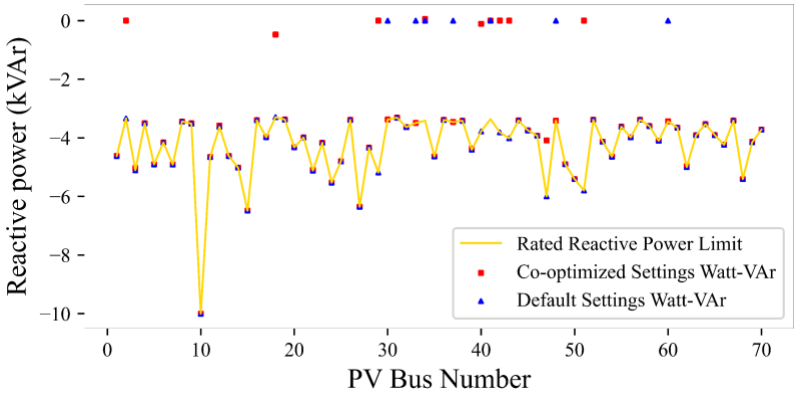

Figure 1.12 Reactive Power Dispatch among SIs Equipped with 70 PV Controllers

Considering the Watt-VAr operational mode with default settings, when active power injection is set at zero, the reactive power absorption is also set to zero, due to the way that the curve is designed. Coupling these factors together, the SIs cannot provide reactive power support without injecting active power which affects the distribution feeder operation. Therefore, a solution is

required, whereby curtailing active power to zero does not affect the SI's ability to provide VAr support for the distribution feeder. This flexibility is observed in the Watt-VAr operational mode with co-optimized settings where even when the active power injection is zero, reactive power is still being absorbed. In this scenario, curves are optimized in such a way that active power injection is maximized, and voltage conditions distribution feeder wide are maintained at nominal operating point. Figure 1.13 exhibits the local voltages at buses where SIs are located with PV controllers enabled. Both operational modes present a good reduction in bus voltages, well within the nominal values.

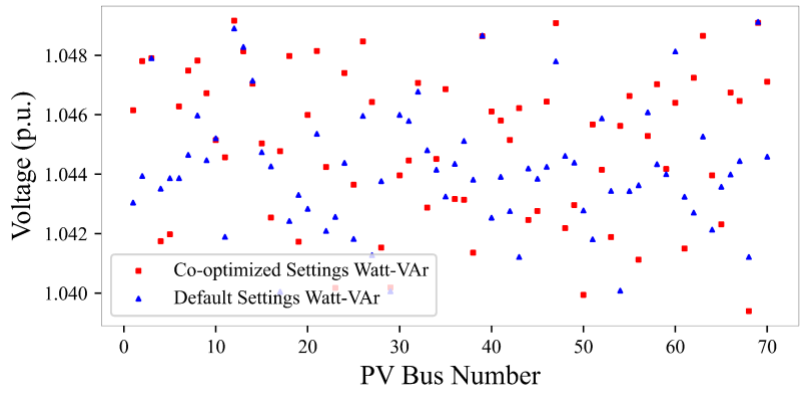

Figure 1.13 Local Bus Voltages of SIs with PV controllers Enabled.

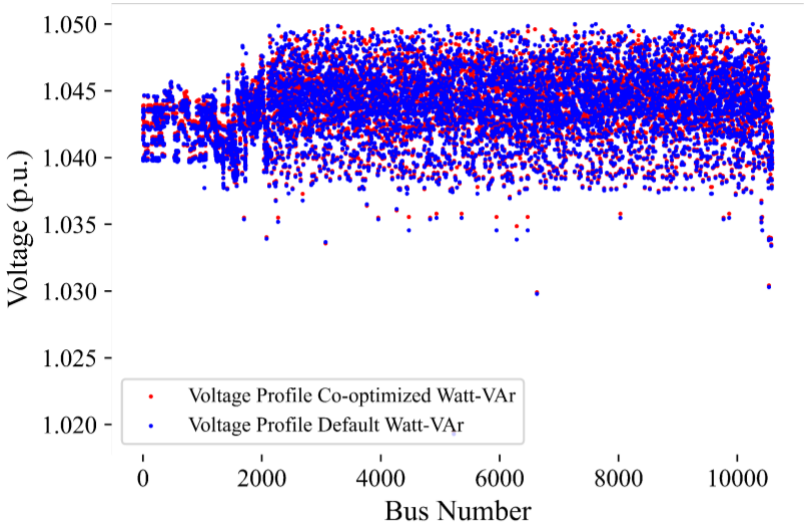

Figure 1.14 System Wide Voltage Profile

Apart from local bus voltage, the DER scheduling tool also dispatched reactive power and active power in such a way that voltage violation issues, distribution feeder-wide are mitigated as shown in Figure 1.14. A huge difference is not observed in the voltage profile between Watt-VAr operational mode with default settings and co-optimized settings. This non-observation is due to

the fact that over-voltage mitigation is constrained within the scheduling tool framework and is not incentivized within the model. Rather, operational cost reduction or active power curtailment reduction is incentivized. The difference is therefore observed within the active power dispatch (which directly indicates active power curtailment) as shown in Figure 1.15. Figure 1.15 presents the clear observation that at a majority of the dispatch points, Watt-VAr operational mode with co-optimized settings performs very well compared to other operational modes.

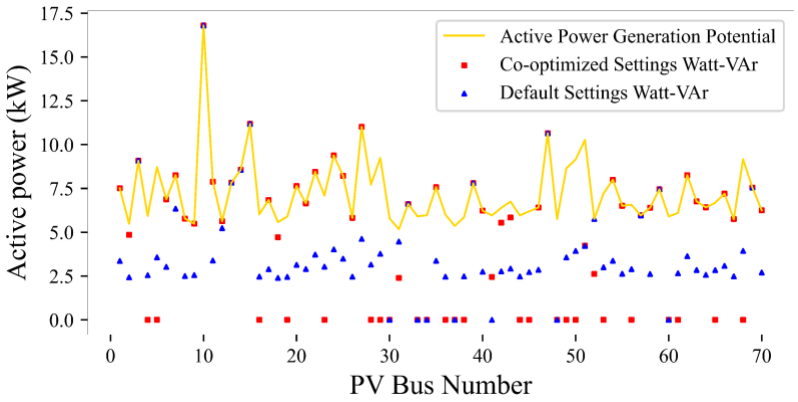

Figure 1.15 Active Power Dispatch among SIs with 70 PV Controllers Enabled

Apart from this observation, Watt-VAr operational mode with default settings also has a thin region of reduced active power dispatch from the actual power generation potential. This reduction is primarily due to the over-absorption of reactive power which infringes on the ability to inject active power.

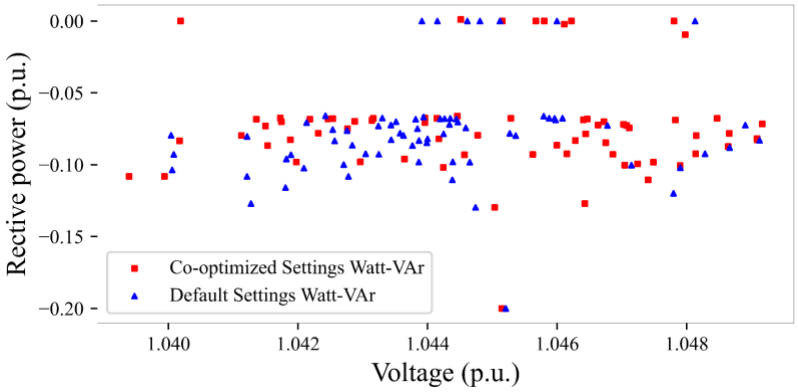

Figure 1.16 Reactive Power Dispatch of SIs with respect to Local Bus Voltage

The issue of reactive power over-absorption is discussed within the chapter, where Watt-VAr operational mode absorbs maximum possible reactive power at high instantaneous PV penetration levels. This over-absorption not only leads to power factor issues, but also causes voltage variations within different sections of the same distribution feeder. As shown in Figure 1.15 and Figure 1.16, Watt-VAr operational mode with co-optimized settings, has the ability to dispatch the

optimal amount of reactive power to mitigate voltage issues locally and feeder-wide, while still maximizing active power injection.

Table 1.7 SI Output Metrics over Different Sets of PV Controllers for Watt-VAr Operational Mode with Co-optimized Settings with respect to Default Settings

No. of PV Controllers		110	85	75	70
Active Power (kW)	Default	707.6	521.8	324.7	266.9
	Optimal	707.6	532.3	372.9	325.4
Reactive Power (kVAr)	Default	-412.8	-343.8	-288.6	-272.4
	Optimal	-339.1	-301.5	-262.9	-258.8
Curtailment (kW)	Default	0	67.2	209.6	239.8
	Optimal	0	56.7	161.4	181.4

Figure 1.16 also exhibits the concentration of high reactive power absorption for any give voltage conditions in Watt-VAr operational mode with default settings versus having a more spread distribution, indicating an optimal reactive power dispatch strategy which is also reflected by the curtailment metrics as presented in Table 1.7. Table 1.7 clearly exhibits the performance gains obtained with the increasing flexibility offered by Watt-VAr operational mode with co-optimized settings, wherein it performs significantly better than default settings at every instance. At every instance, over-absorption of reactive power is reduced in Watt-VAr operational mode with co-optimized settings, without affecting active power dispatch. This factor serves as an important solution for the effects of excessive reactive power injection or absorption within the distribution feeder. Another important observation from Table 1.7 is the effect of sparsity. As the number of PV controllers enabled with SIs reduce within the distribution feeder, the ability to control bus voltage reduces and active power curtailment increases. The gap between the curtailment metrics between the two methods also increases which indicates that Watt-VAr operational mode with co-optimized settings handles the effect of sparsity better. This factor indicates that the same performance of default settings can be replicated with lower number of PV controllers with co-optimized settings which is a significant improvement. Figures 1.17, 1.18 and 1.19 show examples of different co-optimized settings for different buses equipped with SIs and PV controllers, with respect to the default settings.

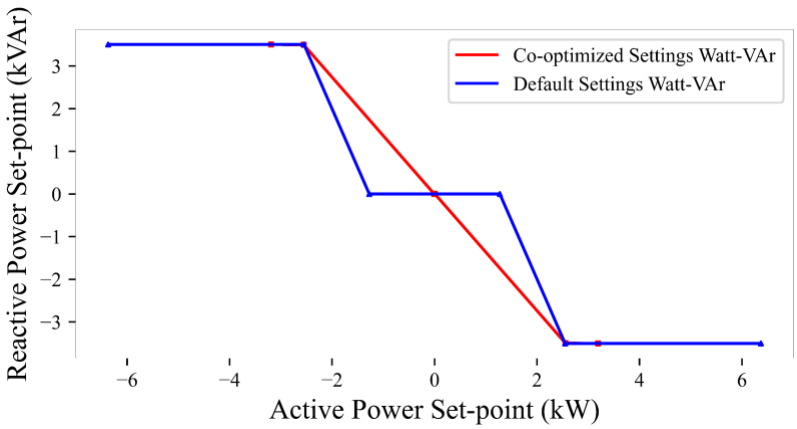

Figure 1.17 Watt-VAr Operational Mode Curves for SI on Bus 2519

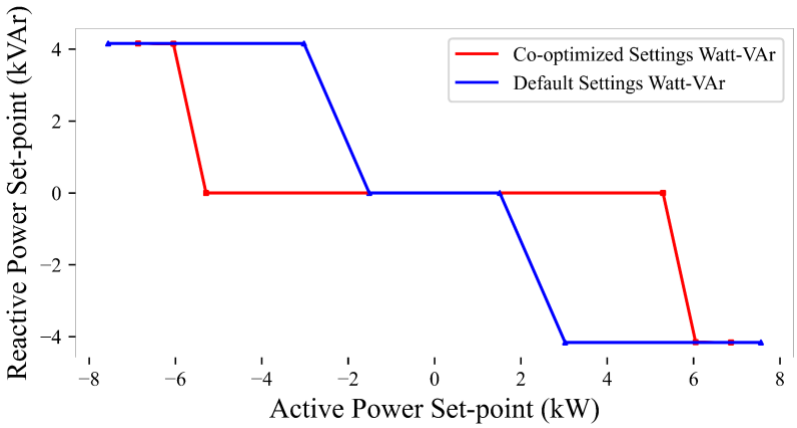

Figure 1.18 Watt-VAr Operational Mode Curves for SI on Bus 2624

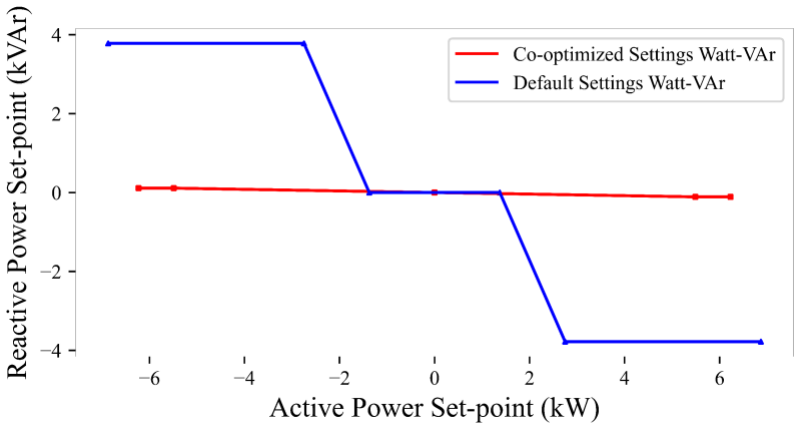

Figure 1.19 Watt-VAr Operational Mode Curves for SI on Bus 6435

1.4 Voltage-Active Power Operational Mode

1.4.1 Volt-Watt Mode

According to the IEEE 1547-2018 standards, Volt-Watt operational mode involves the control of active power dispatch as a function of local bus voltage of the SI. The participation of DERs in active power operational mode with any specified reactive power operational mode for voltage regulation requires the approval of the area EPS (Electric Power System) operator [11]. The specified characteristic is a piece-wise linear voltage-active power function. Figure 4.1 exhibits the Volt-Watt curve as specified by the IEEE 1547-2018 standard. The characteristic curve has 2 different zones of operation including two operating set-points for both voltage and active power. As defined by the default values of the curve settings, each zone represents active power dispatch values to be followed as a linear function of local bus voltage. Zone 1 represents the zone of operation, where for all nominal local bus voltages below the set-point $V_{1,\varphi}^{pvv,vw}$, the SI injects maximum available active power into the grid, as defined by $P_{f,\varphi}^{pvv,av}$. Zone 2 represents the zone

of operation between $V_{1,\varphi}^{pvv,vw}$ and $V_{2,\varphi}^{pvv,vw}$, where the SI curtails active power according to a linear relationship with the local bus voltage as defined by the slope between $(V_{1,\varphi}^{pvv,vw}, P_{f,\varphi}^{pvv,av})$ and $(V_{2,\varphi}^{pvv,vw}, 0)$.

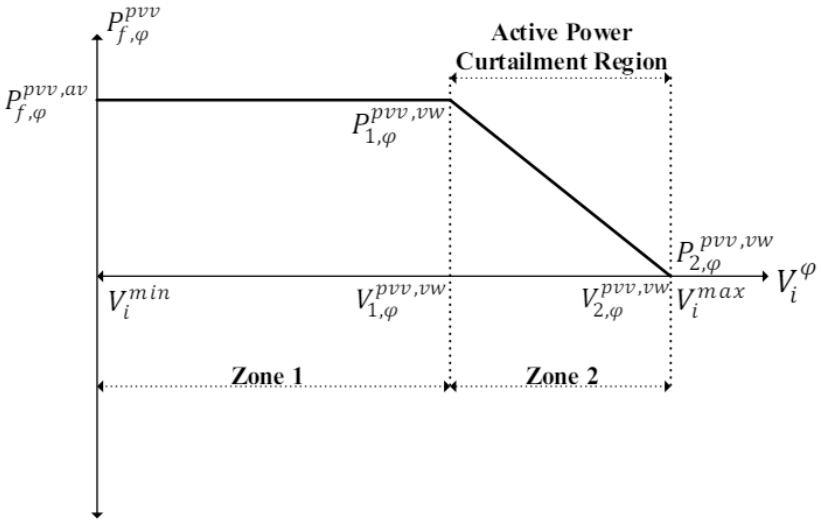

Figure 1.20 The Volt-Watt Piecewise Linear Function According to the IEEE 1547-2018 Standard [11]

The IEEE 1547-2018 standard has enabled SIs to modify these set-points within an allowable range which are to be immediately implemented by the DER operator [11]. Table 1.8 and Table 1.9 describes the default settings utilized and the allowable range of modifications for the set-points as described by the IEEE 1547-2018 standard. $P_{f,\varphi}^{pvv,av}$ corresponds to the maximum available active power generation for each SI f at Phase φ. SIs with BES device, capable of absorbing active power, can continue to absorb active power, after curtailing active power generation to zero until the rated absorption limit is reached.

Table 1.8 Voltage Set-points for the Volt-Watt Operational Mode Curve Following the IEEE 1547-2018 Standard [11]

Voltage Set-Points	Default Settings	Modification Range	
		Minimum	Maximum
$V_{1,\varphi}^{pvv,vw}$	1.05 pu	1.05 pu	1.09 pu
$V_{2,\varphi}^{pvv,vw}$	1.10 pu	$V_{1,\varphi}^{pvv,vw}$ + 0.01 pu	1.10

Table 1.9 Active Power Set-points for the Volt-Watt Operational Mode Curve Following the IEEE 1547-2018 Standard [11]

Active Power Set-Points	Default Settings	Modification Range	
		Minimum	Maximum
$P_{1,\varphi}^{pvv,vw}$	$P_{f,\varphi}^{pvv,av}$	$P_{f,\varphi}^{pvv,av}$	$P_{f,\varphi}^{pvv,av}$

$P_{2,\varphi}^{pvv,vw}$	0	Rated Active Power Absorption Capability	$P_{f,\varphi}^{pvv,av}$

1.4.2 Problem Formulation

The DER scheduling tool presented in this section is formulated with a robust DOPF formulation and enabled along with the Watt-VAr operational mode as mentioned in Section 1.3. As such, the formulation as presented in (1.2)-(1.42) still apply with the notable exception of (1.16), (1.21) and (1.61). Considering the role of Volt-Watt operational mode in shaping the curtailment of active power generation with respect to local bus voltages in the system, the over-voltage mitigation constraints are relaxed to form a much larger continuous operating region according to the IEEE 1547-2018 standards as shown in (1.62).

$$0.88 \leq V_i^{\varphi} \leq 1.10, \forall\, \varphi \in \phi, i \in P \tag{1.62}$$

Considering the effect of active power generation curtailment on local bus voltage, the objective is reformulated to minimize the voltage violation issues, without strictly constraining it to the ANSI standard. As such the upper and lower limit voltage deviation is estimated as shown in (1.63).

$$0.95 - V_i^{\Delta,\varphi,lower} \leq V_i^{\varphi} \leq 1.05 + V_i^{\Delta,\varphi,upper}, \forall\, \varphi \in \phi, i \in P \tag{1.63}$$

$V_i^{\Delta,\varphi,lower}$ and $V_i^{\Delta,\varphi,upper}$ correspond to the respective deviations from the lower and upper limits for voltages according to the ANSI standard. The deviation variables are constrained to be positive real values. The net system voltage deviation is summed across the system and is minimized as the objective function as shown in (1.64).

$$\min_{\substack{V_i^{r,\varphi}, V_i^{im,\varphi}, I_i^{r,\varphi}, I_i^{im,\varphi} \\ I_\ell^{r,\varphi}, I_\ell^{im,\varphi}, P_{f,\varphi}^{pvv}, Q_{f,\varphi}^{pvv}}} \sum_{\varphi \in \phi} \left(\sum_{\forall i} V_i^{\Delta,\varphi,upper} + \sum_{\forall i} V_i^{\Delta,\varphi,lower} \right) \tag{1.64}$$

Equation (1.65) presents the linear piecewise function of the Volt-Watt operational mode according to the IEEE 1547-2018 standard [11].

$$P_{f,\varphi}^{pvv} = \begin{cases} P_{f,\varphi}^{pvv,av} & , V_{f,\varphi}^{min} \leq V_i^{\varphi} \leq V_{1,\varphi}^{pvv,vw} \\ P_{2,\varphi}^{pvv,vw} + \frac{(V_i^{\varphi} - V_{2,\varphi}^{pvv,vw})\left(P_{2,\varphi}^{pvv,vw} - P_{1,\varphi}^{pvv,vw}\right)}{V_{2,\varphi}^{pvv,vw} - V_{1,\varphi}^{pvv,vw}} & , V_{1,\varphi}^{pvv,vw} < V_i^{\varphi} \leq V_{2,\varphi}^{pvv,vw} \end{cases} \tag{1.65}$$

Equation (1.65) can be formulated into MILP constraints using the Big-M method as shown in (1.66)-(1.70). Zone 1 where the SI injects available active power can be represented as shown in (1.66) and (1.67).

$$V_i^{\varphi} \leq M_1 u_{1,f,\varphi}^{vw} + V_{1,\varphi}^{pvv,vw} \tag{1.66}$$

$$-M_1 u_{1,f,\varphi}^{vw} \leq P_{f,\varphi}^{pvv} - P_{f,\varphi}^{pvv,av} \leq M_1 u_{1,f,\varphi}^{vw} \tag{1.67}$$

$u_{1,f,\varphi}^{vw}$, is the binary variable associated with the selection of Zone 1 when it is set to zero. Zone 2, where the SI curtails active power according to a linear relationship to local bus voltage can be represented as shown in (1.68) and (1.69).

$$-M_1 u_{2,f,\varphi}^{vw} + V_{1,\varphi}^{pvv,vw} \leq V_i^{\varphi} \leq M_1 u_{2,f,\varphi}^{vw} + V_{2,\varphi}^{pvv,vw} \tag{1.68}$$

$$-M_1 u_{2,f,\varphi}^{vw} \leq P_{f,\varphi}^{pvv} - P_{2,\varphi}^{pvv,vw} - \frac{(V_i^{\varphi} - V_{2,\varphi}^{pvv,vw})\left(P_{2,\varphi}^{pvv,vw} - P_{1,\varphi}^{pvv,vw}\right)}{V_{2,\varphi}^{pvv,vw} - V_{1,\varphi}^{pvv,vw}} \leq M_1 u_{2,f,\varphi}^{vw} \tag{1.69}$$

$u_{2,f,\varphi}^{vw}$, is the binary variable associated with the selection of Zone 2 when it is set to zero. Equation (1.70) represents the mutual exclusivity constraint which prevents the selection of multiple operating zones at the same time.

$$u_{1,f,\varphi}^{vw} + u_{2,f,\varphi}^{vw} \leq 1 \tag{1.70}$$

Apart from the above mentioned changes, (1.21) is also disregarded. Equation (1.21) enables active power generation curtailment at any system condition without considering local bus voltage which violates the IEEE 1547-2018 standards in case Volt-Watt operational mode is enabled. Essentially, Volt-Watt operational mode controls active power generation curtailment, but is not mandatory to be enabled, unlike reactive power operational modes.

1.4.3 Results and Analysis

The test system utilized for analyzing the performance of the DER scheduling framework, with the Volt-Watt operational mode, is the same as the one described in Section 1.3, with identical system conditions. Considering the excessive over-voltage conditions experienced by the distribution feeder due to high instantaneous PV penetration, a proper DER scheduling framework is required to mitigate over-voltage issues. As shown in Figure 1.21, the primary sections of the feeder experienced high voltages, with the secondary sections experiencing voltages higher than 1.06 pu. Phases B and C especially experience over-voltages due to high levels of PV penetration. Considering the fact that active power is not curtailed at SIs where local bus voltages are nominal, reactive power compensation is still a valid strategy utilized within the framework, using the Watt-VAr operational mode. The results are observed on a set of 70 PV controllers enabled, to analyze the performance of a framework with Volt-Watt operational mode enabled.

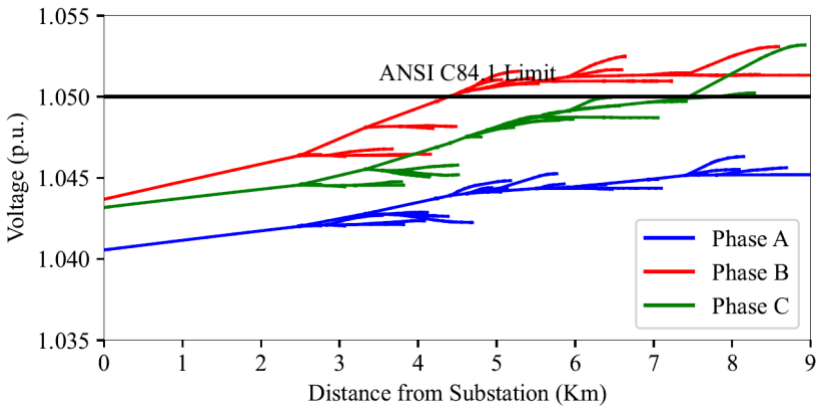

Figure 1.21 Voltage Profile with respect to Distance from Substation in the Primary Sections of the Distribution Feeder prior to VAr Optimization

As shown in Figure 1.22, post VAr optimization, the voltage profile of primary sections exhibit a significant improvement. Phases B and C especially show a significant improvement in part due to the reactive power absorption capability provided by SIs in those phases. Table 1.10 presents the results of the VAr optimization. Even with the reactive power absorption capability, the SIs are unable to limit net voltage deviation in the distribution feeder to zero. Active power generation curtailment is required to complement reactive power absorption in this case to mitigate the over voltages. As shown in Figure 1.23, with respect to available active power generation potential, only a handful of SIs curtail active power, only beyond 1.05 pu.

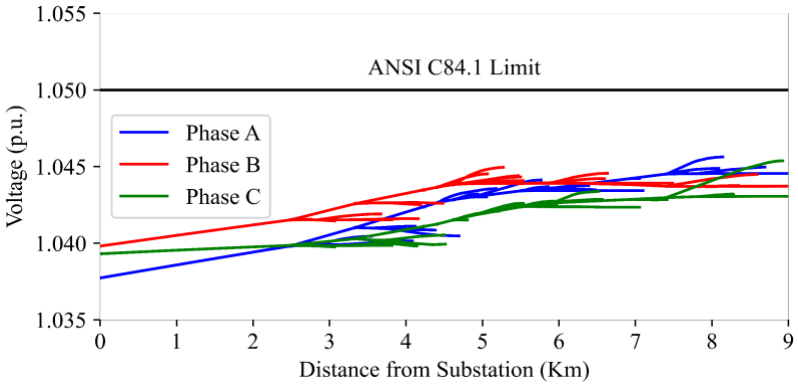

Figure 1.22 Voltage Profile with respect to Distance from Substation in the Primary Sections of the Distribution Feeder Post VAr Optimization considering Volt-Watt and Watt-VAr Operational Modes.

Table 1.10 Active Power Generation Curtailment and Net Voltage Deviation Metrics Post Optimization

Net Voltage Deviation (pu)	Active Power Curtailment (kW)	Active Power Injection (kW)	Reactive Power Absorption (kVAr)
0.16810475	0.1495	506.7	296.4

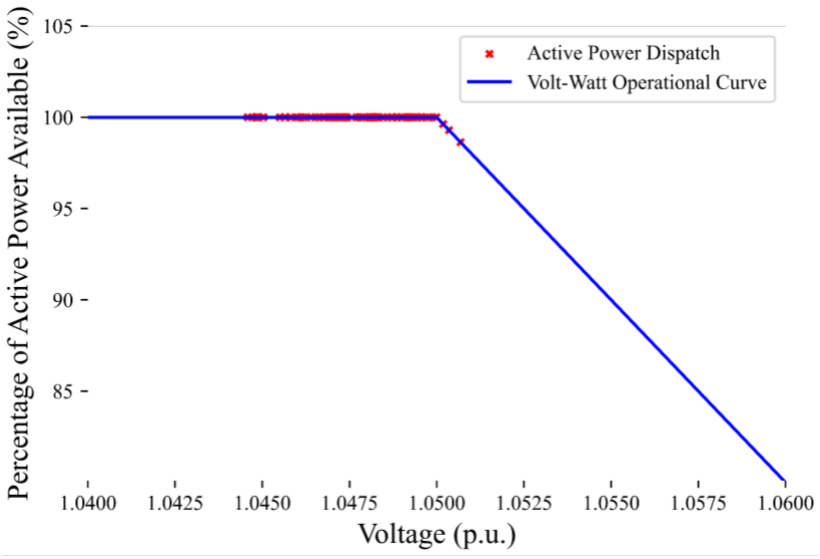

Figure 1.23 Active Power Dispatch as a Percentage of Active Power Available with respect to Local Bus Voltage

To mitigate over-voltage issues feeder-wide, proper SI coordination is required with optimal active and reactive power dispatch. If active power dispatch is constrained by system operating conditions, the ability to mitigate over voltage issues system-wide is inhibited. Reactive power dispatch alone cannot contribute to mitigating voltage issues across the feeder. However sustained operations in over-voltage conditions result in severe economic losses considering nominal distribution equipment operating conditions. One important observation is the fact that primary sections of the distribution feeder exhibit a complete mitigation of over-voltage issues as shown in Figure 1.22, but secondary sections do not. Figure 1.24 exhibits the voltage deviations distribution feeder wide, with the non-zero deviations observed only in the secondary sections.

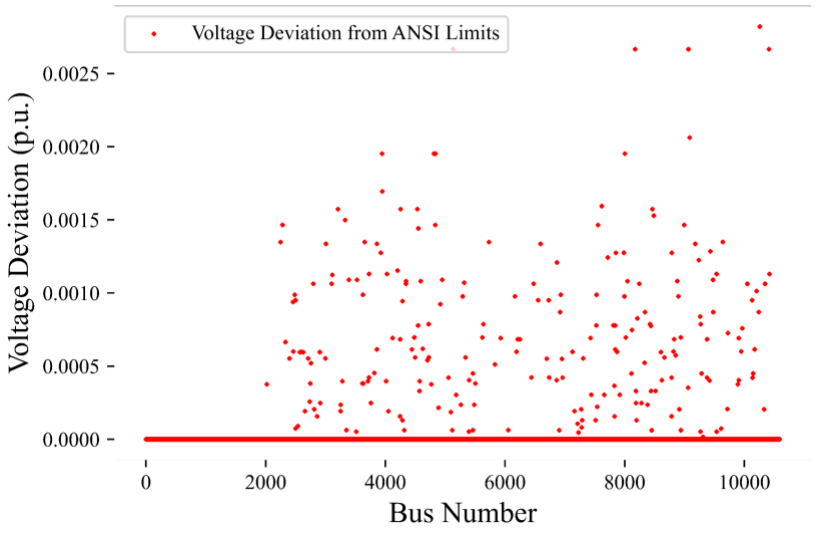

Figure 1.24 Net Voltage Deviation Profile for the Distribution Feeder with the Volt-Watt Operational Mode Enabled

This inability to completely mitigate over-voltage deviations, implies that the Volt-Watt operational mode serves as a passive curtailment measure only for voltages beyond 1.05 pu, and does not actively curtail active power to preserve distribution system operational integrity.

1.5 Unified Mode Selection Framework

In this section, the effect of optimally selecting the operational mode and settings for SIs, while concurrently dispatching them to mitigate distribution feeder power quality issues and maximizing distribution feeder hosting capacity is observed. According to the IEEE 1547-2018 standard [11], four distinct reactive power operational modes are allowed with clearly defined curve characteristics. Among them, Watt-VAr and Volt-VAr operational modes are popular choices for mitigating voltage violation issues at local buses. Both Watt-VAr and Volt-VAr operational modes have different abilities which make them well suited for different distribution system operation scenarios. The UMS (Unified Mode Selection) framework with default settings, presented in this section, optimally identifies the ideal reactive power operational mode for each SI to mitigate issues distribution feeder wide and maximize PV utilization. The section also presents an extension of the UMS framework, where each operational mode curve is concurrently optimized to further extend the flexibility offered by considering default curve characteristics. The DER scheduling tool presented based on the UMS framework optimally selects the operational mode and settings for each individual inverter to mitigate voltage issues distribution feeder-wide and minimize the operational cost. Figure 1.25 presents a flow chart describing the operation of the DER scheduling tool based on the UMS framework with co-optimized settings. The section also presents two distinct formulations to minimize the Phase Voltage Unbalance Factor (PVUF) within the distribution feeder with the help of reactive power dispatch from the SIs including a constraint-based and objective function-based approach.

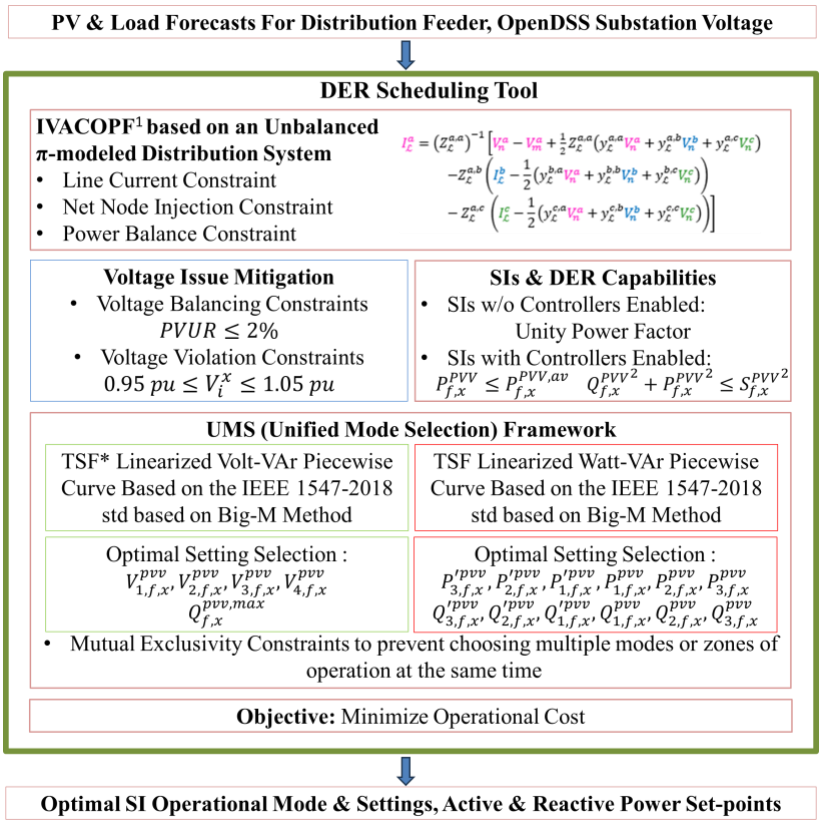

Figure 1.25 DER Scheduling Process Flowchart

1.5.1 Volt-VAr Mode

According to the IEEE 1547-2018 standard, Volt-VAr operational Mode involves the control of reactive power dispatch as a function of voltage at the local bus where the SI is situated. The participation of DERs in any specified reactive power operational mode for voltage regulation requires the approval of the area EPS (Electric Power System) operator [11]. The specified characteristic is a piecewise linear voltage-reactive power function. Figure 1.26 exhibits the Volt-VAr curve as specified by the IEEE 1547-2018 standard. The characteristic curve has 5 different zones of operation including 4 operating set-points for voltage and 2 operating set-points for reactive power. As defined by the default values of the curve settings, each zone represents reactive power dispatch values to be followed as a linear function of local bus voltage of the SI.

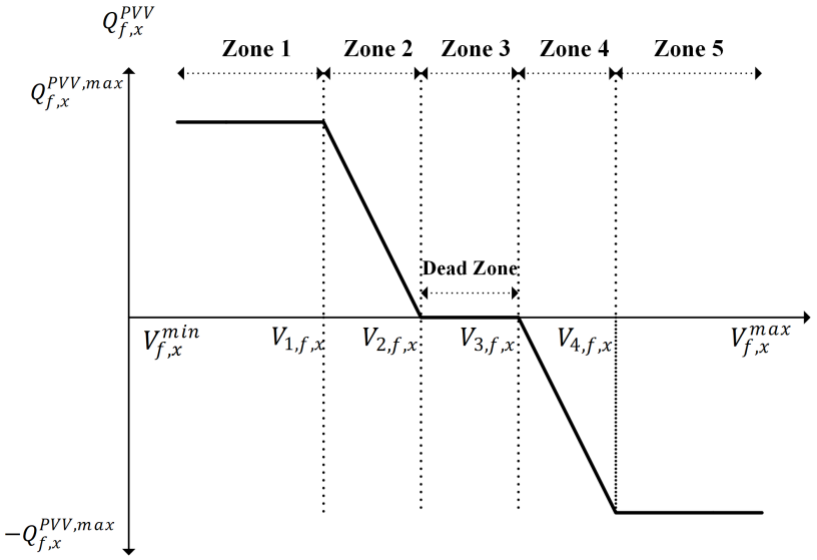

Figure 1.26 The Volt-VAr Piecewise Linear Function According to the IEEE 1547-2018 Standard

Zone 1 represents the zone of operation, where beyond the voltage set point $V_{1,\varphi}^{pvv}$, the SI injects constant reactive power (maximum reactive power injection capability) as defined by $Q_{f,\varphi}^{pvv,max}$. Zone 2 represents the zone of operation, where between the voltage set points $V_{1,\varphi}^{pvv}$ and $V_{2,\varphi}^{pvv}$, the SI injects reactive power according to a linear relationship with the voltage at the local bus as defined by the slope between $(V_{1,\varphi}^{pvv}, Q_{f,\varphi}^{pvv,max})$ and $(V_{2,\varphi}^{pvv}, 0)$. Zone 3 is usually modeled as a dead zone, between the set-points $(V_{2,\varphi}^{pvv}, 0)$ and $(V_{3,\varphi}^{pvv}, 0)$, such that reactive power is neither injected nor absorbed by the SI. Zone 4 represents the zone of operation, where between the voltage set points $V_{3,\varphi}^{pvv}$ and $V_{4,\varphi}^{pvv}$, the SI absorbs reactive power according to a linear relationship with the voltage at the local bus as defined by the slope between $(V_{3,\varphi}^{pvv}, 0)$ and $(V_{4,\varphi}^{pvv}, -Q_{f,\varphi}^{pvv,max})$. Zone 5 represents the zone of operation, where beyond the voltage set point $V_{4,\varphi}^{pvv}$, the SI absorbs constant reactive power (maximum reactive power absorption capability) as defined by $-Q_{f,\varphi}^{pvv,max}$. The IEEE 1547-2018 standard has enabled SIs to modify these set-points within an allowable range which are to be immediately implemented by the DER operator [11]. Table 1.11 and Table 1.12 describes the default settings utilized and the allowable range of modifications for the set-points as described by the IEEE 1547-2018 standard.

Table 1.11 Voltage Set-Points for the Volt-VAr operational mode curve Following the IEEE 1547-2018 Standard [11]

Voltage Set-Points	Default Settings	Modification Range	
		Minimum	Maximum
$V_{1,\varphi}^{pvv}$	0.94 pu.	0.82 pu.	$V_{2,\varphi}^{pvv}$ – 0.02 pu.
$V_{2,\varphi}^{pvv}$	0.98 pu.	0.97 pu.	1.00 pu.
$V_{3,\varphi}^{pvv}$	1.02 pu.	1.00 pu.	1.03 pu.

$V_{4,\varphi}^{pvv}$	1.06 pu.	$V_{3,\varphi}^{pvv}$ – 0.02 p.u.	1.18 pu.

Table 1.12 Reactive Power Set-Points for the Volt-VAr operational mode curve Following the IEEE 1547-2018 Standard [11]

Reactive Power Set-Points	Default Settings	Modification Range	
		Minimum	Maximum
$Q_{1,\varphi}^{pvv}$	100 % $Q_{f,\varphi}^{max,pvv}$	-$Q_{f,\varphi}^{max,pvv}$	+$Q_{f,\varphi}^{max,pvv}$
$Q_{2,\varphi}^{pvv}$	100 % $-Q_{f,\varphi}^{max,pvv}$	-$Q_{f,\varphi}^{max,pvv}$	+$Q_{f,\varphi}^{max,pvv}$

1.5.2 Problem Formulation

The DER scheduling tool presented in this section involves the robust DOPF formulation, IVACOPF as presented in Section 1.3.2 and includes (1.2)-(1.22). Apart from this, the UMS framework with default settings and co-optimized settings as mentioned above, are formulated in the following subsections, along with the two distinct approaches for balancing voltages.

a) Unified Mode Selection Framework: Default Settings

Considering the fact the UMS framework optimally selects the operational mode and zone between the Watt-VAr and Volt-VAr operational modes, both are formulated based on discrete set-points and clear operational bounds. As such the two curves can be represented using piece-wise functions as shown in (1.23) and (1.71).

$$Q_{f,\varphi}^{pvv} = \begin{cases} Q_{f,\varphi}^{pvv,max} & , V_{f,\varphi}^{min} \le V_i^{\varphi} < V_{1,\varphi}^{pvv} \\ \frac{Q_{f,\varphi}^{pvv,max}\left(V_{2,\varphi}^{pvv} - V_i^{\varphi}\right)}{V_{2,\varphi}^{pvv} - V_{1,\varphi}^{pvv}} & , V_{1,\varphi}^{pvv} \le V_i^{\varphi} < V_{2,\varphi}^{pvv} \\ 0 & , V_{2,\varphi}^{pvv} \le V_i^{\varphi} < V_{3,\varphi}^{pvv} \\ \frac{Q_{f,\varphi}^{pvv,max}\left(V_{3,\varphi}^{pvv} - V_i^{\varphi}\right)}{V_{4,\varphi}^{pvv} - V_{3,\varphi}^{pvv}} & , V_{3,\varphi}^{pvv} \le V_i^{\varphi} < V_{4,\varphi}^{pvv} \\ -Q_{f,\varphi}^{pvv,max} & , V_{4,\varphi}^{pvv} \le V_i^{\varphi} < V_{f,\varphi}^{max} \end{cases} \quad (1.71)$$

Apart from the existing set of decision variables, mode selection is performed within the framework using the help of binary decision variables to select or enable one operational mode at a given time. $u_{1,f,\varphi}$ is the binary decision variable associated with selecting Volt-VAr operational mode, where the variable is assigned 1 when the mode is enabled. $u_{2,f,\varphi}$ is the binary decision variable associated with selecting Watt-VAr operational mode, where the variable is assigned 1 when the mode is enabled. Collectively, the piece-wise curves along with the mode selection process are modeled in a mixed-integer linear fashion using the Big-M method. The Volt-VAr operational mode is accordingly formulated as shown in (1.72)-(1.82). Zone 1 is modeled as (1.72) and (1.73), in which the SI injects rated reactive power.

$$M_1 u_{1,f,\varphi}^{qv} + M_2(1 - u_{1,f,\varphi}) + V_{1,\varphi}^{pvv} \ge V_i^{\varphi} \quad (1.72)$$

$$-M_1 u_{1,f,\varphi}^{qv} - M_2(1 - u_{1,f,\varphi}) \le Q_{f,\varphi}^{pvv} - Q_{f,\varphi}^{pvv,max} \le M_1 u_{1,f,\varphi}^{qv} + M_2(1 - u_{1,f,\varphi}) \quad (1.73)$$

Zone 2 is modeled as (1.74) and (1.75) wherein the SI injects reactive power according to a linear relationship to the bus voltage.

$$-M_1 u_{2,f,\varphi}^{qv} - M_2(1-u_{1,f,\varphi}) + V_{1,\varphi}^{pvv} \le V_i^{\varphi} \le M_1 u_{2,f,\varphi}^{qv} + M_2(1-u_{1,f,\varphi}) + V_{2,\varphi}^{pvv} \quad (1.74)$$

$$-M_1 u_{2,f,\varphi}^{qv} - M_2(1-u_{1,f,\varphi}) \le Q_{f,\varphi}^{pvv} - \frac{Q_{f,\varphi}^{pvv,max}\left(V_{2,\varphi}^{pvv} - V_i^{\varphi}\right)}{V_{2,\varphi}^{pvv} - V_{1,\varphi}^{pvv}} \le M_1 u_{2,f,\varphi}^{qv} + M_2(1-u_{1,f,\varphi}) \quad (1.75)$$

Zone 3 is modeled as (1.76) and (1.77) wherein the SI neither injects nor absorbs reactive power. This zone is also referred to as the dead zone.

$$-M_1 u_{3,f,\varphi}^{qv} - M_2(1-u_{1,f,\varphi}) + V_{2,\varphi}^{pvv} \le V_i^{\varphi} \le M_1 u_{3,f,\varphi}^{qv} + M_2(1-u_{1,f,\varphi}) + V_{3,\varphi}^{pvv} \quad (1.76)$$

$$-M_1 u_{3,f,\varphi}^{qv} - M_2(1-u_{1,f,\varphi}) \le Q_{f,\varphi}^{pvv} \le M_1 u_{3,f,\varphi}^{qv} + M_2(1-u_{1,f,\varphi}) \quad (1.77)$$

Zone 4 is modeled as (1.78) and (1.79) wherein the SI absorbs reactive power according to a linear relation to the bus voltage.

$$-M_1 u_{4,f,\varphi}^{qv} - M_2(1-u_{1,f,\varphi}) + V_{3,\varphi}^{pvv} \le V_i^{\varphi} \le M_1 u_{4,f,\varphi}^{qv} + M_2(1-u_{1,f,\varphi}) + V_{4,\varphi}^{pvv} \quad (1.78)$$

$$-M_1 u_{4,f,\varphi}^{qv} - M_2(1-u_{1,f,\varphi}) \le Q_{f,\varphi}^{pvv} - \frac{Q_{f,\varphi}^{pvv,max}\left(V_{3,\varphi}^{pvv} - V_i^{\varphi}\right)}{V_{4,\varphi}^{pvv} - V_{3,\varphi}^{pvv}} \le M_1 u_{4,f,\varphi}^{qv} + M_2(1-u_{1,f,\varphi}) \quad (1.79)$$

Zone 5 is modeled as (1.80) and (1.81) wherein the SI absorbs rated reactive power according to the IEEE 1547-2018 standard [11].

$$-M_1 u_{5,f,\varphi}^{qv} - M_2(1-u_{1,f,\varphi}) + V_{4,\varphi}^{pvv} \le V_i^{\varphi} \quad (1.80)$$

$$-M_1 u_{5,f,\varphi}^{qv} - M_2\left(1-u_{1,f,\varphi}\right) \le Q_{f,\varphi}^{pvv} + Q_{f,\varphi}^{pvv,max} \le M_1 u_{5,f,\varphi}^{qv} + M_2(1-u_{1,f,\varphi}) \quad (1.81)$$

Equation (1.82) represents the mutual exclusivity constraint, which restricts selection of multiple zones of operation at the same time.

$$u_{1,f,\varphi}^{qv} + u_{2,f,\varphi}^{qv} + u_{3,f,\varphi}^{qv} + u_{4,f,\varphi}^{qv} + u_{5,f,\varphi}^{qv} \le 4, \forall f \in F1 \quad (1.82)$$

The Watt-VAr operational mode is accordingly formulated as shown in (1.83)-(1.97). Zone 1 is modeled as (1.83) and (1.84), in which the SI injects rated reactive power.

$$M_1 u_{1,f,\varphi}^{pq} + M_2(1-u_{2,f,\varphi}) + P_{3,\varphi}^{\prime pvv} \ge P_{f,\varphi}^{pvv} \quad (1.83)$$

$$-M_1 u_{1,f,\varphi}^{pq} - M_2\left(1-u_{2,f,\varphi}\right) \le Q_{f,\varphi}^{pvv} - Q_{f,\varphi}^{pvv,max} \le M_1 u_{1,f,\varphi}^{pq} + M_2(1-u_{2,f,\varphi}) \quad (1.84)$$

Zone 2 is modeled as (1.85) and (1.86), in which the SI injects reactive power according to a linear relationship to active power dispatch.

$$-M_1 u_{2,f,\varphi}^{pq} - M_2\left(1 - u_{2,f,\varphi}\right) + P_{3,\varphi}^{\prime pvv} \le P_{f,\varphi}^{pvv} \le M_1 u_{2,f,\varphi}^{pq} + M_2\left(1 - u_{2,f,\varphi}\right) + P_{2,\varphi}^{\prime pvv} \tag{1.85}$$

$$-M_1 u_{2,f,\varphi}^{pq} - M_2(1 - u_{2,f,\varphi}) \le Q_{f,\varphi}^{pvv} - Q_{2,\varphi}^{\prime pvv} + \frac{\left(P_{2,\varphi}^{\prime pvv} - P_{f,\varphi}^{pvv}\right)\left(Q_{3,\varphi}^{\prime pvv} - Q_{2,\varphi}^{\prime pvv}\right)}{P_{2,\varphi}^{\prime pvv} - P_{3,\varphi}^{\prime pvv}} \le M_1 u_{2,f,\varphi}^{pq} + M_2(1 - u_{2,f,\varphi}) \tag{1.86}$$

Zone 3 is modeled as (1.87) and (1.88), in which the SI injects reactive power according to a linear relationship to active power dispatch.

$$-M_1 u_{3,f,\varphi}^{pq} - M_2\left(1 - u_{2,f,\varphi}\right) + P_{2,\varphi}^{\prime pvv} \le P_{f,\varphi}^{pvv} \le M_1 u_{3,f,\varphi}^{pq} + M_2(1 - u_{2,f,\varphi}) + P_{1,\varphi}^{\prime pvv} \tag{1.87}$$

$$-M_1 u_{3,f,\varphi}^{pq} - M_2\left(1 - u_{2,f,\varphi}\right) \le Q_{f,\varphi}^{pvv} - Q_{1,\varphi}^{\prime pvv} - \frac{\left(P_{1,\varphi}^{\prime pvv} - P_{f,\varphi}^{pvv}\right)\left(Q_{2,\varphi}^{\prime pvv} - Q_{1,\varphi}^{\prime pvv}\right)}{P_{1,\varphi}^{\prime pvv} - P_{2,\varphi}^{\prime pvv}} \le M_1 u_{3,f,\varphi}^{pq} + M_2(1 - u_{2,f,\varphi}) \tag{1.88}$$

Zone 4 is modeled as (1.89) and (1.90), in which the SI neither injects nor absorbs reactive power, referred to as a dead zone.

$$-M_1 u_{4,f,\varphi}^{pq} - M_2\left(1 - u_{2,f,\varphi}\right) + P_{1,\varphi}^{\prime pvv} \le P_{f,\varphi}^{pvv} \le M_1 u_{4,f,\varphi}^{pq} + M_2(1 - u_{2,f,\varphi}) + P_{1,\varphi}^{pvv} \tag{1.89}$$

$$-M_1 u_{4,f,\varphi}^{pq} - M_2\left(1 - u_{2,f,\varphi}\right) \le Q_{f,\varphi}^{pvv} - Q_{1,\varphi}^{pvv} - \frac{\left(P_{1,\varphi}^{pvv} - P_{f,\varphi}^{pvv}\right)\left(Q_{1,\varphi}^{\prime pvv} - Q_{1,\varphi}^{pvv}\right)}{P_{1,\varphi}^{pvv} - P_{1,\varphi}^{\prime pvv}} \le M_1 u_{4,f,\varphi}^{pq} + M_2(1 - u_{2,f,\varphi}) \tag{1.90}$$

Zone 5 is modeled as (1.91) and (1.92), in which the SI absorbs reactive power according to a linear relationship to active power dispatch.

$$-M_1 u_{5,f,\varphi}^{pq} - M_2\left(1 - u_{2,f,\varphi}\right) + P_{1,\varphi}^{pvv} \le P_{f,\varphi}^{pvv} \le M_1 u_{5,f,\varphi}^{pq} + M_2\left(1 - u_{2,f,\varphi}\right) + P_{2,\varphi}^{pvv} \tag{1.91}$$

$$-M_1 u_{5,f,\varphi}^{pq} - M_2\left(1 - u_{2,f,\varphi}\right) \le Q_{f,\varphi}^{pvv} - Q_{2,\varphi}^{pvv} - \frac{\left(P_{2,\varphi}^{pvv} - P_{f,\varphi}^{pvv}\right)\left(Q_{1,\varphi}^{pvv} - Q_{2,\varphi}^{pvv}\right)}{P_{2,\varphi}^{pvv} - P_{1,\varphi}^{pvv}} \le M_1 u_{5,f,\varphi}^{pq} + M_2\left(1 - u_{2,f,\varphi}\right) \tag{1.92}$$

Zone 6 is modeled as (1.93) and (1.94), in which the SI absorbs reactive power according to a linear relationship to active power dispatch.

$$-M_1 u_{6,f,\varphi}^{pq} - M_2\left(1 - u_{2,f,\varphi}\right) + P_{2,\varphi}^{pvv} \le P_{f,\varphi}^{pvv} \le M_1 u_{6,f,\varphi}^{pq} + M_2\left(1 - u_{2,f,\varphi}\right) + P_{3,\varphi}^{pvv} \tag{1.93}$$

$$-M_1 u_{6,f,\varphi}^{pq} - M_2\left(1 - u_{2,f,\varphi}\right) \le Q_{f,\varphi}^{pvv} - Q_{3,\varphi}^{pvv} - \frac{\left(P_{3,\varphi}^{pvv} - P_{f,\varphi}^{pvv}\right)\left(Q_{2,\varphi}^{pvv} - Q_{3,\varphi}^{pvv}\right)}{P_{3,\varphi}^{pvv} - P_{2,\varphi}^{pvv}} \le M_1 u_{6,f,\varphi}^{pq} + M_2\left(1 - u_{2,f,\varphi}\right) \tag{1.94}$$

Zone 7 is modeled as (1.95) and (1.96), in which the SI absorbs rated reactive power according to the IEEE 1547-2018 standard [11].

$$-M_1 u_{7,f,\varphi}^{pq} - M_2\left(1 - u_{2,f,\varphi}\right) + P_{3,\varphi}^{pvv} \leq P_{f,\varphi}^{pvv} \tag{1.95}$$

$$-M_1 u_{7,f,\varphi}^{pq} - M_2\left(1 - u_{2,f,\varphi}\right) \leq Q_{f,\varphi}^{pvv} + Q_{f,\varphi}^{pvv,max} \leq M_1 u_{7,f,\varphi}^{pq} + M_2\left(1 - u_{2,f,\varphi}\right) \tag{1.96}$$

Equation (1.97) represents the mutual exclusivity constraint, which restricts selection of multiple zones of operation at the same time.

$$u_{1,f,\varphi}^{pq} + u_{2,f,\varphi}^{pq} + u_{3,f,\varphi}^{pq} + u_{4,f,\varphi}^{pq} + u_{5,f,\varphi}^{pq} + u_{6,f,\varphi}^{pq} + u_{7,f,\varphi}^{pq} \leq 6, \forall f \in F1 \tag{1.97}$$

Equation (1.98) represents the mutual exclusivity constraint, which restricts the selection of multiple modes of operation at the same time.

$$u_{1,f,\varphi} + u_{2,f,\varphi} = 1, \forall f \in F1 \tag{1.98}$$

An alternative formulation is also presented where the operational modes are not explicitly modeled as decision variables. In this approach, the Big-M value M_2 is set to zero, which disables the binary variable. Equations (1.72)-(1.96) are used with the exception of the mode selection term which is nullified by the M_2 value and, (1.82), (1.97) and (1.98) are not considered. These constraints are replaced with (1.99) as shown below.

$$u_{1,f,\varphi}^{qv} + u_{2,f,\varphi}^{qv} + u_{3,f,\varphi}^{qv} + u_{4,f,\varphi}^{qv} + u_{5,f,\varphi}^{qv} + u_{1,f,\varphi}^{pq} + u_{2,f,\varphi}^{pq} + u_{3,f,\varphi}^{pq} + u_{4,f,\varphi}^{pq} + u_{5,f,\varphi}^{pq} + u_{6,f,\varphi}^{pq} + u_{7,f,\varphi}^{pq} \leq 11, \forall f \in F1 \tag{1.99}$$

The above-mentioned modified approach does not involve the binary decision variables to select the mode of operation, but rather arises intrinsically from the zone of operation selected and can theoretically reduce model complexity. The computational efficiency of the two mentioned methods are discussed in the results section.

b) Unified Mode Selection Framework: Co-optimized Settings

Optimally selecting the reactive power operational mode based on the characteristics of Volt-VAr and Watt-VAr operational mode helps improve distribution feeder operations. This improvement is due to the flexibility offered by choosing the right operational mode based on the need for reactive power and ideal functional inputs. The flexibility can be further extended by optimally selecting the settings for the chosen operational mode based on the IEEE 1547-2018 standard [11], by finding the exact margin of need. Given fixed set-points, (1.75), (1.79), (1.86), (1.88), (1.90), (1.92) and (1.94) are mixed-integer and linear. Co-optimizing the set-points, converts the aforementioned constraints into non-linear, non-convex constraints. Therefore, they are linearly approximated using Taylor's series approximation, as mentioned in (1.95)-(1.101). The rest of the equations remain the same due to their convexity being preserved. Terms specified with the superscript (t), correspond to a Taylor's series parameter which are updated every iteration with the previous iteration's solution. Equation (1.75) is approximated and linearly formulated as shown in (1.95), where $u_{2,f,\varphi}^{qv}$ corresponds to the binary variable, associated with the operation of Zone 2 within the Volt-VAr mode of operation.

$$-M_1 u_{2,f,\varphi}^{qv} \le Q_{f,\varphi}^{pvv} - \frac{\left(V_{2,\varphi}^{pvv(t)} - V_i^{\varphi(t)}\right) Q_{f,\varphi}^{pvv,max}}{V_{2,\varphi}^{pvv(t)} - V_{1,\varphi}^{pvv(t)}} + \frac{Q_{f,\varphi}^{pvv,max(t)} V_i^{\varphi}}{V_{2,\varphi}^{pvv(t)} - V_{1,\varphi}^{pvv(t)}} - \frac{Q_{f,\varphi}^{pvv,max(t)} \left(V_{2,\varphi}^{pvv(t)} - V_i^{\varphi(t)}\right) V_{1,\varphi}^{pvv}}{\left(V_{2,\varphi}^{pvv(t)} - V_{1,\varphi}^{pvv(t)}\right)^2} + \frac{Q_{f,\varphi}^{pvv,max(t)} \left(V_{1,\varphi}^{pvv(t)} - V_i^{\varphi(t)}\right) V_{2,\varphi}^{pvv}}{\left(V_{2,\varphi}^{pvv(t)} - V_{1,\varphi}^{pvv(t)}\right)^2} \le M_1 u_{2,f,\varphi}^{qv} \quad (1.95)$$

Equation (1.79) is approximated and linearly formulated as shown in (1.96), where $u_{4,f,\varphi}^{qv}$ corresponds to the binary variable, associated with the operation of Zone 4 within the Volt-VAr mode of operation.

$$-M_1 u_{4,f,\varphi}^{qv} \le Q_{f,\varphi}^{pvv} - \frac{\left(V_i^{\varphi(t)} - V_{3,\varphi}^{pvv(t)}\right) Q_{f,\varphi}^{pvv,max}}{V_{3,\varphi}^{pvv(t)} - V_{4,\varphi}^{pvv(t)}} - \frac{Q_{f,\varphi}^{pvv,max(t)} V_i^{\varphi}}{V_{3,\varphi}^{pvv(t)} - V_{4,\varphi}^{pvv(t)}} + \frac{Q_{f,\varphi}^{pvv,max(t)} \left(V_i^{\varphi(t)} - V_{4,\varphi}^{pvv(t)}\right) V_{3,\varphi}^{pvv}}{\left(V_{3,\varphi}^{pvv(t)} - V_{4,\varphi}^{pvv(t)}\right)^2} - \frac{Q_{f,\varphi}^{pvv,max(t)} \left(V_i^{\varphi(t)} - V_{3,\varphi}^{pvv(t)}\right) V_{4,\varphi}^{pvv}}{\left(V_{3,\varphi}^{pvv(t)} - V_{4,\varphi}^{pvv(t)}\right)^2} \le M_1 u_{4,f,\varphi}^{qv} \quad (1.96)$$

Equation (1.86) is approximated and linearly formulated as shown in (1.97), where $u_{2,f,\varphi}^{pq}$ corresponds to the binary variable, associated with the operation of Zone 2 within the Watt-VAr mode of operation.

$$-M_1 u_{2,f,\varphi}^{pq} \le Q_{f,\varphi}^{pvv} - Q_{2,\varphi}^{\prime pvv(t)} - \frac{\left(Q_{3,\varphi}^{\prime pvv(t)} - Q_{2,\varphi}^{\prime pvv(t)}\right)\left(P_{2,\varphi}^{\prime pvv(t)} - P_{f,\varphi}^{pvv(t)}\right)}{P_{2,\varphi}^{\prime pvv(t)} - P_{3,\varphi}^{\prime pvv(t)}} - \frac{\left(P_{f,\varphi}^{pvv(t)} - P_{3,\varphi}^{\prime pvv(t)}\right)\left(Q_{2,\varphi}^{\prime pvv} - Q_{2,\varphi}^{\prime pvv(t)}\right)}{P_{2,\varphi}^{\prime pvv(t)} - P_{3,\varphi}^{\prime pvv(t)}} - \frac{\left(Q_{3,\varphi}^{\prime pvv(t)} - Q_{2,\varphi}^{\prime pvv(t)}\right)\left(P_{f,\varphi}^{pvv(t)} - P_{3,\varphi}^{\prime pvv(t)}\right)\left(P_{2,\varphi}^{\prime pvv} - P_{2,\varphi}^{\prime pvv(t)}\right)}{\left(P_{2,\varphi}^{\prime pvv(t)} - P_{3,\varphi}^{\prime pvv(t)}\right)^2} - \frac{\left(Q_{3,\varphi}^{\prime pvv(t)} - Q_{2,\varphi}^{\prime pvv(t)}\right)\left(P_{2,\varphi}^{\prime pvv(t)} - P_{f,\varphi}^{pvv(t)}\right)\left(P_{3,\varphi}^{\prime pvv} - P_{3,\varphi}^{\prime pvv(t)}\right)}{\left(P_{2,\varphi}^{\prime pvv(t)} - P_{3,\varphi}^{\prime pvv(t)}\right)^2} + \frac{\left(Q_{3,\varphi}^{\prime pvv(t)} - Q_{2,\varphi}^{\prime pvv(t)}\right)\left(P_{f,\varphi}^{pvv} - P_{f,\varphi}^{pvv(t)}\right)}{P_{2,\varphi}^{\prime pvv(t)} - P_{3,\varphi}^{\prime pvv(t)}} \le M_1 u_{2,f,\varphi}^{pq} \quad (1.97)$$

Equation (1.88) is approximated and linearly formulated as shown in (1.98), where $u_{3,f,\varphi}^{pq}$ corresponds to the binary variable, associated with the operation of Zone 3 within the Watt-VAr mode of operation.

$$-M_1 u_{3,f,\varphi}^{pq} \le Q_{f,\varphi}^{pvv} - Q_{1,\varphi}^{\prime pvv(t)} - \frac{\left(Q_{2,\varphi}^{\prime pvv(t)} - Q_{1,\varphi}^{\prime pvv(t)}\right)\left(P_{1,\varphi}^{\prime pvv(t)} - P_{f,\varphi}^{pvv(t)}\right)}{P_{1,\varphi}^{\prime pvv(t)} - P_{2,\varphi}^{\prime pvv(t)}} - \frac{\left(P_{f,\varphi}^{pvv(t)} - P_{2,\varphi}^{\prime pvv(t)}\right)\left(Q_{1,\varphi}^{\prime pvv} - Q_{1,\varphi}^{\prime pvv(t)}\right)}{P_{1,\varphi}^{\prime pvv(t)} - P_{2,\varphi}^{\prime pvv(t)}} - \frac{\left(Q_{2,\varphi}^{\prime pvv(t)} - Q_{1,\varphi}^{\prime pvv(t)}\right)\left(P_{f,\varphi}^{pvv(t)} - P_{2,\varphi}^{\prime pvv(t)}\right)\left(P_{1,\varphi}^{\prime pvv} - P_{1,\varphi}^{\prime pvv(t)}\right)}{\left(P_{1,\varphi}^{\prime pvv(t)} - P_{2,\varphi}^{\prime pvv(t)}\right)^2} -$$

$$\frac{\left(Q_{2,\varphi}^{\prime pvv^{(t)}}-Q_{1,\varphi}^{\prime pvv^{(t)}}\right)\left(P_{1,\varphi}^{\prime pvv^{(t)}}-P_{f,\varphi}^{pvv^{(t)}}\right)\left(P_{2,\varphi}^{\prime pvv}-P_{2,\varphi}^{\prime pvv^{(t)}}\right)}{\left(P_{1,\varphi}^{\prime pvv^{(t)}}-P_{2,\varphi}^{\prime pvv^{(t)}}\right)^2}+\frac{\left(Q_{2,\varphi}^{\prime pvv^{(t)}}-Q_{1,\varphi}^{\prime pvv^{(t)}}\right)\left(P_{f,\varphi}^{pvv}-P_{f,\varphi}^{pvv^{(t)}}\right)}{P_{1,\varphi}^{\prime pvv^{(t)}}-P_{2,\varphi}^{\prime pvv^{(t)}}}\leq M_1 u_{3,f,\varphi}^{pq} \tag{1.98}$$

Equation (1.90) is approximated and linearly formulated as shown in (1.99), where $u_{4,f,\varphi}^{pq}$ corresponds to the binary variable, associated with the operation of Zone 4 within the Watt-VAr mode of operation.

$$-M_1 u_{4,f,\varphi}^{pq}\leq Q_{f,\varphi}^{pvv}-Q_{1,\varphi}^{pvv^{(t)}}-\frac{\left(Q_{1,\varphi}^{\prime pvv^{(t)}}-Q_{1,\varphi}^{pvv^{(t)}}\right)\left(P_{1,\varphi}^{pvv^{(t)}}-P_{f,\varphi}^{pvv^{(t)}}\right)}{P_{1,\varphi}^{pvv^{(t)}}-P_{1,\varphi}^{\prime pvv^{(t)}}}-\frac{\left(P_{f,\varphi}^{pvv^{(t)}}-P_{1,\varphi}^{\prime pvv^{(t)}}\right)\left(Q_{1,\varphi}^{pvv}-Q_{1,\varphi}^{pvv^{(t)}}\right)}{P_{1,\varphi}^{pvv^{(t)}}-P_{1,\varphi}^{\prime pvv^{(t)}}}-$$
$$\frac{\left(Q_{1,\varphi}^{\prime pvv^{(t)}}-Q_{1,\varphi}^{pvv^{(t)}}\right)\left(P_{f,\varphi}^{pvv^{(t)}}-P_{1,\varphi}^{\prime pvv^{(t)}}\right)\left(P_{1,\varphi}^{pvv}-P_{1,\varphi}^{pvv^{(t)}}\right)}{\left(P_{1,\varphi}^{pvv^{(t)}}-P_{1,\varphi}^{\prime pvv^{(t)}}\right)^2}-\frac{\left(Q_{1,\varphi}^{\prime pvv^{(t)}}-Q_{1,\varphi}^{pvv^{(t)}}\right)\left(P_{1,\varphi}^{pvv^{(t)}}-P_{f,\varphi}^{pvv^{(t)}}\right)\left(P_{1,\varphi}^{\prime pvv}-P_{1,\varphi}^{\prime pvv^{(t)}}\right)}{\left(P_{1,\varphi}^{pvv^{(t)}}-P_{1,\varphi}^{\prime pvv^{(t)}}\right)^2}+$$
$$\frac{\left(Q_{1,\varphi}^{\prime pvv^{(t)}}-Q_{1,\varphi}^{pvv^{(t)}}\right)\left(P_{f,\varphi}^{pvv}-P_{f,\varphi}^{pvv^{(t)}}\right)}{P_{1,\varphi}^{pvv^{(t)}}-P_{1,\varphi}^{\prime pvv^{(t)}}}\leq M_1 u_{4,f,\varphi}^{pq} \tag{1.99}$$

Equation (1.92) is approximated and linearly formulated as shown in (1.100), where $u_{5,f,\varphi}^{pq}$ corresponds to the binary variable, associated with the operation of Zone 5 within the Watt-VAr mode of operation.

$$-M_1 u_{5,f,\varphi}^{pq}\leq Q_{f,\varphi}^{pvv}-Q_{2,\varphi}^{pvv^{(t)}}-\frac{\left(Q_{1,\varphi}^{pvv^{(t)}}-Q_{2,\varphi}^{pvv^{(t)}}\right)\left(P_{2,\varphi}^{pvv^{(t)}}-P_{f,\varphi}^{pvv^{(t)}}\right)}{P_{2,\varphi}^{pvv^{(t)}}-P_{1,\varphi}^{pvv^{(t)}}}-\frac{\left(P_{f,\varphi}^{pvv^{(t)}}-P_{1,\varphi}^{pvv^{(t)}}\right)\left(Q_{2,\varphi}^{pvv}-Q_{2,\varphi}^{pvv^{(t)}}\right)}{P_{2,\varphi}^{pvv^{(t)}}-P_{1,\varphi}^{pvv^{(t)}}}-$$
$$\frac{\left(Q_{1,\varphi}^{pvv^{(t)}}-Q_{2,\varphi}^{pvv^{(t)}}\right)\left(P_{f,\varphi}^{pvv^{(t)}}-P_{1,\varphi}^{pvv^{(t)}}\right)\left(P_{2,\varphi}^{pvv}-P_{2,\varphi}^{pvv^{(t)}}\right)}{\left(P_{2,\varphi}^{pvv^{(t)}}-P_{1,\varphi}^{pvv^{(t)}}\right)^2}-\frac{\left(Q_{1,\varphi}^{pvv^{(t)}}-Q_{2,\varphi}^{pvv^{(t)}}\right)\left(P_{2,\varphi}^{pvv^{(t)}}-P_{f,\varphi}^{pvv^{(t)}}\right)\left(P_{1,\varphi}^{pvv}-P_{1,\varphi}^{pvv^{(t)}}\right)}{\left(P_{2,\varphi}^{pvv^{(t)}}-P_{1,\varphi}^{pvv^{(t)}}\right)^2}+$$
$$\frac{\left(Q_{1,\varphi}^{pvv^{(t)}}-Q_{2,\varphi}^{pvv^{(t)}}\right)\left(P_{f,\varphi}^{pvv}-P_{f,\varphi}^{pvv^{(t)}}\right)}{P_{2,\varphi}^{pvv^{(t)}}-P_{1,\varphi}^{pvv^{(t)}}}\leq M_1 u_{5,f,\varphi}^{pq} \tag{1.100}$$

Equation (1.94) is approximated and linearly formulated as shown in (1.101), where $u_{6,f,\varphi}^{pq}$ corresponds to the binary variable, associated with the operation of Zone 6 within the Watt-VAr mode of operation.

$$-M_1 u_{6,f,\varphi}^{pq}\leq Q_{f,\varphi}^{pvv}-Q_{3,\varphi}^{pvv^{(t)}}-\frac{\left(Q_{2,\varphi}^{pvv^{(t)}}-Q_{3,\varphi}^{pvv^{(t)}}\right)\left(P_{3,\varphi}^{pvv^{(t)}}-P_{f,\varphi}^{pvv^{(t)}}\right)}{P_{3,\varphi}^{pvv^{(t)}}-P_{2,\varphi}^{pvv^{(t)}}}-\frac{\left(P_{f,\varphi}^{pvv^{(t)}}-P_{2,\varphi}^{pvv^{(t)}}\right)\left(Q_{3,\varphi}^{pvv}-Q_{3,\varphi}^{pvv^{(t)}}\right)}{P_{3,\varphi}^{pvv^{(t)}}-P_{2,\varphi}^{pvv^{(t)}}}-$$
$$\frac{\left(Q_{2,\varphi}^{pvv^{(t)}}-Q_{3,\varphi}^{pvv^{(t)}}\right)\left(P_{f,\varphi}^{pvv^{(t)}}-P_{2,\varphi}^{pvv^{(t)}}\right)\left(P_{3,\varphi}^{pvv}-P_{3,\varphi}^{pvv^{(t)}}\right)}{\left(P_{3,\varphi}^{pvv^{(t)}}-P_{2,\varphi}^{pvv^{(t)}}\right)^2}-\frac{\left(Q_{2,\varphi}^{pvv^{(t)}}-Q_{3,\varphi}^{pvv^{(t)}}\right)\left(P_{3,\varphi}^{pvv^{(t)}}-P_{f,\varphi}^{pvv^{(t)}}\right)\left(P_{2,\varphi}^{pvv}-P_{2,\varphi}^{pvv^{(t)}}\right)}{\left(P_{3,\varphi}^{pvv^{(t)}}-P_{2,\varphi}^{pvv^{(t)}}\right)^2}+$$
$$\frac{\left(Q_{2,\varphi}^{pvv^{(t)}}-Q_{3,\varphi}^{pvv^{(t)}}\right)\left(P_{f,\varphi}^{pvv}-P_{f,\varphi}^{pvv^{(t)}}\right)}{P_{3,\varphi}^{pvv^{(t)}}-P_{2,\varphi}^{pvv^{(t)}}}\leq M_1 u_{6,f,\varphi}^{pq} \tag{1.101}$$

The Taylor's series parameters for all the set-points in the first iteration are initialized with the respective default-set-points. The variable set-points are optimized within the permissible ranges as specified by the IEEE 1547-2018 standard [11]. Accordingly, these ranges are formulated as constraints in a linear fashion. Equations (1.102)-(1.105) represent the operational bounds which constrain the range within which voltage set-points of the Volt-VAr operational curve can be optimally selected.

$$0.82 \leq V_{1,\varphi}^{pvv} \leq V_{2,\varphi}^{pvv} - 0.02 \tag{1.102}$$

$$0.97 \leq V_{2,\varphi}^{pvv} \leq 1.00 \tag{1.103}$$

$$1.00 \leq V_{3,\varphi}^{pvv} \leq 1.03 \tag{1.104}$$

$$V_{3,\varphi}^{pvv} + 0.02 \leq V_{4,\varphi}^{pvv} \leq 1.18 \tag{1.105}$$

Equations (1.106) represent the operational bounds which constrain the range within which the reactive power limits for the Volt-VAr operational curve can be modified. The lowering of the set-point is performed if system conditions are nominal, without any requirement for reactive power injection or absorption. The Taylor's series parameters for rated reactive power, $Q_{f,\varphi}^{pvv,max(t)}$ are initialized with the 44% apparent power rating and are down-rated in the above scenario mentioned in each iteration until an optimal set-point is reached.

$$-Q_{f,\varphi}^{pvv,max(t)} \leq Q_{f,\varphi}^{pvv,max} \leq Q_{f,\varphi}^{pvv,max(t)} \tag{1.106}$$

Equations (1.107)-(1.112) represent the operational bounds which constrain the range within which the active power set-points of the Watt-VAr operational curve can be optimally selected.

$$P_{f,\varphi}^{\prime pvv,max} \leq P_{3,\varphi}^{\prime pvv} \leq P_{2,\varphi}^{\prime pvv} + 0.1 \times P_{f,\varphi}^{\prime pvv,max} \tag{1.107}$$

$$0.8 \times P_{f,\varphi}^{\prime pvv,max} \leq P_{2,\varphi}^{\prime pvv} \leq 0.4 \times P_{f,\varphi}^{\prime pvv,max} \tag{1.108}$$

$$P_{2,\varphi}^{\prime pvv} - 0.1 \times P_{f,\varphi}^{\prime pvv,max} \leq P_{1,\varphi}^{\prime pvv} < 0 \tag{1.109}$$

$$0 < P_{1,\varphi}^{pvv} \leq P_{2,\varphi}^{pvv} - 0.1 \times P_{f,\varphi}^{pvv,max} \tag{1.110}$$

$$0.4 \times P_{f,\varphi}^{pvv,max} \leq P_{2,\varphi}^{pvv} \leq 0.8 \times P_{f,\varphi}^{pvv,max} \tag{1.111}$$

$$P_{2,\varphi}^{pvv} + 0.1 \times P_{f,\varphi}^{pvv,max} \leq P_{3,\varphi}^{pvv} \leq P_{f,\varphi}^{pvv,max} \tag{1.112}$$

Equations (1.113)-(1.118) represent the operational bounds which constrain the range within which the reactive power set-points of the Watt-VAr operational curve can be optimally selected.

$$-Q_{f,\varphi}^{pvv,max} \leq Q_{3,\varphi}^{\prime pvv} \leq Q_{f,\varphi}^{pvv,max} \tag{1.113}$$

$$-Q_{f,\varphi}^{pvv,max} \leq Q_{2,\varphi}^{'pvv} \leq Q_{f,\varphi}^{pvv,max} \quad (1.114)$$

$$-Q_{f,\varphi}^{pvv,max} \leq Q_{1,\varphi}^{'pvv} \leq Q_{f,\varphi}^{pvv,max} \quad (1.115)$$

$$-Q_{f,\varphi}^{pvv,max} \leq Q_{1,\varphi}^{pvv} \leq Q_{f,\varphi}^{pvv,max} \quad (1.116)$$

$$-Q_{f,\varphi}^{pvv,max} \leq Q_{2,\varphi}^{pvv} \leq Q_{f,\varphi}^{pvv,max} \quad (1.117)$$

$$-Q_{f,\varphi}^{pvv,max} \leq Q_{3,\varphi}^{pvv} \leq Q_{f,\varphi}^{pvv,max} \quad (1.118)$$

c) Voltage Unbalance Mitigation

Voltage unbalance is an increasing concern for distribution systems with high penetration of roof-top PV and EVs. This subsection presents two distinct approaches to minimize the PVUF within the distribution feeder with optimal scheduling of SIs with VAr operational modes enabled.

I. Unbalance Mitigation: Using Constraints

According to the IEEE 141-1993 standard [41], PVUF across the three phase sections are to be limited to within 2% to protect three phase equipment within the distribution feeder. Consequently, within the DER scheduling framework, constraints are formulated as shown in (1.119)-(1.121), to limit the PVUF between any two given phases of a three phase bus to within 2%.

$$V_i^{avg} = \frac{\sum_{\forall \varphi \in \phi} V_i^{\varphi}}{3} \quad (1.119)$$

$$\left| V_i^{avg} - V_i^{\varphi} \right| \leq V_i^{\Delta max}, \forall \varphi \in \phi \quad (1.120)$$

$$V_i^{\Delta max} \leq 0.02 \times V_i^{avg} \quad (1.121)$$

Equation (1.121) strictly limits the PVUF between any phase to within 2% considering the objective of solely minimizing the cost of operation. Equation (1.120) contains an absolute difference and is reformulated in a linear fashion as shown in (1.122)-(1.123).

$$V_i^{avg} - V_i^{\varphi} \leq V_i^{\Delta max}, \forall \varphi \in \phi \quad (1.122)$$

$$V_i^{\varphi} - V_i^{avg} \leq V_i^{\Delta max}, \forall \varphi \in \phi \quad (1.123)$$

II. Unbalance Mitigation: Using a term in the Objective Function

Considering the active distribution network, extreme scenarios are presented where it would be impossible to limit the PVUF at all the buses to 2%. These scenarios could be due to high instantaneous PV penetration or due to simultaneous connection of multiple charging EVs on a single phase which severely increases loading in one phase. In such cases, setting a hard bound leads to the model being infeasible and an optimal solution not obtained. The approach presented in this section aims to mitigate voltage unbalance through collectively minimizing cost of

operation and voltage unbalance with the objective function as presented in (1.124). With the use of the aforementioned objective function, the one presented in (1.61) is disregarded.

$$\min_{\substack{V_i^{r,\varphi},V_i^{im,\varphi},I_i^{r,\varphi},I_i^{im,\varphi} \\ I_\ell^{r,\varphi},I_\ell^{im,\varphi},P_{f,\varphi}^{pvv},Q_{f,\varphi}^{pvv}}} \sum_{\varphi\in\phi} \begin{pmatrix} \sum_{\forall s(i)} \pi_{s,\varphi}^{B} P_{s,\varphi}^{B} + \sum_{\forall f\in F1(i)} \pi_{f,\varphi}^{pvv} P_{f,\varphi}^{pvv} \\ + \sum_{\forall e\in F2(i)} \pi_{e,\varphi}^{pv} P_{e,\varphi}^{pv} \\ + w_{unbalance} * \sum_{\forall\varphi\in\phi} V_i^{\Delta,\varphi} \end{pmatrix} \tag{1.124}$$

The two components of the objective function presented in (1.124), are opposite quantities in nature, i.e., actions taken to mitigate voltage unbalance involve active power curtailment and reactive power dispatch which affect the cost of operation in an inverse fashion. The significance placed on minimizing voltage unbalance within the distribution feeder as opposed to minimizing cost of operation is controlled by the value of the weight, $w_{unbalance}$. The absolute voltage deviation per phase, $V_i^{\Delta,\varphi}$, is obtained as presented in (1.125) and (1.126).

$$V_i^{avg} = \frac{\sum_{\forall\varphi\in\phi} V_i^{\varphi}}{3} \tag{1.125}$$

$$\left|V_i^{avg} - V_i^{\varphi}\right| \le V_i^{\Delta,\varphi}, \forall\varphi\in\phi \tag{1.126}$$

Equation (1.126) is an absolute difference and is reformulated in a linear fashion as shown in (1.127) and (1.128).

$$V_i^{avg} - V_i^{\varphi} \le V_i^{\Delta,\varphi}, \forall\varphi\in\phi \tag{1.127}$$

$$V_i^{\varphi} - V_i^{avg} \le V_i^{\Delta,\varphi}, \forall\varphi\in\phi \tag{1.128}$$

1.5.3 Results and Analysis

Two DER scheduling models are presented and analyzed including the Mode Selection: Default settings (UMS-D) and Mode Selection: Co-optimized settings (UMS-C). The first subsection presents the description of the two different system conditions tested for the same test system. The second subsection presents the comparison of results obtained with using a DER scheduling tool with UMS-D, UMS-C, Watt-VAr (default settings) and Volt-VAr (default settings), to mitigate over-voltage issues within the distribution feeder. The third subsection presents the comparison of UMS-D and UMS-C in mitigating voltage unbalance issues within the distribution feeder.

a) Test System

I. Over-Voltage Scenario

As discussed in Section 1.3.3 (a), the test system utilized is a large distribution feeder from a utility in Arizona which serves residential prosumers and has one of the largest PV penetration levels among the utility's active feeders. The optimization is performed on a snapshot of the distribution feeder, where it experienced severe over-voltage conditions on March 15, 2019. This typically occurs during spring, where the active power generation potential is high for PV resources and the

residential cooling load is low due to nominal ambient temperatures. An instantaneous PV penetration level of 232% was observed with 3.625 MW of active power injected, with respect to only 1.563 MW of active power demand. The extensive model used to perform the simulation serves as an evidence to the scalability of the model proposed in the below sections. The model includes 8095 buses, 7943 lines and 742 PV units, out of which varying amounts of PV units are equipped with controllers to observe the effects of sparsity. The location of PV units is decided using an optimization model for optimal placement in a previous work [42]. The cost associated with purchase of substation power is obtained from [43] and the cost associated with the retail price of PV power is obtained from net metering policy as in [44]. More information about this feeder is presented in [40].

II. Voltage Unbalance Scenario

The test system used for this scenario is the same as described in the previous subsection. The system conditions were manually modified to simulate the effect of high penetration of roof-top PV, corresponding to the growing rate of installation. This modification includes the addition of 230 roof-top PV units, solely on secondary sections of Phase 2. The addition not only simulates the effect of increased penetration but also of increased adoption of EVs within the residential sectors. The increased penetration not only led to significant voltage violation, with voltages exceeding 1.08 pu in the secondary sections, but also voltage unbalance issues across the primary sections of the distribution feeder, causing PVUFs to exceed 2%. The additional PVs installed follow a PV insolation profile identical to existing PV units in close proximity within the secondary sections. The collective injection of the PV units was 5.221 MW, compared to 1.563 MW of load, leading to an instantaneous PV penetration of 334%.

b) Over-Voltage Scenario

This subsection presents the comparison of results obtained by using a DER scheduling tool with UMS-D, UMS-C, Watt-VAr (default settings) and Volt-VAr (default settings), to mitigate over-voltage issues within the distribution feeder. The optimization is performed over three iterations, for the linearization error to converge and is performed on different sets of PV controllers including 110, 85, 75, 70 controllers. Figure 1.27 exhibits the voltage profile of the primary sections of the distribution feeder with respect to the distance from the substation, before optimal reactive power dispatch is performed. Phases B and C show elevated levels of voltage, well above the ANSI limits in the primary sections due to the increased penetration of PV units and injection of available active power at unity power factor. The voltages in the secondary sections are higher due to the fact that active power flow is back to the substation from the end nodes of the distribution feeder. The highest voltages in the secondary sections of the distribution feeder exceeded 1.06 pu.

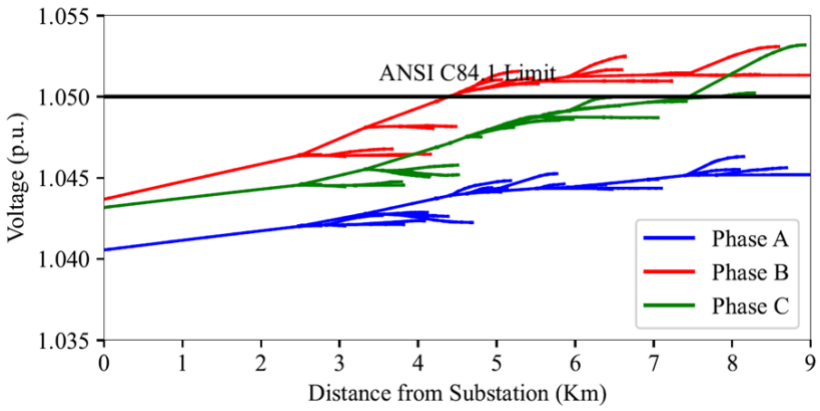

Figure 1.27 Voltage Profile with respect to Distance from Substation in the Primary Sections of the Distribution Feeder prior to VAr Optimization.

The DER scheduling tools analyzed in the section have the ability to dispatch active and reactive power from individual SIs in the distribution feeder. Considering such a mechanism, overvoltage is limited to the ANSI limits within all the buses in distribution feeder, including the primary and secondary sections of the feeder as shown in Figure 1.28. The elevated voltage profiles for Phases B and C in the primary sections also show a significant improvement, considering the reactive power absorption capability. Reactive power injection and absorption capability yields flexibility to maximize the PV utilization without having to affect distribution system operation. As such, the performance of Watt-VAr operational mode and Volt-VAr operational mode with default settings were discussed in Section 1.3.3, with both modes having specific operational abilities. The main focus of the UMS framework as mentioned in this section is to maximize the capabilities of SIs, subject to system conditions, to gain the added flexibility of DERs.

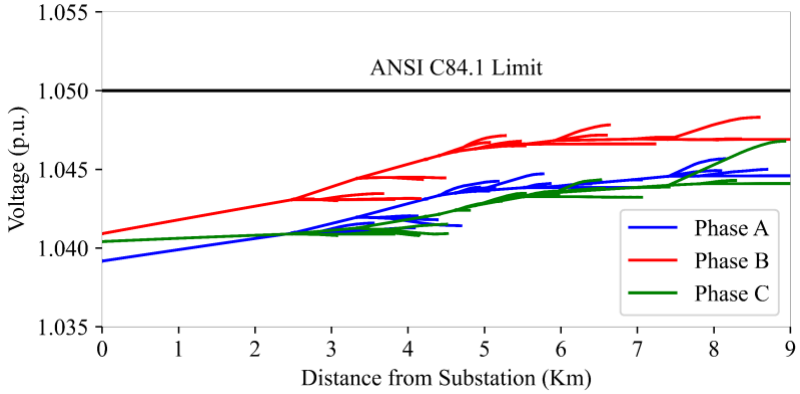

Figure 1.28 Voltage Profile with respect to Distance from Substation in the Primary Sections of the Distribution Feeder Post Optimization with UMS Framework

Figure 1.29 exhibits the reactive power dispatch points of Watt-VAr and Volt-VAr operational modes with default settings as compared to UMS-D. As concluded in the earlier chapters, the inability of Volt-VAr operational mode with default settings, to absorb sufficient reactive power as exhibited by the thin yellow region in Figure 1.29, inhibits it from injecting more active power due to over-voltages. Watt-VAr operational mode over-absorbs reactive power in multiple

instances which infringes on the ability to inject more active power as the inverter apparent power limits are reached. UMS-D optimally chooses between the two operational mode with default settings, based on the reactive power needs and system conditions. As shown in the figure, generally, UMS-D absorbs maximum reactive power by choosing Watt-VAr wherever it is required. When the requirements for reactive power are lower Volt-VAr operational mode is chosen.

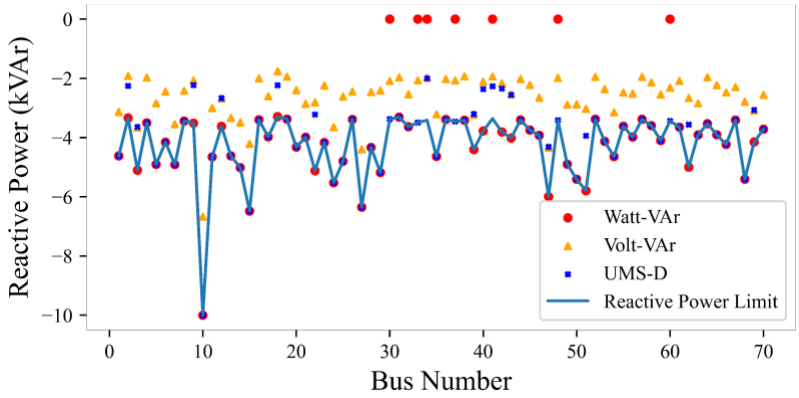

Figure 1.29 Reactive Power Dispatch among SIs Equipped with 70 PV Controllers with UMS-D

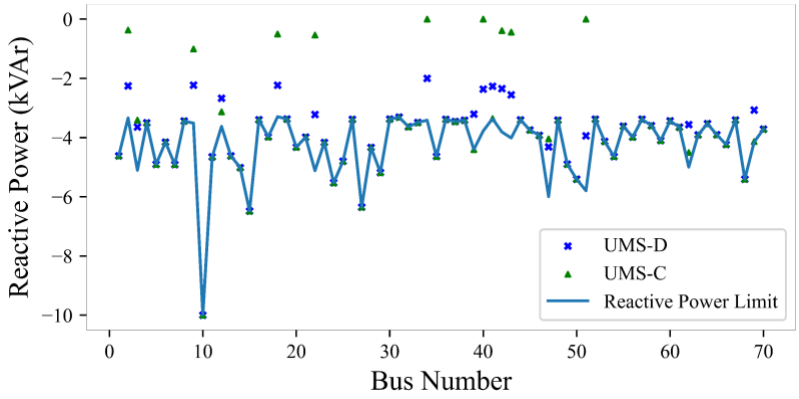

Figure 1.30 Reactive Power Dispatch among SIs Equipped with 70 PV Controllers with UMS-C

UMS-C extends on the ability of UMS-D by optimally choosing the set-points according to the margin of need as shown in Figure 1.30. In the instances where reactive power absorption is less than the reactive power limits, reactive power requirements are lower. Therefor UMS-D chooses operational mode which supports lower reactive power absorption based on functional input. Based on voltage or active power input, the absorption can only be reduced to a certain extent by UMS-D due to high penetration of PV which causes high voltages and active power injection. The limitation mentioned previously does not affect UMS-C as settings are optimally chosen in such a way that high active power injection or voltage does not imply high reactive power absorption. The ability to modify reactive power absorption regardless of system conditions improve PV utilization as the reactive power absorption does not infringe on the ability to inject active power.

As shown in Figure 5.7, dispatching the optimal amount of reactive power not only maximizes active power injection but also maintains the local bus voltages well within the nominal range.

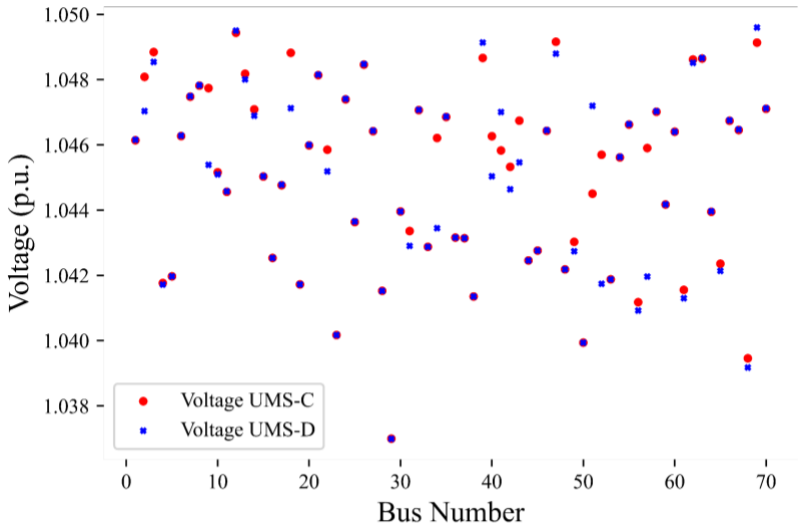

Figure 1.31 Local Bus Voltages of SIs with PV controllers Enabled

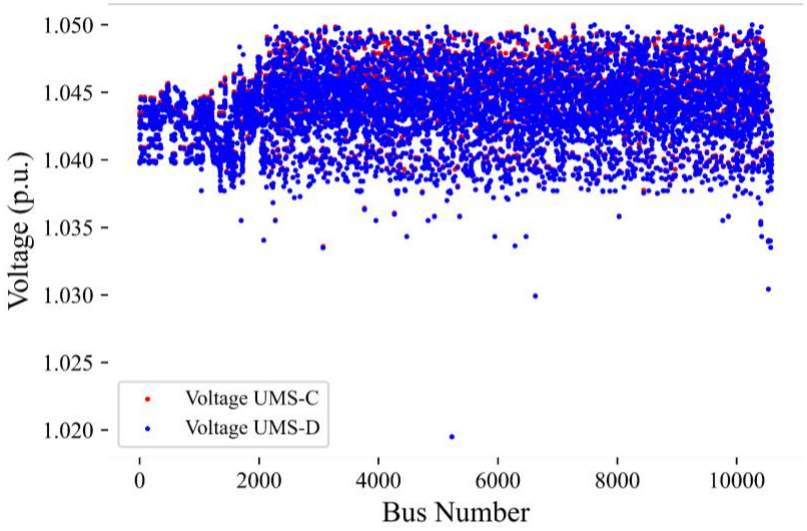

Figure 1.32 System Wide Voltage Profile

Apart from local bus voltages, the DER scheduling tool also dispatched reactive power and active power in such a way that voltage violation issues, distribution feeder-wide are mitigated as shown in Figure 1.32. Due to over-voltage mitigation being constrained to limits and not incentivized to be reduced further at the expense of active power curtailment, the DER scheduling tool optimally maximizes PV utilization without affecting distribution system operation. The non-incentivized nature of over-voltage mitigation leads to the voltage profile not showing any significant changes. However, this effect is directly observed within the active power dispatch of SIs as shown in Figure 1.33. Figure 1.33 exhibits the active power dispatch of SIs with UMS-D compared to the case with Volt-VAr or Watt-VAr operational mode with default settings.

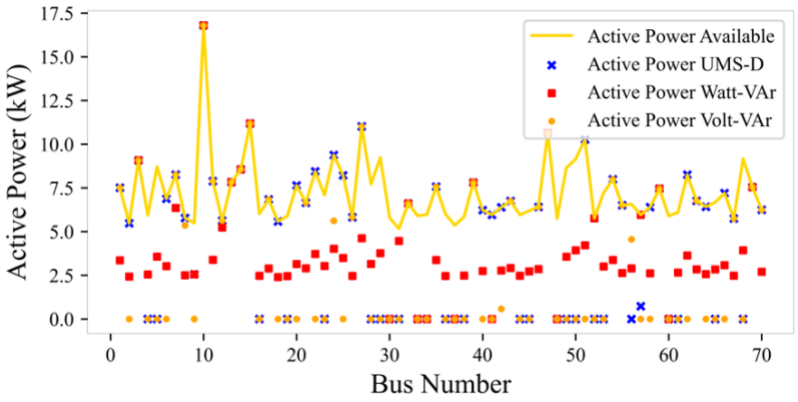

Figure 1.33 Active Power Dispatch among SIs with 70 PV Controllers Enabled with UMS-D

Considering the inability of Volt-VAr operational mode with default settings to absorb sufficient reactive power, active power curtailment is the only strategy to mitigate voltage violation issues. The active power curtailment is observed in Figure 1.33, where SIs with only Volt-VAr operational mode with default settings, causing a thin region of active power dispatch points at zero injection. The over-absorption tendency of SIs with only Watt-VAr operational mode with default settings, infringes on the ability to inject active power, thereby reducing the utilization of renewable resources. Compared to the two operational modes, UMS-D optimally chooses the operational mode for each SI based on reactive power needs and system conditions. Such optimal selection leads to greater flexibility as sections with close to nominal system conditions can continue to inject maximum active power available with reduced reactive power support using Volt-VAr operational mode and sections with excessive over-voltage conditions can continue to provide reactive power support based on Watt-VAr operational mode for greater reactive power absorption capability as shown in Figure 1.33. Almost at every instance, UMS-D performs better than having Watt-VAr or Volt-VAr operational mode with default settings.

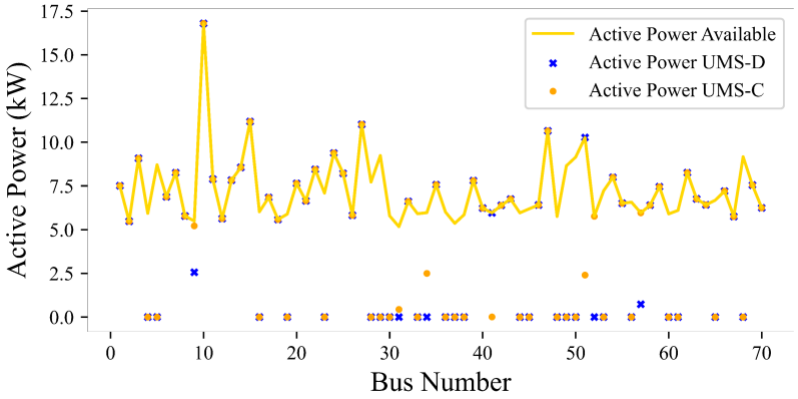

Figure 1.34 Active Power Dispatch among SIs with 70 PV Controllers Enabled with UMS-C

Considering the greater flexibility offered by UMS-C, at every instance, the operational scheme performs equally or better than UMS-D as shown in Figure 1.34. Considering the exact instances where the UMS-C is strictly better than UMS-D, the reactive power absorption is reduced for

UMS-C compared to UMS-D. The underlying explanation for this reduction is due to the fact that reactive power requirement is lower for these instances, but due to the fixed nature of the curves in UMS-D, the scheme over absorbs reactive power and leads to more active power curtailment to facilitate this fact. UMS-C modifies the settings of the underlying operational modes to find the exact margin of need for reactive power and dispatches the exact amount, thereby preventing increased curtailment of active power. Table 1.13 exhibits the curtailment metrics pertaining to the different operational schemes.

Table 1.13 SI Output Metrics over Different Sets of PV Controllers for Over-Voltage Scenario

No. Of PV Controllers	Volt-VAr (kW)		Watt-VAr (kW)		UMS (Default Settings) (kW)		UMS (Co-optimized Settings) (kW)	
	P_{Gen}^{PV}	$P_{Curtail}^{PV}$	P_{Gen}^{PV}	$P_{Curtail}^{PV}$	P_{Gen}^{PV}	$P_{Curtail}^{PV}$	P_{Gen}^{PV}	$P_{Curtail}^{PV}$
110	707.6	0	707.6	0	707.6	0	707.6	0
85	481.6	107.4	521.8	67.2	533.4	55.6	538.5	50.5
75	272.9	261.4	324.6	209.6	384.4	161.5	386.8	159.0
70	223.2	283.6	266.9	239.8	324.9	181.9	327.6	179.1

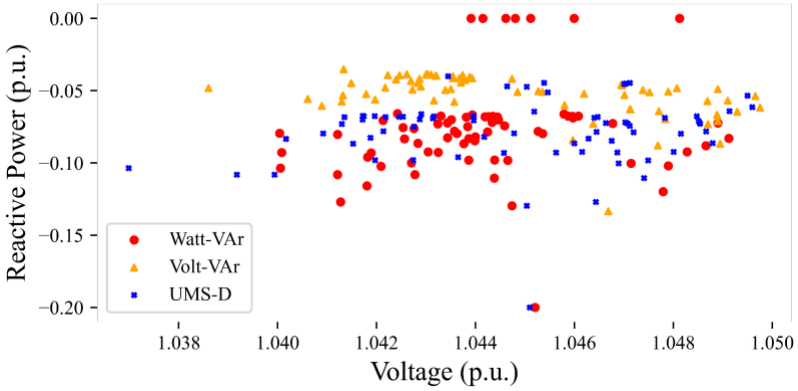

Figure 1.35 Reactive Power Dispatch of SIs with respect to Local Bus Voltages with UMS-D

Considering the issue of reactive power over-absorption and reactive power under-absorption with Watt-VAr and Volt-VAr operational modes respectively, UMS-D optimally selects the operational mode based on reactive power need. The ability of Watt-VAr operational mode with default settings to over-absorb reactive power is shown in Figure 1.35, where for any given voltage condition, reactive power absorption is high. The ability of Volt-VAr operational mode with default settings to under-absorb reactive power is shown in Figure 1.35, where regardless of system conditions reactive power absorption is not high unless local bus voltage is high, which affects system wide over-voltage mitigation. The distribution of UMS-D with respect to reactive power dispatch is less concentrated indicating optimal reactive power dispatch. Nevertheless, UMS-D is still limited to choosing between the two operational modes with default settings and fixed characteristics which inhibit the ability to maximize active power injection. The distribution of UMS-C reactive power dispatch points as shown in Figure 1.36, is more spread compared to UMS-

D. Non-incentivized over-voltage mitigation implies instances with reduced reactive power absorption as shown in Figure 1.36 for UMS-C, is solely to maximize active power injection.

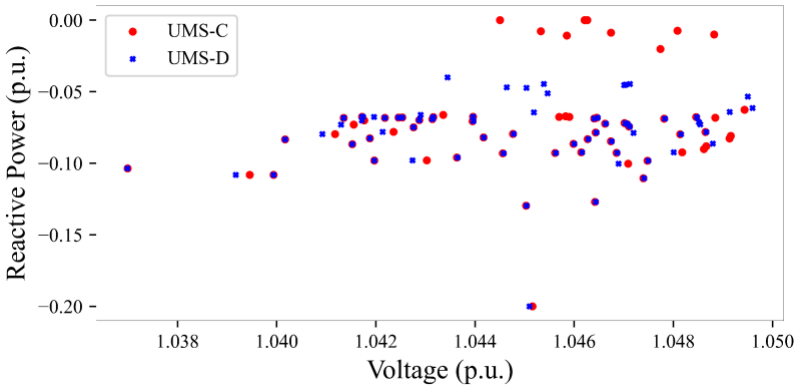

Figure 1.36 Reactive Power Dispatch of SIs with respect to Local Bus Voltages with UMS-D

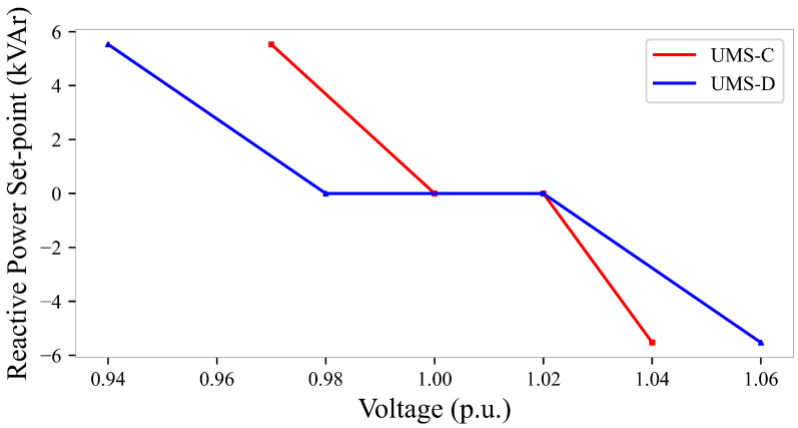

Figure 1.37 Co-optimized Volt-VAr Operational Mode Curve for Bus 4532

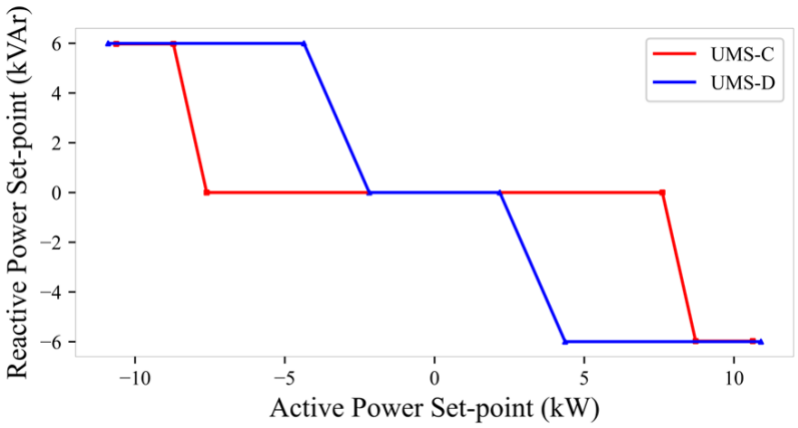

Figure 1.38 Co-optimized Watt-VAr Operational Mode Curve for Bus 7212

Figures 1.37 and 1.38 exhibit the chosen operational modes for SIs along with the co-optimized settings, with respect to UMS-C. Figure 1.37 shows the optimized set-points for Bus 4532 with Volt-VAr operational mode being selected. Considering the requirement for high reactive power absorption, the set-point $V_{4,\varphi}^{pvv}$ is modified from 1.06 pu to 1.04017 pu, to facilitate maximum reactive power absorption. Similarly, the Watt-VAr operational mode is selected and optimized for Bus 7212 as shown in Figure 1.38.

c) Voltage Unbalance Scenario

The results presented in this subsection compare the performance of the DER scheduling tool equipped with either the UMS-D or UMS-C operational schemes, to mitigate voltage unbalance issues through the distribution feeder. Two distinct approaches are presented to mitigate voltage unbalance in the above sections. The modified test system with the increased penetration in Phase 2 is used to test the ability of the UMS framework to mitigate voltage unbalance issues.

I. Unbalance Mitigation: Using Constraints

In this subsection, voltage unbalance mitigation is accomplished by strictly limiting the PVUF profile to 2% according to the IEEE 141-1993 standard [41]. The UMS-D and the UMS-C operational schemes are compared on the basis of active power curtailment metrics, distribution feeder-wide, across different sets of PV controllers including 340, 330, 320, 310, and 300.

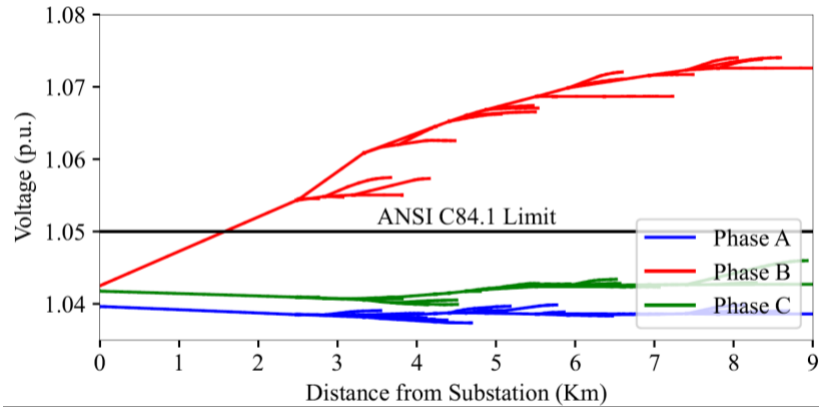

Figure 1.39 Voltage Profile with respect to Distance from Substation in the Primary Sections of the Distribution Feeder before VAr Optimization

Figure 1.39 presents the voltage profile with respect to substation distance before any reactive power operational mode is enabled within SIs. The modified test system simulates an increased penetration of roof-top PV in Phase B, which causes severe over-voltages. The primary sections of the distribution feeder experience voltages over 1.07 pu, in Phase B, with the secondary sections experiencing voltages higher than 1.08 pu. The increased adoption of EVs also threaten excessive voltage unbalance and under voltage issues, due to the instantaneous penetration of charging load caused by simultaneous charging of multiple EVs on a given phase. The ability of SIs to provide reactive power support and curtail active power can be utilized to mitigate voltage unbalance issues within the distribution feeder, without affecting consumer experience utilizing PV resources. Figure 1.40 presents the voltage profile of the distribution feeder with respect to substation distance

exhibiting significant improvement in not only Phase B, but also Phase A and C considering reactive power dispatch using the UMS framework.

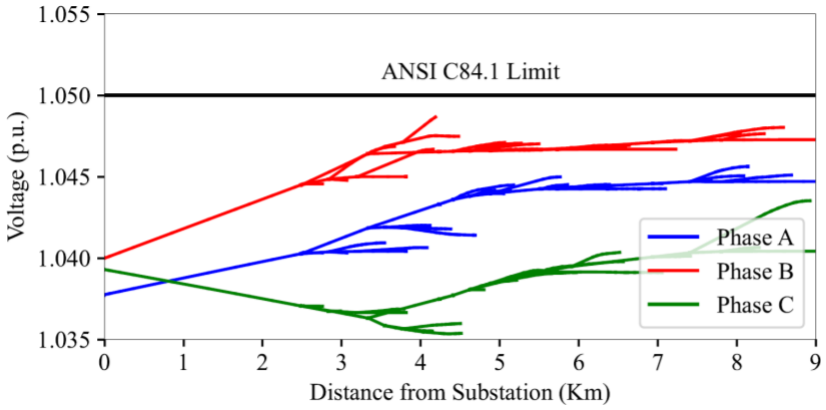

Figure 1.40 Voltage Profile with respect to Distance from Substation in the Primary Sections of the Distribution Feeder Post VAr Optimization using UMS-C

The ability to maximize PV utilization depends on the ability to manage active and reactive power dispatch subject to distribution system operation. Considering this fact, the ability to absorb reactive power helps reduce voltage to a certain extent, beyond which active power curtailment has to be utilized. The ability to stretch this margin and reduce active power curtailment depends on the flexibility offered for the SIs to dispatch active power and reactive power, regardless of system conditions and fixed operating rules. UMS-C provides this flexibility over UMS-D, of deviating from fixed operating rules, to maximize utilization without violating operating standards. Table 1.14 presents the active power curtailment across the PV units with SIs within the distribution feeder, for UMS-C and UMS-D, subject to the fact that PVUF across the primary sections are maintained within the 2% limit.

Table 1.14 Active Power Curtailment and Maximum PVUF across the Distribution Feeder

No. of PV Controllers	UMS (Default Settings)		UMS (Co-optimized Settings)	
	Curtailment (kW)	Maximum Voltage Unbalance (%)	Curtailment (kW)	Maximum Voltage Unbalance (%)
340	957.73	0.6032	916.85	0.5657
330	1032.46	0.5515	972.97	0.5521
320	1042.90	0.5445	994.30	0.5343
310	1185.65	0.4434	1156.75	0.4345
300	1333.30	0.3803	1308.10	0.3445

The results observed in Table 1.14 clearly exhibit the flexibility offered by optimally selecting the set-points, in dispatching the exact required amount of reactive power, to maximize the active power injection. The ability of UMS-C to provide this flexibility enables the operational scheme to provide a better PVUF and active power curtailment metric at every instance compared to UMS-D. The results also infer the ability of UMS-C operational scheme to handle the effect of sparsity better, which implies less amount of SIs are required with PV controllers for nominal distribution system operation. One important observation is the fact that lower maximum PVUFs for the distribution feeder are observed as the active power curtailment increases. This observation is due to the fact that the distribution system bus voltages are more sensitive to active power changes, caused by the high R/X ratio.

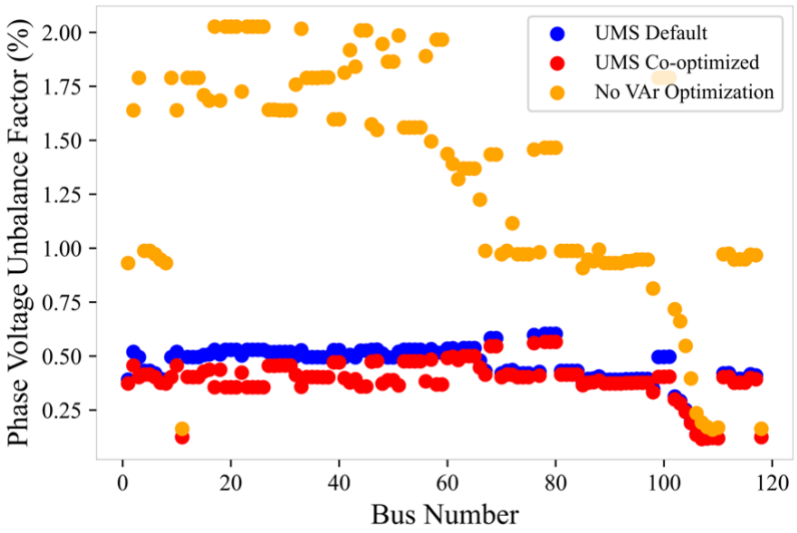

Figure 1.41 Phase Voltage Unbalance Factor Profile among Primary sections of the Distribution Feeder Pre and Post VAr-Optimization.

The profile shown in Figure 1.41 clearly exhibit the ability of SIs with PV resources to mitigate voltage unbalance issues within the distribution feeder with reactive power support. Before VAr optimization, the unity power factor injection of SIs with available active power causes severe voltage unbalance, with PVUFs exceeding 2%. Post VAr optimization, the maximum PVUF within the distribution feeder is reduced to 0.6%. The PVUF profile of UMS-C operational scheme entirely lies below that of UMS-D operational scheme. Coupled with the fact that active power curtailment metrics are also better at each instance, the added flexibility of UMS-C operational provides significant gains compared to the UMS-D operational mode. The operational performance not only aids distribution system operation but also aids in the improvement of distribution system aggregated DER hosting capacity as shown in Figure 1.42.

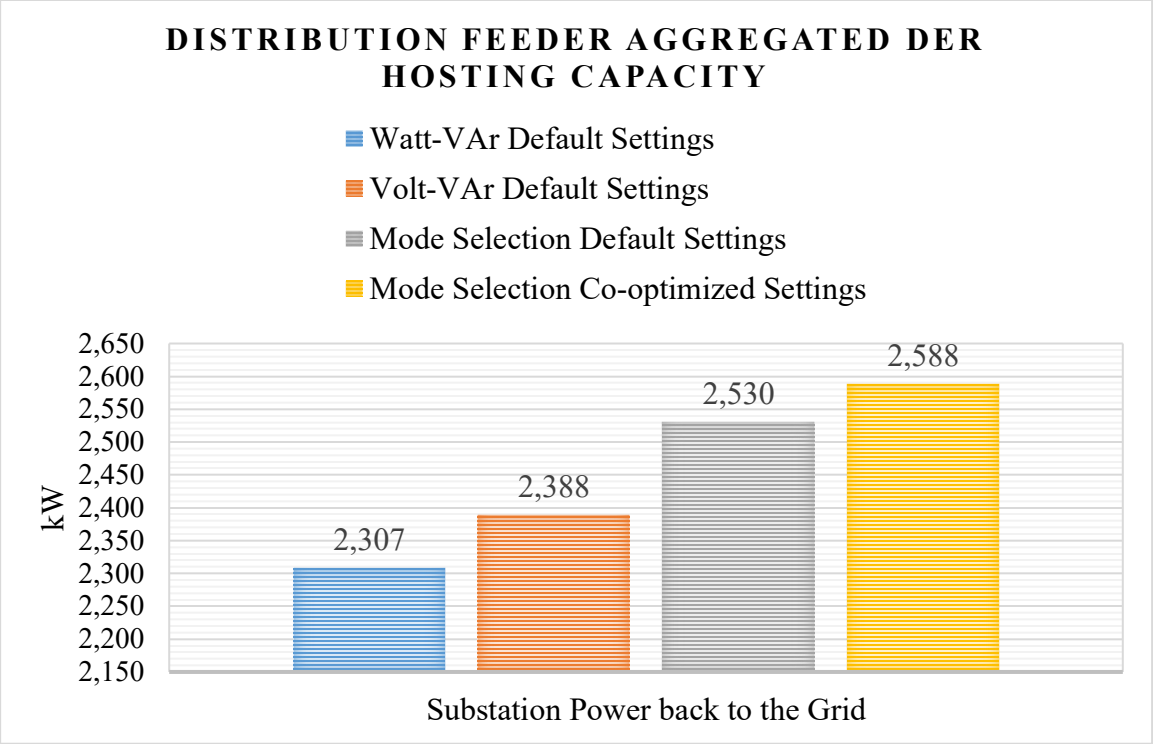

Figure 1.42 Distribution Feeder Aggregated DER Hosting Capacity

The improvement of hosting capacity of the distribution feeder significantly helps greater participation of DER aggregators in the wholesale markets, according to FERC order 2222. The greater flexibility offered by the UMS framework also improves the reliability of services provided by the DER aggregators, leading to greater awards from Transmission System Operators (TSOs).

II. Unbalance Mitigation: Using a term in the Objective Function

Considering the extreme scenarios, where PVUF cannot be constrained to 2% at all the primary sections of the distribution feeder, an alternative objective function is considered as in (1.124). Equation (1.124) considers a weight on minimizing the amount of unbalance in the system versus cost of operation. Table 1.15 presents the net PV curtailment metrics distribution feeder-wide, considering different weights to minimize the unbalance with respect to the UMS-D and UMS-C operational schemes. With the weight zero assigned to the balancing component of the objective function, UMS-C exhibits reduced curtailment compared to UMS-D, solely to mitigate over-voltages. As the weight is increased, UMS-C performs better at each instance, until 70, where the active power curtailment metric considering UMS-C is seemingly worse compared to that obtained with UMS-D operational scheme. Both the operational schemes continue the trend of more active power curtailment to mitigate unbalance due to two possible reasons:

- Active power curtailment proves for a sharper reduction in voltage due to the high R/X ratio for effective voltage unbalance mitigation.
- The inability to absorb more reactive power due to SIs reaching their reactive power and apparent power limits, which implies further voltage reduction can be achieved only through active power curtailment.

Table 1.15 Active Power Curtailment considering Incremental Weights for Balancing System Voltage with respect to UMS-D and UMS-C Operational Schemes

Weight $w_{unbalance}$	UMS (Default Settings) Curtailment (kW)	UMS (Co-optimized Settings) Curtailment (kW)
0	955.90	914.35
1	959.71	917.40
10	1009.68	939.34
20	1060.71	995.38
25	1215.93	1102.68
30	1308.51	1213.46
40	1369.56	1329.81
50	1489.45	1485.63
70	1538.33	1645.90
90	1574.50	1670.60
100	1588.96	1714.55

The weight, 70, from where UMS-D seemingly performs better than UMS-C operational scheme is due to the fact that above 70, the model intrinsically places a natural priority to mitigating voltage unbalance, compared to operational cost reduction. The analysis mentioned above is confirmed by Figure 1.43, where UMS-C operational scheme's the curve representing system wide unbalance with respect to curtailment, entirely lies below that of UMS-D operational scheme indicating a better performance at each instance. This factor also indicates that for a specified amount of system voltage unbalance, UMS-C provides greater flexibility and consequently yields a reduced net curtailment metric compared to UMS-D. The pareto optimal solution can be obtained from the figure for obtaining the optimal weight for the objective function.

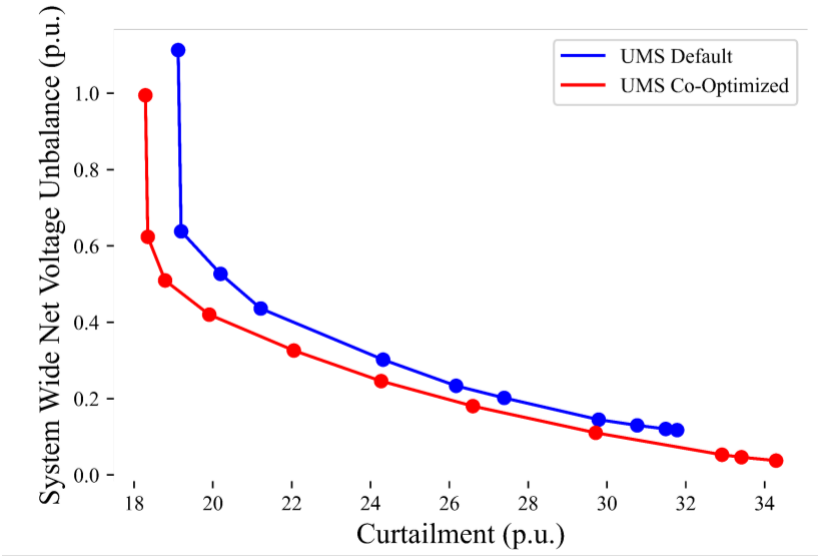

Figure 1.43 System Wide Voltage Unbalance with respect to Net Active Power Curtailment

d) Computation Metrics

As mentioned in Section 1.5.2, the alternative formulation for the UMS framework which does not involve modeling the operational mode explicitly as a decision variable, should reduce model complexity. This reduction is due to the reduced number of binary variables which effectively reduces the search space for MILP problems. An analytic comparison is shown in Table 1.16, where for the same exact model, the two approaches yield the same results. The same results are however presented with a 60.3% reduction in run-time, which implies model results do not change considering the mode of operation as a decision variable or not, however it does simplify the model.

Table 1.16 Run-time and Objective Value Comparison for the Two Distinct UMS Framework Approaches

Approach	Run-Time (Seconds)	Objective Function Value ($)	Active Power Curtailment (kW)
Explicitly modeling mode of operation as a decision variable	355.91	101.37	0.0
Mode of operation arises intrinsically from zone of operation	141.09	101.37	0.0

The DER scheduling tools presented in this chapter are all performed over three iterations for the Taylor's series approximation error to converge well into insignificant values as shown in Table 1.17. The average computation time for such a large system is around 3.05 minutes, ensuring the scalability of such a model is effective.

Table 1.17 Linearization Error Metrics for the IVACOPF

No. of PV Controllers	Linearization Error Metrics		
	Active Power (kW)	Reactive Power (kW)	Computation Time (min)
110	2.0e-03	2.0e-03	3.1
85	1.6e-03	1.6e-03	3.0
75	1.3e-04	1.3e-04	3.0
70	6.1e-02	6.1e-02	3.1

2. Coordination of Transmission-Distribution Services and Enhancing Distribution System Flexibility

2.1 Introduction

2.1.1 Background and Motivation

The penetration level of Distributed Energy Resources (DERs) is overgrowing due to their cost-effective and environmental benefits. Generally, DERs placed in the Distribution System (DS), due to the minimum size requirement, are not allowed to participate in the wholesale market individually. However, as a potential approach, Distributed Energy Resources Aggregators (DERAs) that satisfy the minimum market size requirements can manage and/or own a number of DERs and participate in the wholesale market. FERC order No. 2222 requires ISOs to propose new operation and market rules for DERAs to participate in the wholesale markets, namely, capacity, energy, and ancillary services markets [7]. Essentially, this order attempts to encourage competition in the wholesale markets by removing barriers that prevent DERAs from market participation. Apart from this, there is a rising need for Distribution System Operators (DSOs), who have some functionalities over today's Distribution Utility (DU) operators. It is pertinent to mention that the DSO is defined as "the entity responsible for planning and operational functions associated with a DS that is modernized for high levels of DERs"[45]. Depending on the regulations and market structures, the responsibilities of DSOs can range from only the safe operation of the DS, to aggregating and dispatching all DERs and DERAs within the DS to submit a single bid to the Day-Ahead (DA) wholesale market, and hosting retail electricity markets. The role of the DSO can reside with either the DU/transmission and distribution company/load serving entity or an independent entity.

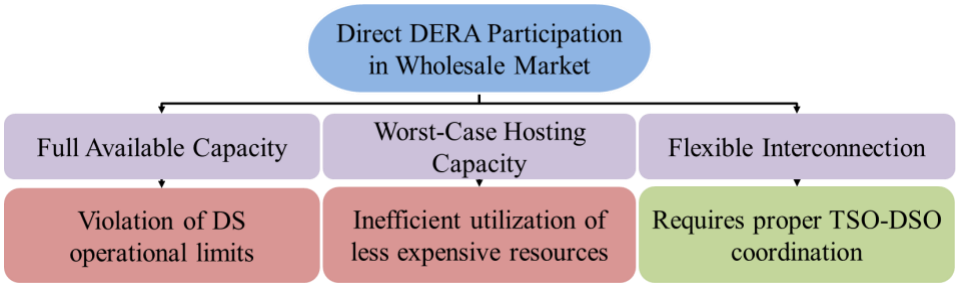

Figure 2.1 Direct DERA Participation Schemes in Wholesale Markets

The ISOs are facing different operational challenges such as single-/multi-node aggregation of DERs, telemetry requirements, and deliverability of DERA services via DS. Among these challenges, proper coordination framework between the ISO, DERA, and DSO is regarded a prominent requirement as specified in the Notice of Proposed Rulemaking (NOPR) [7]. These frameworks should ensure that the DERA's participation stays within DS limits to prevent violations and safety concerns. To this point, there are three possible scenarios of direct DERA participation in the market as shown in Figure 2.1. In the first scenario, a DERA may participate with full capacity without considering DS limits, which may result in violations of DS limits.

DERAs may participate with the "worst case hosting capacity" where the injection of a DER will never violate DS limits. This scenario leads to inefficient utilization of inexpensive resources and may even disqualify DERAs due to minimum size requirements.

The best scenario would be to enable flexible interconnection, whereby, the injection potential of DERAs dynamically changes for each time interval, to accommodate DS constraints. To this extent, in this work, the concept of Operational Short-Term Nodal (OSTN) hosting capacity is developed which is time-varying and changes with DS operational conditions. One potential coordination framework is that ISO manages the wholesale market, incorporating DERAs without visibility over DS constraints. However, the actual amount of deliverable services to ISO by DERAs during any operating condition depends on the DS limits (e.g., voltage limits, thermal limits, and DS unbalance condition). This issue of not being able to respond to the ISO dispatch instructions without posing a major risk to the DS, was also raised by the commission in FERC order No. 2222 [7].

Apart from the DS limits, the actual amount of deployable products by DERAs during transmission system (TS)-level uncertain events is dependent on the available flexibility in the DS. Flexibility can come from various sources, i.e., VAr support from DERs Smart Inverters (SIs), legacy VAr devices, and DS reconfiguration. If managed correctly, these flexibilities can mitigate violations in the DS even if DERAs participate beyond pre-identified DS hosting capacity limits. Therefore, the need for creating an effective framework for the DSO to coordinate concerns or issues with the ISO before allowing DERA to participate in the organized wholesale electric market is raised [7]. It is essential to mention that an effective and practical coordination framework should preemptively and dynamically consider time-varying DS OSTN hosting capacity (due to changing DERA bids, DS conditions, and network topology).

The proposed framework of this work achieves this goal without real-time ISO-DSO communication requirements. Thus, two questions to answer are: (i) how much can ISOs rely on DERAs to provide a certain amount of product considering the DS limits, and (ii) how can DS flexibility be utilized to increase the deployability of DERA's promised services to the ISOs. Based on the above discussion, one of the goals of this work is to create a coordination framework using statistical information of the DS to provide ISOs with a dynamic DS OSTN hosting capacity, which inherently limits total active power services (e.g., energy and reserve) by DERAs to the wholesale market. The limit presented per this coordination framework can capture voltage and thermal line limits in the feeders or substation, or the "deliverability" of power to the substation, while considering the flexibility offered by the distributed roof-top Photovoltaics (PV) SI units.

2.1.2 Literature Survey

Generally, DERs participation in the wholesale markets can be categorized into three subgroups. The first subgroup is DERs directly (without aggregation) participating in the wholesale markets (ideal) [46]. Apart from the minimum size requirement issue [47], a large number of DERs participating in the wholesale market can cause huge computational complexities for the ISOs' market processes, e.g., DA SCUC, RTUC, and RTD [48].

The second subgroup is associated with the DSOs being fully responsible for aggregating and dispatching DERs within its DS region, either through a retail market or not [49], [50]. Generally,

in this subgroup, ISOs run the market engine for transmission level resources while the DSO submits a single aggregated bid to ISO for its respective DS, DER, and DERA participants. Although there is some literature work on the second subgroup [48], [50]–[54], the implantation of such approaches in practice, is limited [7]. Furthermore, if an independent DERA in the DS is willing to directly participate in the wholesale market, there should be clear and transparent market rules for the DSOs to maintain neutrality and to not practice market power. This condition applies when the DU/Load Serving Entity (LSE) is also a market participant in the wholesale market and manages the DS network as a DSO.

Considering how ISOs have started streamlining the integration process for DERAs [55]-[56], the third subgroup includes DERs participating through the DERAs in the wholesale market. In this case, the DSO is primarily responsible for the safe and reliable operation of the DS network while the ISO manages and dispatches DERAs directly. Since the DERAs participate in the wholesale market and are located at the DS while receiving dispatch signals from ISOs, a coordination framework between the ISO and DSO becomes essential for the safe and reliable operation of the DS network. This subgroup is a more compatible option with the current ISO's market structures and participation models. There are some works in the literature [57]–[66] on DERs participating in the wholesale markets by DERAs.

Reference [57] investigates the market efficiency impacts of DERs participating in the wholesale market either directly or through aggregation, with the DS modeled as an aggregated entity. The interaction between the DERA and prosumers are modeled as a Stackelberg game and the "price of aggregation" quantity derived, is used to define the aggregation efficiency. The role of DERA was presented in [58] to enable a portfolio of DERs, which store and convert a set of energy carriers (i.e., solar energy, gas, thermal energy, and electricity), to maximize the expected DERA profit by finding its optimal bidding strategy. A study was presented in [59], wherein the DERA manages Electric Vehicles (EVs) only based on their grid-to-vehicle charging characteristics to assess the DERA's ability to affect the market clearing prices. This model has two levels; in the first level, the DERA minimizes the charging cost of the EVs, while in the second level, the wholesale market is simulated. A risk-averse optimal bidding formulation was proposed in [60] to manage a set of flexible demand-side resources, namely, plug-in EVs and distributed generation, through the role of a DERA. The conditional Value-at-Risk (CVaR) measure was used for risk-averse DERA optimal bidding under the uncertainty of renewable generation, electricity demand, and real-time price. A DERA model managing commercial compressed air energy storage and wind power DERA was proposed in [61] to simultaneously participate in DA, intra-day, and balancing markets. The proposed model was formulated as a three-stage stochastic optimization problem, considering Value-at-Risk to control the financial risks. However, in [57]–[61], DERAs participate in the wholesale market without considering the DS operational limits, which is challenging for the DS security.

A robust optimization model for a DERA managing batteries and PV was proposed in [62] for participation in the wholesale DA markets. In [62], a "local constraint support" in terms of the maximum allowed net exchange at the Point of Common Coupling (PCC) with the DS was considered for the DERA to ensure that its local portfolio will not cause DS violations. However, this approach is based on the assumption that the DSO knows the maximum net exchange and provides this value to the DERA, implying that its static in nature, forcing participation to either "worst-case" or full available capacity. As mentioned previously, both of these affect DERA

participation and market efficiency. Reference [63] presents both robust and stochastic optimization auction models to determine net injection limits for DERs at the point of aggregation, based on DS limits and DERA preference. The forward auction is run by the DSO, with the risk of constraint violation being limited using the CVaR measure. The framework assigns an access payment to DERAs. While this could be one viable approach, the additional access payments could become detrimental to the profitability of DERAs participating in the wholesale markets.

A prequalification process was proposed in [64] to modify bids of the DERAs before submitting them to the ISO wholesale market. However, the model is an iterative process that uses sensitivity analysis and power flow to modify the bid instead of optimally determining the DS OSTN hosting capacity. An aggregate power flexibility estimation technique using an inner box approximation is presented in [65], based on different types of DERs. A two-stage optimization model is developed, where the Maximal flexibility Power Aggregation model (MPA) evaluates the flexibility of the DS at the PCC, which is in turn utilized to create the aggregated bid for to ISO. However, the effects of the proposed models in [64] and [65] were not investigated on the deployability of the DERAs to the ISO's dispatch signals, and requires a more active DSO role and real time coordination between the ISO, DSO and the DERA which could be deemed impractical. A service-centric methodology and cooperation of the DERA and the DSO were proposed in [66] to consider the DA wholesale market participation of DERAs while providing congestion relief service to the DS in the intra-day scheduling process. During the DA scheduling in [66], the DS limitations are not considered. In the intraday scheduling process, power flow analyses followed by DERA dispatch adjustment is presented to address network constraints in the DS without considering overvoltage. Furthermore, the proposed models in [64] and [66], are based on balanced DS networks, limiting validity for prevalent single phase DERs.

Moreover, in the above-mentioned works, the accurate effect of VAr support from inverter-based resources on improving the DS OSTN hosting capacity and flexibility are not considered. With the introduction of the IEEE 1547-2018 standard [11], SIs are allowed to participate in providing VAr support. As such, mitigating voltage issues with localized VAr support reduces dependency on active power curtailment, thereby improving the DERA's injection capacity. References [67] and [68] investigate the relation between SI based VAr support and voltage management of DS. Apart from providing flexibility to the DS, the coordination and dispatch of SIs can limit the long-term effects of violations on DS assets, thereby deferring frequent investments into replacements and upgrades.

2.1.3 Contributions

In this work, first, a DSO and ISO coordination framework (Architecture I) is presented, wherein the DERAs directly participate in the wholesale market and ISOs do not consider the DS limits while making decisions on the DERA's awards. Then, a proposed ISO-DSO-DERA coordination framework (Architecture II) is presented, where the ISO considers DS OSTN hosting capacity while deciding DERA awards. The DS OSTN hosting capacity, i.e., maximum nodal DERs aggregation penetration considering DS limits, can be used to qualify and disqualify different services provided by DERAs before the wholesale market clearing. Architecture II utilizes the statistical information obtained using different DS operating conditions and data-mining algorithms (trained during offline analysis) to predict the DS OSTN hosting capacity considering DS limits and DS flexibility tools available. Finally, a DSO-DERAs scheduling framework is

utilized to compare the performance of Architectures I and II where the DSO acts only on managing DS violations by utilizing VAr support from distributed roof-top PV SIs and other flexibility tools. Scenarios of TS uncertainty is included in this comparison. The primary contributions of this work concerning the DERs participation in the wholesale markets are:

- Design and development of a novel ISO-DSO-DERA coordination framework which circumvents the need for real-time operational coordination between the ISO and DSO. The ISO-DSO coordination is reduced to a passive exchange of trained statistical models.
- Proposing a data-driven framework to identify the maximum qualified capacity of the total services provided by each DERA in DS. To this end, the proposed work identifies DS nodal hosting capacity, i.e., DS OSTN hosting capacity, which could be used as the maximum qualified capacity for the total combination of services awarded to a DERA at the specific DS node. Incorporating this maximum qualified capacity prediction into the wholesale market does not require any significant modification in ISO market models.
- Impact of SI Var capabilities based on IEEE 1547-2018 on DS OSTN hosting capacity estimation is shown. Effective utilization of SI capabilities in DS could enhance DS hosting capacity and increase qualified DERA services.
- A DSO-DERAs scheduling approach is presented for evaluating real-time deliverability of DERAs services during TS uncertainty. In this approach, DSO allows full delivery of DERAs promised services to ISO while leveraging PV SIs capabilities to overcome DS operational limits.

2.2 General Aggregator Participation in the Wholesale Market: Architecture I

2.2.1 Architecture I Structure

As mentioned earlier, in Architecture I, the ISO manages the wholesale market without visibility over DS limitations, as shown in Figure 2.2. Thus, the DS limitations and hosting capacity are not considered during wholesale market clearing process.

Figure 2.2 DERA Participation in the Wholesale Market for Architecture I

2.2.2 DA Formulation

The DA wholesale market formulation based on Architecture I is presented in (2.1)-(2.11), wherein the DERAs bid their maximum available market capacity without considering the DS limitations. The objective function of the DA wholesale market model, i.e., (2.1), is to minimize the total operating costs of the generators and the DERAs.

$$min \ \sum_g \sum_t (c_g^A P_{g,t}^A + c_g^{SU} v_{g,t} + c_g^{SD} w_{g,t} + c_g^{Res} r_{g,t}) + \sum_a \sum_t (c_a^A P_{a,t}^A + c_a^{Res,A} r_{a,t}^A) \quad (2.1)$$

The objective function is subject to the operational constraints of the generators, DERAs, and the transmission network constraints. The operational constraints of the generators in DA wholesale market and the transmission network constraints were adopted from [69]-[70] and is extended to include DERAs as shown in (2.2)-(2.9). These constraints respectively present ramping limits, maximum and minimum energy and reserve operational limits, as well as the DERAs commitment, startup, and shutdown constraints.

$$P_{a,t}^{A} - P_{a,t-1}^{A} \leq R_{a}^{HR} u_{a,t-1} + R_{a}^{SU} v_{a,t}, \forall a, t \geq 2 \tag{2.2}$$

$$P_{a,t-1}^{A} - P_{a,t}^{A} \leq R_{a}^{HR} u_{a,t} + R_{g}^{SD} w_{a,t}, \forall a, t \geq 2 \tag{2.3}$$

$$P_{a,t}^{A} + r_{a,t}^{A} \leq P_{a,t}^{max} u_{a,t}, \forall a, t \tag{2.4}$$

$$P_{a,t}^{A} - r_{a,t}^{A} \geq P_{a,t}^{min} u_{a,t}, \forall a, t \tag{2.5}$$

$$0 \leq r_{a,t}^{A} \leq R_{a}^{10} u_{a,t}, \forall a, t \tag{2.6}$$

$$v_{a,t}^{A} - w_{a,t}^{A} = u_{a,t}^{A} - u_{a,t-1}^{A}, \forall a, t \tag{2.7}$$

$$v_{a,t}^{A} + w_{a,t}^{A} \leq 1, \forall a, t \tag{2.8}$$

$$u_{a,t}^{A}, v_{a,t}^{A}, w_{a,t}^{A} \in \{0,1\}, \forall a, t \tag{2.9}$$

In (2.4), $P_{a,t}^{max}$ is the maximum available capacity, which represents the total of the services (i.e., energy and reserve) related to a DERA active power in the wholesale market. The maximum capacity could be time-varying if the DERA manages different types of DERs (e.g., solar generation and energy storage system). The total system reserve is enforced at each interval to be larger than a percentage of demand through (2.10). Also, the system must withstand the loss of any single bulk power generation as represented through equation (2.11). It is pertinent to note that DERA's deployment based on $P_{a,t}^{max}$, during a TS-level uncertain event, can cause DS violations.

$$\sum_{g} r_{g,t} + \sum_{a} r_{a,t}^{A} \geq \eta\% \sum_{n} Load_{n,t}, \forall t \tag{2.10}$$

$$\sum_{j} r_{j,t} + \sum_{j} r_{j,t}^{A} \geq P_{g,t} + r_{g,t}, \forall g, t \tag{2.11}$$

2.3 DSO-DERA Scheduling: Evaluation of DS Operational Limits During TS-Level Uncertain Events

DSO-DERA scheduling approaches are essential to show the effectiveness of different DSO and ISO coordination frameworks. During a TS-level uncertain event, e.g., contingencies, ramping, and load uncertainty, the ISOs perform different analyses to determine New Desired Dispatch Point (NDDP) based on the promised energy and ancillary services awards of resources. Then, these NDDP signals are sent to the resources, including DERAs. The NDDP estimation of DERAs is done without insight into the DS limits and may cause DS voltage and line thermal limit violations. To mitigate DS violations while avoiding curtailment of DERA's promised awards, the flexibility of the DS, e.g., VAr support, can also be employed. In the following subsection, a DSO-

DERA scheduling approach is proposed based on an unbalanced IVACOPF formulation [37] that incorporates VAr support from PV SIs, to determine the DS violations caused by DERAs responding to the ISO NDDP signals.

2.3.1 ISO Signals to Aggregators During Transmission-Level Uncertain Events

As mentioned previously, the ISO sends NDDP signals to each DERA based on a particular TS-level uncertain event and the DERAs energy and ancillary services awards from the wholesale market. For the sake of simplicity in this framework, without loss of generality, the ISOs NDDP signals for DERAs in response to uncertain Scenario s at Time t is mimicked by a random output power, generated in the range $\overline{P_a^A} \in [P_{a,t}^A - r_{a,t}^A, P_{a,t}^A + r_{a,t}^A]$. Thus, $\overline{P_a^A}$ represents the requested ISO NDDP from the DERA a during a particular scenario and time interval.

2.3.2 Evaluation of DS Operational Limits: IVACOPF with PV Units SI VAr Support Model

This section presents the formulation to evaluate DS operational limits during TS-level uncertain events, including the proposed formulation for accurately modeling the VAr support capability of SIs. For the sake of simplicity, all the PV units are assumed to be interfaced with SIs. The formulation comprehensively models the DS, including line losses and untransposed DS lines with mutual admittances and impedances. The objective function is to evaluate DS conditions, minimizing the total DS violation as shown in (2.12).

$$min \begin{Bmatrix} \sum_{ni\in\mathcal{P}} \sum_{x\in\phi} V_{ni}^{x,+} + V_{ni}^{x,-} \\ + \sum_{l\in\mathcal{K}} \sum_{x\in\phi} I_l^{x,+} \end{Bmatrix} \tag{2.12}$$

Due to untransposed nature of DS, the current in Phase x depends not only on the voltages of Phase x, but also on the current and voltage of other phases due to the mutual impedances and admittances as shown in (2.13).

$$I_l^x = \left(Z_l^{x,x}\right)^{-1} \left[V_{ni}^x - V_{nj}^x - \sum_{m\in\phi, m\neq x} Z_l^{x,m} I_l^m + \frac{1}{2}\sum_{m\in\phi} Z_l^{x,m} \left(\sum_{n\in\phi} y_l^{m,n} V_{ni}^n\right)\right], \forall\, x \in \phi, l \in \mathcal{K} \tag{2.13}$$

It is worth noting that (2.13) is a linear constraint. In rectangular coordinates, the net injected current in each DS bus-phase is modeled by (2.14) and (2.15).

$$I_{ni}^{r,x} = \sum_{l\epsilon\hbar(ni)} I_l^{r,x}, \forall\, x \in \phi, ni \in \mathcal{P} \tag{2.14}$$

$$I_{ni}^{im,x} = \sum_{l\epsilon\hbar(ni)} I_l^{im,x}, \forall\, x \in \phi, ni \in \mathcal{P} \tag{2.15}$$

The active and reactive power balance constraints for each bus-phase are given in (2.16) and (2.17), respectively.

$$P_{ni,x} = \sum_{\forall sb\epsilon sb(ni)} P_{sb,x}^B + \sum_{\forall a\epsilon a(ni)} \overline{P_{a,x}^A} + \sum_{\forall f\epsilon f_1(ni)} P_{f,x}^{PVV} + \sum_{\forall e\epsilon f_2(ni)} P_{e,x}^{PV} - \sum_{\forall d\epsilon d(ni)} D_{d,x}^P = V_{ni}^{r,x} I_{ni}^{r,x} + V_{ni}^{im,x} I_{ni}^{im,x}, \forall\, x \in \phi, ni \in \mathcal{P} \tag{2.16}$$

$$Q_{ni,x} = \sum_{\forall sb \epsilon sb(ni)} Q^{B}_{sb,x} + \sum_{\forall f \epsilon f_1(ni)} Q^{PVV}_{f,x} + \sum_{kc \forall kc(ni)} Q^{C}_{kc,x} = V^{im,x}_{ni} I^{r,x}_{ni} - V^{r,x}_{ni} I^{im,x}_{ni} \forall\, x \in \phi, ni \in \mathcal{P} \quad (2.17)$$

Since the second portion of constraints (2.16) and (2.17) are nonconvex and nonlinear, they are reformulated as linear constraints (2.18) and (2.19) around $V^{r,x(it)}_{ni}$, $V^{im,x(it)}_{ni}$ and $I^{r,x(it)}_{ni}$, $I^{im,x(it)}_{ni}$ by Taylor Series First-order Approximation (TSFA).

$$P_{ni,x} = V^{r,x(it)}_{ni} I^{r,x}_{ni} + V^{im,x(it)}_{ni} I^{im,x}_{ni} + I^{r,x(it)}_{ni} V^{r,x}_{ni} + I^{im,x(it)}_{ni} V^{im,x}_{ni} - V^{r,x(it)}_{ni} I^{r,x(it)}_{ni} - V^{i,x(it)}_{ni} I^{im,x(it)}_{ni}, \forall x \in \phi, ni \in \mathcal{P} \quad (2.18)$$

$$Q_{ni,x} = V^{im,x(it)}_{ni} I^{r,x}_{ni} - V^{r,x(it)}_{ni} I^{im,x}_{ni} + I^{r,x(it)}_{ni} V^{im,x}_{ni} - I^{im,x(it)}_{ni} V^{r,x}_{ni} - V^{im,x(it)}_{ni} I^{r,x(it)}_{ni} + V^{r,x(it)}_{ni} I^{im,x(it)}_{ni}, \forall x \in \phi, ni \in \mathcal{P} \quad (2.19)$$

The IVACOPF is an iterative approximation model, wherein the parameters of TSFA, denoted by superscript (it), in each iteration, are updated based on the results of the previous iteration. The voltage magnitude in each bus-phase can be formulated as (2.20), which is a nonlinear and nonconvex constraint. TSFA is utilized to linearize this constraint to (2.21).

$$V^{x}_{ni} = \sqrt{V^{r,x2}_{ni} + V^{im,x2}_{ni}}, \forall\, x \in \phi, ni \in \mathcal{P} \quad (2.20)$$

$$V^{x}_{ni} = \frac{V^{r,x(it)}_{ni}}{\sqrt{V^{r,x(it)2}_{ni} + V^{im,x(it)2}_{ni}}} V^{r,x}_{ni} + \frac{V^{im,x(it)}_{ni}}{\sqrt{V^{r,x(it)2}_{ni} + V^{im,x(it)2}_{ni}}} V^{im,x}_{ni}, \forall\, x \in \phi, ni \in \mathcal{P} \quad (2.21)$$

Each bus-phase voltage magnitude limits, and the associated voltage violation variables, are modeled through (2.22). The thermal line limit, and the associated thermal line violation variable for each line-phase, is presented by (2.23).

$$-V^{x,-}_{ni} + 0.95 \leq V^{x}_{ni} \leq 1.05 + V^{x,+}_{ni}, \forall\, x \in \phi, ni \in \mathcal{P} \quad (2.22)$$

$$I^{r,x2}_{l} + I^{im,x2}_{l} \leq (I^{max,x}_{l} + I^{x,+}_{l})^2, \forall\, x \in \phi, l \in \mathcal{K} \quad (2.23)$$

Flexibility devices such as capacitor bank's reactive power injection/absorption is limited by (2.24) in the DS.

$$Q^{C}_{kc,x} \leq Q^{C,max}_{kc,x}, \forall\, x \in \phi, kc \in \mathcal{C} \quad (2.24)$$

Two types of PV units are modeled in the problem. PV units without VAr capability, can only generate the available active power, which is modeled through (2.25). On the other hand, the PV units, with VAr capability, can generate both active and reactive power, restricted through its apparent power rating by (2.26). The active power curtailment of such PV units is enabled as in (2.27). The VAr support capacity is restricted by their reactive power rating as presented in (2.28).

$$P_{e,x}^{PV} = P_{e,x}^{PV,av}, \forall\, x \in \phi, e \in f_2 \tag{2.25}$$

$$Q_{f,x}^{PVV\,2} + P_{f,x}^{PVV\,2} \leq S_{i,x}^{PVV\,2}, \forall\, x \in \phi, f \in f_1 \tag{2.26}$$

$$P_{f,x}^{PVV} \leq P_{f,x}^{PVV,av}, \forall\, x \in \phi, f \in f_1 \tag{2.27}$$

$$-Q_{f,x}^{PVV,max} \leq Q_{f,x}^{PVV} \leq Q_{f,x}^{PVV,max}, \forall\, x \in \phi, f \in f_1 \tag{2.28}$$

DERA participation in the wholesale market without considering the DS OSTN hosting capacity may cause violations in the DS. The DSO may constrain DERA injection to manage these issues, thereby causing ineffective utilization. The PV units, with VAr capability, can mitigate these challenges with VAr support in the DS. It is pertinent to mention that in this work, VAr support is only considered from PV units which are DSO customers, and not a part of DERA managed resources. Participating in DER aggregation and DSO net metering programs are mutually exclusive in these coordination frameworks. DSO managed PVs do not participate in the ISO market.

Most of the work in the literature model this VAr support based only on constraints (2.26)-(2.28), which may lead to unrealistic results due to ignoring the SI VAr dispatch curve. In this work, the VAr support from SIs is modeled based on the IEEE 1547-2018 standard [11], which represents the accurate VAr curves of SIs, as shown in Figure 2.3. The Volt-VAr (Q-V) and the Watt-VAr (P-Q) modes, as in the IEEE 1547 standard, determine the reactive power injection/absorption based on the input SI bus voltage and the SI active power injection/absorption respectively. Given default settings, both modes of operation have different characteristics for different DS operating conditions. Accordingly, to further enhance the DS flexibility, a mode selection approach based on [68] is modeled within the IVACOPF.

The Q-V curve shown in Figure 2.3 can be represented by equation (2.29) with five different operating zones. The P-Q curve shown in Fig. 3 can be represented by (2.30) with seven different operating zones. Depending on the operational state, either one of these functions, i.e., (2.29) and (2.30), are active for each VAr support-enabled PV unit. This selection is done by modeling and optimizing binary variables as described later in this section. In this work, these functions, i.e., (2.29) and (2.30), are converted into a MILP formulation for selecting optimal modes of operation as well as the corresponding piecewise section of the curves/functions using the Big-M method.

$$Q_{f,x}^{PVV} = \begin{cases} Q_{f,x}^{PVV,max}, & V_{f,x}^{min} \leq V_{f,x} < V_{1,f,x} \\ \frac{Q_{f,x}^{PVV,max}(V_{2,f,x} - V_{f,x})}{V_{2,f,x} - V_{1,f,x}}, & V_{1,f,x} \leq V_{f,x} < V_{2,f,x} \\ 0, & V_{2,f,x} \leq V_{f,x} < V_{3,f,x} \\ \frac{Q_{f,x}^{PVV,max}(V_{f,x} - V_{3,f,x})}{V_{3,f,x} - V_{4,f,x}}, & V_{3,f,x} \leq V_{f,x} < V_{4,f,x} \\ -Q_{f,x}^{PVV,max}, & V_{4,f,x} \leq V_{f,x} < V_{f,x}^{max} \end{cases} \tag{2.29}$$

$$Q_{f,x}^{PVV} = \begin{cases} Q_{f,x}^{PVV,max} & , P_{f,x}^{PVV} < P'_{3,f,x} \\ Q'_{2,f,x} + \frac{\left(P'_{2,f,x} - P_{f,x}^{PVV}\right)\left(Q'_{3,f,x} - Q'_{2,f,x}\right)}{P'_{2,f,x} - P'_{3,f,x}} & , P'_{3,f,x} \le P_{f,x}^{PVV} < P'_{2,f,x} \\ Q'_{1,f,x} + \frac{\left(P'_{1,f,x} - P_{f,x}^{PVV}\right)\left(Q'_{2,f,x} - Q'_{1,f,x}\right)}{P'_{1,f,x} - P'_{2,f,x}} & , P'_{2,f,x} \le P_{f,x}^{PVV} < P'_{1,f,x} \\ Q_{1,f,x} + \frac{\left(P_{1,f,x} - P_{f,x}^{PVV}\right)\left(Q'_{1,f,x} - Q_{1,f,x}\right)}{P_{1,f,x} - P'_{1,f,x}} & , P'_{1,f,x} \le P_{f,x}^{PVV} < P_{1,f,x} \\ Q_{2,f,x} + \frac{\left(P_{2,f,x} - P_{f,x}^{PVV}\right)\left(Q_{1,f,x} - Q_{2,f,x}\right)}{P_{2,f,x} - P_{1,f,x}} & , P_{1,f,x} \le P_{f,x}^{PVV} < P_{2,f,x} \\ Q_{3,f,x} + \frac{\left(P_{3,f,x} - P_{f,x}^{PVV}\right)\left(Q_{2,f,x} - Q_{3,f,x}\right)}{P_{3,f,x} - P_{2,f,x}} & , P_{2,f,x} \le P_{f,x}^{PVV} < P_{3,f,x} \\ -Q_{f,x}^{PVV,max} & , P_{f,x}^{PVV} \ge P_{3,f,x} \end{cases} \quad (2.30)$$

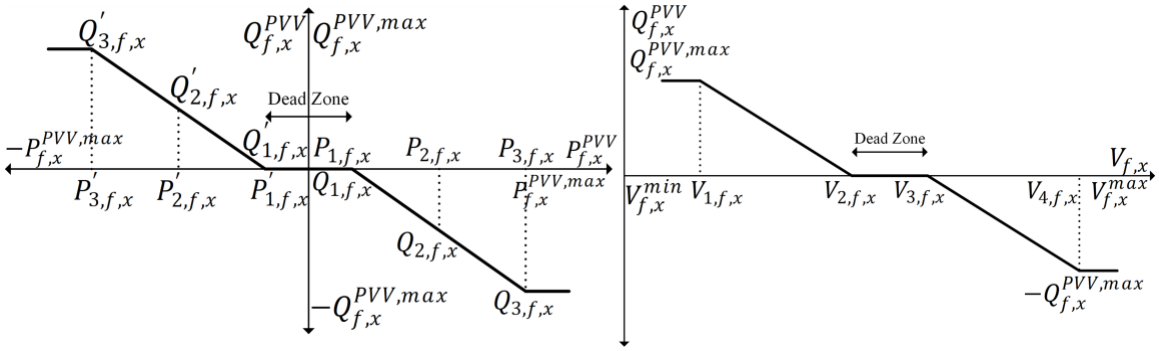

Figure 2.3 P-Q and Q-V Characteristic of a Smart Inverter [11].

Each operational zone (one to five) of the Q-V curve of Figure 2.3 is represented by the corresponding binary variable as given below in (2.31)-(2.40).

$$V_{f,x} \le V_{1,f,x} + Mu_{1,f,x}^{qv} \quad (2.31)$$

$$-Mu_{1,f,x}^{qv} \le Q_{f,x}^{PVV} - Q_{f,x}^{PVV,max} \le Mu_{1,f,x}^{qv} \quad (2.32)$$

$$-Mu_{2,f,x}^{qv} + V_{1,f,x} \le V_{f,x} \le V_{2,f,x} + Mu_{2,f,x}^{qv} \quad (2.33)$$

$$-Mu_{2,f,x}^{qv} \le Q_{f,x}^{PVV} - \frac{Q_{f,x}^{PVV,max}\left(V_{2,f,x} - V_{f,x}\right)}{V_{2,f,x} - V_{1,f,x}} \le Mu_{2,f,x}^{qv} \quad (2.34)$$

$$-Mu_{3,f,x}^{qv} + V_{2,f,x} \le V_{f,x} \le V_{3,f,x} + Mu_{3,f,x}^{qv} \quad (2.35)$$

$$-Mu_{3,f,x}^{qv} \le Q_{f,x}^{PVV} \le Mu_{3,f,x}^{qv} \quad (2.36)$$

$$-Mu_{4,f,x}^{qv} + V_{3,f,x} \le V_{f,x} \le V_{4,f,x} + Mu_{4,f,x}^{qv} \quad (2.37)$$

$$-Mu_{4,f,x}^{qv} \leq Q_{f,x}^{PVV} - \frac{Q_{f,x}^{PVV,max}(V_{f,x}-V_{3,f,x})}{V_{3,f,x}-V_{4,f,x}} \leq Mu_{4,f,x}^{qv} \tag{2.38}$$

$$-Mu_{5,f,x}^{qv} + V_{4,f,x} \leq V_{f,x} \tag{2.39}$$

$$-Mu_{5,f,x}^{qv} \leq Q_{f,x}^{PVV} + Q_{f,x}^{PVV,max} \leq Mu_{5,f,x}^{qv} \tag{2.40}$$

Each operational zone (one to seven) of the P-Q curve of Figure 2.3 is represented by the corresponding binary variable as given below in (2.41)-(2.54).

$$M_1 u_{1,f,x}^{pq} + P'_{3,f,x} \geq P_{f,x}^{PVV} \tag{2.41}$$

$$-M_1 u_{1,f,x}^{pq} \leq Q_{f,x}^{PVV} - Q_{f,x}^{PVV,max} \leq M_1 u_{1,f,x}^{pq} \tag{2.42}$$

$$-M_1 u_{2,f,x}^{pq} + P'_{3,f,x} \leq P_{f,x}^{PVV} \leq M_1 u_{2,f,x}^{pq} + P'_{2,f,x} \tag{2.43}$$

$$-M_1 u_{2,f,x}^{pq} \leq Q_{f,x}^{PVV} - Q'_{2,f,x} - \frac{\left(P'_{2,f,x}-P_{f,x}^{PVV}\right)\left(Q'_{3,f,x}-Q'_{2,f,x}\right)}{P'_{2,f,x}-P'_{3,f,x}} \leq M_1 u_{2,f,x}^{pq} \tag{2.44}$$

$$-M_1 u_{3,f,x}^{pq} + P'_{2,f,x} \leq P_{f,x}^{PVV} \leq M_1 u_{3,f,x}^{pq} + P'_{1,f,x} \tag{2.45}$$

$$-M_1 u_{3,f,x}^{pq} \leq Q_{f,x}^{PVV} - Q'_{1,f,x} - \frac{\left(P'_{1,f,x}-P_{f,x}^{PVV}\right)\left(Q'_{2,f,x}-Q'_{1,f,x}\right)}{P'_{1,f,x}-P'_{2,f,x}} \leq M_1 u_{3,f,x}^{pq} \tag{2.46}$$

$$-M_1 u_{4,f,x}^{pq} + P'_{1,f,x} \leq P_{f,x}^{PVV} \leq M_1 u_{4,f,x}^{pq} + P_{1,f,x} \tag{2.47}$$

$$-M_1 u_{4,f,x}^{pq} \leq Q_{f,x}^{PVV} - Q_{1,f,x} - \frac{\left(P_{1,f,x}-P_{f,x}^{PVV}\right)\left(Q'_{1,f,x}-Q_{1,f,x}\right)}{P_{1,f,x}-P'_{1,f,x}} \leq M_1 u_{4,f,x}^{pq} \tag{2.48}$$

$$-M_1 u_{5,f,x}^{pq} + P_{1,f,x} \leq P_{f,x}^{PVV} \leq M_1 u_{5,f,x}^{pq} + P_{2,f,x} \tag{2.49}$$

$$-M_1 u_{5,f,x}^{pq} \leq Q_{f,x}^{PVV} - Q_{2,f,x} - \frac{\left(P_{2,f,x}-P_{f,x}^{PVV}\right)(Q_{1,f,x}-Q_{2,f,x})}{P_{2,f,x}-P_{1,f,x}} \leq M_1 u_{5,f,x}^{pq} \tag{2.50}$$

$$-M_1 u_{6,f,x}^{pq} + P_{2,f,x} \leq P_{f,x}^{PVV} \leq M_1 u_{6,f,x}^{pq} + P_{3,f,x} \tag{2.51}$$

$$-M_1 u_{6,f,x}^{pq} \leq Q_{f,x}^{PVV} - Q_{3,f,x} - \frac{\left(P_{3,f,x}-P_{f,x}^{PVV}\right)(Q_{2,f,x}-Q_{3,f,x})}{P_{3,f,x}-P_{2,f,x}} \leq M_1 u_{6,f,x}^{pq} \tag{2.52}$$

$$-M_1 u_{7,f,x}^{pq} + P_{3,f,x} \leq P_{f,x}^{PVV} \tag{2.53}$$

$$-M_1 u_{7,f,x}^{pq} \leq Q_{f,x}^{PVV} + Q_{f,x}^{PVV,max} \leq M_1 u_{7,f,x}^{pq} \tag{2.54}$$

Equation (2.55) represents the constraint which prevents the selection of multiple modes and settings of operation at the same time.

$$u_{1,f,x}^{qv} + u_{2,f,x}^{qv} + u_{3,f,x}^{qv} + u_{4,f,x}^{qv} + u_{5,f,x}^{qv} + u_{1,f,x}^{pq} + u_{2,f,x}^{pq} + u_{3,f,x}^{pq} + u_{4,f,x}^{pq} + u_{5,f,x}^{pq} + u_{6,f,x}^{pq} + u_{7,f,x}^{pq} \leq 11, \forall f \in f_1 \quad (2.55)$$

The problem presented above is a mixed-integer quadratically constrained program (MIQCP) and is solved at each Time interval t for each uncertain Scenario s.

2.4 Proposed Aggregator Participation in the Wholesale Market: Architecture II

2.4.1 Architecture II Structure

In this Architecture, the ISOs manage the wholesale market with visibility over the DS limits. Before running the wholesale market, the ISO estimates the level of qualification and disqualification for different services provided by DERAs using statistical models obtained from DSOs, as shown in Figure 2.4. To this end, the hosting capacity (i.e., maximum per-feeder DER penetration considering safe and reliable DS network operation [46]) is predicted using data-mining algorithms based on the statistical information obtained from different DS conditions by the DSO. Then, these models are shared and coordinated in an offline setting with the ISO. It is pertinent to note that such offline coordination circumvents the need for real-time operational coordination infrastructure, and its associated financial burdens and complexities. It is also worth noting that this type of coordination already exists between LSEs/DUs and the ISO for load forecasts and other critical planning operations.

Figure 2.4 DERA Participation in the Wholesale Market for Architecture II

2.4.2 Evaluating Qualified Maximum Capacity

a) Data Generation for Data-Mining Algorithm

To generate data for the data-mining stage, different DS load scenarios using the corresponding forecast value and forecast error are generated through Monte Carlo simulation. Then, the IVACOPF problem with the objective function of maximizing the instantaneous penetration (i.e., active power generation) of the DER aggregations within their maximum available capacity is solved, subject to DS limits, for each scenario. Each scenario includes: (i) the maximum available capacity of a DERA, and (ii) different loading conditions in the DS, which can be used in the data-mining stage. Consequently, the DERAs maximum available capacity that is qualified to participate in the wholesale market under different DS conditions is obtained. In other words, the obtained maximized active power generation can determine the level of qualification and

disqualification of the total capacity of the services provided by DERAs for that specific DS operational condition without violating DS limits.

$$max\ \{\sum_{a\in A}\sum_{x\in\phi} P_{a,x}^{A}\} \tag{2.56}$$

Subject to:

$$\text{(2.13)-(2.15), (2.18)-(2.19), (2.21), (2.24)-(2.28), (2.31)-(2.55)} \tag{2.57}$$

$$0.95 \le V_{ni}^{x} \le 1.05, \forall\, x \in \phi, ni \in \mathcal{P} \tag{2.58}$$

$$I_{l}^{r,x^2} + I_{l}^{im,x^2} \le I_{l}^{max,x^2}, \forall\, x \in \phi, l \in \mathcal{K} \tag{2.59}$$

$$P_{a,x}^{A} \le P_{a,x}^{max} \tag{2.60}$$

The optimization model (2.56)-(2.60) includes the effect of the VAr support from the SIs on the DS OSTN hosting capacity and is solved for each scenario and time interval. The maximum qualified capacity incorporates nodal and per-feeder information of DERAs (depending on the location in the DS).

b) Data-Mining Stage: Obtaining Aggregators Maximum Qualified Capacity (DS OSTN hosting capacity)

In this section, Neural Network (NN) regression is utilized to create functions that predict the maximum qualified capacity of the DERAs, i.e., $P_{a,t}^{max,qualified}$, for safe and reliable DS operation, as shown in Figure 2.5. Each scenario from the data generation stage represents an instance that includes (i) target value that is the maximum qualified capacity of the DERAs in the feeder and (ii) the features that are load summation at each phase at each feeder in the DS network. So, the total number of features would be $3 \times (number\ of\ feeders)$. Each NN function is trained by the DSO for a given time period and all the DERAs in one specific feeder and shared with the ISO (weekly/monthly). Training one single NN model for all the DERAs in a specific radial feeder for a given time period, circumvents the need to handle switches in the network. Even if the network topology changes, the internal composition of the feeder does not change, preserving model validity.

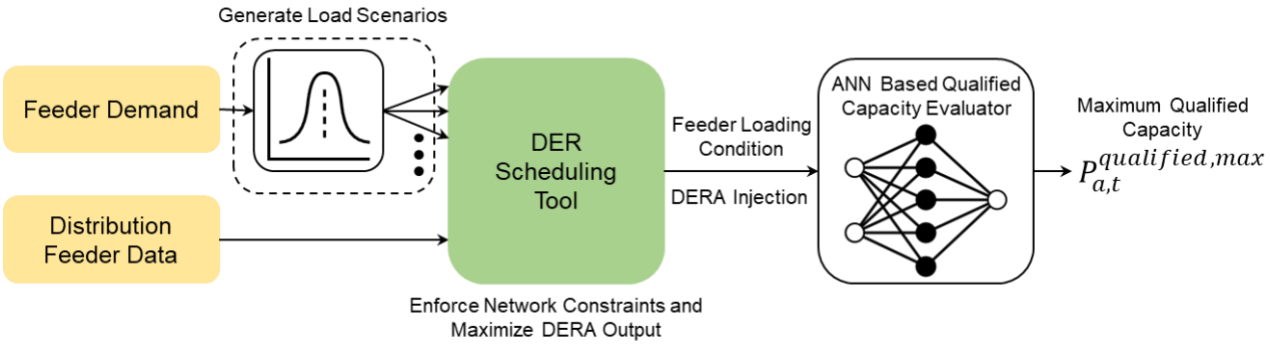

Figure 2.5 Maximum Qualified Capacity Estimation

2.4.3 DA Formulation Considering Qualified Maximum Capacity

This section presents the DA wholesale market, which assigns the total services (i.e., energy and reserve) to a DERA based on its realized $\overline{P_{a,t}^{max,qualified}}$. After obtaining the NN functions from offline process, the maximum qualified capacity is predicted based on the most-updated DS operational forecasts and conditions close to running the DA wholesale market. Therefore, there is no need to perform different time-consuming DS analyses before the DA wholesale market for determining DS OSTN hosting capacity and also mitigates problems where the DERA's NDDP cannot be achieved due to DSO constraints. It is worth mentioning that the qualified maximum capacity is always lower than or equal to the available maximum capacity, $P_{a,t}^{max}$, as shown in Figure 2.6. The DA wholesale market model considering predicted qualified maximum capacity is:

$$min \sum_g \sum_t (c_g^A P_{gt}^A + c_g^{SU} v_{gt} + c_g^{SD} w_{gt} + c_g^{Res} r_{gt}) + \sum_a \sum_t (c_a^A P_{at}^A + c_a^{Res,A} r_{at}^A) \quad (2.61)$$

Subject to:

(2.2)-(2.3),(2.5)-(2.9) (2.62)

$$P_{at}^A + r_{at}^A \leq P_{a,t}^{max,qualified} u_{at}, \forall a, t \quad (2.63)$$

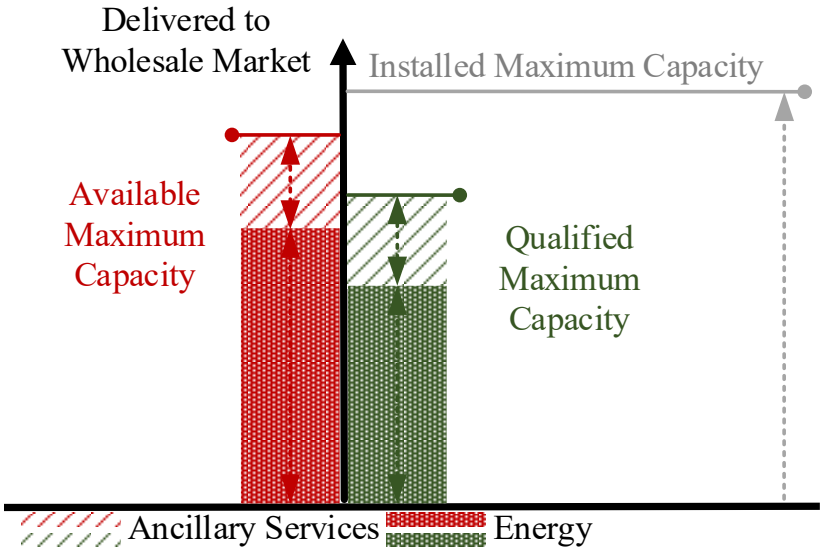

Figure 2.6 DERA's Installed, Available and Qualified Maximum Capacity

2.5 Results and Analysis

Pyomo [71] and DOcplex [72] modeling libraries were used to solve the DA wholesale market and IVACOPF model on a computer with an Intel Core i7 @ 2.40 GHz and 32 GB RAM. In addition, the NNs for the qualified capacity of DERAs were trained using the TensorFlow library [73]. Two case studies are presented as shown below:

- Case study I: To analyze the effect of VAr support from SIs on aiding real-time DS operations when responding to TS-level uncertainties and improving the maximum qualified capacity of DERAs.
- Case study II: To compare the performance of proposed Architecture II to Architecture I on improving the security of DS operations, while allowing DERA participation in the wholesale market.

2.5.1 Assumptions and System Data

The 118-bus IEEE test system is used for modeling the TS; this system includes 91 loads, 54 generators, and 186 lines [74]. The DS substation with three feeders, based on 240-bus distribution test system [75], is assumed to be connected to Bus #71 of the 118-bus IEEE test system. Fifteen DERAs (five DERAs in each of the three feeders) with 0.25, 0.5, 1, 1.5 MW maximum capacity and a maximum total of 8.25 MW were added to the 240-bus distribution test system. These DERs are only classified as time varying or not for the sake of general concept representation. Seven of these DERAs have time-varying available capacity and the rest have a non-time-varying available capacity. DERAs bids were randomly generated in the range of the minimum and average wholesale market bids. Fifteen additional aggregated PV units were added to the DS based on data from a local utility in Arizona. For these PV units, the hourly solar generation profile of CAISO's actual data, February 10, 2022, were chosen [76]. The number of iterations for the IVACOPF is set to 2. Relative MIP gap is set at 0.2%. For the data-mining stage associated with Architecture II, 1000 DS load scenarios were generated, 80% and 20% of which were used as training and testing datasets, respectively. The NN models for Architecture II have five hidden layers with 100, 100, 75, 50, and 25 neurons. The IVACOPF model utilized, exhibits better accuracy, compared to the widely utilized LinDistFlow model [37]. Based on the errors in Figure 2.7, the maximum voltage magnitude approximation error is less than 4.5E-04, showing the precision of the IVACOPF for solving OPF problems for the unbalanced DS with SI modeling. It is worth mentioning that other unbalanced DS OPF approaches can be used instead of IVACOPF in the proposed framework.

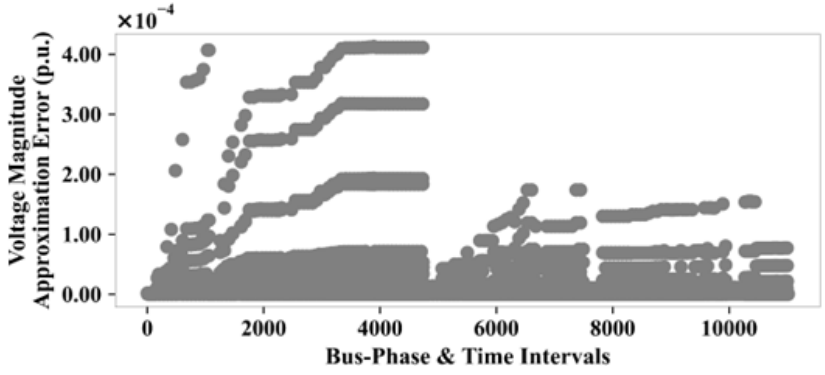

Figure 2.7 Bus Voltage Linearization Error using the IVACOPF

2.5.2 Case Study I: Effect of VAr Support from SIs on DS Operations and DERA Utilization

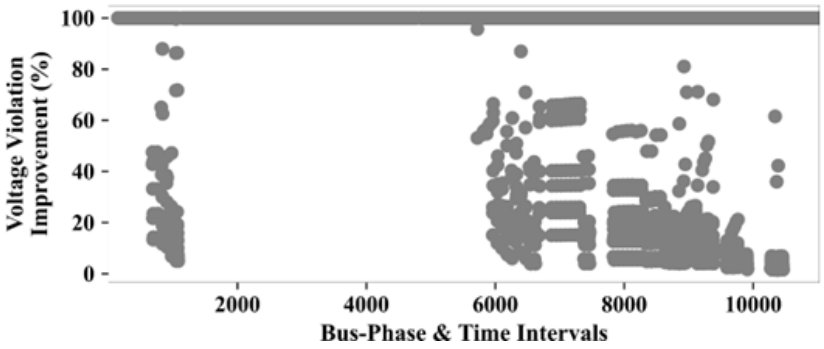

Figure 2.8 Voltage Violation Improvement of PV Model 1 compared to Model 2

Considering the effect of VAr support on improving voltage profile, the first study looks at how enabling VAr support from PV unit SIs aid DS real-time operations when DERAs respond to ISO NDDPs. Accordingly, two PV capability models are considered. In "PV model 1", all PV units have VAr capability, while in "PV model 2", none of the PV units have VAr capability. A single scenario is used as a benchmark, where the same ISO NDDPs are used for DERAs. Figure 2.8 presents voltage violation improvement for the 11016 bus-phase and time interval instances, due to having PV model 1. As exhibited, localized VAr support from SIs in the DS can reduce the voltage issues associated with the DERAs meeting the ISOs NDDPs during real-time operations. In Figure 2.8, all 11016 or 100% of instances have the same or less voltage violation compared to PV model 2. Although VAr support from SIs reduces the magnitude, it cannot entirely remove the issue. Table 2.1 shows the maximum cumulative violation of all bus phases, i.e., summed over all buses, across different time intervals. This maximum cumulative violation is observed in Hour 10. As shown in Table I, with more penetration of roof-top PV units with SIs, the flexibility of the DS system increases in managing voltage issues due to increasing VAr support capacity from interfaced SIs. This translates to improved deployability during TS-level uncertain events and overcoming DS limitations.

Table 2.1 Maximum Bus-Phase DS Cumulative Voltage Violation Over All Time Intervals, Architecture I (p.u.).

PV %	PV model 1	PV model 2	Improvement of PV model 1 to model 2 (%)
15	0.38	0.44	13.63
30	0.36	0.47	23.40
45	0.34	0.51	33.33

Apart from aiding real-time DS operations, preemptively considering VAr support, can significantly improve maximum qualified capacity and consequently, DERA utilization. To observe this, a second study is presented where two maximum qualified capacity estimation models are utilized: MQC1 and MQC2 with 120% roof-top PV penetration. MQC1 model is

trained on data where both PV unit curtailment and VAr support is allowed. MQC2 model is trained on data where no flexibility from PV SIs is allowed to mitigate violations. As shown in Figure 2.9, the predicted qualified capacity using MQC1 always exceeds MQC2 for this case. It is important to note that MQC1 will always perform the same or better than MQC2. As roof-top PV penetration increases during the middle of the day, due to a lack of flexibility, DERA output is curtailed to maintain DS limits in the generated MQC2 dataset. MQC1 has more qualified capacity during the same period due to flexibility from VAr support, preventing DERA curtailment. For the given DS conditions, over twenty-four hours, cumulative DERA qualified capacity of MQC1 is 173.50 MW compared to 162.37 MW of MQC2, corresponding to a 11.12 MW improvement.

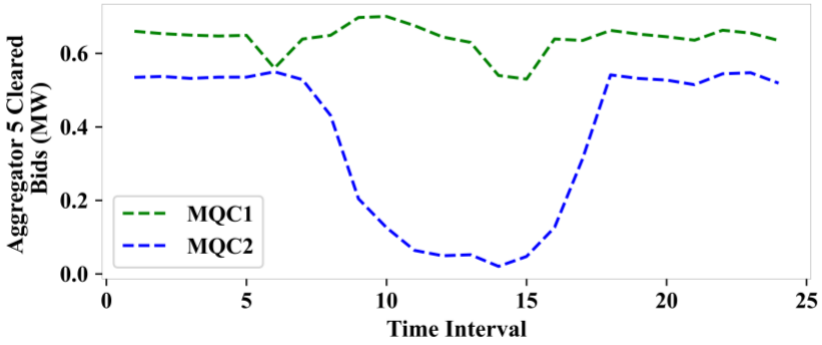

Figure 2.9 Maximum Qualified Capacity with and without VAr Support..

2.5.3 Case Study II: Architecture II Versus Architecture I

Table 2.2 Instances With Non-Zero Voltage Violation

	Architecture I	Architecture II
No. of voltage upper limit violation	111811 (10.1%)	218 (~0%)
No. of voltage lower limit violation	0 (0%)	0 (0%)

The main goal of this study is to compare the performance of Architecture II with Architecture I in improving DS operational security and reliability. The number of aggregated roof-top PV units with VAr support is five for both Architectures, at ~15% penetration of roof-top PV units. One hundred TS-level uncertain event scenarios (different ISO NDDPs) are generated in the DSO-DERAs scheduling phase for both frameworks to evaluate DS operational violations while responding to ISO NDDPs. Table 2.2 lists the number of instances in which each Architecture leads to non-zero voltage violation while evaluating DS operational limits during uncertain events. The total number of instances is 1101600, which is obtained through multiplying the number of bus phases (459), by the number of time intervals (24), and by the number of uncertain scenarios (100). Based on this table, approximately 10.1 percent of all instances of Architecture I experience violations, considerably higher than that of Architecture II (0.02%). This reduction is due to Architecture II proactively and dynamically considering the DS OSTN hosting capacity on the products awarded to the DERAs located in the DS network. The resulting awards less frequently cause voltage violation in DS by a considerable margin. The corresponding histogram of the voltage violations with non-zero value is given in Figure 2.10 for both Architectures. From Figure 2.10, the voltage violation issue happens more frequently for Architecture I, with a maximum

value around 0.014 pu. In comparison, this value for Architecture II is 0.0005 pu with lower frequency

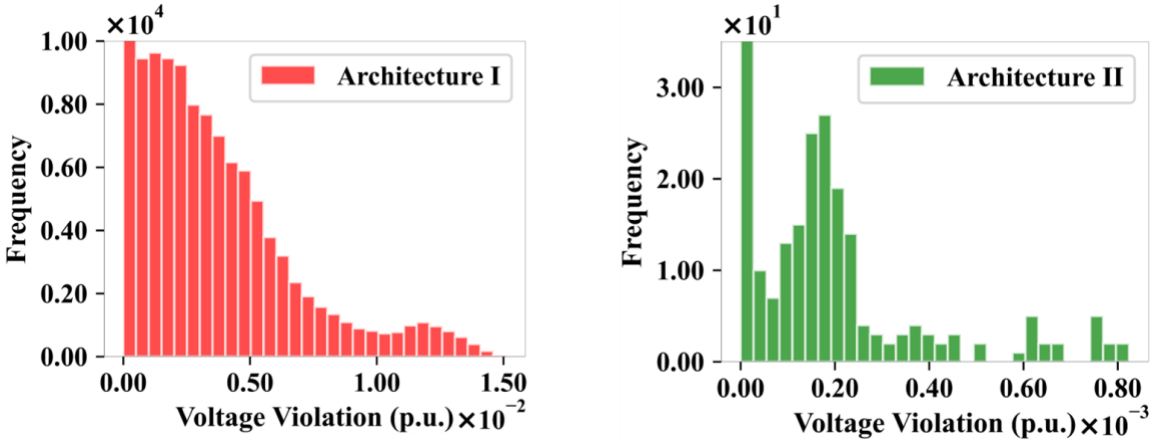

Figure 2.10 Histogram of Voltage Violations with Non-Zero Value: Architecture I (111811 Cases) & Architecture II (218 Cases).

Figure 2.11 exhibits the DA energy award, maximum available, and qualified capacity from which ISO NDDPs are generated for DERA # 5. Based on Figure 2.11, Architecture I leads to the DERA's energy awards being beyond the DS OSTN hosting capacity. More specifically, any energy award beyond the dashed green line, i.e., qualified capacity, affects reliable and safe operation of DS. However, in Figure 2.11, Architecture II will result in lower awards of energy products to the DERA. The lower capacity qualifications also correspond to an increase in operational costs. The total operating cost marginally increases to \$2599.5k from \$2598.2k by implementing Architecture II, due to reduced DERA capacity participation. The reduced cost of operation for Architecture I jeopardizes the DS network operational security and reliability, as participating capacity could potentially be beyond the DS OSTN hosting capacity. These results show that bidding within the OSTN hosting capacity of DERAs consequently leads to the effective, reliable and safe operation of the DS, while allowing the DERAs to participate in the wholesale markets.

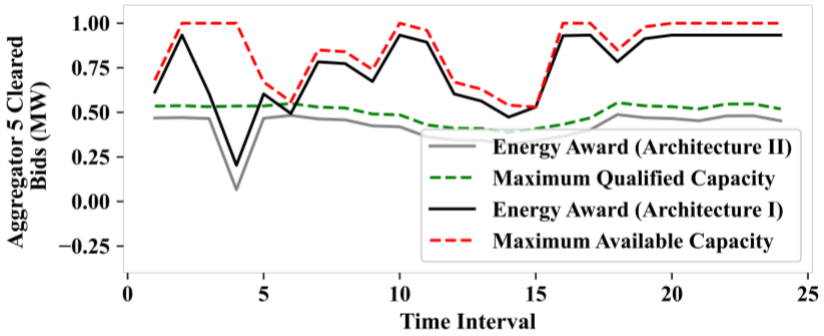

Figure 2.11 Energy, Maximum Available, and Qualified Capacity of DERA # 5

3. Conclusion

First, this work analyses the effect of reactive power and active power operational modes in mitigating voltage issues caused by an increased penetration of residential rooftop PV, not just in a local scope, but distribution feeder wide. A solution is presented by modeling the capabilities of a SI within a robust DOPF framework to create a comprehensive DER scheduling tool, capable of mitigating power quality issues within the distribution feeder, while maximizing PV utilization by dispatching individual SIs within the distribution feeder. As an alternative to the popularly utilized Volt-VAr operational mode, Watt-VAr operational mode is formulated and inducted within the DOPF model to create a DER scheduling tool. The performance of such a tool is analyzed with respect to utilizing the Volt-VAr operational mode for the same purpose. Different characteristics of the operational modes are analyzed and noted. An extension is also presented where the set-points of the Watt-VAr operational mode are optimally selected according to system conditions. Active power operational mode such as the Volt-Watt operational mode is analyzed within the scope of a DER scheduling tool and the performance of the operational mode in mitigating voltage issues is noted. Finally considering the different characteristics and performance of the two operational modes, a UMS framework is proposed which is capable of optimally selecting the mode of operation for each individual SI within the distribution feeder to mitigate voltage violation, voltage unbalance issues and minimize cost of operation. An extension of the work is also presented where the set-points are optimally selected for the chosen mode of operation, further extending the flexibility of the DER scheduling tool, to maximize gains.

The learnings from this work, including the ability of SIs to affect DS conditions, improve overall DS hosting capacity and improve DS flexibility, is leveraged to improve overall transmission and distribution operations. Accordingly, under the guidance of FERC order 2222 [7], other applications are also investigated, including coordinated transmission and distribution operations. An effective ISO-DSO-DERA coordination framework allows direct DERA participation in wholesale markets, while DSOs ensures safe and reliable DS operation without the need for real-time coordination between the ISO and DSO. If the DS OSTN hosting capacity is not proactively considered on the DERA's submitted bids to the wholesale market, deploying services awarded to DERAs may pose significant risks to the DS operation. In this work, two ISO-DSO-DERA coordination frameworks were proposed along with the corresponding distinction and definition of the participants roles and the required information exchange in the market management systems. Architecture II enables the ISO to proactively and dynamically have visibility over the DS limits, without the computational and communication hassles of modeling the DS and coordinating with the DSO in real-time operations. To this end, Architecture II employed the statistical information obtained using different DS conditions to predict the hosting capacity with the most-updated DS information and conditions before conducting the DA wholesale market. Finally, the DSO-DERAs scheduling phase to compare the performance of Architecture II with Architecture I. The DSO-DERAs scheduling phases goal is to mimic the DS condition during a TS-level uncertain event. In addition, the VAr support capability provided by PV SIs was leveraged to minimize DS violation. The simulation results showed that the VAr support from the PV unit with SIs could mitigate the DS voltage issues caused by the DERAs following ISO NDDPs. Furthermore, the proposed Architecture II outperforms Architecture I concerning ISO awards for DERAs that does not impose reliability and safety issues for DS as prescribed by FERC order No. 2222 [7].

References

[1] U.S. Energy Information Administration-EIA-Independent Statistics and Analysis*, Available [Online]: https://www.eia.gov/todayinenergy/detail.php?id=60341.*

*[2] A. Sokolov, et al., "*An Economic Analysis for Residential Rooftop Solar Photovoltaic Panels in the State of Texas*" In 13th Annual International Conference on Industrial Engineering and Operations Management,* 2023. https://doi.org/10.46254/AN13.20230010*.*

*[3] T. A. Short, "*Electric Power Distribution Handbook*". Boca Raton, FL, USA*: CRC, 2004*.*

*[4] M. Karimi, et al., "*Photovoltaic penetration issues and impacts in distribution network – A review*" in Renewable and Sustainable Energy Reviews,* vol. 53, pp. 594-605, 2016. https://doi.org/10.1016/j.rser.2015.08.042.

*[5] K. Butler-Purry, M. Marotti, "*Impact of Distributed Generators on Protective Devices in Radial Distribution Systems*" in 2005/2006 IEEE/PES Transmission and Distribution Conference and Exhibition, Dallas, TX, USA,* pp. 87-88, 2006. https://doi.org/10.1109/TDC.2006.1668462.

*[6] Y. Wu, C. Chen, et al., "*Advanced Analysis of Clustered Photovoltaic System's Performance Based on the Battery-Integrated Voltage Control Algorithm*" in International Journal of Emerging Electric Power Systems,* vol. 10, no. 4, 2009. https://doi.org/10.2202/1553-779X.2201.

[7] FERC, FERC Order No. 2222*. [Online]. Available: https://www.ferc.gov/media/ferc-order-no-2222-fact-sheet.*

*[8] V. Sharma, S. Aziz, et al., "*Effects of high solar photovoltaic penetration on distribution feeders and the economic impact*" in Renewable and Sustainable Energy Reviews,* vol. 131, 2020. https://doi.org/10.1016/j.rser.2020.110021.

*[9] N. Mahmud, A. Zahedi, "*Review of control strategies for voltage regulation of the smart distribution network with high penetration of renewable distributed generation*" in Renewable and Sustainable Energy Reviews,* vol. 64, pp. 582-595, 2016. https://doi.org/10.1016/j.rser.2016.06.030.

*[10] M. M. Rezvani, S. Mehraeen, et al., "*Interaction of Transmission-Distribution System in the Presence of DER Units–Co-simulation Approach*" in IEEE Open Journal of Industry Applications,* vol. 1, pp. 23-32, 2020. https://doi.org/10.1109/OJIA.2020.2981455*.*

*[11] "*IEEE Standard for Interconnection and Interoperability of Distributed Energy Resources with Associated Electric Power Systems Interfaces*", IEEE Std 1547™-2018,* 15 February 2018*.*

[12] F. Shahnia, A. Ghosh, et al., "Predicting Voltage Unbalance Impacts of Plug-in Electric Vehicles Penetration in Residential Low-voltage Distribution Networks" *in Electric Power Components and Systems,* vol. 41, no. 16, pp. 1594–1616, 2013. https://doi.org/10.1080/15325008.2013.834004

*[13] W. H. Kersting, "*Causes and effects of unbalanced voltages serving an induction motor*" in 2000 Rural Electric Power Conference. Papers Presented at the 44th Annual Conference (Cat. No.00CH37071), Louisville, KY, USA,* pp. B3/1-B3/8, 2000. https://doi.org/10.1109/REPCON.2000.848042.

*[14] N. Jabalameli, A. Ghosh, "*Online Centralized Coordination of Charging and Phase Switching of PEVs in Unbalanced LV Networks with High PV Penetrations*" in IEEE Systems Journal,* vol. 15, no. 1, pp. 1015-1025, 2021. https://doi.org/10.1109/JSYST.2020.3000504*.*

*[15] N. Leemput, F. Geth, et al., "*Impact of Electric Vehicle On-Board Single-Phase Charging Strategies on a Flemish Residential Grid*" in IEEE Transactions on Smart Grid,* vol. 5, no. 4, pp. 1815-1822, 2014. https://doi.org/10.1109/TSG.2014.2307897.

*[16] X. Sun, J. Qiu, J. Zhao, "*Optimal Local Volt/Var Control for Photovoltaic Inverters in Active Distribution Networks*" in IEEE Transactions on Power Systems,* vol. 36, no. 6, pp. 5756-5766, 2021. https://doi.org/10.1109/TPWRS.2021.3080039.
*[17] M. Farivar, et al., "*Optimal inverter VAR control in distribution systems with high PV penetration*" in 2012 IEEE Power and Energy Society General Meeting, San Diego, CA, USA,* pp. 1-7, 2012. https://doi.org/10.1109/PESGM.2012.6345736.
*[18] A. Savasci, et al., "*Distribution Grid Optimal Power Flow Integrating Volt-Var Drop of Smart Inverters*" in 2021 IEEE GreenTech, Denver, CO, USA*, pp. 54-61, 2021.
*[19] E. Dall'Anese, S. V. Dhople, G. B. Giannakis, "*Optimal Dispatch of Photovoltaic Inverters in Residential Distribution Systems*" in IEEE Transactions on Sustainable Energy,* vol. 5, no. 2, pp. 487-497, 2014. https://doi.org/10.1109/TSTE.2013.2292828.
*[20] X. Su, M. Masoum, P. J. Wolfs, "*Optimal PV Inverter Reactive Power Control and Real Power Curtailment to Improve Performance of Unbalanced Four-Wire LV Distribution Networks*" in IEEE Transactions on Sustainable Energy,* vol. 5, no. 3, pp. 967-977, 2014. https://doi.org/10.1109/TSTE.2014.2313862.
*[21] M. K. Singh, et al., "*Joint Grid Topology Reconfiguration and Design of Watt-VAR Curves for DERs*" in 2022 IEEE Power & Energy Society General Meeting (PESGM), Denver, CO, USA,* pp. 1-5, 2022. https://doi.org/10.1109/PESGM48719.2022.9917023.
*[22] A. Ali, et al., "*Probabilistic Approach for Hosting High PV Penetration in Distribution Systems via Optimal Oversized Inverter with Watt-Var Functions*" in IEEE Systems Journal,* vol. 15, no. 1, pp. 684-693, 2021, https://doi.org/10.1109/JSYST.2020.2982467.
[23] K. Girigoudar, L. Roald, "On the impact of different voltage unbalance metrics in distribution system optimization" *in Elec. Power Sys. Res.,* vol. 189, 2020, 106656.
*[24] T. O. Olowu, et al., "*Optimal Mode and Droop Setting of Smart Inverters*" in 2023 IEEE Power & Energy Society General Meeting (PESGM), Orlando, FL, USA, 2023,* pp. 1-5. https://doi.org/10.1109/PESGM52003.2023.10252918.
*[25] T. O. Olowu, et al., "*Two-Timescale Control of Smart Inverters and Legacy Devices in Unbalanced Distribution Feeders*" in 2023 IEEE Industry Applications Society Annual Meeting (IAS), Nashville, TN, USA, 2023,* pp. 1-6. https://doi.org/10.1109/IAS54024.2023.10406521.
*[26] V. Vijayan, A. Mohapatra, S. N. Singh, "*Impact of Modes of Operation of Smart Inverters on Volt-VAR Optimization*" in 2019 IEEE PES Innovative Smart Grid Technologies Europe (ISGT-Europe), Bucharest, Romania,* 2019, pp. 1-5. https://doi.org/10.1109/ISGTEurope.2019.8905646.
*[27] R. R. Jha, et al., "*Distribution Grid Optimal Power Flow (D-OPF): Modeling, Analysis, and Benchmarking*" in IEEE Transactions on Power Systems,* vol. 38, no. 4, pp. 3654-3668, 2023. https://doi.org/10.1109/TPWRS.2022.3204227.
*[28] Y. Liu, J. Li, L. Wu, "*ACOPF for three-phase four-conductor distribution systems: semidefinite programming-based relaxation with variable reduction and feasible solution recovery*" in IET Generation, Transmission & Distribution,* Volume 13, Issue 2, 2019, p. 266 – 276. https://doi.org/10.1049/iet-gtd.2018.5033.
*[29] A. Inaolaji, A. Savasci, S. Paudyal, "*Distribution Grid Optimal Power Flow in Unbalanced Multiphase Networks with Volt-VAr and Volt-Watt Droop Settings of Smart Inverters*" in IEEE Transactions on Industry Applications,* vol. 58, no. 5, pp. 5832-5843, 2022. https://doi.org/10.1109/TIA.2022.3181110.

*[30] A. Savasci, A. Inaolaji, S. Paudyal, "*Two-Stage Volt-VAr Optimization of Distribution Grids with Smart Inverters and Legacy Devices*" in IEEE Transactions on Industry Applications,* vol. 58, no. 5, pp. 5711-5723, 2022, https://doi.org/10.1109/TIA.2022.3183182.
*[31] D. Bertsekas, H. Yu, "*A Unifying Polyhedral Approximation Framework for Convex Optimization*" in SIAM Journal on Optimization,* vol. 21, no. 1, pp. 333-360, 2011. https://doi.org/10.1137/090772204
*[32] D. B. Arnold, et al., "*Optimal dispatch of reactive power for voltage regulation and balancing in unbalanced distribution systems*" in 2016 IEEE Power and Energy Society General Meeting (PESGM), Boston, MA, USA,* 2016, pp. 1-5, https://doi.org/10.1109/PESGM.2016.7741261.
*[33] R. Wagle, et al., "*Optimal power flow based coordinated reactive and active power control to mitigate voltage violations in smart inverter enriched distribution network*" in International Journal of Green Energy,* vol. 21, no.2, pp. 359–375. https://doi.org/10.1080/15435075.2023.2196324.
*[34] Q. Tang, et al., "*A Particle Swarm Optimization Algorithm Based on Genetic Selection Strategy*" in Advances in Neural Networks. Lecture Notes in Computer Science,* vol. 5553. Springer, Berlin, Heidelberg. https://doi.org/10.1007/978-3-642-01513-7_14.
*[35] A. Samadi, R. Eriksson, et. al., "*Coordinated Active Power-Dependent Voltage Regulation in Distribution Grids with PV Systems*" in IEEE Transactions on Power Delivery,* vol. 29, no. 3, pp. 1454-1464, 2014. https://doi.org/10.1109/TPWRD.2014.2298614.
*[36] A. Safayet, P. Fajri, I. Husain, "*Reactive Power Management for Overvoltage Prevention at High PV Penetration in a Low-Voltage Distribution System*" in IEEE Transactions on Industry Applications,* vol. 53, no. 6, pp. 5786-5794, 2017. https://doi.org/10.1109/TIA.2017.2741925.
*[37] Z. Soltani, M. Khorsand, S. Ma, "*Current–Voltage Unbalanced Distribution AC Optimal Power Flow for Advanced Distribution Management System Applications*" in IEEE Open Journal of Industry Applications,* vol. 5, pp. 155-167, 2024. https://doi.org/10.1109/OJIA.2024.3367547.
*[38] Z. Soltani, S. Ma, M. Khorsand, V. Vittal, "*Simultaneous Robust State Estimation, Topology Error Processing, and Outage Detection for Unbalanced Distribution Systems*" in IEEE Transactions on Power Systems,* vol. 38, no. 3, pp. 2018-2034, 2023. https://doi.org/10.1109/TPWRS.2022.3181118.
*[39] Z. Soltani, S. Ma, M. Ghaljehei, M. Khorsand, "*Volt-VAr Optimization of PV Smart Inverters in Unbalanced Distribution Systems*" in 2023 IEEE PES Grid Edge Technologies Conference & Exposition (Grid Edge), San Diego, CA, USA,* 2023, pp. 1-6. https://doi.org/10.1109/GridEdge54130.2023.10102744.
*[40] K. Montano-Martinez, et al., "*Detailed Primary and Secondary Distribution System Model Enhancement Using AMI Data*" in IEEE Open Access Journal of Power and Energy,* vol. 9, pp. 2-15, 2022, https://doi.org/10.1109/OAJPE.2021.3125900.
*[41] "*IEEE Recommended Practice for Electric Power Distribution for Industrial Plants*" in IEEE Std 141-1993,* 29 April 1994.
[42] M. Chen, S. Ma, Z. Soltani, R. Ayyanar, V. Vittal, M. Khorsand, "Optimal Placement of PV Smart Inverters with Volt-VAr Control in Electric Distribution Systems*" in IEEE Systems Journal,* vol. 17, no. 3, pp. 3436-3446, 2023. https://doi.org/10.1109/JSYST.2023.3256121.
*[43] California ISO (CAISO), CA, USA, "*Market Price Map*." [Online]. Available: http://www.caiso.com/PriceMap/Pages/default.aspx.*

[44] Pacific Gas and Electric (PG&E), CA, USA, "Net Surplus Compensation Rates for Energy." *[Online]. Available: https://www.pge.com/pge_global/common/pdfs/solar-and-vehicles/green-energy-incentives/AB920_RateTable.pdf*
*[45] P. De Martini and L. Kristov, "*Distribution Systems in a High Distributed Energy Resources Future*" Oct. 2015. Available: https://eta-publications.lbl.gov/sites/default/files/lbnl-1003797.pdf*
*[46] P. De Martini and L. Kristov, "*Distribution Systems in a High Distributed Energy Resources Future: Planning, Market Design, Operation and Oversight*" Nov. 2015. Available: https://eta-publications.lbl.gov/sites/default/files/lbnl-1003797_presentation.pdf*
*[47] C. Cano, "*FERC Order No. 2222: A New Day for Distributed Energy Resources*"* Sep. 2020*. Available: https://www.ferc.gov/media/ferc-order-no-2222-fact-sheet*
*[48] M. Mousavi and M. Wu, "*A DSO Framework for Market Participation of DER Aggregators in Unbalanced Distribution Networks*" IEEE Tran. Pow. Sys.,* pp. 1–1, 2021.
*[49] S. Thomas, "*Evolution of the Distribution System & the Potential for Distribution-level Markets: A Primer for State Utility Regulators," Jan. 2018. *Available: https://www.naruc.org/default/assets/File/201801%20Evolution%20of%20the%20Distribution%20System.pdf*
*[50] Y. K. Renani, et al., "*Optimal Transactive Market Operations With Distribution System Operators*" IEEE Tran. Sma. Gr.,* vol. 9, pp. 6692–6701, 2018.
*[51] G. Muñoz-Delgado, et al., "*Distribution System Expansion Planning Considering Non-Utility-Owned DG and an Independent Distribution System Operator*" IEEE Tran. Pow. Sys.,* vol. 34, pp. 2588–2597, 2019.
*[52] S. Chen, et al., "*Forming Bidding Curves for a Distribution System Operator*" IEEE Tran. Pow. Syst., vol. 33, pp. 5389–5400, 2018.*
*[53] T. Soares, et. al., "*Active Distribution Grid Management Based on Robust AC Optimal Power Flow*" IEEE Tran. Sma. Gr.,* vol. 9, 2018.
*[54] S. Wang, et. al., "*Real-Time Coordination of Transmission and Distribution Networks via Nash Bargaining Solution*" IEEE Tran. Sus. Ene.,* vol. 12, pp. 2238–2254, 2021.
*[55] CAISO, "*PDR-DERP-NGR-LFA Summary Comparison Matrix*." Available: https://www.caiso.com/documents/participationcomparison-proxydemand-distributedenergy-storage-forecastadjustment.pdf*
*[56] NYISO, "*Aggregation Manual*", Available: https://www.nyiso.com/documents/20142/2923301/M-38-Aggregation-Final-v1-0.pdf/488117aa-43ec-85c3-423d-4aba592e5895?t=1713279580926*
*[57] K. Alshehri, et. al., "*Quantifying market efficiency impacts of aggregated distributed energy resources*" IEEE Tran. on Pow. Sys.,* vol. 35, pp. 4067–4077, 2020*.*
*[58] M. Di Somma, et al., "*Optimal Bidding Strategy for a DER Aggregator in the Day-Ahead Market in the Presence of Demand Flexibility*" IEEE Tran. Ind. Elec*., vol. 66, pp. 1509–1519, 2019.
*[59] M. González Vayá and G. Andersson, "*Optimal Bidding Strategy of a Plug-In Electric Vehicle Aggregator in Day-Ahead Electricity Markets Under Uncertainty*" IEEE Tran. Pow. Sys.,* vol. 30, pp. 2375–2385, 2015.
*[60] Z. Xu, et. al., "*Risk-Averse Optimal Bidding Strategy for Demand-Side Resource Aggregators in Day-Ahead Electricity Markets Under Uncertainty*" IEEE Tran. Sma. Gr.,* vol. 8, pp. 96–105, 2017.

*[61] S. Ghavidel, et. al., "*Risk-Constrained Bidding Strategy for a Joint Operation of Wind Power and CAES Aggregators*" IEEE Tran. Sus. Ene.,* vol. 11, pp. 457–466, 2020.
*[62] C. A. Correa-Florez, et al., "*Optimal Participation of Residential Aggregators in Energy and Local Flexibility Markets*" IEEE Tran. Sma. Gr.,* vol. 11, pp. 1644–1656, 2020.
*[63] C. Chen, et. al., "*wholesale market Participation of DERAs: DSO-DERA-ISO Coordination*" IEEE Tran. on Pow. Sys.,* vol. 39, pp. 6605-6614, 2024.
*[64] H. S. Moon, et. al., "*Prequalification Scheme of a Distribution System Operator for Supporting wholesale market Participation of a Distributed Energy Resource Aggregator*" IEEE Acc.,* vol. 9, pp. 80434–80450, 2021.
*[65] X. Chen, et. al., "*Aggregate Power Flexibility in Unbalanced Distribution Systems*" IEEE Tran. on Sma. Gr.,* vol. 11, pp. 258-269, 2020.
*[66] D. Koraki and K. Strunz, "*Wind and Solar Power Integration in Electricity Markets and Distribution Networks Through Service-Centric Virtual Power Plants*" IEEE Tran. Pow. Sys.,* vol. 33, pp. 473–485, 2018.
*[67] H. K. A. Parthasarathy, et al., "*Operational DER Scheduling Tool for Unbalanced Distribution Systems Considering Watt-VAr Controllers of PV Smart Inverters*" 2023 NAPS, NC, USA,* pp. 1-6
*[68] H. K. A. Parthasarathy, "*A Unified Mode Selection Framework for DER Scheduling Tool Considering Unbalanced Distribution Systems*"* Order No. 31336937*, Arizona State University, United States* -- Arizona, 2024.
*[69] M. Ghaljehei and M. Khorsand, "*Day-ahead Operational Scheduling with Enhanced Flexible Ramping Product: Design and Analysis*" IEEE Tran. Pow. Sys.,* pp. 1–1, 2021.
*[70] M. Ghaljehei and M. Khorsand,"*Representation of Uncertainty in Electric Energy Market Models: Pricing Implication and Formulation*" IEEE Sys. J.,* vol. 15, pp. 3703–3713, 2021.
[71] W. E. Hart, et al.. "Pyomo: modeling and solving mathematical programs in Python." *Math. Prog. Comp.* 3(3) (2011): 219-260
*[72] IBM Decision Optimization, "*IBM Decision Optimization CPLEX Modeling for Python*", Available: https://ibmdecisionoptimization.github.io/docplex-doc/#.*
*[73] M. Abadi, et al.. "*TensorFlow: Large-scale machine learning on heterogeneous systems." 2015*, Available: tensorflow.org.*
[74] IEEE 118 bus test system, 2015*, Available: motor.ece.iit.edu/Data/118bus_ro.xls*
[75] "Iowa Distribution Test Systems", *Available: http://wzy.ece.iastate.edu/Testsystem.html.*
*[76] CAISO, "*Today's Outlook*", Available: http://www.caiso.com/TodaysOutlook/Pages/default.aspx.*

Part III

Stable and Fair Uniform Price Allocations of Community Aggregation Gains in Retail Electricity Markets

Shmuel S. Oren
Tomas Valencia Zuluaga, Graduate Student

University of California Berkeley

For information about this project, contact

Shmuel S. Oren
University of California Berkeley
Department of Industrial Engineering and Operations Research
4141 Etcheverry Hall
Berkeley, CA 94720
Phone: (510)-908-3102
Email: oren@ieor.berkeley.edu

Power Systems Engineering Research Center

The Power Systems Engineering Research Center (PSERC) is a multi-university Center conducting research on challenges facing the electric power industry and educating the next generation of power engineers. More information about PSERC can be found at the Center's website: http://www.pserc.org.

For additional information, contact:

Power Systems Engineering Research Center
Arizona State University
527 Engineering Research Center
Tempe, Arizona 85287-5706
Phone: 480-965-1643
Fax: 480-727-2052

Notice Concerning Copyright Material

Table of Contents

List of Figures

List of Tables

1. Introduction

This report addresses two specific research tasks that fall under the scope of project M44 that were performed at UC Berkeley. Detailed descriptions are given below.

- In Chapter 2, we consider the case of a Wind Power Producer (WPP) who wants to install a Battery Energy Storage System (BESS) on site to mitigate the uncertainty in the production of electric power by firming its output and thereby increasing revenue. The WPP is interested in finding the optimal size to maximize their long-term average profit. We propose a modeling framework in which the wind power output of the plant and the market prices of eletricity are modeled as a joint Markovian stochastic process. The ergodicity of the process is exploited to reduce the expression of the infinite-horizon average profit to a low-dimensional function that can be optimized numerically. Special attention is paid to the case where market prices are constant, i.e. the WPP sells its power through forward contracts. A full solution of the model is derived in that case, and a numerical implementation is presented to illustrate how the model lends itself to performing sensitivity analyses.

  The contributions of this chapter are: a stylized Markovian stochastic model for battery sizing of colocated storage in WPPs; a solution method for the aforementioned model in the case with constant prices via a bridge between a recent algorithm for numerically computing limiting distributions in multiregime fluid queues; and initial results in characterizing the optimal control policy for BESSs for the case with variable prices, potentially providing a path towards a usable implementation for that case as well. A substantial part of the results of this chapter were published in [1].

- In Chapter 3, we consider a problem of stable and fair market design in Community Choice Aggregation (CCA) settings. We adopt an existing cooperative game model from the literature to distribute the collective savings resulting from aggregation of demand in a group of prosumers at the retail level, and make several major theoretical contributions to improve it and complement it. First, we characterize a set of allocations of interest, which we call *uniform price stable allocations*, and prove that they are guaranteed to exist. Moreover, we propose a computationally scalable methodology, based on solving a pair of primal, dual Linear Programs (LPs), to find a uniform price stable allocation. Next, we illustrate that uniform price allocations may not be unique and may not be equally preferred by a social planner. We propose an optimization framework for selecting the most-preferred uniform price allocation. Finally, we show that although a computationally efficient and scalable methodolgy for exactly solving the optimization problem proposed is not available at the moment, satisfactory and computationally tractable solutions can be obtained via sampling by bridging existing results from the statistical learning literature. Most of the chapter is dedicated to studying the

deterministic case, but a stochastic version that takes into account the uncertainty induced by renewable sources and demand is also discussed.

The results of this chapter are under consideration for publication at the time of publishing of this report. A part of the results of this chapter were presented in [2].

2. A Markovian model for optimal sizing of colocated storage for wind power production [1]

Abstract

We propose a high-level stochastic steady-state model to analyze the value of co-located energy storage systems for wind power producers that participate in an electricity market through forward contracts and use storage to unlock access to capacity payments. In particular, we try to find optimal storage and contract sizing, as well as stationary operating policies for profit maximization in the long-run. We propose a stylized model calibrated to actual wind power production that allows us to obtain limiting distributions of battery storage levels, assess the value of storage size and perform a sensitivity analysis on key parameters such as contract prices, capacity payments and storage efficiency. We develop the case with contracts of constant price, outline how this model can be extended to a variable-price setting and discuss potential challenges in that avenue.

Acknowledgments

We are grateful to Professor Nail Akar of Bilkent University in Ankara, Turkey, for making us aware of the improved method of [5] and for generously sharing his code implementation of it with us, which we have used for obtaining the results presented here.

2.1 Introduction

The impending consequences of climate change have driven massive proliferation of Renewable Energy Sources (RES) around the world. However, a key obstacle to large-scale integration of RES in power systems is the short-term uncertainty and variability of their output. This poses both technical challenges for the reliable operation of the power system and financial challenges for investors in RES, since it is hard to guarantee a reliable income flow without RES incentives through policies such as feed-in tariffs and mandatory contracting for retailers. Such policies however are not sustainable and are being challenged due to their cost to consumers; many systems are now moving toward imposing scheduling requirements and forward commitments on RES forcing them to compete on a level playing field with other resources. The addition of BESSs to renewable power plants can help mitigate their uncertainty and thus can help towards solving both the technical and financial issues. While it is intuitive to understand how storage can mitigate uncertainty, sizing and

[1] A substantial part of the text that constitutes this chapter was published in *IEEE Transactions in Energy Markets, Policy and Regulation* under the name "Data-Driven Sizing of Co-located Storage for Uncertain Renewable Energy", authored by Tomas Valencia Zuluaga and Shmuel S. Oren [1]. An early version of that manuscript was presented as a conference paper at the 2022 IREP Conference in Banff, Canada. The conference paper was published in [3]. This chapter has also been published in the doctoral thesis of Tomas Valencia Zuluaga [4]

managing BESSs is not obvious.

Optimizing contracting and operation for intermittent power plants has been a very active research topic in both theory and application. In [6], a theoretical analysis is performed for the case of a wind farm that uses storage to optimize its bidding strategy on the day-ahead market in order to minimize imbalance penalties. In this, and other works that study the behavior of WPPs in day-ahead markets [7, 8], it is observed that the optimal bidding strategy for WPPs takes the form of an optimal fractile, as in the solution to the well-known Newsvendor problem. This highlights the fact that the bidding problem of a WPP is a *reverse* newsvendor problem, where the uncertainty lies not on the demand but on the supply side.

There are also numerous references that address the issue of optimal sizing and optimal management of co-located energy storage. In [9], the infinite-horizon average cost of electricity purchases is minimized by finding an optimal storage management policy and optimal storage size for a power plant that serves a local demand and purchases any shortfall from the grid in presence of dynamic pricing. The authors prove the optimality of a dual threshold policy , reminiscent of optimal (s,S) policies for inventory control. In [10], the optimal size of a BESS is found for a grid-connected photovoltaic system that can purchase and sell energy from the grid under time-of-use pricing, and the convexity of profit in storage size is shown. In [11], the value of co-located storage is analyzed for the case of the UK market as subsidies are phased out by comparing different contracting schemes with help of a model using stochastic differential equations describing wind power production and prices.

The application of high-scale, steady state models, such as fluid queues, to energy storage remains relatively rare. Fluid queue models provide a method to characterize steady-state behavior of a fluid container whose intake/outlet operates stochastically under certain conditions, without need for Monte Carlo simulations, which is relevant for long-term decisions such as sizing said container, as we do in this work. Limiting distributions for fluid queue models have been most commonly used in high-speed communication networks, but also for manufacturing [12], and energy systems, with early applications in hydro dam management models [13]. In an approach qualitatively similar to ours, in [14], a two-state Markov-Modulated Fluid Queue (MMFQ) is used for optimizing the size and management policy of the US national strategic petroleum reserve.

There are also more recent applications of fluid queue models to renewable power plants with BESSs. In [15], a model-predictive control algorithm is proposed for optimally sizing and managing storage, and the MMFQ framework is used to analyze the reliability performance of the method. In [16], the authors consider a case in which there is no control over the charge/discharge rate (akin to a balancing policy), and use MMFQs to find an asymptotic relation between the battery size and the loss of load probability for a given grid configuration, so that the problem of finding the optimal size of storage to hit a target loss-of-load probability can be solved. Unlike in these cases, here we use the MMFQ framework in the objective function of our optimization model directly.

While short term operation of co-located storage can be optimized using dynamic programming

techniques and accounting for current information on state of charge, wind forecast and prices, the optimal sizing of the co-located storage is based on long run average behavior of the production/storage system under an optimized stationary policy. For this purpose we employ a method based on the spectral analysis for characterizing limiting distributions of n-dimensional MMFQs described in [12, 17]. This is a numerically challenging problem for which algorithms with proven numerical stability have been developed [18, 19], but with the limitation of having a single state with negative drift, too restrictive for our setting. In [20], an algorithm is proposed for calculating limiting distributions of MMFQs without solving any eigenvalue problems, and was improved and extended to also handle multi-regime fluid queues in [5], which we use in our approach. The method employed there makes no assumptions regarding the structure of the fluid queue, which is a key feature for general application models like ours.

In this chapter, we use limiting distributions directly to obtain simple expressions of long-run profits of the system, suitable for use in a sensitivity analysis. In particular, we are interested in investigating the effect of some key parameters such as available contract prices on the financial outcome of the project, the optimal storage size and the optimal contract size of a wind power plant trying to maximize its profit. This simple model would be of interest to a wind power plant operator and project developer for early-stage project feasibility analysis. It could also be of interest for policy designers, to evaluate the financial viability of storage projects for wind power plants with and without special incentives.

There are several examples of modeling wind speed and wind power output as a Markov chain in the literature, with applications in simulation of wind data series [21–23] but also in long-run analysis [15, 16]. It has been found that performing a max likelihood parameter estimation can result in a very good approximation of the limiting distribution, but that a key metric to obtain a more accurate model is the autocorrelation [24]. In [24], in the context of co-located storage sizing for robust operation of microgrids, it is found that Markovian models with an autocorrelation that poorly reflects that of the original data series can lead to underestimation of necessary storage by as much as 50%. Autocorrelation performance can be improved by increasing the order of the Markov chain, but this increases the size of the state space exponentially, so that only chains of second or third order are of practical relevance. In [25], a rolling-average method is proposed to obtain higher autocorrelation performance in the lower range (0-6h) without increasing the size of the state space. More recently, authors have proposed non-homogeneous Markov chains [23,26] to more accurately reproduce the autocorrelation of real data series, with much better results replicating the daily behavior of wind (i.e. the autocorrelation around integer multiples of 24h). These results can also be leveraged to capture seasonal changes of longer duration in the wind distribution. The expected range of optimal storage sizes should also inform the decision of how much autocorrelation needs to be captured by the model. If these sizes lie in the 0-6 hour range, capturing daily autocorrelation is less crucial than if storage is expected to be in the 24h+ range.

We could find no references in the literature of modelling wind power production and electricity prices as a joint Markov chain as our general framework proposes, but the discussion above provides what we deem sufficient justification for our modelling of wind power output as such a

process in the constant prices case that is addressed in this chapter, as supported by the empirical results shown in Section 2.4.1. We do not claim that a Markovian assumption is appropriate to find the actual day-to-day operating policy of a wind power plant with co-located storage. As mentioned above, dynamic programming approaches (possibly with reinforcement learning) that utilize updated status and forecasts are best-suited for those purposes (see e.g. [15]). However, for investment planning, a simpler, higher-level representation is not only appropriate but necessary to get a tractable and thus useful model. This is not in essence different from other commonly performed simplifications, just as unrealistic but widely accepted, like using linear regressions to represent complex socio-economic dynamics in the context of capacity expansion. We leave a more thorough discussion of the variable-price case for future work in which that version of this model is developed.

The remainder of this chapter is organized as follows. Section 2.2 describes the setting for our problem. In Section 2.3, we present in detail our optimization model, as well as the solution algorithm. Results are presented and discussed in Section 2.4. Section 2.5 presents an exploration of the path to obtain a full solution in the case of long-term contracts with variable prices (supply functions). Finally, we conclude and discuss possible next steps for the development of this model in Section 2.6.

2.2 Problem setting

We consider the case of a WPP that participates in the wholesale electricity market and has access to a long-term forward market. The WPP is also evaluating the construction of a collocated BESS, which will be used to mitigate imbalance costs. In our setting, the wind farm operator needs to answer two main questions: how much storage should be installed and how much energy should be sold in a long-term contract. To answer these questions, it is also relevant to determine a stationary management (charge/discharge) policy for the BESS. Further aspects of our setting are described in more detail in the paragraphs below.

We consider that the WPP is a price-taker in the long-term forward market, where it has access to three contracts:

1. A long-term fixed quantity contract, where it can choose how much to sell for a fixed price in every period of the wholesale electricity market.

2. A pay-as-demanded forward contract, which can be used to cover any shortfall in generation with respect to the commitment in contract 1.

3. A pay-as-produced forward contract, which can be used to sell any excess generation with respect to the commitment in contract 1.

In order to avoid arbitrage opportunities, which cannot exist in efficient markets in the steady-state case considered here, contract 2 must have a higher price than contract 1 and contract 3 must have

a lower price than contract 1.

In this setting, the WPP commits to delivering any quantity up to its capacity before the actual output, over which he has no control, is known. An imbalance penalty is paid for the difference between the energy commitment and the actual energy delivered. The case studied here is the special case where the commitment is the same for all periods, the imbalance penalty for shortfall is non-negative and constant, and the imbalance penalty for surplus is non-positive (i.e. it is a reward, not a penalty) and constant.

To mitigate the imbalance cost, the wind power producer can charge/discharge the BESS, so that the net output of the plant, i.e. that perceived by the market is the combined production of the wind farm and the BESS. Having a co-located BESS will have the effect of firming the WPP's energy output, thus giving it access to the capacity market. We also include this source of income in our model, by considering that the WPP is a price taker in the capacity market and is remunerated for the capacity committed in contract 1, derated by the long-run probability of not honoring that contract.

The scope of our work is a high-level analysis that could be of interest for early-stage project developers or policy makers. We are interested in looking at infinite-horizon average profits by considering the steady-state behavior of the model proposed and performing sensitivity analyses on a number of key parameters. To be consistent with this approach, we do not consider the possibility of using storage for arbitrage, since planned use of capacity for opportunistic arbitrage would not be profitable in the long run if the market is efficient.

Admittedly, this is a limited representation of real electricity markets, where producers can and do participate simultaneously in different ways: short-term arbitrage, ancillary services, and a sequence of medium-term forward contracts to name a few. However, in the long-run efficient equilibrium, a long-term contract price will adjust so that participation through the scheme modeled here will be equivalent to the other forms available to the WPP. In essence we invoke here a no arbitrage principle, which should hold in a long run equilibrium, implying financial equivalence of any market participation mode of a fully utilized production/storage facility. This equivalence enables us to choose the most convenient market participation mode for the purpose of our analysis even if in reality the resulting production/storage facility will participate in the market differently. Hence, there are two direct interpretations of the assumptions used in our model: the forward contract is assumed to always renew at maturity with identical conditions, or, alternatively, it is a long-term forward contract with a price that makes the contract equivalent to a sequence of contracts with shorter maturities or any other form of efficient market participation (that does not leave money on the table).

This raises the question of whether the results obtained by the model presented here are applicable to actual market participants who may not have a long-term contract but rather sequence of forward contracts with shorter maturity and possibly changing prices and quantities. The possible changes in future forward prices can be accounted for through sensitivity analyses on the price of the con-

tract, that our method allows. We are also assuming that efficient utilization of a production/storage facility under a long term contract involves capturing of capacity payments, if available, which is consistent with commitment not changing significantly across subsequent forward contracts. For WPPs that participate through a more varied combination of market mechanisms (arbitrage, balancing, etc.), it is more of an open question whether this model will be directly applicable, although this model will still be of interest.

Our approach suggests the assumption of existence of a long-run equilibrium in the forward market, which depends on many factors that are not considered in our model, such as long-run demand behavior and a stabilization of the cost of new capacity (which in the case of storage, for instance, is actually expected to continue declining for some years [27]). We do not make any such strong assumptions. While such an equilibrium may be far from being reached, this model is a high-level analysis for which this coarse approximation of reality is sufficient.

Finally, we do not specify any particular battery technology. We include in our analysis the issues of charge/discharge conversion efficiency and energy dissipation. However, we do not include the degradation of the battery because of usage and aging in our model. It has been found that this can be an important characteristic to take into account in sizing studies [11], so this could be an interesting feature to add to future versions of our model. In our closing remarks in Section 2.6.1 we discuss how considering this issue could affect our model and outline how this feature could be included in an extension, but otherwise consider this topic out of the scope of this project.

2.3 Mathematical Model

2.3.1 Description of the model

To emphasize the flexibility of our model and lay the groundwork for a future extension, we describe first the model of a forward contract that allows variable prices, and then focus on the special case addressed in this chapter.

The energy market

We consider a market in which the WPP is a price taker, so it commits to produce an amount q_t (in MWh) during market period t at a price p_t (in \$/MWh), which is known at the time the commitment is made. During period t, the actual wind power output of the farm is w_t (in MWh), while r_t is the amount energy injected into the BESS ($r_t < 0$ if the energy is extracted), so that the net output of the plant is $w_t - r_t$. The imbalance is $y_t = q_t - (w_t - r_t)$ and the imbalance penalty charged to the WPP is $\Xi_t = \Xi(y_t, p_t)$. We assume $\Xi(\cdot)$ to be a known, deterministic, time-invariant function of the imbalance and the energy price. The profit Π_t at period t is thus given by (2.1).

$$\Pi_t = p_t q_t - \Xi(y_t, p_t) \tag{2.1}$$

For the case with constant prices, p_t is constant and $\Xi(\cdot)$ is defined by (2.2). Note that the negative

sign in front of κ' implies that the WPP is not penalized for excess injection, but, on the contrary, sells it on the forward market. To avoid arbitrage opportunities, with $\kappa', \kappa \geq 0$, we must have $\kappa' < 1$ and $\kappa > 1$.

$$\Xi(y_t, p_t) = \begin{cases} \Xi^+(y_t, p_t) = -\kappa' p_t y_t & \text{if } y_t \geq 0 \\ \Xi^-(y_t, p_t) = \kappa p_t y_t & \text{if } y_t < 0 \end{cases}. \tag{2.2}$$

The capacity market

The WPP is also assumed to be a price taker in the capacity market. We define here capacity payments for the case with constant prices, i.e. $q_t = q$, and note that this definition would need to be extended to handle variable prices. The WPP is remunerated periodically (for simplicity, we assume hourly) for the capacity committed for sale in forward contracts at a price p^{cap} (in \$/(MW·h)). This committed capacity is derated by the historic probability of not honoring the contract, which in our model corresponds to the steady-state probability of being in shortfall. The capacity payment Π^{cap} is thus given by (2.3)

$$\Pi^{cap} = p^{cap} \cdot q \left(1 - \lim_{t \to \infty} \mathbb{P}(y_t < 0)\right) \tag{2.3}$$

The BESS

Let ρ_c and ρ_d be the conversion efficiencies of charge and discharge respectively. Thus, the round-trip efficiency is $\rho = \rho_c \rho_d$. The quantity r_t is measured from the exterior of the BESS, so the energy effectively injected to the battery is $\rho_c r_t$ (for $r_t > 0$) and the energy effectively extracted from the battery is $-r_t/\rho_d$ (for $r_t < 0$).

The capacity (size) of the battery is b (in MWh) and its power inversion capacity, i.e. the maximum rate at which energy can be charged to or discharged from the battery, is g (in MW). For simplicity, we assume the limit is the same for charging and discharging, but the method can easily be extended to consider the asymmetric case. In order to determine an optimal size, we need to model the cost of installing and operating the battery. We break it down into a cost for storage capacity and a cost for inversion capacity. Both are expressed as linear, amortized costs and are denoted by c_s in \$/(MWh·h) and c_p in \$/(MW·h) respectively. By doing this, we assume that the battery is replaced at the end of its lifetime with the same capacity and at the same cost.

An important factor in BESSs is energy dissipation, i.e. the proportion of energy stored in the BESS that is spontaneously lost without any charging or discharging performed. This is usually expressed as a fraction η of stored energy per unit time, which is the representation adopted in our model, with some limitations described in section 2.3.2.

Objective

In the previous paragraphs, we have referred to t as a period for ease of exposition, given its similarity with standard electricity markets. However, we propose here a continuous-time model, so t actually, and in all instances in the remainder of this document, refers to an instant, and, consequently, the quantities q_t, w_t, r_t represent power levels at time t (in MW). Note that the price p_t is indeed in \$/MWh, so that our profit Π_t is an instantaneous profit rate at time t, in \$/h.

We are interested in the long-run average profit Π, as defined in (2.4). The expectation is taken with respect to the stochastic process of interest here, (w_t, p_t), as described next.

$$\begin{aligned}\Pi &= \lim_{T\to\infty} \mathbb{E}\left[\frac{1}{T}\int_0^T (\Pi_t + \Pi^{cap})\, dt\right] - c_s b - c_p g \\ &= \Pi^{cap} + \lim_{T\to\infty} \mathbb{E}\left[\frac{1}{T}\int_0^T \Pi_t dt\right] - c_s b - c_p g \end{aligned} \tag{2.4}$$

Sources of uncertainty

We consider two sources of uncertainty in our model: wind power output and energy prices. This is done by considering (w_t, p_t) as a joint continuous-time stochastic process. In particular, we model it as a Continuous-Time Markov Chain (CTMC) with a discrete state space $\mathscr{S} = \mathscr{W} \times \mathscr{P}$, with $\mathscr{W}$ and $\mathscr{P}$ being the discrete state spaces of w_t and p_t respectively. This stylized model allows for a convenient formulation of limiting distributions, as described in the next subsection.

Optimization model

Putting the previous pieces together, we are interested in solving the infinite-horizon average profit optimization problem in (2.5).

$$\begin{aligned} \max_{q_t, r_t, b, g} \quad & \Pi \\ \text{s.t.} \quad & b, g \geq 0, \\ & q_t \in [0, W]\ \forall t, \\ & q_t, r_t, b \in \mathbb{R}\ \forall t \end{aligned} \tag{2.5}$$

W is the plant capacity (in MW). Furthermore, we intend here to model an electricity market, so we will restrict our analysis to stationary policies where the bid is a function of the price, i.e. $q_t = q(p_t)$. We can also write this as $q_t = q^s$ when $p_t = p^s$, for $s \in \mathscr{S}$.

Finally, we will also be interested in stationary charge-discharge policies $r_t = r(w_t, q_t, p_t)$, which

we write $r_t = r(w_t, q_t, p_t) = r^s$ when $(w_t, q_t, p_t) = (w^s, q^s, p^s)$. We must note, however, that this definition must be overriden if the storage is empty or full as summarized below.

$$r^s > 0 \text{ \& storage full } \Rightarrow r_t = 0$$
$$r^s < 0 \text{ \& storage empty } \Rightarrow r_t = 0$$

In this chapter, we focus on cases where strategic storage of wind-generated energy is not attractive because prices and imbalance penalties are constant in time. For this case, it is known that the optimal (cost-minimizing) policy is a balancing policy, i.e. $r^s = w^s - q^s$ [7, 9]. It is not hard to see that this is still true in the presence of capacity payments, since any deviation will only increase the amount by which the committed capacity is derated and hence reduce capacity payments. Coupling this policy with the finite power inversion capacity gives (2.6).

$$r^s = \max\left(\min\left(w^s - q^s, g\right), -g\right) \tag{2.6}$$

2.3.2 Steady-state analysis

By the ergodicity of CTMCs, and since we are restricting our analysis to stationary policies, we can express the long-run average profit of (2.4) in terms of limiting distributions as in (2.7). In words, the long-run average profit is the sum over all states of the income minus the imbalance penalty, for which there are two cases: if storage is available, the policy can be followed; if storage is not available (empty or full), the policy must be overriden.

$$\begin{aligned}
\Pi =& \Pi^{cap} + \sum_{s\in\mathscr{S}} \Big(p^s q^s \pi^s - \psi^s \Xi^s (q^s - w^s) \\
& - (\pi^s - \psi^s) \Xi^s (q^s + r^s - w^s) \Big) - c_s b - c_p g \\
=& \Pi^{cap} + \sum_{s\in\mathscr{S}} \Big(p^s q^s \pi^s - \psi^s \kappa p^s (q^s - w^s)^+ \\
& + \psi^s \kappa' p^s (w^s - q^s)^+ - (\pi^s - \psi^s) \kappa p^s (q^s + r^s - w^s)^+ \\
& + (\pi^s - \psi^s) \kappa' p^s (w^s - q^s - r^s)^+ \Big) - c_s b - c_p g
\end{aligned} \tag{2.7}$$

, where r^s is given by (2.6), $\pi = (\pi^s)_{s\in\mathscr{S}}$ is the limiting distribution of the CTMC (w_t, p_t) and $\psi = (\psi^s)_{s\in\mathscr{S}}$ is the long-run probability of storage unavailability (empty or full). The second equality is obtained by plugging in the definition of the imbalance in (2.2).

We present first the case with uncapacitated power conversion ($c_p = 0$ so that g can be made as large as necessary to make $r^s = w^s - q^s$); the capacitated case is presented at the end of this section. In this

uncapacitated case, since the optimal charge/discharge policy is balancing the output, $q^s + r^s - w^s = 0$ whenever storage is available, so that we can simplify (2.7) and obtain (2.8).

$$\begin{aligned}\Pi =& \Pi^{cap} + \sum_{s\in\mathscr{S}} \Big(p^s q^s \pi^s - \psi^s \kappa p^s (q^s - w^s)^+ \\ &+ \psi^s \kappa' p^s (w^s - q^s)^+ \Big) - c_s b \end{aligned} \tag{2.8}$$

$\boldsymbol{\pi}$ can be easily determined from the generator of the CTMC (w_t, p_t). The long-run probability of unavailable storage ψ can be determined from some results of fluid queue theory, as shown next.

Limiting distribution

Our model corresponds to the model of a Markov-modulated fluid queue with finite buffer. A characterization of the long-run distribution of this process can be obtained through spectral analysis, which we overview next. This is based on the presentation in [17], with more details of the proofs available in [12]. For ease of exposition, in the following overview we omit the efficiency factor ρ.

Define $\mathbf{r} = [r^s]_{s\in\mathscr{S}}$, a vector with the discrete values taken by r_t, $\mathbf{D} = \text{diag}(\mathbf{r})$, a diagonal matrix with $\mathbf{r}$ in its diagonal. In the field of fluid queues, $\mathbf{r}$ is called the drift vector. We assume for now that $r^s \neq 0 \forall s \in \mathscr{S}$. The special case with $r^s = 0$ is considered at the end. Let $\mathbf{Q}$ be the infinitessimal generator matrix of the CTMC and $\mathbf{F}$ the limiting distribution of the level state of the battery, i.e.: $F(x,s) = \lim_{t\to\infty} \mathbb{P}\Big(X_t \leq x, (w_t, p_t) = s\Big)$, $\mathbf{F}(x) = [F(x,s)]_{s\in\mathscr{S}}$. Then, it can be shown [17] that $\mathbf{F}$ satisfies the differential equation

$$\frac{d\mathbf{F}}{dx}\mathbf{D} = \mathbf{F}\mathbf{Q} \tag{2.9}$$

with boundary conditions

$$\begin{aligned} F(0,s) &= 0 \text{ if } r^s > 0 \\ F(b,s) &= \pi^s \text{ if } r^s < 0 \end{aligned}$$

A spectral solution to these equations can be obtained introducing generalized eigenvalues λ and eigenvectors $\mathbf{u}$, so that $\lambda\mathbf{u}\mathbf{D} = \mathbf{u}\mathbf{Q}$. The general solution to (2.9) takes then the form

$$\mathbf{F}(x) = \sum_{i=1}^{|\mathscr{S}|} a_i \exp(\lambda_i x)\mathbf{u}^i$$

, where the values of coefficients a_i can be found by solving a linear system from the boundary conditions. For brevity in later use, we denote $\psi_0^s = F(0,s)$, $\psi_f^s = F(b,s)$ and $\psi^s = \psi_0^s + \psi_f^s$.

In this manner, the long-run probability of unavailable storage can be calculated as a function of $\mathbf{r}$ and b. Note, however, that the method requires solving a generalized eigenvalue problem, which has three implications of importance for our work. First, we cannot obtain a closed-form expression of ψ_0 or ψ_f in terms of b and $\mathbf{r}$, so that numerical calculating approaches are necessary. Secondly, this function is not convex in general, which makes our optimization problem possibly non-convex as well. Finally, the linear system posed by the boundary conditions can be very ill-conditioned because of the presence of both very large and very small eigenvalues, which is a major challenge for the method. We address this in more detail in the description of the algorithm.

Cases with zero drift

If $r^s = 0$ for some state $s \in \mathscr{S}$, then $F(x,s)$ can be expressed as a linear combination of $F(x,z)$ for states $z : r^z \neq 0$. Thus, for these cases, the method described above is performed on a reduced system that includes only states $\{z : r^z \neq 0\}$. Then those values are used to find the distribution for the null states. Details are omitted here, but can be found in the appendix of [19] or in [5].

Dissipation

We next address the issue of modelling dissipation. As mentioned before, it is standard to consider that energy dissipates from the battery at a rate that is a fix multiple of the current storage level. This would mean that an additional term should be included in the drift vector: $r_t = r^s - \eta x_t$, where x_t is the current storage level in the battery (in MWh), and η is the proportion of energy stored lost per unit time (here, per hour). The addition of this term makes the drift dependent on the storage level, so that the spectral analysis performed earlier would no longer be valid.

A way to handle this within the framework of fluid queues is through multi-regime fluid queues. The key idea here is that the battery capacity is divided in bins (discretized), with drifts allowed to variate across different bins, but being level-independent within each bin. Introducing some notation, this can be expressed as in (2.10). Then, a system of ordinary differential equations like in (2.9) can be formulated for each bin, with additional boundary conditions for inter-bin boundaries.

$$\begin{aligned} r_t &= r(w_t, q_t, p_t, x_t) \\ &= r^{s,j} \text{ for } (w_t, q_t, p_t) = (w^s, q^s, p^s),\ b_{j-1} \leq x_t < b_j \end{aligned} \tag{2.10}$$

, where the BESS is divided into J bins with boundaries $0 = b_0 < b_1 < \cdots < b_{J-1} < b_J = b$. Note that this significantly increases the dimension of the eigenvalue problem, so that having a numerically stable method to find the limiting distribution becomes paramount for the success of this method. For brevity, we don't describe this modification of the approach in further detail and point the interested reader to [17] or [5].

The introduction of $\eta > 0$ could affect the optimality of the balancing policy. Indeed, for sufficiently large η, it could be more profitable to sell surplus energy immediately than to store it and

have a large proportion of that lost to dissipation. To simplify our analysis, we make the following restriction: we make a sensitivity analysis on η with $\kappa' = 0$ and a sensitivity analysis on κ' with $\eta = 0$, so that the balance policy is optimal for all these situations.

2.3.3 Units

In the previous paragraphs, we defined all quantities in their appropriate physical units. However, it is more convenient and illustrative for the purposes of this work to express them in per unit of power plant capacity and storage capacity, by introducing:

$$\begin{aligned} \mathbf{w} &= \tilde{\mathbf{w}}W & q &= \tilde{q}W & b &= \tilde{b}W \\ g &= \tilde{g}W & \mathbf{r} &= \tilde{\mathbf{r}}b & c_s &= \tilde{c}_s p^{max} \\ p &= \tilde{p}p^{max} & p^{cap} &= \tilde{p}^{cap} p^{max} & c_p &= \tilde{c}_p p^{max} \end{aligned}$$

, with $p^{max} = \max \mathscr{P}$, so that $\tilde{\mathbf{w}}, \tilde{q}, \tilde{p}, \tilde{g} \in [0,1]$, $\tilde{b}$ is in hours of storage of full plant capacity, and $\tilde{\mathbf{r}}$ is in units of [p.u. of b]/h, which is interpreted as the number of times that the total storage would be charged starting from an empty state in one hour at full plant capacity. Equation (2.8) becomes:

$$\frac{\Pi}{p^{max}W} = \frac{\Pi^{cap}}{p^{max}W} + \sum_{s\in\mathscr{S}} \left(\tilde{p}^s \tilde{q}^s \pi^s - \psi^s \kappa \tilde{p}^s (\tilde{q}^s - \tilde{w}^s)^+ + \psi^s \kappa' \tilde{p}^s (\tilde{w}^s - \tilde{q}^s)^+ \right) - \tilde{c}_s \tilde{b} \tag{2.11}$$

It is not hard to check that this change of units does not affect the spectral decomposition and hence the values of ψ. In this chapter we are interested in the case where the price is constant, i.e. $|\mathscr{P}| = 1$, $p^s = p^{max}\ \forall s \in \mathscr{S}$ and hence $\tilde{p}^s = 1$ for all s. Finally, for readability and ease of notation, the tildes will be omitted in the remainder of this chapter, but we will always refer to values in per unit.

With these unit changes and simplifications, the optimization model (2.5) for the uncapacitated case with constant prices is written as in (2.12).

$$\begin{aligned} \max_{q,b} \quad & \sum_{s\in\mathscr{S}} \left(q\pi^s - \psi^s \kappa (q - w^s)^+ + \psi^s \kappa' (w^s - q)^+ \right) \\ & + p^{cap} q \left(1 - \sum_{s\in\mathscr{S}} \psi_0^s \right) - c_s b \\ \text{s.t.} \quad & b \geq 0, \\ & q \in [0,1] \end{aligned} \tag{2.12}$$

2.3.4 Solution algorithm

There are two challenges in finding the optimal solution to problem (2.12). The first difficulty lies in evaluating the objective function. The spectral method described in Section 2.3.2 requires solving a linear system with coefficients that stem from both very large and very small exponential terms, which makes the system very ill-conditioned and the method numerically unstable.

This was overcome thanks to the algorithm proposed by [5], which uses a stable matrix decomposition to obtain the limiting distribution of fluid queues without explicitly finding eigenvalues or relying on exponentially growing terms and results on enhanced numerical stability. This method allows multi-regime fluid queues like the one in our model when considering non-zero dissipation and does not require any special structure in generator or drift.

The second difficulty is that we have a non-linear, possibly non-convex objective function, so that using a gradient descent algorithm does not provide a guarantee of global optimality. For the scenario with constant prices, our search space only has a dimension of 2; it is thus reasonable to start exploring the search space by means of a grid, to then use the best candidate as starting point for a finite-difference descent algorithm, which is the algorithm that was implemented in our tests.

2.3.5 Capacitated power conversion

We finally address the case with capacitated power conversion. In the capacitated case with symmetric capacities, $r^s = \max(\min(w^s - q^s, g), -g)$, so $q^s + r^s - w^s$ is not always 0 and (2.8) does not hold in general. We must therefore use the expression for Π given by (2.7). The computation of ψ is only affected by this change to the extent that the entries in $\mathbf{r}$ change, but the method itself is still valid, so the only consequence of this capacitation is having two more terms in the objective function and one extra decision variable, as well as changing the expression of the capacity payments, which would be now given by (2.13). We can, however, show with help of Theorem 1 that these changes do not make the optimization significantly more difficult.

$$\Pi^{cap} = p^{cap} q \sum_{s \in \mathscr{S}: w^s - r^s - q \geq 0} (\pi^s - \psi_0^s) \tag{2.13}$$

Theorem 1. *Let (q^*, b^*, g^*) be an optimal solution to optimization problem (2.5). If $c_p > 0$, then $g^* = \left| w^{s^*} - q^{s^*} \right|$ for some $s^* \in \mathscr{S}$ or $g^* < \min_s |w^s - q^s|$.*

Proof. If $g^* \leq \min_s |w^s - q^s|$, the statement clearly holds, so we only need to prove that if $g^* > \min_s |w^s - q^s|$, then $g^* = \left| w^{s^*} - q^{s^*} \right|$ for some $s^* \in \mathscr{S}$. We prove by contradiction.

Suppose $g^* > \min_s |w^s - q^s|$ but the statement does not hold. To create our contradiction, let $\tilde{s} \in \operatorname{argmax}_s \{|w^s - q^s| : |w^s - q^s| < g^*\}$ and let $\tilde{g} = \left| w^{\tilde{s}} - q^{\tilde{s}} \right|$. We want to show that the point $(q^*, b^*, \tilde{g})$ achieves a higher profit than (q^*, b^*, g^*), which would contradict its optimality. First, note that by construction of $\tilde{g}$, for any $s \in \mathscr{S}$, $\max(\min(w^s - q^s, \tilde{g}), -\tilde{g}) = \max(\min(w^s - q^s, g^*), -g^*)$. This

implies that the charge/discharge vectors in both cases are identical: $r(q^*, b^*, \tilde{g}) = r(q^*, b^*, g^*)$. Since ψ is a function of b and the drift vector, $\psi(b^*, \tilde{r}) = \psi(b^*, r^*)$. Thus, the terms inside the summation in (2.7) are identical for $\Pi(q^*, b^*, g^*)$ and $\Pi(q^*, b^*, \tilde{g})$. And hence, $\Pi(q^*, b^*, g^*) - \Pi(q^*, b^*, \tilde{g}) = c_p(\tilde{g} - g^*) < 0$, which concludes the proof. □

The takeaway from Theorem 1 is that we do not need to consider the entire feasible set spanned by g when optimizing (2.5), as only a handful candidate solutions need to be tried. We can thus define $\overline{\Pi}$ as in (2.14), and optimize for $\overline{\Pi}$ over $\mathbf{q}$ and b only.

$$\overline{\Pi}(\mathbf{q}, b) = \max_{s \in \mathscr{S}} \{(2.6) : g = |w^s - q^s|\} \tag{2.14}$$

For the case with constant prices, this takes the form of (2.15).

$$\begin{aligned} \max_{q,b} \quad & \overline{\Pi}(q, b) \\ \text{s.t.} \quad & b \geq 0, \\ & q \in [0, 1] \end{aligned} \tag{2.15}$$

To close this section, we make two comments about this method. First, each evaluation of $\overline{\Pi}$ requires $|\mathscr{S}|$ calls to the routine that calculates ψ. Thanks to the algorithm in [5], this routine is very efficient, so this calls are not very costly computationally. They can also be easily parallelized if several cores are available. Moreover, for the case with constant prices, $\mathscr{S}$ is the discretized state space of wind power outputs, which we expect would have a cardinality in the order of tens in most applications [25], keeping the computational cost of each evaluation of $\overline{\Pi}$ manageable. Finally, our tests suggest that when sorting $|w^s - q^s|$ in ascending order, expression (2.7) is concave in g. If this can be verified, it can further reduce the number of calls necessary to evaluate $\overline{\Pi}$, which could be of value in extensions to variable prices, where $|\mathscr{S}|$ may be larger.

And secondly, we note that the method outlined above only finds an optimal solution to (2.5) if the condition in Theorem 1 holds, i.e. if $g^* \geq \min_s |w^s - q^s|$. We make two observations to argue, omitting some mathematical details, that this would not be an issue in practical applications. Suppose the condition is not true. Then, the optimal solution has $g^* < \min_s |w^s - q^s|$, which implies $r^s = -g$ if $w^s - q^s < 0$ and $r^s = g$ if $w^s - q^s > 0$. Note also that g^* is upper-bounded by the mesh size of $\mathscr{W}$, so it is a relatively small value. This in turn implies that $q^s - w^s$ and $q^s + r^s - w^s$ are close to each other, which can also be said of the penalties $\Xi(q^s - w^s)$ and $\Xi(q^s + r^s - w^s)$. The summation term in (2.7) for this point would therefore be similar to that of the no-storage case. Since the case with storage must also take into account the cost terms, this can only be possible if both b^* and g^* are quite small. In other words, our method may fail to find the optimal solution in a case where the optimal solution would be to build a storage of positive, but very small size in both

Table 2.1: Reference values for sensitivity analyses

Parameter	Value	Parameter	Value	Parameter	Value
κ	1.35	c_s	0.005	η	0
κ'	0	c_p	5E-4	ρ_d	0.95
p^{cap}	0			ρ_c	0.95

energy capacity and power conversion capacity. Such a case can be constructed, but would not be of practical interest.

2.4 Results and discussion

2.4.1 Model data estimation

Wind model

To obtain the values of the generator matrix that defines the CTMC, the methodology outlined in [25] is followed. The methodology consists in first passing the wind power output through an averaging window of one hour, then discretizing the output with $N = 15$ levels, and finally performing a max-likelihood estimation on the resulting data sequence, i.e. finding the transition probabilities from counting transitions in the sequence. The number of states chosen is identified in [25] as a level of resolution that captures well the autocorrelation of the wind power series used as data source without the need for introducing a second-order Markov model. As in [15], the wind data available in [28] was used.

Reference parameters

We perform sensitivity analyses on the other model parameters. Reference values are given in Table 2.1. We comment on the choice of the reference cost of storage in the following paragraphs.

Empirical validation

To provide an empirical reference for comparison with our model, we use the same data series to solve the ex-post sizing and contracting optimization problem (2.16).

$$\begin{aligned} \max_{q,b,g} \quad & h(q,b,g) \\ \text{s.t.} \quad & b,g \geq 0, \\ & q \in [0,1] \end{aligned} \tag{2.16}$$

, where $h(q,b,g)$ is a function that computes the ex-post average profit over the time available in the data series for contract quantity q and storage size b. The value of function g can be computed easily using the fact that the the balancing policy is known to be optimal.

The results of the model (2.12) and (2.16) are shown in Figure 2.1 and discussed below. In terms of model validation, it is worth mentioning that there is a good level of agreement between the curves given by the model and the empirical ex-post best. An interesting continuation of this work would be to perform a similar analysis using a non-homogeneous Markov chain to model the wind power output as in [23, 26].

2.4.2 Value of storage

As a first step before doing sensitivity analyses, we are interested in observing the value of storage for the WPP in the setting described. To do this, we fix b and g at different values and solve (2.12) and (2.16) for q only to find the optimal commitment and corresponding profit. The profit is compared to the profit that would be obtained from a feed-in-tariff contract with the same price. For the case without capacity payments, this profit is an upper-bound reference for comparison.

We can make four important observations from the results in Figure 2.1. First, without capacity payments, as expected, even with unlimited storage, recovering feed-in-tariff profits is not possible, which is explained by efficiency losses in storage discharge. If there is access to capacity payments, the additional profits are higher, but the overall shape of the value curve remains unchanged. Secondly, we note that the optimal bidding function does not have the form of an optimal fractile of wind power production here. Observe that since the support $\mathscr{W}$ is discrete, such a function would be step-shaped, while our optimal curve is not.

Third, in line with the results of other authors under different structural assumptions [7,9], the value of storage in the reference case studied has diminishing marginal profit. This allows identifying two quantities of interest. First, the marginal profit at $b = 0$ gives the critical amortized cost of storage: if storage costs more than this quantity, it is not worth having co-located storage. The second quantity is the optimal size; for an amortized cost of storage c_s, the optimal size of storage is the quantity for which the marginal profit is equal to c_s. These results justify our choice of a descent algorithm to find the optimal storage size. These observations also seem to hold for the value of power conversion.

Finally, as anticipated, expected imbalances are reduced as storage sizes grows without limit. It is worth observing, however, that positive imbalances increase for the lowest range of storage sizes. This can be explained by the fact that in our model for the given reference values, the optimal contracting strategy in absence of storage is to commit the entire capacity of the plant, which eliminates positive imbalances. As storage drives the optimal commitment down, positive imbalances appear. With enough storage, these imbalances are then brought down too.

For the reference case shown in Fig. 2.1, the critical cost is found at $c_o = 0.0193$, which for a reference price of energy of 60$/MWh, corresponds to an amortized cost of 10.14$/kWh-yr. Note that this is a whole order of magnitude below the reference cost of 100$/kWh-yr for 2020 [29], meaning that under this setting and the reference values used, installing co-located storage is not profitable. Access to capacity payments does not seem to significantly change this conclusion (Fig.

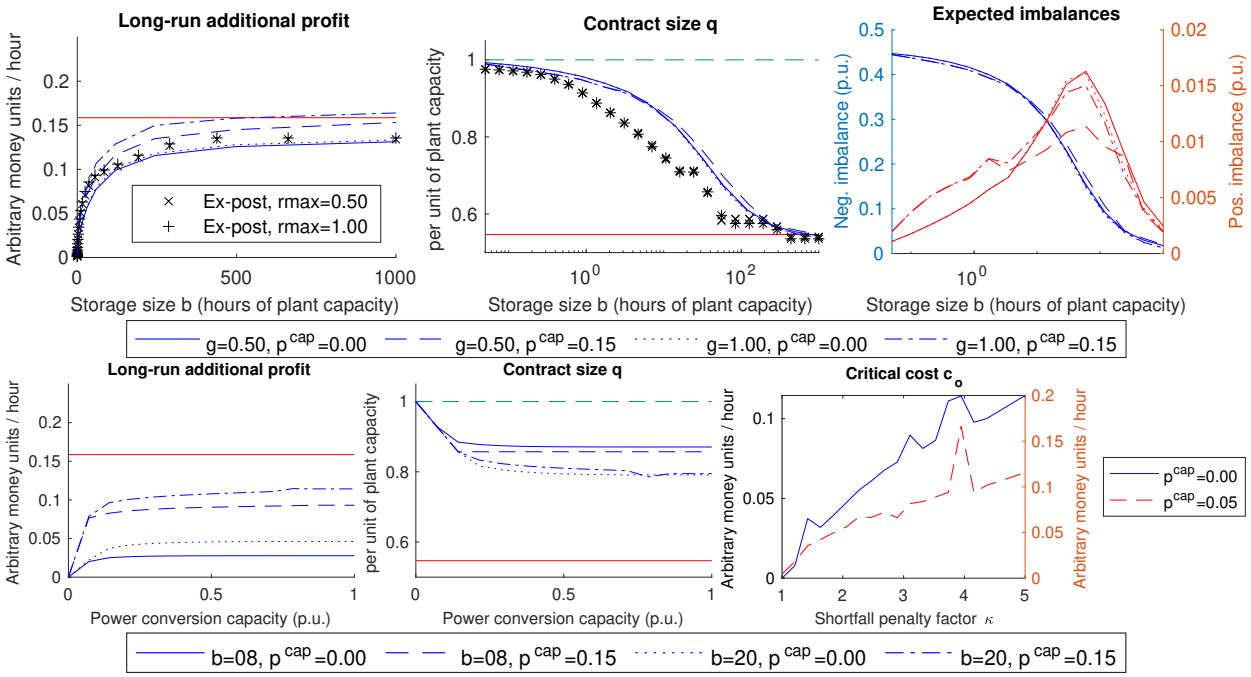

Figure 2.1: Plots of value of storage obtained solving the contract size problem for fixed storage capacity. *Top-left*: Long-run average profit in excess of no-storage profit for different storage sizes. The feed-in-tariff benchmark (red) is equal to the average output of the power plant (because price is normalized to 1). *Top-center*: Optimal energy commitment for different storage sizes compared to no-storage and average plant output benchmarks. *Top-right*: Expected positive and negative imbalance for different storage sizes. *Bottom-left*: Long-run average profit in excess of no-storage profit for different power inversion capacities. *Bottom-left*: Long-run average profit in excess of no-storage profit for different power inversion capacities. Feed-in-tariff benchmark in red. *Bottom-center*: Optimal energy commitment for different power inversion capacities compared to no-storage and average plant output benchmarks. *Bottom-right*: Critical storage cost for different values of shortfall penalty factor and capacity payment. Critical storage cost is the slope of the profit curve vs. storage size at $b = 0$.

2.1, bottom-right). Even taking into account that the cost of storage is declining rapidly, a tenfold reduction is beyond what we should expect to see in the near future. So according to these results, a different setting would need to be in place for co-located storage to be attractive.

In fact, in our setting, the WPP is not sufficiently exposed to uncertainty to justify paying for expensive storage. Indeed, the WPP is already covered against prices higher than κp by the pay-as-demanded forward contract, so that further risk hedging via storage is only modestly attractive. In Fig. 2.1 (bottom-right), we see that as the coverage cap κ is increased and the WPP is exposed to higher penalties, the critical cost c_o at which it is willing to invest in storage also rises. However, the pay-as-demanded forward contract would need to be available at a premium of several times the WPP's normal selling price to get anywhere near the actual current critical cost.

Figure 2.2 depicts the value of storage considering non-zero energy dissipation η. Two observa-

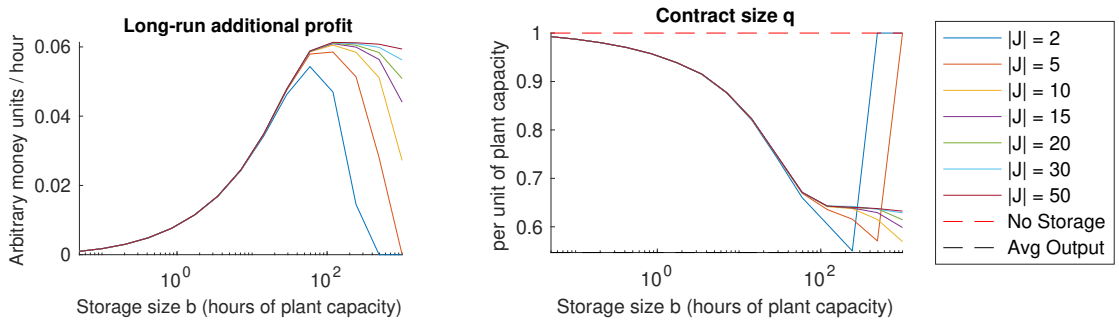

Figure 2.2: Value of storage and optimal contract size for $\eta = 0.2\%$/h with multi-regime fluid queue model, for different number of regimes $|J|$. *Left*: Long-run average profit in excess of no-storage profit for different storage sizes. *Right*: Optimal commitment for different storage sizes compared to no-storage and average plant output benchmarks.

tions are worth highlighting here. First, considering a non-zero value of losses to dissipation has an important effect of reducing the value of storage. For a reference value of $\eta = 0.2\%/h$, this reduction can be as high as 50%. This shows the importance of considering this effect when evaluating collocated storage. Results suggest that the overall shape of the value curve remains unchanged, i.e. we have decreasing marginal value of storage, with an upper bound being met asymptotically for very large values of storage. This asymptotic behavior can only be observed when the refinement of the discretization of storage is increased.

The second set of observations has to do with the limitations of the model used here and the effect of the granularity of the discretization of storage levels when considering dissipation. For very large values of storage, the model assumption of considering dissipation level-independent within each bin is too coarse and leads to artificial reductions in the value of storage. As expected, this effect is mitigated by increasing the number of bins in the discretization (at the cost of more computational burden).

For values of storage in the order of less than ten hours, it seems like a level-independent model is sufficiently accurate. For storage in the order of 10 to 100 hours, it seems necessary to include a multi-regime formulation with at least 10 to 20 bins to accurately model the value of storage. This implies a state space with size in the hundreds of states, which highlights the importance of having a numerically stable algorithm in this state range.

2.4.3 Sensitivity analyses

The main scope of the model proposed here is performing sensitivity analyses at a high level, such as during a project feasibility study or for policy evaluation. In this section, we show the results of some of these analyses. Despite the previous discussion regarding current costs, sensitivity analyses to changes in some key parameters are of interest, since they provide understanding regarding the interplay between some key quantities.

We are interested in observing the behavior of the model as key parameters are modified. The current cost of storage, $c_s \approx 0.2$ is above the critical cost for the reference case, so the optimal size would be 0, and the behavior of the results to changes in other parameters would be hidden. To avoid this, we take a reference storage cost of $c_s = 0.005$. Although unrealistically low, it allows observing the behavior of the optimal size as some parameters of interest change. Sensitivity curves are shown in Figure 2.6 and are commented in the following paragraphs.

Forward contract prices

The sensitivity to changes in shortfall penalty is aligned with intuition: larger storage becomes more attractive as the penalty for energy shortfall grows, i.e. as the exposure to high penalties increases. On the other hand, the change with respect to the price of the pay-as-generated forward contract shows a more interesting dynamic. As κ' is raised and the value of surplus energy increases, it becomes less undesirable to have excess energy, so that the optimal commitment q decreases. This leaves room for increasing the optimal storage size, as more energy is available for accumulation. After a certain point, however, the price of the pay-as-generated contract is so close to the price of the long-term fixed contract that the latter becomes less attractive, so that the commitment drops. With a very low commitment in the long-term contract, the motivation for investing in storage also disappears progressively, leading to a smaller optimal storage size.

Capacity payments

Access to capacity payments provides an important incentive for storage deployment, for both storage and powe¡r inversion capacities.

Efficiency and dissipation

The behavior when the round-trip efficiency and dissipation vary is in line with our expectation. As the system becomes more inefficient, storage becomes less attractive. For discharge efficiency parameter ρ_d, the relation between optimal size and efficiency appears to be close to linear. The sensitivity to the charge efficiency ρ_c is very similar and is omitted. Again, the curves highlight the importance of including dissipation in our model, with optimal storage capacity being most sensitive to this parameter for values near 0.

2.5 Extension to variable prices

The model introduced in 2.3 allows for a general Markovian process where both prices and wind power production are stochastic. However, throughout this chapter, we have focused on the case where prices are constant. A complete incorporation of the varable-price case into the model is out of the scope of this project. However, in this section, we discuss some challenges to our solution approach when this assumption is relaxed, briefly overview how they could be overcome, and present some preliminary results in that avenue. Although the work presented in this section is in a relatively early stage of maturity, we include here as it may prove helpful to a reader interested in extending our work to handle variable prices.

2.5.1 Challenges

There are two main challenges to extending the methodology presented in this chapter to a case with variable prices. The first one is one of validity: while assuming that the stochastic process of wind power output has a Markovian behavior may be an acceptable approximation for a high-level analysis, as we presented before, it is less clear that this assumption can be justified for the joint process of wind power output and prices. Some validation work based on historical data should be performed to guarantee the soundness of that approach. Assuming the validity of that assumption, a technical challenge remains: the balancing policy is no longer optimal in general in the variable-price case. We overview next how this challenge could be overcome leveraging known literature results.

2.5.2 Potential solution strategy

Consider the extension of the optimization problem of (2.5) to the case with variable prices:

$$\begin{array}{ll} \max\limits_{q,r,b,g} & \Pi \\ \text{s.t.} & b,g \geq 0 \end{array} \tag{2.17}$$

, where b and g are scalars, as in the case with constant prices, but q and r are now general functions of the state of the system. In a case with variable prices, a conceivable q would take the form of a supply function, so we would have $q = q(p_t)$, and if we restrict ourselves to stationary policies under a discrete state space, q is a vector with same size as the state space of the stochastic process p_t. To reduce the search space for r, we leverage the results of [9], where it is shown that the optimal charging policy in the discrete time case, when surplus energy is curtailed at no cost and no penalty (i.e. $\kappa' = 0$ in our model), is a double-threshold policy.

Double-threshold policy

The double-threshold policy is described in equation form in (2.18) and graphically for the iid[2] case in Fig. 2.3. In words, the charging policy is battery-level dependent. If the level x_t is below a threshold h^-, then the optimal policy dictates that the battery should be charged back to h^-, regardless of the imbalance status. If the level is above a threshold h^+, the battery should be used for balancing, i.e. store any surplus generation and compensate any shortfall in generation by discharging from the battery as necessary, going no further than h^+. If the level is between both thresholds, any excess should be stored, but no power should be extracted from the battery. The values of the thresholds h^- and h^+ are functions of the state of the system, i.e. functions of the price p_t and the imbalance $q_t - w_t$.

[2] iid=independent and identically distributed

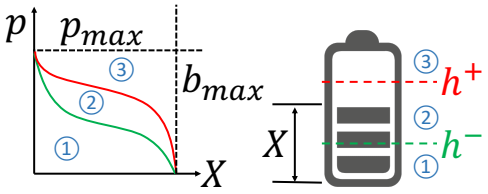

Figure 2.3: Graphical description of double-threshold policy for the case where thresholds only depend on the price process (not the imbalance). ①: stock up to h^-, ②: Store excess only, ③: balancing policy. Observe the thresholds h^- and h^+ depend on the price p_t.

$$r_t = \begin{cases} h^- - x_t & \text{if } x_t < h^- \\ (w_t - q_t)^+ & \text{if } h^- \leq x_t \leq h^+ \\ w_t - q_t & \text{if } x_t > h^+ \end{cases} \tag{2.18}$$

For simplicity, the version given in (2.18) is a simplified version where we assume perfect round-trip efficiency of the charge/discharge cycle, and ignore ramping limitations on the charge and discharge and energy dissipation. The results of [9] consider these cases as well. We note here three additional results of [9] that are of relevance for our work. First, if the round-trip efficiency of the charge/discharge cycle is perfect, $h^- = h^+$. Next, for states where p_t takes its maximum value (recall we assume a finite discrete state space), $h^+ = h^- = 0$. And finally, for the case where the stochastic process $(q_t - w_t, p_t)$ is iid, the thresholds depend only on the price p_t, not on the imbalance.

Conjecturing that the optimal policy in the continuous time case also has a double-threshold structure, optimization problem (2.17) takes the form of (2.19).

$$\begin{array}{ll} \max\limits_{q,h^+,h^-,b,g} & \Pi \\ \text{s.t.} & b,g \geq 0 \end{array} \tag{2.19}$$

, where h^+ and h^- are functions of the state of the system, so they can be represented by vectors with same size as the state space. Moreover, if the optimal thresholds depended only on prices, the size of the variables h^+ and h^- would only be that of the space state of p_t, which considerably reduces the search space.

2.5.3 Preliminary results

We put this conjecture to the test, i.e., whether the optimal charge/discharge policy has a double-threshold structure, and if so, whether the thresholds depend on prices only or also on the imbalance, by conducting an experiment on a small test instance, which we describe in this section.

Consider the continuous-time setting described in this chapter, where the commitment $q_t = q$ is constant and known, and the processes w_t and p_t are each an independent CTMC with discrete, finite state-space $\mathscr{W}$ and $\mathscr{P}$ respectively, so that the joint stochastic process (w_t, p_t) is a CTMC with discrete finite state space $\mathscr{S} = \mathscr{W} \times \mathscr{P}$. We next consider a discrete-time problem by sampling from (w_t, p_t) periodically at intervals of length Δt.

From standard results in Markov chains, we know that if (w_t, p_t) has generator $\mathbf{Q}$, this sampling procedure results in a discrete-time stochastic process (w_{t_k}, p_{t_k}) with transition matrix $\mathbf{P}^{\Delta t} = \exp(\Delta t \mathbf{Q})$. If we assume that the wind power output and price remain constant during the period $[t_k, t_{k+1})$, the resulting problem falls exactly in the setting of [9]. Therefore, we know that the optimal policy for that case has a double-threshold form. If, as conjectured, the optimal policy in continuous time has a double-threshold form as well, we expect those thresholds to converge as $\Delta t \to 0$. We next make this idea more precise.

Let $\xi_t = (w_t, p_t)$, let $\xi_k^{\Delta t} = (w_{t_k}, p_{t_k})$, $k \in \mathbb{N}$, be the discrete-time stochastic process resulting from sampling from ξ_t at periodic intervals Δt. Let $h^{\Delta t}(w, p)$, for $(w, p) \in \mathscr{S}$ be the function that returns the optimal threshold for each state of the discrete system with sampling period Δt. Recall that since we are considering perfect round-trip efficiency, both thresholds coincide, i.e. $h^+ = h^- = h$. We expect to obtain $\lim_{\Delta t \to 0} h^{\Delta t}(\cdot) = h^*(\cdot)$ for some h^*.

Next, we present the method used to obtain the optimal thresholds for each discretized problem. In [9], conventional dynamic programming techniques (LP formulation) are used to obtain the optimal values for the numerical examples solved, which involves discretizing the space of storage levels also as space $\mathscr{B}$. In this context, an action is how much energy to charge or discharge into (from) the BESS. Therefore, if the storage level is discretized, this automatically discretizes the action space as well. In fact, we can interpret the system dynamics in the two following equivalent forms.

- An action u_{t_k} is the energy (in MWh) that is injected into the BESS (which we interpret as extraction if < 0), so that the BESS level at the next time period is $x_{t_{k+1}} = x_{t_k} + u_{t_k}$
- An action μ_{t_k} is the BESS level at which the BESS will be at the next time period: $x_{t_{k+1}} = \mu_{t_k}$.

It is clear that these two definitions of an action are related by $\mu_{t_k} = x_{t_k} + u_{t_k}$. The second definition makes evident that discretizing the state space of x_{t_k} also discretizes the action state space. We will use both definitions to describe the policy iteration algorithm.

One important consideration in our discretization as Δt becomes smaller is maintaining precision. Let Δb be the granularity of the discretization of the storage capacity (in MWh). If we maintained this granularity constant, the energy imbalance $(w - q)\Delta t$ would become negligible compared to Δb as $\Delta t \to 0$, so our analysis would become meaningless, as results would trivially converge due to lack of precision. We thus need to adjust the granularity of the storage discretization. To avoid noise introduced by rounding, we choose Δb such that $(w - q)\Delta t$ is a multiple of Δb for all $w \in \mathscr{W}$.

This significantly augments the size of our problem as $\Delta t \to 0$ and makes it harder to solve, but is a necessary step.

2.5.4 Policy iteration algorithm

We omit here many details and assume the reader is familiar with optimality in infinite-horizon average cost problems. For a deeper presentation of this topic, see [30]. To describe the policy iteration algorithm used, consider first the optimality equation (2.20) of the infinite-horizon average cost problem, with $v(\cdot)$ the relative cost function and λ the optimal average cost. This optimality equation is satisfied because our process satisfies the *Weak Accessibility* assumption of [30], as verified in the proof of Theorem 8 of [9].

$$\begin{aligned} v(x_{t_k}, w_{t_k}, p_{t_k}) + \lambda = \min_{r_t} \Big\{ & p_{t_k} \big(q - (w_{t_k} - r_{t_k})\big)^+ \\ & + \mathbb{E}\left[v\big(x_{t_k} + r_{t_k}, w_{t_{k+1}}, p_{t_{k+1}}\big) \middle| w_{t_k}, p_{t_k} \right] \Big\} \end{aligned} \tag{2.20}$$

Since our state space is finite, we can express this equation introducing a vector V to represent the relative cost function, a vector g_r to represent the cost incurred at the current step and a matrix $\mathbf{P}_r$ to represent the the transition matrix under policy r. Formally,

$$\begin{aligned} V &= [v(x,w,p)]_{(x,w,p)\in\mathscr{B}\times\mathscr{S}} \\ g_r &= [p(q-w+r(x,w,p))^+]_{(x,w,p)\in\mathscr{B}\times\mathscr{S}} \\ \mathbf{P}_r\big((x_1,s_1),(x_2,s_2)\big) &= \mathbb{P}\Big((x_{t_{k+1}}, s_{t_{k+1}}) = (x_2,s_2) \Big| (x_{t_k}, s_{t_k}) = (x_1,s_1), r_{t_k} = r(x_1,s_1) \Big) \end{aligned}$$

, so that the policy iteration algorithm can be implemented as in Algorithm 1. In words, we start from a balancing policy: $r(x,w,p) = w - q \ \forall (x,w,p) \in \mathscr{B} \times \mathscr{S}$. In the policy evaluation step, we construct the matrix $\mathbf{P}_r$ (which can be defined as a sparse matrix to enhance performance) and solve a linear system to update the values of V and λ. In the policy improvement step, for each $(x,w,p) \in \mathscr{B} \times \mathscr{S}$, the action that minimizes the right-hand-side in (2.20) is found by enumeration of the entire action space.

In the general form shown in Algorithm 1, the entire action space is searched looking for the optimal policy. As Δt gets smaller and $N_b = |\mathscr{B}|$ becomes larger, this enumeration of the action space becomes prohibitively time-consuming.

An alternative, in order to make possible testing smaller values of Δt is thus to replace the policy improvement step with one in which only threshold policies are considered. This is shown in Algorithm 2. Note that for this class of policies, once the optimal action for the first storage level $x = 0$ is determined for some (w,p), the action for all other storage levels x corresponding to the

/* We start with balancing policy */
for $x \in \mathscr{B}$ **do**
  for $w \in \mathscr{W}$ **do**
    for $p \in \mathscr{P}$ **do**
      $u^0(x,w,p) \leftarrow w - q$
      $\mu^0(x,w,p) \leftarrow \min\{b_{max}, \max\{0, x+w-q\}\}$
    end
  end
end
$\ell \leftarrow 0$
repeat
  // Policy evaluation
  $\mathbf{P}_r \leftarrow \mathbf{0}_{NN_kN_b \times NN_kN_b}$ **for** $x \in \mathscr{B}$ **do**
    for $w \in \mathscr{W}$ **do**
      for $p \in \mathscr{P}$ **do**
        $\mathbf{P}_r\big((x,w,p),(\mu^\ell(x,w,p),:,:)\big) \leftarrow \mathbf{P}^{\Delta t}$
        $g_r\big((x,w,p)\big) \leftarrow p(q-w+u^\ell(x,w,p))^+$
      end
    end
  end
  /* Solve linear system to obtain V and λ */
  $\mathbf{A} \leftarrow [\mathbf{P}_r, -\mathbf{1}; 1, \mathbf{0}]$
  $b \leftarrow [-g_r; 0]$
  $\chi \leftarrow A^{-1} \cdot b$
  $V \leftarrow \chi(1 : \text{end} - 1)$
  $\lambda \leftarrow \chi(\text{end})$
  // Policy improvement
  for $x \in \mathscr{B}$ **do**
    for $w \in \mathscr{W}$ **do**
      for $p \in \mathscr{P}$ **do**
        $u^{\ell+1}(x,w,p) \leftarrow$
        $\quad \arg\min_y \left\{ p(q-w+y)^+ \sum_{w' \in \mathscr{W}, p' \in \mathscr{P}} \mathbf{P}^{\Delta t}(w',p') \cdot V(x+y,w',p') \right\}$
        $\mu^{\ell+1}(x,w,p) \leftarrow u^{\ell+1}(x,w,p) + x$
      end
    end
  end
  $\ell \leftarrow \ell + 1$
until $\mu^{\ell+1} == \mu^\ell$ *or iteration limit*

Algorithm 1: General policy iteration algorithm used

same (w,p) is determined as well: we have $\mu(x,w,p) = \min\{b_{max}, \max\{x+w-q, \mu(0,w,p)\}\}$. This allows saving one loop execution of length N_b, which is significant since N_b is the size of the largest space in our problem.

```
// Policy improvement, threshold policies only
for w ∈ 𝒲 do
    for p ∈ 𝒫 do
        u^{ℓ+1}(0,w,p) ← arg min_y { p(q−w+y)^+ Σ_{w'∈𝒲, p'∈𝒫} P^{Δt}(w',p') · V(0+y,w',p') }
        μ^{ℓ+1}(0,w,p) ← u^{ℓ+1}(0,w,p) + x
        for x ∈ ℬ do
            μ^{ℓ+1}(x,w,p) ← min{b_max, max{x+w−q, μ^{ℓ+1}(0,w,p)}}
            u^{ℓ+1}(x,w,p) ← μ^{ℓ+1}(x,w,p) − x
        end
    end
end
```

Algorithm 2: Policy improvement step searching only the space of threshold policies.

The size of the search space can be further reduced if thresholds depend only on prices, as shown in Algorithm 3. In this case, once the optimal action has been determined for $w = 0, x = 0$ for one value of p, it is just copied over for all (x,w) for the same value of p as $\mu(x,w,p) = \min\{b_{max}, \max\{x + 0 - q, \mu(0,0,p)\}\}$. Note that if thresholds that depend on prices only are optimal, the values of w and x chosen to perform the policy improvement step will not matter.

```
// Policy improvement, price-dependent threshold policies only
for p ∈ 𝒫 do
    w ← 0
    u^{ℓ+1}(0,w,p) ← arg min_y { p(q−w+y)^+ Σ_{w'∈𝒲, p'∈𝒫} P^{Δt}(w',p') · V(0+y,w',p') }
    μ^{ℓ+1}(0,w,p) ← u^{ℓ+1}(0,w,p) + x
    for x ∈ ℬ do
        for w ∈ 𝒲 do
            μ^{ℓ+1}(x,w,p) ← min{b_max, max{x+w−q, μ^{ℓ+1}(0,0,p)}}
            u^{ℓ+1}(x,w,p) ← μ^{ℓ+1}(x,w,p) − x
        end
    end
end
```

Algorithm 3: Policy improvement step searching only the space of price-dependent threshold policies.

2.5.5 Numerical tests

The algorithms presented earlier were implemented in Matlab to run tests on a small system as a first approach to test our conjectures. Historical wind power output and price data were obtained

Parameter	Value
$N = \lvert\mathscr{W}\rvert$	3
$\mathscr{W}$	{0,0.5,1}
$N_p = \lvert\mathscr{P}\rvert$	2
$\mathscr{P}$	{0.22,1}
Δw	0.1 p.u.
b_{max}	2 hours (at 1 p.u. capacity)
q	0.4 p.u.

Table 2.2: Numerical test parameters

from [28] and used to get a generator $\mathbf{Q}$ that represents (w_t, p_t), following the method described in [25]. To obtain a model of manageable size, the discretization of the state space was done with $N = |\mathscr{W}| = 3$, $N_p = |\mathscr{P}| = 2$. Separate generator matrices were first obtained for each process, and then combined into a larger generator matrix $\mathbf{Q}$ making sure to maintain independence.

All quantities were converted to per unit (p.u.) with respect to the wind power plant capacity. Storage capacity and level is expressed in hours of storage (at full plant capacity). Prices are also expressed in per unit (normalized) with respect to the maximum price. The most important parameters are summarized in Table 2.2.

For the test system defined, the discrete-time problems were solved successively for decreasing values of Δt. The results are discussed next.

2.5.6 Results

As expected from the results in [9], even when searching the space of all possible policies, the optimal policy found has always a double-threshold form. Moreover, as predicted, we obtain $h^- = h^+$ and $h = 0$ for the states with maximum price (w, p), $p = p_{max} = 1$. The results of the thresholds obtained for system states with price $p = 0.208$, for the different values of Δt tested, are shown in Figure 2.4.

There are several insights to extract from these plots. First, contrary to what we hoped for, and although the price and wind power output processes are independent from each other, we find that the optimal thresholds depend on the value of the wind power output, i.e. they are different for different values of $w \in \mathscr{W}$. This implies,that restricting the space of policies to policies where the threshold depends only on the price excludes the optimal policy.

This is confirmed when looking at the optimal average cost, which is higher for the latter class of policies. It is worth noting, however, that the cost increases by less than 2% for all values of Δt tested. This suggests that although suboptimal, price-dependent policies might provide an acceptable heuristic.

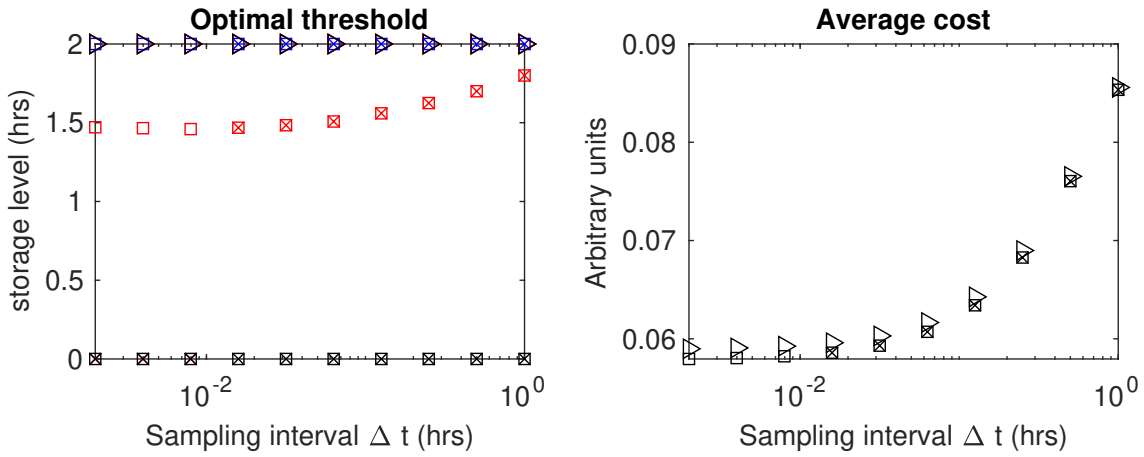

Figure 2.4: Optimal thresholds obtained for discrete-time model with decreasing sampling interval Δt. At the top, optimal threshold $h^+ = h^- = h(w,p)$ for each value of Δt. Colors represent different values of w: $w = 0$ in blue, $w = 0.5$ in red, $w = 1$ in black. All values correspond to $p = 0.22$. It was found $h(w,1) = 0 \forall w$ and is not included in the plot.
At the bottom, optimal average cost obtained, in arbitrary money units. For both plots, $\times$ represent values obtained when searching the entire space of policies (this was not possible within the time execution limit defined for the three smallest values of Δt tested). $\square$ represents values obtained when restricted to threshold policies, $\triangleright$ represents values obtained when restricted to price-dependent threshold policies.

Next, observe that it was not possible to run the policy iteration algorithm to completion when searching the entire space of policies for the three smallest values of Δt. However, the optimal solution found when restricting the search to threshold policies is the same as the one found when searching the entire policy space for all values of Δt for which both were computed, which suggests the optimal solutions found for the smallest values of Δt would also be globally optimal. However, note that we do not have a guarantee of this at this point, as it is pointed out in [9] that convexity of the problem could be lost when applying this restriction, and hence convergence to local optima is possible.

Finally, and most importantly, there seems to be a convergence of optimal thresholds as Δt is decreased. This is consistent with the conjecture of the optimal policy for the continuous-time case also having a double-threshold form. This is of course only one particular case and is hence far from being a proof, but is encouraging for pursuing this research avenue. We might be tempted to also suggest that the discretization and policy iteration path taken here could be a way to approximately compute the optimal thresholds of the continuous-time case. Although in principle this is correct, for a problem of a more realistic size, it seems unlikely that the discrete-time problem could be solved quickly enough for this approach to be appealing.

2.6 Conclusion and future research

In sum, we are proposing a model to perform a high-level steady-state analysis of the value of co-located storage for a wind power producer that participates in the electricity market through long-

term forward contracts. In particular, we assess the optimal size of storage and optimal quantity to sell in forward contracts under different values of key parameters regarding contract prices and storage efficiency. We find that in a setting such as the one considered in this chapter the producer is not exposed to enough uncertainty in income for storage to be attractive at current prices. This is likely to be different with variable prices, which is the natural extension of our model.

In this avenue, we regard the result of the model with non-zero dissipation as very important because of its implications for the extension to a variable-price setting, which are twofold. First, these results demonstrate the ability of the method to handle larger dimensions, which in our case appear as we refine the discretization of the storage levels. In the tests performed, we introduced as many as 750 states, which the algorithm of [5] could handle without issues. This is encouraging since introducing variable prices increases the dimension of the system in a similar way. Second, it is proved in [9] that the optimal charge/discharge policy when prices are variable is a dual-threshold policy, a policy in which the charge/discharge decision is level-dependent, which lends itself to be easily handled through the formulation proposed here. These two facts in conjunction allow regarding an extension of this method to variable prices as promising from a technical point of view. In [5], they find the algorithm to be numerically stable with a state size of more than 2000. Combining the factors discussed above, it would not be hard to reach a model of this size, which is why it is key for these cases to verify that the algorithm remains numerically stable as the size grows and to reduce as much as possible the number of states introduced, e.g. by using non-uniform bin sizes (with lower resolution at lower levels) and only the number of bins necessary to accurately depict storage sizes in a reasonable range using engineering criteria.

We close this work with a discussion of how we envision addressing the problem of battery aging and battery replacement through an extension of the model presented in this report.

2.6.1 Battery replacement

All the models covered here assume that battery capacity does not decay during its lifetime and that when it is replaced, it can be done at the same cost and size as the initial decision. All these assumptions can be lifted by considering an additional decision variable in the problem, namely the time of replacement of the battery. Figure 2.5 depicts the pattern that is obtained from considering a linear capacity decay with periodic replacement. As can be seen there, in order to get a system with an average storage capacity over its lifetime equal to a certain desired value (e.g. the constant value for which our current model designs), some oversizing of the initial installation is necessary, which implies some additional cost. There is a tradeoff between the magnitude of this oversizing and the replacement period T. More frequent replacement reduces the magnitude of oversizing necessary to maintain some average capacity, and hence the total installation cost, but increases the amortized cost, as it reduces the amortization period.

A first simple approximation to incorporate the effect of this phenomenon into our model could be an ad hoc post-processing stage where after finding the optimal battery size, a replacement period is chosen arbitrarily, and the battery oversize is selected to maintain the average size that

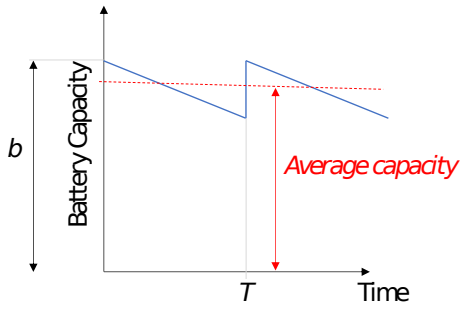

Figure 2.5: Pattern of battery capacity decay with linear decay and periodic replacement T. The initial capacity b must be oversized in order to obtain some desired average capacity.

was designed. The cost implications of this oversizing can then be computed and fed back to adjust the selected battery size. A more sophisticated approach, which could balance better this tradeoff, would be to include T as a decision variable in an extended version of our model.

Finally, we note that this same framework can be utilized to address one more relevant feature in the context of battery storage investment, which is that of falling costs due to technological advancements. In this case, the cost of replacing the battery at the end of the replacement period would be a decreasing function of time. An additional tradeoff would therefore appear, as a longer replacement period would require a larger initial oversizing, and would decrease the amortized cost as mentioned before, but would in addition allow for a cheaper installation cost for the replacement battery. It is conceivable that the abundant literature in machine replacement problem, which handles a case with many similarities to this, would be of great value to formulate this model extension.

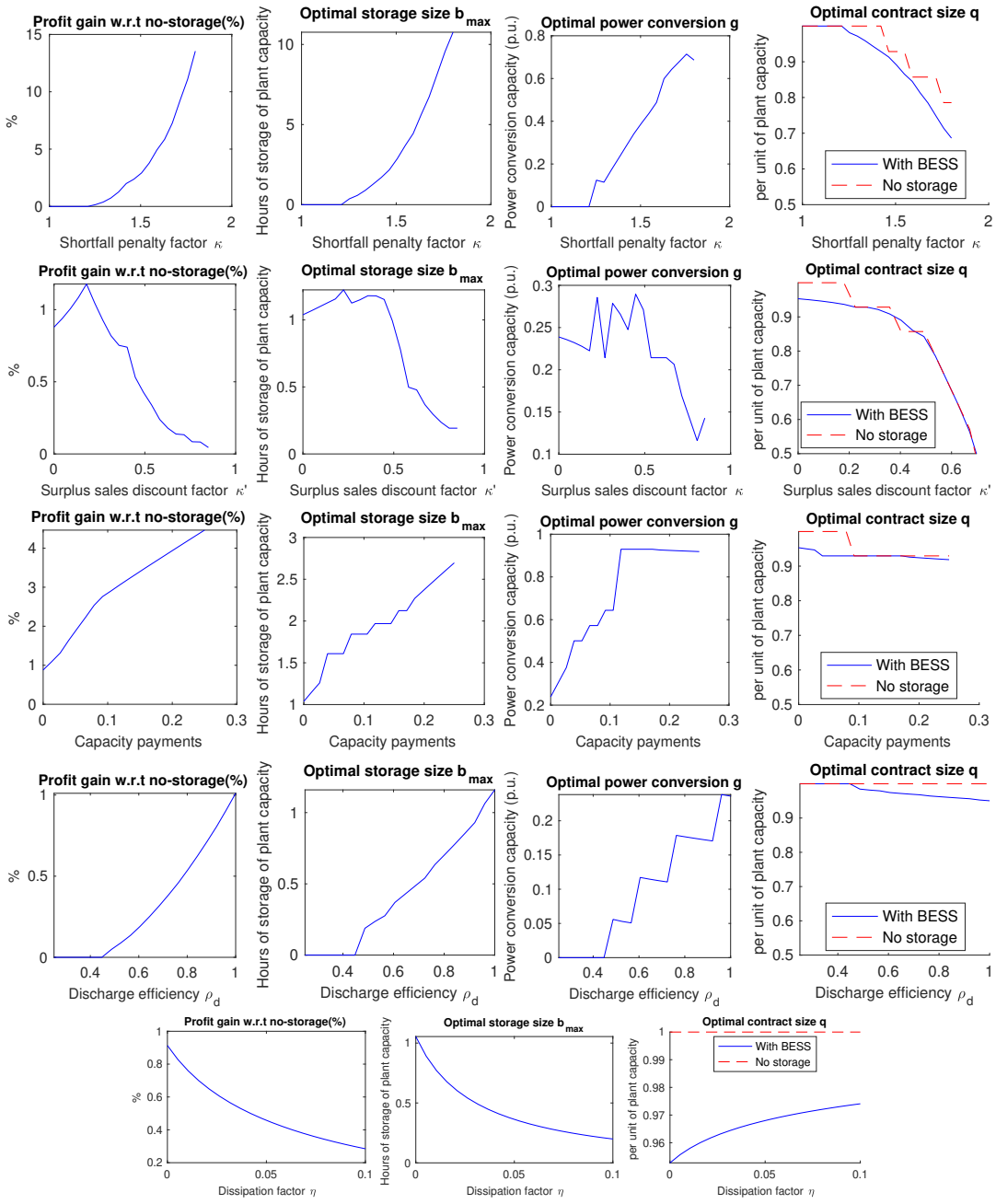

Figure 2.6: Sensitivity of optimal quantities (by column) to some model parameters (by row).
Columns: *Left*: Profit gain with respect to no-storage. *Center-left*: Optimal storage size. *Center-right*: Optimal power inversion size. *Right*: Optimal contract size.
Rows: Sensitivities with respect to changes in... *Top row*: Shortfall penalty factor κ. *Second row*: Discount factor κ'. *Third row*: Capacity payments p^{cap}. *Fourth row*: Discharge efficiency ρ_d. *Bottom row*: Dissipation losses factor η (in p.u. of storage lost per hour). These tests were run on the uncapacitated model and thus do not include the optimal power inversion output.

3. Stable and Fair Uniform Price Allocations of Community Choice Aggregation Gains in Retail Electricity Markets [1]

Abstract

The advent of differentiated prices for consuming (buying) and injecting (selling) electricity at the residential level promotes the emergence of local peer-to-peer electricity markets for prosumers, which can deliver savings to participants as long as an attractive cost sharing mechanism can be designed. Building on cooperative game theory models that have been proposed in the literature, we define the uniform price core, a class of desirable distribution of savings in this context, and prove constructively that it is not empty. We propose the shadow price imputation, a computationally efficient stable uniform price imputation, which we show to be equivalent to a dual imputation in the sense of cooperative linear production games. In the second part of the chapter, we compare the shadow price imputation to other imputations in the uniform price core through the lens of fairness. To overcome the challenge of tractability for larger numbers of participants, we extend an existing sampling methodology and apply it to optimization problems devised to obtain a fair imputation. The long-term incentive implications for different stakeholders, as well as a generalization to a stochastic case where the uncertainty in renewable production and local demand is considered, are also discussed. We present theoretical results and numerical experiments and examples to illustrate our approach.

3.1 Introduction

After years of incentive measures like *Net Metering*, and even mandatory installation of rooftop Photovoltaic (PV) and local BESSs in new buildings in certain jurisdictions ([31]), the so-called prosumer, a consumer of electricity with local means of production, is expected to become nearly ubiquitous in modern distribution systems. With the advent of the end of net metering subsidy programs, the use of different retail prices for consuming (buying) and injecting (selling) electricity is likely to become more common. In this way, public utilities may reconcile their non-convex cost structure, driven by significant fixed costs, with a need to maintain linear (volumetric) prices, as shown by [32]. In this context, prosumers find that trading among each other can offer savings compared to the conventional scheme where all transactions are settled with the public utility, and so forming local markets, usually called peer-to-peer markets or local aggregation markets becomes

[1] A substantial part of the text that constitutes this chapter was submitted for publication under the name "Uniform Price Allocations of Community Choice Aggregation Gains in Retail Electricity Markets", authored by Tomas Valencia Zuluaga and Shmuel S. Oren, and was under review at the time of publishing of this report. A conference paper version of the sampling methodology presented in Section 3.5 was presented and published in [2]. This chapter has also been published in the doctoral thesis of Tomas Valencia Zuluaga [4]

naturally attractive. One of the main challenges when setting up such a market is designing a mechanism to distribute the collective savings in such a way that participants are incentivized to remain in the market.

In this chapter, we approach this problem through a cooperative game theoretic model, where we formally define some desired characteristics of a distribution mechanism: uniform prices, computational efficiency and a certain notion of fairness.

We propose an efficient mechanism that satisfies the two former desiderata, and analyze a framework to obtain more fair distributions in a computationally efficient way. We also investigate through numerical examples if more fair distributions exist as the number of participants grows. We close with a discussion of long-term incentive implications of the scheme proposed here.

3.1.1 Related research

There are numerous examples of cooperative game models applied to peer-to-peer electricity markets in the literature, which differ in the market structure (centralized or decentralized), the representation of the grid and flows (copper-plate, linear, non-linear), among numerous other model details. Recent, comprehensive reviews are available in [33] and [34].

Our approach is closest to the models of [35] and [36], which analyze the obtention of a profit distribution mechanism using a centralized, linear model with several time periods linked through storage devcies, like ours. The former authors find that the Shapley value is often not in the core of the game and can fail to incentivize participation. The nucleolus is proposed as a stable, albeit computationally challenging, alternative. The latter authors, whose formulation and notation we adopt in this chapter, propose overcoming the computational challenges of the nucleolus computation with a linear optimization problem to obtain the least core allocation, although the least core LP proposed still requires an exponential number of constraints in its description. They also restrict allocations to the ones that can be described as uniform prices, but do not formalize it or analyze it like we do here.

In our model, the value of a coalition is obtained from solving an LP. In this chapter, we exploit LP strong duality to obtain an imputation that is guaranteed to be in the core of the game. This is the same approach followed for example by [37] in the context of inventory centralization problems. All these problems are special cases of the *linear production games* proposed by [38], who shows that such games are totally balanced and that the dual imputation, sometimes called in the literature *Owen imputation*, is guaranteed to be in the core. [38] also shows that although the core and the set of dual imputations are not the same for general linear games, they become the same in the limit as the number of players grows to infinity through replication.

Fairness in the context of cooperative games can have numerous interpretations and has been the subject of extensive study (for a textbook reference, see e.g. [39]). A classic notion of fairness in this context is that of Shapley, who proposes through an axiomatic approach that a fair allocation

should reflect each individual's contribution to other potential allocations. It is in this light that we analyze unfairness in Example 2: essential participants may be allocated zero profits by a dual imputation, which are thus unfair in this regard. This phenomenon was identified by [40] for general linear production games, where they characterize a class of more fair allocations, but find that their existence in the core cannot be guaranteed.

This analysis of unfairness in our context is related to finding a uniform price that is intermediate between the utility selling and buying prices and thus distribute savings between buyers and sellers. This is addressed by [41] by proposing a *mid-market rule (MMR)*, which is somewhat similar to our price-control mechanism introduced in Section 3.4. However, their model is a single-period model without storage, and the MMR is not in the core of the game, as shown in the numerical tests of [36].

Our approach of finding the best core allocation via optimization can be interpreted as the social planner's problem of finding a social optimum, with our objective value being a *social welfare function*, in the sense of classic Welfare Economics as covered e.g. in [42]. We do not expand on this angle of analysis, but point the interested reader to [43] for a related approach of finding an *egalitarian allocation* in cooperative games.

Describing the core in general games requires a number of constraints exponential in the number of players. This is a known shortcoming of finding stable imputations in general settings. In the statistical learning literature, [44] propose two probabilistic relaxations of the core and show that imputations therein can be learned from a number of samples that is polynomial in the number of players. This is adapted by [2] to the same setting studied in our work to find the least core allocation in a relaxation of the core of the game for p2p markets with larger numbers of participants. In Section 3.5, we apply that approach to optimization problems with general objective functions.

3.1.2 Contributions of this work

The contributions of this work can be summarized as follows:

- In the context of P2P electricity markets, we formalize a class of imputations that is desirable in a cost sharing mechanism: imputations that can be described through uniform prices. Although numerous models in the literature use this class of imputations, we have not found examples where the difference between this class and the regular game core is formally analyzed.

- We prove that core of the game and the uniform price core are not the same, which justifies the formalization of the uniform price core. We prove that the uniform price core is not empty for the peer-to-peer electricity market.

- We give a methodology to obtain a uniform price imputation in the core of the game, which we call the shadow price imputation. This methodology only requires solving a primal, dual

LP pair of moderate size, and is thus computationally efficient for p2p markets with larger numbers of participants. We show that this imputation is a dual, or Owen imputation, when our model is interpreted as a linear production game in the sense of [38].

- To our knowledge, the relation of this structure of p2p market with the aforementioned linear production games has not been established in the literature before. Besides its academic interest, this bridge is of value because it allows applying the asymptotic result that dual imputations are the unique core imputations for large enough markets, for which we find some evidence in numerical tests.

- We show that shadow price imputations may be unfair in a Shapley sense and propose a framework for obtaining better uniform price imputations through optimization. The proposed framework has scalability challenges. To overcome them, a sampling technique is proposed based on statistical learning results that are shown to be applicable to this setting.

3.1.3 Structure of this chapter

In Section 3.2, we present the setting of the peer-to-peer electricity market and describe in detail the cooperative game model adopted. We also present the preliminary results about cooperative game theory necessary for our approach. In Section 3.3, we introduce the class of uniform price imputations and show that the set of such imputations in the core is not empty through the introduction of shadow price imputations. In Section 3.4, we show how shadow price imputations, despite their desirable characteristics, might be unfair and propose an optimization framework to find the most desirable imputation. In Section 3.5, we present a sampling methodology to overcome the challenge of scalability in implementing that optimization framework in markets with larger numbers of prosumers, and present numerical tests that validate the methodology. In Section 3.6, we discuss some considerations about long-term responses of participants and the public utility which are not captured in our model. Section 3.7 discusses the generalization of this model to a stochastic case that considers uncertainty in the local production and electricity demand. Finally, conclusions are presented in Section 3.8.

3.2 Setting and preliminaries

In this section, we present the setting for our peer-to-peer electricity market, and introduce the cooperative game chosen to model it. Other than some minor exposition and notation choices, the model is identical to that of [36].

After presenting the model, we define the class of *uniform price imputations* and the *uniform price core*, a related refinement of the core, and illustrate how they differ through a small example. Finally, we prove that the uniform price core is not empty and provide a methodology to efficiently find an imputation therein, which constitutes one of the main contributions of this work.

3.2.1 Nomenclature

Sets
N: Set of all market participants, i.e. prosumers. Indexed by i.
T: Set of time periods considered in horizon, indexed by t.
Variables
Primal
$s^c_{i,t}$: energy (in kWh) charged into i's BESS during period t.
$s^d_{i,t}$: energy (in kWh) drawn from i's BESS during period t.
$e_{i,t}$: energy (in kWh) in i's BESS at the end of period t.
$\ell_{i,t}$: net consumption of i during period t.
z_t: net collective consumption of all prosumers during period t.
w_t: net collective generation of all prosumers during period t.
Dual
π_t: dual variable of energy balance constraint at period t.
$\alpha_{i,t}$: dual variable of i's BESS charge limit constraint in period t.
$\beta_{i,t}$: dual variable of i's BESS discharge limit constraint in period t.
$\underline{\gamma}_{i,t}, \overline{\gamma}_{i,t}$: dual variable of i's BESS lower and upper energy storage limit constraint in period t.
δ_i: dual variable of i's BESS zero net usage constraint.
Parameters
p_t: utility price for consuming (buying) electricity during period t (in \$/kWh).
h_t: utility price for injecting (selling) electricity during period t (in \$/kWh).
$d_{i,t}$: Prosumer i's gross demand (in kWh) during period t.
$g_{i,t}$: Prosumer i's gross PV production (in kWh) during period t.
$\underline{s}_i, \overline{s}_i$: i's discharge and charge limit during one period.
$\underline{E}_i, \overline{E}_i$: i's lower and upper energy storage level limit.
η^c_i, η^d_i: prosumer i's BESS charge and discharge efficiency.
e^0_i: prosumer i's BESS initial state of charge.

Notation

Unless otherwise specified, the vector is noted by omitting the corresponding index, e.g. $\pi = [\pi_t]_{t \in T}$.

3.2.2 Model description

We consider a set of prosumers N who have some electricity consumption needs, and some of which have local generation (solar PV) and/or a BESS. The utility company has a pair of predetermined import and export prices p_t, h_t for each period t in the day, with $p_t > h_t$. During period t, any customer may purchase any amount of electricity from the utility company at a price p_t \$/kWh, and sell any amount of electricity for a price h_t \$/kWh. A subset $S \subseteq N$ of prosumers may get together and form a coalition; a coalition is treated as a single customer by the utility company, i.e. the coalition is charged for the combined net consumption of all members, and remunerated for the

combined net injection.

Members of a coalition can coordinate the usage of their BESSs to shift their consumption in order to minimize the collective electricity bill of the coalition. We assume that utility prices, as well as the generation and demand profile for each customers is known for the entire horizon (day) when the coordination plan is determined. The coordination problem for a coalition $S \subseteq N$ is denoted (P_S) and given by (3.1).

$$
\begin{aligned}
&(P_S) : C(S) = \\
&\min_{\substack{s^c, s^d \\ z, w}} \sum_{t \in T} p_t z_t - h_t w_t && && (3.1a)\\
\text{s.t } & z_t - w_t = \sum_{i \in S} \ell_{i,t} && \forall t \in T && [\pi_t] && (3.1b)\\
& s^c_{i,t} \leq \overline{s_i} && \forall i \in S, t \in T && [\alpha_{i,t}] && (3.1c)\\
& s^d_{i,t} \leq \overline{s_i} && \forall i \in S, t \in T && [\beta_{i,t}] && (3.1d)\\
& \underline{E_i} \leq e^0_i + e_{i,t} \leq \overline{E_i} && \forall i \in S, t \in T && [\underline{\gamma_{i,t}}, \overline{\gamma_{i,t}}] && (3.1e)\\
& \sum_{t \in T} \left(\eta^c_i s^c_{i,t} - s^d_{i,t} \right) = 0 && \forall i \in S && [\delta_i] && (3.1f)\\
& \ell_{i,t} = d_{i,t} + s^c_{i,t} - \eta^d_i s^d_{i,t} - g_{i,t} && \forall i \in S, t \in T && && \\
& e_{i,t} = \sum_{\tau=0}^{t} \left(\eta^c_i s^c_{i,\tau} - s^d_{i,\tau} \right) && \forall i \in S, t \in T && && \\
& s^c_{i,t}, s^d_{i,t}, z_t, w_t \geq 0 && && && (3.1g)
\end{aligned}
$$

Note $\ell_{i,t}$ and $e_{i,t}$ are just shorthands for customer i's net consumption and BESS level during period t respectively, and can be substituted directly into (3.1b) and (3.1e), so they are not assigned a dual variable. Constraints (3.1c) and (3.1d) enforce the charging and discharging limits of the batteries, while (3.1e) ensures that battery levels remain within limits. To avoid end-of-horizon effects, (3.1f) makes sure that the battery ends the day with the same level as it started. Constraint (3.1b) computes the combined net load of the coalition during each time period t and assigns its positive and negative parts to auxiliary variables z_t and w_t, which are used in (3.1a) to compute the total cost (revenue) of energy purchased from (sold to) the utility. It is not hard to verify that because $h_t < p_t$, any optimal solution will satisfy $z_t \cdot w_t = 0$, which justifies the interpretation $z_t = (\sum_{i \in S} \ell_{i,t})^+$, $w_t = (\sum_{i \in S} \ell_{i,t})^- \ \forall\, t \in T$.

We consider a cooperative game model G defined by the set of prosumers N and the characteristic

function $V : S \in 2^N \to \mathbb{R}^+$ given by (3.2).

$$V(S) = \sum_{i \in S} C(\{i\}) - C(S) \tag{3.2}$$

The characteristic function V can be interpreted as the surplus that can be achieved by a coalition comparing their collective bill to the situation where each customer deals with the utility individually. We next show that getting together is attractive for prosumers.

3.2.3 Other preliminaries

Next, we go over some preliminaries of cooperative game theory and results from related research that is relevant to our approach.

Definition 1. *We say a function $f : S \subseteq N \to \mathbb{R}$ is superadditive if for all disjoint sets $S, T \subseteq N$, we have $f(S \cup T) \geq f(S) + f(T)$.*

Theorem 2 (Theorem 1 of [36])**.** *The value function V is superadditive.*

Proof. To make this report self-contained and to account for differences in model description, a proof is provided in Section 3.A. □

Theorem 2 implies that for any partition $\mathscr{P}$ of the set N, $V(N) \geq \sum_{S \in \mathscr{P}} V(S)$, and thus, it is socially optimal for all customers to join the same coalition, which is called the *grand coalition*. The next natural question is if all participants can be incentivized to do the socially optimal action of joining the grand coalition.

Definition 2. *An allocation or imputation is a vector $x \in \mathbb{R}^{|N|+} : \sum_{i \in N} x_i = V(N)$.*

The value of the grand coalition $V(N)$ is the total surplus that the entire set of prosumers can achieve by coordinating. An allocation is one possible distribution of this surplus among the participants.

Definition 3. *We say that a coalition S blocks or is blocking for allocation x if $\sum_{i \in S} x_i < V(S)$*

If a coalition S is blocking for allocation x, the prosumers in S could abandon the grand coalition, coordinate only among themselves and find an alternative allocation in which they would all receive no less surplus than they are receiving under allocation x, with some receiving strictly more. Therefore, the existence of blocking coalitions provokes the collapse of the grand coalition. This introduces the concept of stability: an imputation x is said to be *stable* if there exists no coalition that is blocking for x. The set of all stable coalitions is called the *core* of game G. We denote the core of G with $\mathscr{C}$.

The *Shapley allocation* is an important concept from the cooperative game theory literature; it represents the allocation that best remunerates each participant's contribution to the group, and is the most fair allocation in that sense. It is unique, denoted by ϕ and can be computed from (3.3). Note that the expression in (3.3) requires enumerating all combinations of coalitions in N, which

becomes computationally intractable for larger games. Moreover, the Shapley imputation is only guaranteed to be in the core of the game for convex games.

$$\phi_i = \frac{1}{N} \sum_{S \subseteq N \setminus \{i\}} \frac{(V(S \cup \{i\}) - V(S))}{\binom{n-1}{n-|S|-1}},\ i \in N \tag{3.3}$$

Theorem 2 of [36] shows that this game is balanced, and thus has a nonempty core. However, the game is not convex, so the Shapley imputation is not guaranteed to be stable. [35] find in their numerical tests several such instances. We provide a small example of an unstable Shapley imputation in an instance of our game in Example 3.

We are not interested in just any stable imputation; in the next section, we define a particular class of imputations on which we will focus for the remainder of the chapter.

3.3 Uniform price imputations

In this section, we present the first of our main contributions. We formalize the set of imputations that we are interested in obtaining, prove that this set is not empty, and provide an efficient method to get an imputation therein.

First, it will be useful in our context to interpret allocations not just as distributions of surplus, but also as proposals for splitting the collective bill, so we introduce one more definition.
Definition 4. *A bill splitting is a vector* $b \in \mathbb{R}^{|N|} : \sum_{i \in N} b_i = C(N)$ *with* $b_i \leq C(\{i\})$ *for all* $i \in N$.

We interpret b_i as the amount charged to customer i's by the local electricity market, i.e. their local electricity bill. If negative, $|b_i|$ is the amount paid to customer i. It is easy to verify that there is a 1:1 correspondence between bill splittings and imputations given by $b_i = C(\{i\}) - x_i$ for each $i \in N$. Similarly, a coalition S is blocking for x if and only if $\sum_{i \in S} b_i > C(S)$. For a given imputation, we refer to its corresponding bill splitting as its *bill-splitting form*. We denote the core in bill-splitting form $\mathscr{B}$. The core can be expressed in regular and bill-splitting form respectively as:

$$\mathscr{C} = \left\{ x \in \mathbb{R}^{|N|+} : \sum_{i \in N} x_i = V(N), \sum_{i \in S} x_i \geq V(S)\ \forall S \subseteq N \right\} \tag{3.4}$$

$$\mathscr{B} = \left\{ b \in \mathbb{R}^{|N|} : \sum_{i \in N} b_i = C(N), \sum_{i \in S} b_i \leq C(S)\ \forall S \subseteq N \right\}. \tag{3.5}$$

3.3.1 The uniform price core

To facilitate the implementation of the cost sharing mechanism, we want imputations to be describable through uniform prices. In other words, we want to define local selling and buying prices of

Table 3.1: Values of the collective bill for all coalitions in Example 1.

S	$C(S)$	S	$C(S)$
$\{A\}$	-2	$\{A,B\}$	-1
$\{B\}$	5	$\{A,C\}$	5
$\{C\}$	15	$\{B,C\}$	20
$\{A,B,C\}$	10		

electricity, such that each participant's bill can be expressed as the result of a sequence of buying and selling transactions, performed at prices that are common to all market participants.

Definition 5. *A uniform price imputation or uniform price allocation in the context of game G is an imputation x (or b, in bill-splitting form) for which there exist prices $\lambda^b, \lambda^s \in \mathbb{R}^{|T|+}$ such that $h_t \leq \lambda_t^b, \lambda_t^s \leq p_t$ for each $t \in T$, and:*

$$b_i = \sum_{t \in T} \left(\lambda_t^b \left(\ell_{i,t}^* \right)^+ - \lambda_t^s \left(\ell_{i,t}^* \right)^- \right) \ \forall i \in N \tag{3.6}$$

, where $\ell_{i,t}^*$ is the value of $\ell_{i,t}$ in an optimal solution of (P_N).

We denote the set of uniform price allocations with $\mathscr{U}$, and its bill-splitting form with $\mathscr{V}$. Its intersection with the core is called the *uniform price core*. We have found no examples in the P2P electricity market literature where the concepts of uniform price allocations and uniform price core are formalized as we have done here, although they are implicitly defined by [36]. We believe this formalization is not a moot point, because the *core* and the *uniform price core* are not the same, as shown in Example 1.

Example 1 ($\mathscr{U} \cap \mathscr{C} \neq \mathscr{C}$)**.** *Consider a simple case with three participants $N = \{A,B,C\}$, and one time period. We drop the time subscript for this example. The utility prices are p=5$/kWh, h=1$/kWh. Participant A has a net generation of 2kWh. B has a net consumption of 1kWh and C a net consumption of 3kWh. There are no BESSs in this example. Table 3.1 gives the collective bill $C(S)$ for each coalition, i.e. the optimal value of (P_S) for each $S \subseteq N$.*

Substituting the values in Table 3.1 into (3.5) and working through some algebra we get the characterization of the core in bill-splitting form:

$$\mathscr{B} = \{(b_A, b_B, b_C) = (\sigma, 5, 5-\sigma), \sigma \in [-10, -6]\}.$$

Now let us characterize the uniform price core for this example. With λ^s the local price for selling and λ^b the local price for buying, uniform price imputations in bill-splitting form are

$$\mathscr{V} = \Big\{ (b_A, b_B, b_C) = (-2\lambda^s, \lambda^b, 3\lambda^b), \\ 2\lambda^b - \lambda^s = 5, 1 \leq \lambda^s, \lambda^b \leq 5 \Big\}.$$

, which implies $b_C = 3b_B$, so that the only uniform price allocation in the core is obtained making $\sigma = -10$, and is $\mathscr{B} \cap \mathscr{V} = \{(b_A, b_B, b_C) = (-10, 5, 15)\}$. In other words, allocations in bill-splitting form $(b_A, b_B, b_C) = (\sigma, 5, 5-\sigma), \sigma \in (-10, -6]$ are all in the core, but cannot be expressed through uniform prices.

3.3.2 Shadow price imputations

We are now ready to introduce shadow price imputations. These imputations are related to (D_S), the dual of (P_S). In fact, we will show that shadow price imputations are *Owen imputations* for our linear game. A description of (D_S) is given in (3.7).

$$
\begin{aligned}
&(D_S): W(S) = \\
&\max_{\substack{\pi,\alpha,\beta \\ \underline{\gamma},\overline{\gamma},\delta}} \sum_{t\in T, i\in S} \pi_t \left(d_{i,t} - g_{i,t}\right) + \alpha_{i,t}\overline{s_i} + \beta_{i,t}\overline{s_i} + \underline{\gamma_{i,t}} \left(\underline{E_i} - e_i^0\right) + \overline{\gamma_{i,t}} \left(\overline{E_i} - e_i^0\right) && \text{(3.7a)} \\
&\text{s.t. } -\pi_t + \alpha_{i,t} + \sum_{\tau=t}^{|T|-1} \eta_i^c \underline{\gamma_{i,\tau}} + \eta_i^c \overline{\gamma_{i,t}} + \eta_i^c \delta_i \leq 0 \ \forall i \in S, t \in T && [s_{i,t}^c] \quad \text{(3.7b)} \\
&\eta_i^d \pi_t + \beta_{i,t} - \sum_{\tau=t}^{|T|-1} \left(\underline{\gamma_{i,t}} + \overline{\gamma_{i,t}}\right) - \delta_i \leq 0 \ \forall i \in S, t \in T && [s_{i,t}^d] \quad \text{(3.7c)} \\
&\pi_t \leq p_t \ \forall t \in T && [z_t] \quad \text{(3.7d)} \\
&-\pi_t \leq -h_t \ \forall t \in T && [w_t] \quad \text{(3.7e)} \\
&\alpha_{i,t}, \beta_{i,t}, \overline{\gamma_{i,t}} \leq 0, \underline{\gamma_{i,t}} \geq 0 && \text{(3.7f)}
\end{aligned}
$$

The first main result of this work is given by the following theorem.

Theorem 3. *Let $\left(z^*, w^*, s^{c*}, s^{d*}\right)$ and $(\pi^*, \alpha^*, \beta^*, \underline{\gamma}^*, \overline{\gamma}^*, \delta^*)$ be an optimal solution pair to the primal-dual pair $(P_N), (D_N)$. Then the imputation given in bill-splitting form for each $i \in N$ by (3.8) is in the uniform price core of the game.*

$$\theta_i = \sum_{t\in T} \pi_t^* \ell_{i,t}^* \tag{3.8}$$

, where $\ell_{i,t}^*$, as usual, is a shorthand for $d_{i,t} - g_{i,t} + s_{i,t}^{c*} - \eta_i^d s_{i,t}^{d*}$.

The crux of our proof is in the following proposition.

Proposition 1. *Let $(z^*, w^*, s^{c*}, s^{d*})$, $(\pi^*, \alpha^*, \beta^*, \underline{\gamma}^*, \overline{\gamma}^*, \delta^*)$ be a pair of optimal primal-dual solu-*

tions to the primal-dual pair $(P_N), (D_N)$. Then, for each $i \in N$:

$$\begin{aligned}\sum_{t\in T} \pi_t^* \ell_{i,t}^* = \sum_{t\in T} [&\pi_t^* (d_{i,t} - g_{i,t}) \\ &+ \alpha_{i,t}^* \overline{s_i} + \beta_{i,t}^* \overline{s_i} \\ &+ \underline{\gamma}_{i,t}^* \left(\underline{E_i} - e_i^0\right) + \overline{\gamma}_{i,t}^* \left(\overline{E_i} - e_i^0\right)\Big] \end{aligned} \tag{3.9}$$

Proof. See Appendix 3.A.2. □

Proof of Theorem 3. We first check that θ is indeed a uniform price allocation in bill-splitting form. θ satisfies the form of Definition 5 with $\lambda^b = \lambda^s = \pi^*$, with $h_t \le \pi_t^* \le p_t$ by (3.7d) and (3.7e), so we need only verify that it is an allocation, i.e. that $\sum_{i\in N} \theta_i = C(N)$. Applying Proposition 1 and summing over $i \in N$, we get

$$\begin{aligned}\sum_{i\in N} \theta_i &= \sum_{i\in N, t\in T} \pi_t^* \ell_{i,t}^* \\ &= W(N) \\ &= C(N)\end{aligned}$$

, where the second equality is true because summing over $i \in N$, the right-hand side of (3.9) becomes (3.7a), the optimal value of (D_N), and the last equality is true by strong duality of $(P_N), (D_N)$.

Next, we need to check that no coalition blocks allocation θ, i.e. we need to verify that $\sum_{i\in S} \theta_i \le C(S)$ for all $S \subseteq N$. Consider any $S \subseteq N$. Then applying Proposition 1 and summing over $i \in S$, we have:

$$\sum_{i\in S} \theta_i = \sum_{i\in S, t\in T} \left[\pi_t^* (d_{i,t} - g_{i,t}) + \alpha_{i,t}^* \overline{s_i} + \beta_{i,t}^* \overline{s_i} + \underline{\gamma}_{i,t}^* \left(\underline{E_i} - e_i^0\right) + \overline{\gamma}_{i,t}^* \left(\overline{E_i} - e_i^0\right)\right]. \tag{3.10}$$

Observe that the right-hand side of (3.10) is the objective value of (D_S) corresponding to the solution $\left(\pi^*, \left(\alpha^*, \beta^*, \underline{\gamma}^*, \overline{\gamma}^*, \delta^*\right)_{i\in S}\right)$, which it is easy to check is feasible for (D_S). Then:

$$\sum_{i\in S} \theta_i \le W(S) = C(S)$$

, where in the last equality we applied strong duality to the pair $(P_S), (D_S)$.

□

Remark 1. *Proposition 1 in the proof of Theorem 3 shows that shadow price allocations are just a different way of expressing a dual (or Owen) imputation of game G. As mentioned before, dual imputations are shown by [38] to be in the core for games with a linear production structure.*

Therefore, a different way to prove this result would be to verify that game G has the structure of a linear production game, and prove that the shadow price imputation corresponds to the Owen imputation, by e.g. invoking Proposition 1. Since the latter already includes most of the work of the whole proof, we decided to make this proof self-contained.

Theorem 3 gives us a uniform price allocation that is guaranteed to be in the core. Moreover, it is a uniform price allocation that has equal selling and buying prices for each time period. This implies the two corollaries below.

Corollary 1 (Non-emptiness of the uniform price core)**.** *The uniform price core of game G is not empty.*

Corollary 2 (Non-emptiness of the uniform price core with identical prices)**.** *The set of allocations in the uniform price core of game G with equal selling and buying prices is not empty.*

To close this section, we discuss some important consequences of Theorem 3. First, in [36], optimization problems are formulated where the feasible set is restricted to the set of uniform price imputations. Because the existence of core imputations was proven, it is assumed by the authors that stable uniform price imputations also exist, but there was no guarantee that the least-core optimization problem is feasible. Corollary 1 guarantees the existence of such imputations, and thus the soundness of that method.

In fact, Theorem 3 does more than just that: it also makes the method somewhat obsolete. The methodology in [36] requires solving a linear problem with an exponential number of constraints. [2] propose a sampling methodology to address this issue by working with a relaxation of the core. Both return an imputation in the uniform price core (or a relaxation thereof), without any preference among different imputations in that set. The shadow price imputation is guaranteed to be in the uniform price core and only requires solving a pair of primal-dual linear problems of small size, so it outperforms these two methods.

Now that we have a guarantee that the uniform price core is not empty, it makes sense to ask ourselves which of the imputations therein is the best one. We delve into that topic, through the lens of fairness, in Section 3.4.

3.3.3 Asymptotic uniqueness of shadow price imputations in the core

[38] also shows that although the core and the set of dual solutions are not the same (cf. Example 1), they do asymptotically become the same as the number of players grows to infinity through replication. In particular, all core allocations of the limit game are dual allocations. For our application, this has the important implication that as the number of participants grows to infinity, shadow price imputations are the only core imputations. This suggests that for markets with very large numbers of participants, no core allocation other than the shadow price imputation may exist, so the search for more fair allocations could be a pointless endeavor, unless core membership is sacrificed.

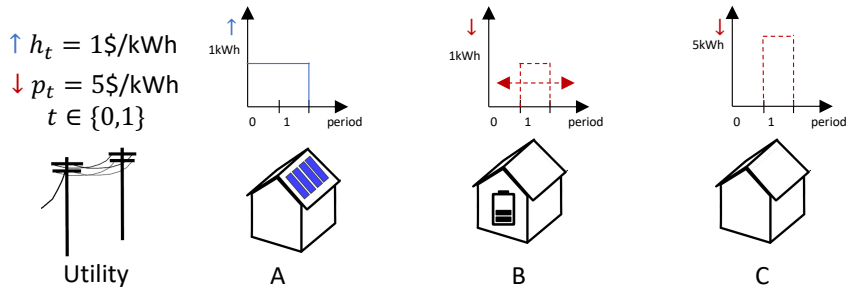

Figure 3.1: Schematic representation of Example 2. Case with three participants $N = \{A, B, C\}$, and two time periods $T = \{0, 1\}$. Participant A is a net producer of 1kWh each period; C is a net, inflexible consumer of 5kWh in the second period and 0kWh in the first period; and B has a lossless BESS, so B is a flexible consumer: B needs to consume 1kWh, but it can be in either period.

Two important clarifications are necessary here: first, Owen's result only shows that in the limit, all core imputations are dual imputations. However, because optimal solutions to (D_N) may not be unique, it is not true in general that, in the limit, the core is a singleton set. Second, this is only an asymptotic result, so numeric tests are necessary to see if this behavior is perceivable for markets with a meaningful number of participants.

3.4 Fairness of stable uniform price allocations

3.4.1 Motivation through some examples

At the end of Section 3.3, we introduced the shadow price imputation, an imputation that satisfies two of our stated desiderata: it is in the uniform price core and can be computed efficiently. In this section, by taking the perspective of fairness, we analyze whether other uniform price imputations might be preferred over the shadow price imputation. We first motivate this section with a couple of examples.

First, we introduce some notation: we denote $\mathscr{U}^\dagger$ (and $\mathscr{V}^\dagger$ in bill-splitting form) a restriction of the set of uniform price allocations to allocations where the buying price and the selling price are equal to each other at each time period.

Example 2 (Unfairness of the shadow price imputation)**.** *Consider a simple case with three participants $N = \{A, B, C\}$, and two time periods $T = \{0, 1\}$. Participant A is a net producer of 1kWh each period; C is a net, inflexible consumer of 5kWh in the second period and 0kWh in the first period; and B has an ideal BESS (no losses), so B is a flexible consumer: B needs to consume 1kWh, but it can be in either period. The situation of Example 2 is summarized in Figure 3.1.*

It is not hard to verify that minimal collective cost is achieved by having B shift their consumption to the first period. Table 3.2 gives the collective bill $C(S)$ for each coalition.

We will first restrict ourselves to uniform price imputations with equal selling price and buying

Table 3.2: Values of the collective bill for all coalitions in Example 2.

S	$C(S)$	S	$C(S)$
$\{A\}$	-2	$\{A,B\}$	-1
$\{B\}$	5	$\{A,C\}$	19
$\{C\}$	25	$\{B,C\}$	30
$\{A,B,C\}$	20		

price, i.e. $\lambda_t^b = \lambda_t^s = \lambda_t, t = 0,1$. *In bill-splitting form, these imputations are* $(b_A, b_B, b_C) = (-\lambda_0 - \lambda_1, \lambda_0, 5\lambda_1)$, *with* $b_A + b_B + b_C = C(N) = 20$. *This implies* $\lambda_1 = 5$, *so that the set of uniform price imputations with same selling price and buying price is given, in bill-splitting and regular imputation form respectively, by:*

$$\mathscr{V}^\dagger = \{(b_A, b_B, b_C) = (-5 - \lambda_0, \lambda_0, 25), \lambda_0 \geq 0\}$$
$$\mathscr{U}^\dagger = \{(x_A, x_B, x_C) = (3 + \lambda_0, 5 - \lambda_0, 0), \lambda_0 \geq 0\}$$

Note that participant C is being allocated \$0 savings by all these imputations, which include the shadow price imputation. However, C makes a positive contribution to the grand coalition: $V(A,B,C) = \$8$, $V(A,B) = \$4$. *In this case, the shadow price imputation would be unfair, as it is not remunerating participant C for their contribution. Such unfairness could fail to motivate C to join the local market, resulting in an overall loss for the whole community.*

As discussed in section 3.1, the best allocation in the sense of remunerating average contribution is the Shapley value, which we can compute from 3.3 and the values in Table 3.2 as $(\phi_A, \phi_B, \phi_C) = (4,2,2)$. *By relaxing the constraint of equal selling and buying prices* $\lambda_t^b = \lambda_t^s$, *the set of achievable imputations becomes, in bill-splitting form,* $\mathscr{V} = \left\{(b_A, b_B, b_C) = (-\lambda_0^s - \lambda_1^s, \lambda_0^b, 5\lambda_1^b), -\lambda_0^s - \lambda_1^s + \lambda_0^b + 5\lambda_1^b = 20\right\}$. *The Shapley allocation can thus be achieved with* $\lambda_1^b = 3, \lambda_2^b = 4.6, \lambda_1^s = \lambda_2^s = 3$.

Example 2 gives a situation where the shadow price allocation is unfair, in the sense that it allocates zero savings to a participant that provides a positive contribution to the grand coalition. In this example, allowing selling and buying prices to be different allows the implementation of a preferable allocation, namely the Shapley imputation. However, the Shapley value is not necessarily a suitable target imputation, since it may not be in the core of game G, as shown in Example 3.

Example 3 ($\phi \notin \mathscr{C}, \phi \notin \mathscr{U}$)**.** *Consider again the situation of Example 1. It was established there that the core imputations in bill-splitting form are given by*

$$\mathscr{B} = \{(b_A, b_B, b_C) = (\sigma, 5, 5 - \sigma), \sigma \in [-10, -6]\}.$$

We can compute the Shapley value in this example from 3.3 and Table 3.1 as $(\phi_A, \phi_B, \phi_C) = (14/3, 2/3, 8/3)$, *which it is straightforward to check is not in* $\mathscr{C}$ *because it is blocked by* $S = \{A, C\}$.

Moreover, the set of uniform price allocations is

$$\mathscr{V} = \left\{ (b_A, b_B, b_C) = \left(-2\lambda^s, \lambda^b, 3\lambda^b \right), -\lambda^s + 2\lambda^b = 5 \right\},$$

which implies $b_C = 3b_B$, so the Shapley imputation is not implementable through uniform prices either.

[35] propose the *nucleolus* as a desirable alternative to the Shapley value, since it is guaranteed to be in the core of the game. As the Shapley value, it quickly becomes computationally intractable for larger games, so it is a challenging target. Moreover, in our case, it may not be describable through uniform prices, as shown in Example 4.

Example 4 (Nucleolus not in $\mathscr{U}$)**.** *Consider again the situation of Example 1. Now, we target the nucleolus allocation, which can be computed to be $(x_A, x_B, x_C) = (6, 0, 2)$, or, in bill-splitting form, $(-8, 5, 13)$. Since the set of uniform price allocations has the form $(b_A, b_B, b_C) = \left(-2\lambda^s, \lambda^b, 3\lambda^b\right)$, the nucleolus is not implementable through uniform prices either.*

Although admittedly toy-sized, the previous examples are aimed at illustrating the following three ideas: there are other stable uniform price allocations that could be preferred over the shadow price imputation; preferable mechanisms could be achieved by allowing buying and selling prices to be different (Example 2); and the Shapley value and the nucleolus, conventional cost-sharing mechanisms from the cooperative game theory literature, besides being computationally intractable, may be unsuitable target allocations in our case. These three observations motivate the framework we propose next.

3.4.2 Finding the most fair allocation through optimization

In Section 3.3.2, we showed that the uniform price core is not empty and that one imputation therein, namely the shadow price imputation, can be efficiently computed. However, this allocation is not necessarily the most desirable one in $\mathscr{C} \cap \mathscr{U}$, as illustrated in Example 2. Here, we propose explicitly finding a most-desirable imputation in the uniform price core via an optimization problem:

$$\min_{x \in \mathscr{C} \cap \mathscr{U}} f(x),$$

, where f is an objective function that represents a preference over imputations. We can interpret $f(x)$ as a metric of the unfairness (or, more generally, the undesirability) of imputation x. f can also be thought of as a *welfare function*, as discussed in Section 3.1. In fact, we allow the preference over uniform price imputations to also be affected by the associated prices λ^b, λ^s, so the optimization problem can be written, with imputations expressed in bill-splitting form, as

$$(A): \quad \min_{b \in \mathscr{B} \cap \mathscr{V}} f(b, \lambda^b, \lambda^s).$$

Mechanisms of this form admit a version where selling and buying prices are restricted to be the same, which we denote with the superscript †:

$$(A^{\dagger}): \qquad \min_{b \in \mathscr{B} \cap \mathscr{V}^{\dagger}} f(b, \lambda).$$

We next illustrate our framework by introducing three possible options for the function f and discuss some of their characteristics.

Egalitarian mechanism

In the egalitarian mechanism, the imputation sought is that which minimizes the dispersion in the allocations to participants. This is achieved by making the objective function in (A) equal to f_e defined below:

$$f_e(x) = \sum_{i \in N} \left| x_i - (1/N) \sum_{j \in N} x_j \right|,$$

i.e. the standard deviation of the allocations with respect to the L^1 norm.

Minmax mechanism

In the *minmax* mechanism, we define f_m to measure the maximal difference in allocation of savings between prosumers, so that the mechanism finds the stable uniform price allocation that minimizes that difference.

$$f_m(x) = \max_{i \in N} x_i - \min_{i \in N} x_i.$$

Note that the ideal allocation with respect to both functions (i.e. the one with minimal value) would be one where all participants receive equal savings. So if the *equal division* allocation is feasible, both mechanisms are identical. However, the equal division allocation is not guaranteed to be in the uniform price core (cf. Example 1). If that is the case, these two mechanisms differ. An optimal allocation in the egalitarian mechanism is an allocation in $\mathscr{C} \cap \mathscr{U}$ that is closest to the equal division allocation, in L^1 distance (i.e. the L^1 projection onto $\mathscr{C} \cap \mathscr{U}$). In the minmax mechanism, on the other hand, only the imputations of the two most unequal participants matter.

These two definitions of fairness, although intuitive, have an important drawback in our context: users would have an incentive to misrepresent themselves as multiple agents and thereby multiply their allocations. For the scope of this project, we assume that it is verified that no agent misrepresents themselves.

Price-control mechanism

The last mechanism we consider is specific to our context and is a *price-control* mechanism. A way of describing the unfairness in Example 2 is that no surplus is allocated to the inflexible, net consumer C and most surplus is allocated to the net producer A. This is likely to happen when

electricity is priced at the marginal cost of procurement, as the shadow price allocation does. An intuitive compromise to make sure that both consumers and producers perceive benefits is to settle all local transactions at an intermediate price between the utility's export and import prices.

In this vein, one can define an ideal imputation as that induced by having the local selling and buying prices be equal to each other, and equal to the average between the utility's import and export prices, for each time period $\overline{p_t} = (1/2)(p_t + h_t)$. Since those prices are not guaranteed to support a stable, uniform price allocation, one can use its projection onto the uniform price core. With an L^1 projection, this results in an objective function f_p as follows,

$$f_p(b, \lambda^b, \lambda^s) = \sum_{t \in T} \left| \lambda_t^b - \overline{p_t} \right| + \sum_{t \in T} |\lambda_t^s - \overline{p_t}| .$$

3.4.3 Preliminary discussion

The three mechanisms presented before are simple, intuitive mechanisms to obtain the most-preferred allocation among all stable uniform price allocations according to three different, but reasonable preferences. Here, we discuss some limitations of the objective functions chosen, and possible improvements that are out of the scope of this project, but could be achieved with the framework presented here. We discuss this at this stage to highlight the relevance and versatility of this framework.

Projected Shapley value

In the examples presented as motivation for these mechanisms, we looked at fairness through a Shapley lens, i.e. the unfairness was understood as a failure of allocations to reflect the average marginal contribution of each participant to the grand coalition. However, the mechanisms proposed here do not compute or incorporate contributions when defining the allocation, and are instead based on simple, albeit reasonable, heuristics.

A better mechanism could be aimed at finding the uniform price stable allocation that is closest to the Shapley value, i.e. the projection of the Shapley allocation onto $\mathscr{C} \cap \mathscr{U}$. For smaller cases, the Shapley value is easily computable, so this is an easily implementable mechanism. However, for larger markets, this would become an intractable approach. Applying machine learning results to try to learn the projection of Shapley onto the uniform price core through sampling is an interesting avenue of research, but is considered out of the scope of this project.

Weighted egalitarian

An immediate extension of the egalitarian mechanism presented here is a weighted version, with different weights given to each participant. Such weights could be updated with some frequency based on historical data and be intended to reflect the historical marginal contribution of each participant, in the vein of learning the Shapley projection from data.

Fairness could also be seen through a social lens. In this case, these weights could be fixed values dependent on some structural data, like household income or household size. So this framework is also compatible with a *social* interpretation of fairness.

L^p projections

In all the mechanisms presented here, we use L^1 for all projections and measures of dispersion of allocations. We have done this for simplicity, to maintain the linearity of all the optimization problems of type (A). However, note that the the non-emptiness of $\mathscr{C} \cap \mathscr{U}$ is independent of the structure of function f, so non-linear objective functions, including L^p projections with $p > 1$ could be used instead. Investigating the effect of such choices on the resulting imputations is an interesting problem, but is considered out of the scope of this project.

Adding a regularization term

The uniform prices resulting from these mechanisms may oscillate frequently between the utility sell and buy prices. This could be considered undesirable, and could be corrected through the inclusion of a regularization term of the form $\rho(\lambda_t - \lambda_{t-1})^2$. As mentioned in the previous paragraph, non-linearities are not an issue for this framework, so regularization could be added to any of these mechanisms.

Restricting prices to be equal

Since problems of form (A) are a relaxation of problems of form $(A^\dagger)$, their objective functions will be no worse than that of the restricted counterparts. Moreover, Example 2 shows a case where allowing different prices results in a more desirable imputation that was unreachable before. Thus, it seems that mechanisms with same prices are weakly dominated by mechanisms that allow different prices and there should be no reason to consider the restricted version. We give here two reasons why we consider them.

First, note that the weakly dominance is true *with respect to each problem's objective function*, but not across metrics. So it is possible that a mechanism with prices restricted to being equal outperforms others with respect to an external benchmark. Secondly, a mechanism with the same price for selling and buying could be considered easier to communicate to participants, so it could be preferred by market designers if its performance is comparable to that of the mechanism with different prices.

Scalability

All of these mechanisms share one issue: the description of the uniform price core requires an exponential number of constraints. This is not a problem for markets of moderate size, like the ones used for the numerical tests that are presented next, but leads to an intractable mechanism as the number of participants increases. The issue of scalability is addressed in Section 3.5.

3.4.4 Numerical tests

To test the proposed framework and observe how the different proposed objective functions might lead to different outcomes, numerical tests are conducted on two test cases. The test cases are constructed by taking a set of buildings from the Resstock database of [45], which contains simulated consumption and PV production data for buildings across the U.S. for an entire year at 15-minute intervals. This dataset does not contain storage information, so it is completed by assigning BESSs of two sizes to certain prosumers, with BESS data adapted from [36]. Two instances are created: one with $n = 4$ prosumers and one with $n = 8$ prosumers. The time horizon is a day, so for each case, 365 instances of problem (A) for each of the three definitions of the objective function f are solved. For each mechanism, we solve the version with and without the restriction of equal selling and buying prices, i.e. (A) and $(A^\dagger)$. Note that to describe each of these optimization problems, we need to solve (P_S) for each $S \subseteq N$, but this only needs to be done once, since the optimal schedule is the same for all (A) and $(A^\dagger)$. The resulting imputations are compared to the shadow imputation, which only requires solving (P_N), (D_N) once. Additionally, these two test cases are sufficiently small that the Shapley value can be computed for each of the 365 instances using (3.3), so that the distance to the Shapley value can be used as benchmark for comparing results.

Extensive details about the test cases and results obtained are presented in Appendix 3.C.2. Due to space constraints, we present here only Fig. 3.2, where we use the distance to the Shapley imputation as benchmark. Three observations are noteworthy here. First, all three proposed mechanisms serve their purpose: imputations about 30% more fair on average are obtained with this framework for the smaller test case, compared to the shadow imputation. The improvement decreases to about 18% for the larger test case. Second, no mechanism seems to clearly outperform the others with respect to this benchmark. The same is true for allowing prices to be different: there seems to be no significant difference between the two versions of each mechanism, and no version is consistently better than the other. Lastly, the differences between the mechanisms proposed are significantly reduced for the larger case, both with respect to each other, and with respect to the shadow imputation. This is in line with the asymptotic result of Section 3.3.3, and suggests that for moderate-size markets, the size of the core is already sufficiently small, that implementing the shadow price imputation does not constitute a significant sacrifice of achievable fairness. Identifying if this tendency continues as the number of participants increases requires a special handling of the exponential number of constraints in the description of $\mathscr{C} \cap \mathscr{U}$, which we address in Section 3.5.

3.5 Addressing scalability through learning

Solving any of the optimization problems of type (A) or $(A^\dagger)$ introduced in Section 3.4 requires enumerating an exponential number of constraints (cf. (3.5)). If an efficient algorithm can be devised to test whether a candidate imputation is in the uniform price core or not, then the number of constraints is not an issue, because a constraint-generation strategy can be easily implemented to only include relevant constraints in the representation of (A).

We do not have a proof at hand to show that this uniform price membership test is *hard* in a formal sense. However, in the absence of an efficient separation algorithm, we propose a sampling ap-

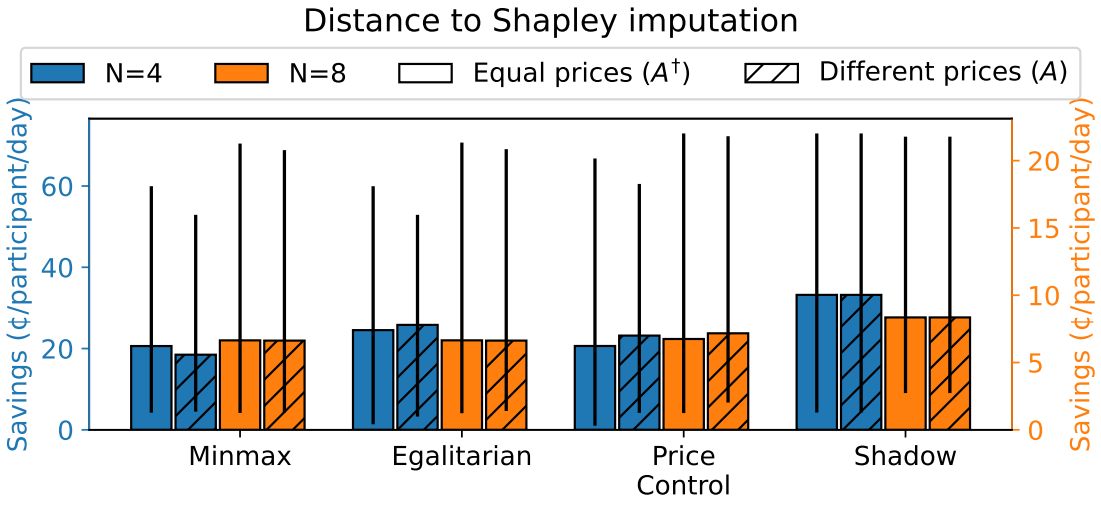

Figure 3.2: Euclidean distance between each the resulting allocation and the Shapley imputation for each mechanism. To meaningfully compare distances of different dimensions, we divide by the number of participants, so the distance plotted here is $(1/|N|)\left(\sum_{i\in N}(\phi_i - x_i)^2\right)^{1/2}$, where x is the imputation returned by each mechanism and ϕ is the Shapley imputation. Main bars represent the average across the 365 daily instances of the test case. Error bars show the min and max distances across the same dataset. Average savings achieved by the aggregation market are 54.56¢/participant/day for $n = 8$ and 99.99¢/participant/day for $n = 4$.

proach based on statistical learning to obtain satisfactory, scalable versions of the fair mechanisms proposed in Section 3.4.

3.5.1 Relaxations of the uniform price core

[44] introduce the concept of *probably stable core* and *probably, approximately stable core*. We adapt those concepts to the setting of peer-to-peer markets and formalize a definition for our uniform price core by considering the intersection with $\mathscr{V}$, as follows.

Definition 6. *Given $\delta > 0$, we say a uniform price imputation in bill-splitting form $b \in \mathscr{V}$ for game G is in the δ-probably stable uniform price core of game G if for any distribution $\mathscr{D}$ on coalitions, we have*

$$\mathrm{P}_{S\sim\mathscr{D}}\left[\sum_{i\in S} b_i \leq C(S)\right] \geq 1-\delta$$

Definition 7. *Given $\delta, \varepsilon > 0$, we say a uniform price imputation in bill-splitting form $b \in \mathscr{V}$ for game G is in the (ε,δ)-probably, approximately stable uniform price core of game G if for any distribution $\mathscr{D}$ on coalitions, we have*

$$\mathrm{P}_{S\sim\mathscr{D}}\left[(1-\varepsilon)\sum_{i\in S} b_i \leq C(S)\right] \geq 1-\delta$$

If a proposed bill-splitting b is in the (ε,δ)-probably, approximately stable uniform price core, then for any subset S of prosumers drawn from a distribution $\mathscr{D}$, the probability that the coalition S would be better off by forming their own P2P market and could profit by a fraction of at least ε of their collective bill dictated by b is less than δ.

In other words, a mechanism that gives imputations in the (δ,ε)-probably, approximately stable core with δ and ε sufficiently small is a satisfactory mechanism: participants are unlikely to find a combination of prosumers with which it would be profitable to deflect from the grand coalition. They could find one, but it is unlikely that the collective profit compared to the proposed mechanism would be sufficiently large to motivate a deflection.

3.5.2 A sampling method to obtain satisfactory imputations

[44] show for general cooperative games that allocations in the two aforementioned relaxations of the core can be learned efficiently as the number of players in the game increases by sampling only a subset of all the possible coalitions. A conceivable strategy could therefore be to first find a general allocation that minimizes the desired objective function, and then find a set of uniform prices that supports the obtained allocation. We discard this strategy for two reasons: first, it would exclude functions f that depend on the local prices themselves; secondly, not all allocations in the core are guaranteed to be supported by uniform prices (cf. Example 1).

We show next that allocations supported by prices can be learned directly via sampling by solving an optimization problem of the form $(A^\star)$,

$$
\begin{aligned}
(A^\star): \quad & \min_{b,\lambda^b,\lambda^s} f(b,\lambda^b,\lambda^s) && \text{(3.11a)}\\
& \text{s.t.} \sum_{i\in N} b_i = C(N) && \text{(3.11b)}\\
& b_i \le C(\{i\})\ \forall i\in N && \text{(3.11c)}\\
& \sum_{i\in N} b_i \le C(S)\ \forall S\in\mathscr{S} && \text{(3.11d)}\\
& b_i = \sum_{t\in T} \lambda_t^b \left(\ell_{i,t}^*\right)^+ - \lambda_t^s \left(\ell_{i,t}^*\right)^-\ \forall i\in N && \text{(3.11e)}\\
& h_t \le \lambda_t^s, \lambda_t^b \le p_t\ \forall t\in T && \text{(3.11f)}
\end{aligned}
$$

, which is a relaxation of (A) where constraint (3.11d) is enforced just for the coalitions in a sample set $\mathscr{S}$ instead of for all $S\subseteq N$.

Theorem 4. *Assuming the uniform price core is not empty, solving optimization problem* $(A^\star)$ *with* $|\mathscr{S}| = m$ *samples of coalitions results in an imputation in the* δ*-probably stable uniform price core with probability* $1-\Delta$*. The number of samples necessary m has complexity* $O\left(\frac{|N|+\log(1/\Delta)}{\delta^2}\right)$

Proof. See Section 3.A.3. □

Theorem 5. *Assuming the uniform price core is not empty, solving optimization problem* $(A^\star)$ *with* $|\mathscr{S}| = m$ *samples of coalitions results in an imputation in the* (ε, δ)*-probably approximately stable uniform price core with probability* $1 - \Delta$*. The number of samples necessary m has complexity* $O\left(\nu^2 \frac{\log|N| + \log(1/\Delta)}{\varepsilon^2 \delta^2}\right)$*, where* $\nu = (\max_S C(S)) \,/\, \left(\min_{S \neq \emptyset} |C(S)|\right)$ *is the spread of function C.*

Proof. See Section 3.A.4. □

Theorems 4 and 5 are important because they guarantee, asymptotically, that with a sufficiently large, but tractable, number of samples m, an allocation can be obtained such that it will be unlikely that a participant can find a set of other prosumers with whom it could be profitable to form a new peer-to-peer market. Moreover, if they find such a set, it is unlikely that the profit they could reap by deflecting is significant. Since these are only asymptotic guarantees, they need to be validated with numerical experiments.

Note $(A^\star)$ is a relaxation of (A). Theorems 4 and 5 give an asymptotic, probabilistic guarantee that, although the imputation obtained with $(A^\star)$ may not be strictly feasible for (A), it can be arbitrarily close to the feasible set, in a probabilistic sense. However, they do not give any bounds on the quality of the approximation in terms of objective value. We want to argue that this is not a weakness of the approach.

One could be tempted to give some structure to the metric functions f chosen (e.g. Lipschitz continuity) and obtain similar bounding results for the approximation quality. This could be of value if the approach was driven by a tradeoff between stability and fairness, i.e. if we were adopting $(A^\star)$ instead of (A) because we are willing to sacrifice some guarantee of stability to achieve a more fair distribution of savings. In fact, our approximation is driven by computational intractability. The solution obtained from $(A^\star)$ is sufficiently close to the feasible set of (A) to prevent the collapse of the local market. Moreover, the solution obtained is guaranteed to be at least as fair as the optimal solution of (A). Therefore, this methodology results in a satisfactory mechanism, provided the number of samples necessary is not too large.

3.5.3 Numerical tests

We do a numerical implementation to test the results presented above. First, since the results of Theorems 4 and 5 are only asymptotic, we want to verify that they can be observed with a reasonably small number of samples. Secondly, Section 3.3.3 suggests that for large enough markets, all core imputations may be shadow price imputations, so it may not be possible to find stable allocations significantly more fair than the shadow price imputation. We want to check if this behavior can be observed in numerical tests.

The tests are performed on cases with 10, 12, 15, 20 and 50 participants, constructed in the same fashion of Section 3.4.4, for one arbitrary day in the dataset. For each case and objective function,

problem $(A^\star)$ is solved on a random sample $\mathscr{S}$ of coalitions, with increasing values of $|\mathscr{S}|$. The allocation returned is then tested against all coalitions in a verification set. For cases with $n \leq 15$, the verification set is 2^N. For the others, 20,000 coalitions are sampled and this set is used for verification. For simplicity, coalitions were sampled uniformly, so that probabilities correspond to just proportion of coalitions that were found to be blocking.

Fig. 3.4 shows a validation of the sampling method for the minmax mechanism. For space constraints, we omit the results for the other mechanisms, which are similar and can be consulted in the appendix. In short, the validation of Theorems 4 and 5 is successful: the introduction of more samples in $\mathscr{S}$ consistently reduces the probability of finding blocking coalitions. By slightly relaxing the stability requirement that defines when a coalition is blocking, ($\varepsilon = 0.005$), that probability drops much more quickly: with as little as 200 samples, the number of blocking coalitions found is close to 0 for all test cases. The bottom plot in Fig. 3.4 provides perhaps a more direct interpretation of this result: as the number of samples in $\mathscr{S}$ is increased, the expected shortfall for the remaining blocking coalitions decreases very quickly, and therewith the potential motivation for leaving the p2p market.

For these larger cases, computing the Shapley value is too much of a computational burden; however, the shadow imputation can be efficiently found for all these instances from solving the dual solution to (D_N). We compute the distance of the imputation obtained with each of the three mechanisms to the shadow imputation. Results are shown in Fig. 3.3. The trend observed in Fig. 3.2, and suggested by the asymptotic result of [38], mentioned in Section 3.3.3, indeed continues. As the number of participants increases, the imputations obtained with all the mechanisms are closer to the shadow imputation.

Further research in this topic on the rate of convergence, or otherwise put, the rate at which the size of the core shrinks, would be welcome. The results presented here provide a strong argument in favor of using the shadow price imputation as a mechanism in local, p2p markets.

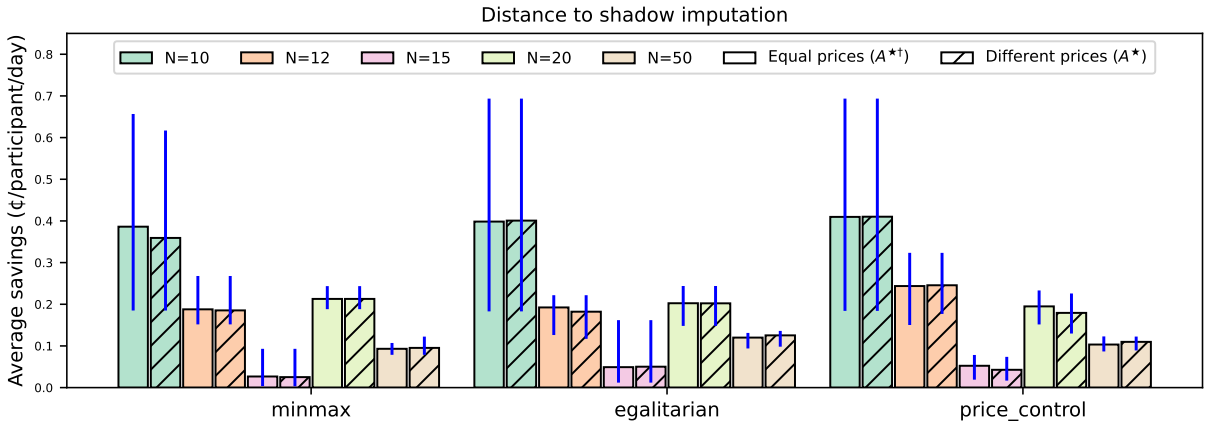

Figure 3.3: Euclidean distance[a] of resulting allocation from shadow imputation for each mechanism. Main bars represent the average distance across the 10 repetitions. Error bars show the min and max. For the day tested, the savings achieved by the aggregation market are 68.69 ¢/participant/day, so the difference allocations obtained are all within 0.5% of each other.

[a] To meaningfully compare distances of different dimensions, we divide by the number of participants, so the distance is $(1/|N|)\left(\sum_{i\in N}(\theta_i - x_i)^2\right)^{1/2}$, where x is the imputation returned by each mechanism and θ is the shadow imputation.

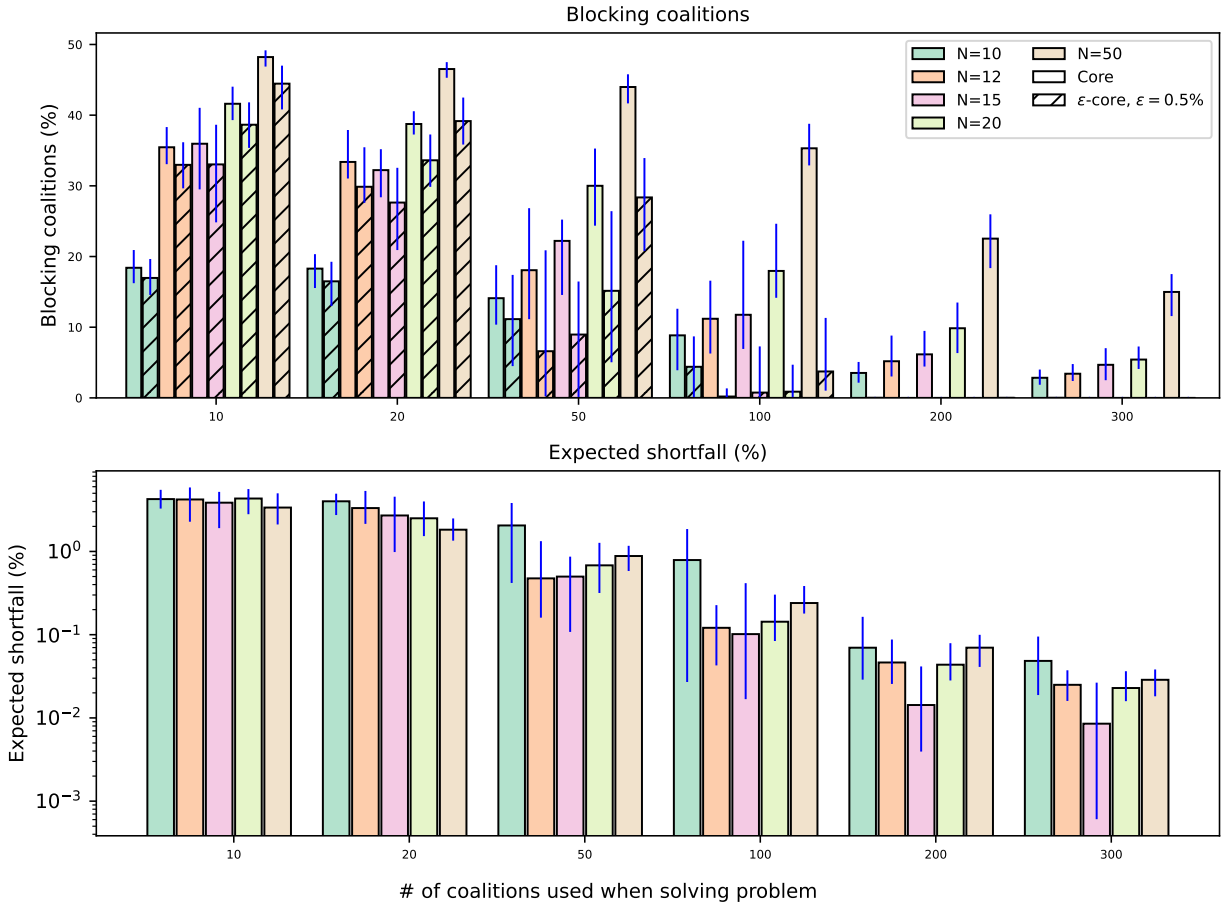

Figure 3.4: Results of validation tests of sampling methods for the minmax mechanism, with different test case sizes. *Top*: Proportion of coalitions that block the allocation proposed by the mechanism by at least a proportion ε of the collective bill, for $\varepsilon = 0$ and $\varepsilon = 0.005$. *Bottom*: Expected conditional shortfall[b] expressed as a proportion of collective bill in log scale. Similar results are obtained with the price-control and egalitarian mechanisms (see Appendix 3.C.2). Main bars represent the average over 10 repetitions. Error bars show the whole range of results obtained.

[b] Let Λ be the collection of blocking coalitions, i.e. $\Lambda = \{S \subseteq N : \sum_{i \in S} b_i > C(S)\}$, then the conditional expected shortfall shown is $(1/|\Lambda|) \sum_{S \in \Lambda} \left(\sum_{i \in S} b_i - C(S)\right) / \left(\sum_{i \in S} b_i\right)$.

3.6 Long-term participant and utility response

None of the modeling and analysis presented before consider the long-term response of the different stakeholders. In response to the distribution mechanism proposed, prosumers may choose to invest in local generation and/or storage to get a larger piece of the collective savings. Similarly, the utility may try to change its tariff structure in response to the revenue reduction that such an aggregation scheme would impose on them. Although a complete incorporation of these questions into our model is out of the scope of this work, we discuss some important points about the long-term considerations, and how the results presented here remain relevant in that context.

3.6.1 Long-term investments and participants response

In Examples 1 and 2, producers get a significantly higher share of the collective savings than pure consumers. This is also the dynamic we observe in the numeric tests (see Appendix 3.C.2). Under these conditions, in the long term, net consumers would have an incentive to invest in solar panels and/or battery storage to reap a larger fraction of the collective savings. However, that might be socially detrimental. In the extreme case, if all participants become net producers they would have no choice but to sell their electricity to the public utility, and there would be no possibility of achieving savings by aggregating demand.

An interesting avenue of future research for this work would thus be analyzing and characterizing long-term equilibrium conditions when individual investment decisions are considered. Alternatively, the investment decisions could be added to the cooperative game model. If investments can be modeled as linear variables, the mathematical results of this work could be easily extended to that case. This would correspond to a community where some generation and/or storage equipment is collectively owned, and the associated collective benefits need to be distributed among members.

3.6.2 Regulatory constraints and utility response

The analysis and concepts presented in this chapter are predicated on the assumption that the regulatory framework and the distribution system infrastructure enable the aggregation and peer-to-peer market that our mechanism supports. This is however not the case in most jurisdictions. In California, for example, separate properties may not, save limited exceptions, share one electricity meter, and allowing the distribution of generation credits corresponding to collectively owned solar systems among multiple customers is the subject of recent regulation and ongoing debate [46, 47]. Injections of power by prosumers may induce reverse energy flows in distribution systems, which usually have a radial topology. While coping with this reality has been the subject of research and development for well over a decade, most distribution systems maintain significant restrictions to bidirectional flow, posing limitations to peer-to-peer mechanisms like the ones proposed here. Changes to both the regulatory framework and the distribution system infrastructure would thus be necessary, before an implementation of any of the mechanisms proposed here can occur.

For these changes to happen, it is necessary to understand how public utility companies might react to an eventual sprout of local community aggregation schemes. As we have shown, significant

savings by customers can be achieved by aggregating demand, exploiting the spread between the public utility's buying and selling prices. Those savings come directly at the utility's expense, who would presumably react to such a reduction of revenue. We list below a few conceivable responses, and analyze how our proposed mechanism could be affected by them.

Adding a fixed charge

Perhaps the most likely response by the utility would be to replace its volumetric-only pricing structure with a two-part tariff with a fixed charge per billing period and a per-kWh charge. In the context of natural monopolies like electricity retail, such schemes have some desirable characteristics, like allowing electricity to be priced at a value closer to its marginal cost, thus enabling more efficient market outcomes. Additionally, if the fixed value charged to customers is made a function of their wealth or income, as proposed in [48], the mechanism would have the aggregated value of contributing to social equity.

Adding a capacity charge

A different, but related option would be to introduce a non-volumetric part of the tariff, but make it a charge per-kW of installed capacity. This could serve as a long-term incentive to reduce oversizing of installations and peak-shaving at the distribution level, both of which would increase long-term efficiency. Both of these options respond not only to the challenge of emerging CCAs, but to the reduction of revenue driven by the installation of local generation by individual residential customers, even in the absence of aggregation schemes.

Charging transaction costs

Another conceivable response from the utility company could be to charge prosumers a usage fee for using the utility's grid to trade energy among members of the CCA. In this scenario, volumetric rates would be maintained, but a usage fee per-kWh would be charged to prosumers who inject power into the utility's grid. Provided that the sum of the usage fee and the utility's injection price is less than the utility's selling price, the incentive for aggregation would still exist, although attainable collective savings would be smaller.

The three alternatives considered above guarantee that the utility recoups at least part of their fixed costs, even if the revenue from energy sales decreases. Under such a scenario, at least part of the reason for using distinct prices for energy consumed and energy injected would disappear, so the spread between these prices (h_t and p_t in our model) could be reduced. As long as the spread is positive, the results that we present in this chapter remain valid: there is an incentive for community aggregation and the mechanisms proposed here are implementable methodologies to distribute the savings, possibly with a measure of fairness in mind.

It is even conceivable that, as proposed in the transactive energy system paradigm, the utility may become a pure infrastructure provider and bow out of the energy retail business, remaining only as

a provider of last resort [49]. In such a scenario, the utility would have an incentive to make sure that agents trade chiefly among themselves. A high spread between buying and selling price would be a way to achieve that, making the results of this chapter relevant for that framework as well.

A thorough analysis of the dynamics of spread reduction and the formation of CCAs is out of the scope of this work, but is relevant and necessary research that should be taken into account by the regulator when determining the just and reasonable transaction fee or fixed charge that the utility may charge its customers.

3.7 Addressing the stochastic case

Before concluding, we discuss how the methodology presented here can be extended to handle the stochastic case, i.e. the case where solar PV production and electricity consumption are not known at the time when the scheduling problem (3.1) is solved. We consider a thorough analysis and development of the extended stochastic model out of the scope of this project and will only briefly outline how a stochastic model could be posed, and which challenges need to be overcome in that avenue of research.

Consider the case where the aforementioned uncertainty is represented through a discrete set of scenarios Ω. The scenarios could thus be added to a new dimension in the linear problem (3.1) along with their corresponding probabilities, so that (3.1) becomes a stochastic program. Under the assumption of relatively complete recourse, the validity of the strong duality results that we leverage in this work continue to hold [50]. It is thus also possible to solve the dual problem and obtain dual imputations which will be guaranteed to be in the core of the game. One important remark here is that imputations would now correspond to the result of transactions that are settled at uniform prices that are determined *ex-ante*.

The result above has an important implication regarding the strength of the mechanism. In particular, the concept of stability and core would be somewhat weaker than in the deterministic case. We will consider a uniform price imputation to be stable if no coalition can obtain a better outcome *in expectation* (i.e. ex-ante) Blocking ex-post coalitions, however, may exist. Stronger notions of stability have been proposed, but finding stable mechanisms is more challenging in those cases. See [51] for a deeper analysis of this issue in general linear stochastic games.

In the case where the net demand of participants is uncertain, the community demand aggregation can be thought of to a certain extent as an inventory centralization problem. In that vein, the methodology described before is analogous to that proposed in [37] in the context of stochastic inventory centralization games, which served as inspiration for this proposed extension.

3.8 Conclusions

In this chapter, we have adopted a game-theoretic approach to analyze the problem of fair cost sharing in peer-to-peer electricity markets where aggregation of prosumers is socially optimal. We have formally described a set of desired distributions of savings in this setting: uniform price

allocations, and showed that the set of stable uniform price allocations form a strict subset of the core of the game. Observing that the model considered is a linear production game, we have shown that imputations stemming from the dual problem, i.e. pricing electricity at the shadow price of the energy balance constraint, results in an imputation that satisfies all these desiderata and is computationally efficient for larger numbers of participants.

We then showed that in spite of its good qualities, the shadow price imputation could be considered unfair, and proposed a framework to obtain the most preferred allocation through optimization. A sampling approach is utilized to overcome the challenge of tractability posed by solving these optimization problems, supported by theoretical, asymptotic results from the statistical learning literature. Numerical tests validate the approach proposed.

By noting that the results of [38] apply to the setting considered here, we conclude that for sufficiently large markets, shadow price imputations are the only stable imputations in the market. Our numerical tests suggest that this trend begins to show for markets in the order of tens of participants. On the one hand, this offers strong support for using the shadow price imputation in real local markets of a certain size with a centralized aggregator, since no other stable alternative may exist. But, as we have demonstrated, this may result in net consumers failing to have an incentive to join the local community, so on the other hand this may be considered a reason to limit the size of such aggregations, so that there may be room in the uniform price core for more fair solutions, which can be found via optimization as we propose here.

Finally, we discussed two important considerations that were out of the scope of the work presented here. The first was long-term incentives and response by market participants and by the public utility. Although a thorough development of that analysis would be necessary and welcome before an implementation of the scheme proposed here is possible, we argue that our approach would still be relevant once those implications are considered. The second extension discussed is how the mechanism can be turned into a stochastic model to address the uncertainty associated with PV production and electricity demand. We outline that our results can be extended to handle that case as well.

Appendix

3.A Proof of theorems

This section contains the theorem proofs that were not included in the main text.

3.A.1 Proof of Theorem 2

Theorem 2 is identical to Theorem 1 of [36]. We provide a proof for completeness, to account for differences in notation and representation of the model.

Proof. Consider $S, T \subseteq N$, such that $S \cap T = \emptyset$. We will use q as a shorthand for (z, w, s^c, s^d). Let q^* be an optimal solution of $(P)_S$ and q^{**} an optimal solution of $(P)_T$. We construct $\hat{q}$ as follows: for $i \in S \cup T$, $\hat{s}_i^c = s_i^{c*}$ for $i \in S$, $\hat{s}_i^c = s_i^{c**}$ for $i \in T$. $\hat{s}_i^d$ is defined in the same manner. z and w are defined by $\hat{z}_t = \max\{0, z_t^* - w_t^* + z_t^{**} - w_t^{**}\}$, $\hat{w}_t = \max\{0, -(z_t^* - w_t^* + z_t^{**} - w_t^{**})\}$ for $t \in T$.

It is straightforward to verify that $\hat{q}$ is feasible for $(P)_{S\cup T}$. Let u be the objective value of $(P)_{S\cup T}$ corresponding to the feasible solution $\hat{q}$. We have therefore $C(S \cup T) \leq u$. We want to prove that $u \leq C(S) + C(T)$.

We introduce an auxilliary variable $v_t, t \in T$ to decompose $u - (C(S) + C(T))$, as follows.

$$u - (C(S) + C(T)) = \sum_{t \in T} v_t$$
$$v_t = p_t\left(\hat{z}_t - (z_t^* + z_t^{**})\right) - h_t\left(\hat{w}_t - (w_t^* + w_t^{**})\right)$$

We claim that for all t, $v_t \leq 0$. Recall that because $h_t < p_t$, optimal solutions to $(P)_S$ and $(P)_T$ satisfy $z_t^* w_t^* = 0$ and $z_t^{**} w_t^{**} = 0$ for all $t \in T$. We have thus four cases:

- $w_t^* = w_t^{**} = 0 \Rightarrow \hat{w}_t = 0, \hat{z}_t = z_t^* + z_t^{**} \Rightarrow v_t = 0$
- $z_t^* = z_t^{**} = 0 \Rightarrow \hat{z}_t = 0, \hat{w}_t = w_t^* + w_t^{**} \Rightarrow v_t = 0$
- $w_t^* = 0$, $z_t^{**} = 0$. Two cases:
  - If $z_t^* \geq w_t^{**}$, $\hat{w}_t = 0$, $\hat{z}_t = z_t^* - w_t^{**} \Rightarrow v_t = w_t^{**}(h_t - p_t) \leq 0$
  - If $z_t^* < w_t^{**}$, $\hat{z}_t = 0$, $\hat{w}_t = w_t^{**} - z_t^* \Rightarrow v_t = z_t^*(h_t - p_t) < 0$
- Same as *case 3*, swapping the roles of z_t^*, w_t^* and $z_t^{**}, w_t^{**} \Rightarrow v_t \leq 0$

Therefore, $v_t \leq 0$ for all $t \in T$. Summing over t, we get $u \leq C(S)+C(T)$, and thus $C(S \cup T) \leq u \leq C(S)+C(T)$. Finally, we have:

$$\begin{aligned}
& C(S \cup T) \leq C(S)+C(T) \\
\Leftrightarrow & -C(S \cup T) \geq -C(S)-C(T) \\
\Leftrightarrow & \sum_{i \in S \cup T} C(\{i\}) - C(S \cup T) \\
& \geq \sum_{i \in S} C(\{i\}) - C(S) + \sum_{i \in T} C(\{i\}) - C(T) \\
\Leftrightarrow & V(S \cup T) \geq V(S)+V(T)
\end{aligned}$$

□

3.A.2 Proof of Proposition 1

Proof. We denote $(LR-P)_S(\pi)$ the problem obtained by doing a Lagrangian relaxation of constraint (3.1b) in (P_S) and assigning it multiplier π. The objective function in $(LR-P)_S(\pi)$ is thus:

$$\begin{aligned}
& \sum_{t \in T} \left[p_t z_t - h_t w_t + \pi_t \sum_{i \in S} \left[d_{i,t} - g_{i,t} + \eta_i^d s_{i,t}^d - s_{i,t}^c \right) - (z_t - w_t) \right] \Bigg] \\
= & \sum_{i \in S, t \in T} \pi_t (d_{i,t} - g_{i,t}) + \sum_{t \in T} \left[(p_t - \pi_t) z_t - (h_t - \pi_t) w_t + \pi_t \sum_{i \in S} (\eta_i^d s_{i,t}^d - s_{i,t}^c) \right]
\end{aligned}$$

With constraint (3.1b) relaxed, there are now no constraints coupling z, w with s^c, s^d. Similarly, there are no constraints coupling s_i^c, s_i^d for different values of $i \in S$. Thus, $(LR-P)(\pi)$ can be separated into subproblems $(LR-P)_i(\pi)$ as described below. Let $(LR-D)_i(\pi)$ be the dual of $(LR-P)_i(\pi)$.

$$
\begin{aligned}
(LR-P)_S(\pi): & \sum_{i\in S, t\in T} \pi_t (d_{i,t} - g_{i,t}) && + \min_{z,w} \sum_{t\in T} \left[(p_t - \pi_t) z_t - (h_t - \pi_t) w_t\right] \\
& && + \sum_{i\in S} (LR-P)_i(\pi) \\
(LR-P)_i(\pi): & \min_{s_i^c, s_i^d} \sum_{t\in T} \pi_t (\eta_i^d s_{i,t}^d && - s_{i,t}^c) \\
& \text{s.t.} (3.1\text{c}) - (3.1\text{f}) \text{ for just } i && \\
(LR-D)_i(\pi): & \max_{\substack{\alpha_i, \beta_i, \delta_i \\ \overline{\gamma_i}, \underline{\gamma_i}}} \sum_{t\in T} \overline{s_i} \alpha_{i,t} + \overline{s_i} \beta_{i,t} && + \overline{\gamma}_{i,t} \left(\overline{E_i} - e_i^0\right) + \underline{\gamma}_{i,t} \left(\underline{E_i} - e_i^0\right) \\
& \text{s.t.} (3.7\text{b}) - (3.7\text{c}) \text{ for just } i &&
\end{aligned}
$$

By strong duality, $(z^*, w^*, s^{c*}, s^{d*})$ is also an optimal solution of $(LR-P)_N(\pi^*)$, so $\left(s_i^{c*}, s_i^{d*}\right)$ is an optimal solution to $(LR-P)_i(\pi^*)$ for each $i \in N$.

We claim that $(\alpha^*, \beta^*, \underline{\gamma}^*, \overline{\gamma}^*, \delta^*)_i$ is also optimal for $(LR-D)_i(\pi^*)$ for each $i \in N$. We prove this by contradiction and use q as shorthand for $(\alpha, \beta, \underline{\gamma}, \overline{\gamma}, \delta)$. It is easy to check that q_i^* is feasible for $(LR-D)_i(\pi^*)$. So if q_i^* is not optimal for $(LR-D)_j(\pi^*)$ for some $j \in S$, there exists q_j^{**} with higher objective value than q_j^*. But since the feasible sets are uncoupled, the solution $\left(\pi^*, (q_i^*)_{i\in S\setminus\{j\}}, q_j^{**}\right)$ is feasible for (D_N) and would have higher objective value than (π^*, q^*), which violates the optimality of (π^*, q^*) for $(D)_N$.

We thus have that $(s^{c*}, s^{d*}, (\alpha^*, \beta^*, \underline{\gamma}^*, \overline{\gamma}^*, \delta^*)_i$ is an optimal primal-dual solution for pair $(LR-P)_i(\pi^*), (LR-D)_i(\pi^*)$. Applying again strong duality to this pair, we obtain:

$$
\begin{aligned}
\sum_{t\in T} \pi_t^* \left(\eta_i^d s_{i,t}^{d*} - s_{i,t}^{c*}\right) = \sum_{t\in T} & \overline{s_i} \alpha_{i,t}^* + \overline{s_i}^* \beta_{i,t}^* \\
& + \overline{\gamma}_{i,t}^* \left(\overline{E_i} - e_i^0\right) \\
& + \underline{\gamma}_{i,t}^* \left(\underline{E_i} - e_i^0\right)
\end{aligned}
$$

, which adding $\sum_{t\in T} \pi_t^* (d_{i,t} - g_{i,t})$ to both sides yields (3.9). □

3.A.3 Proof of Theorem 4

Proof. Theorem 4 is a replica of Theorem 3 of [44], substituting the probably stable core with the probably stable uniform price core we have defined. We follow the steps of their proof, i.e. we find a class of functions that contains the uniform price core, verify that its VC-dimension is low, and use that to find an asymptotic bound on the number of samples necessary to find points in the uniform price core.

Proposition 2. *Let $n = |N|$, $u \in \mathbb{R}^{n+1}$, and $\ell \in \mathbb{R}^{n|T|}$. Let $\mathscr{H}'$ be the class of functions that define uniform price allocations in bill-splitting form, i.e.*

$$\mathscr{H}' := \left\{ u \to \operatorname{sign}\left(\sum_{i=1}^{n} b_i u_i - u_{n+1} \right) b \in \mathbb{R}^n, \lambda^b, \lambda^s \in \mathbb{R}^{|T|}, \right.$$
$$\left. \sum_i b_i = C(N), b_i = \sum_{t \in T} \left(\lambda_t^b \left(\ell_{i,t}\right)^+ - \lambda_t^s \left(\ell_{i,t}\right)^- \right) \ \forall i \in N \right\}.$$

Then, $\mathscr{H}'$ has VC-dimension at most $n+1$.

Proof. Following the argument of Corollary 1 of [44]:

$$\mathscr{H}' \subseteq \left\{ u \to \operatorname{sign}\left(\sum_{i=1}^{n} b_i u_i - u_{n+1} \right) : b \in \mathbb{R}^n \right\} \subseteq \mathscr{H} := \left\{ u \to \operatorname{sign}(w^\top u) : w \in \mathbb{R}^{n+1} \right\}$$

By Theorem 2 of [44], $\mathscr{H}$ has VC-dimension $n+1$. If $\mathscr{H}' \subseteq \mathscr{H}$, then $\operatorname{VCdim}(\mathscr{H}') \leq \operatorname{VCdim}(\mathscr{H})$.

□

To conclude, we follow the last step of the proof of Theorem 3 of [44] as follows. Consider $q^* = (b^*, \lambda^{b*}, \lambda^{s*})$, an optimal solution to $(A^\star)$, which is guaranteed to exist because the uniform price core is non-empty by assumption. We will show q^* is in the δ probably stable core. Let $h(u) = \operatorname{sign}\left(\sum_{i=1}^n b_i^* u_i^S - u_{n+1}^S\right)$, where $u_i^S = \mathbf{1}_{i \in S}$ and $u_{n+1}^S = C(S)$. Let $f(u) = -1$ for all u. Since (3.11d) is satisfied for all samples in $\mathscr{S}$, $f(u) = h(u)$ on all the samples, and thus, $(1/m)\sum_{i=1}^m \mathbf{1}_{h(u) \neq f(u)} = 0$.

$$\begin{aligned}
&\mathrm{P}_{S \sim \mathscr{D}} \left[\sum_{i \in S} b_i \leq C(S) \right] \\
&= 1 - \mathrm{P}_{u^S : S \sim \mathscr{D}} \left[\operatorname{sign}\left(\sum_{i=1}^{n} b_i u_i^S - u_{n+1}^S \right) \neq -1 \right] \\
&= 1 - \mathrm{P}_{u^S : S \sim \mathscr{D}} \left[h(u^S) \neq f(u^S) \right] \\
&= 1 - \left| \mathrm{P}_{u^S : S \sim \mathscr{D}} \left[h(u^S) \neq f(u^S) \right] - (1/m) \sum_{i=1}^{m} \mathbf{1}_{h(u^S) \neq f(u^S)} \right| \\
&\geq 1 - \delta
\end{aligned}$$

, where the last step is true by Theorem 1 of [44], with $\mathscr{O}\left(\left(n + \log(1/\Delta)\right)/\delta^2\right)$ samples because the VC-dimension of our hypothesis class $\mathscr{H}'$ is at most $n+1$ by Proposition 2. □

3.A.4 Proof of Theorem 5

The proof is a replica of the proof of Theorem 5 of [44], substituting the probably, approximately stable core with the probably, approximately stable uniform price core. It is easy to check that allocations in the uniform price core satisfy all the conditions of the theorem: they have bounded ℓ_1 norm because they are in the core (Lemma 2 of their proof), and candidate solutions to $(A^\star)$ can be found efficiently because it is a convex problem. It only remains to verify that $\min_{S\subset N, S\neq\emptyset} C(S) > 0$, where $C(S)$ is the characteristic function of the game in cost-minimization form.

The assumption is not true for game G, as we may have $C(S) \leq 0$. We show here that we can construct a game G' that satisfies this condition and has a 1:1 correspondence with game G.

Let $K \geq 0$ be a constant such that $C(S) > -K|S|$ for all $S \subseteq N$. Then, we can define G' as the game with set of players N and value function $V'(S) = \sum_{i\in S} C'(\{i\}) - C'(S)$, with $C'(S) = C(S) + |S|K$. Note that $V'(S) = V(S)$ for all $S \subseteq N$, $S \neq \emptyset$, so the correspondence between G and G' is clear, i.e. C' is a cost-minimization version of V, and clearly, $C'(S) > 0$ for all $S \subseteq N$. Therefore, we only need to prove that such a K exists.

Claim 1. $K = |T|\left(\max_{t\in T} p_t\right)\left(\max_{i\in N, t\in T} g_{i,t} + \max_{i\in N} \overline{s}_i\right)$ *satisfies* $C(S) > -K|S|\ \forall S \subseteq N$.

Proof. Let $p^\star = \max_{t\in T} p_t$, $g^\star = \max_{i\in N, t\in T} g_{i,t}$, $\overline{s}^\star = \max_{i\in N} \overline{s}_i$

Then, for any nonempty $S \subseteq N$, we have:

$$
\begin{aligned}
C(S) &= \sum_{t\in T} p_t z_t^* - h_t w_t^* \\
&= \sum_{t\in T} p_t \left(\sum_{i\in S} \ell_{i,t}^*\right)^+ - h_t \left(\sum_{i\in S} \ell_{i,t}^*\right)^- \\
&\geq \sum_{t\in T} -h_t \left(\sum_{i\in S} \ell_{i,t}^*\right)^- \\
&> -\sum_{t\in T} p_t \left(\sum_{i\in S} \ell_{i,t}^*\right)^- \\
&\geq -\sum_{t\in T} p_t \sum_{i\in S} \left(g_{i,t} + \eta_i^d s_{i,t}^{d*}\right) \\
&\geq -\sum_{t\in T} p_t |S| \left(g^\star + s^\star\right) \\
&\geq -|T| p^\star |S| \left(g^\star + s^\star\right) \\
&= -|S| K
\end{aligned}
$$

□

Table 3.B.1: Battery energy storage systems and price data used in test cases, adapted from [36].

Storage Type	$\overline{E_i}$	$\underline{E_i}$	$\overline{s_i}$	η_i^c	η_i^d
Small	7kWh	0.7 kWh	11.2kW	0.95	0.95
Big	14kWh	1.4 kWh	22.4kW	0.95	0.95

Time of day	p_t	h_t
Midnight - 7AM	7 ¢/kWh	4.03 ¢/kWh
7AM - Midnight	14.71 ¢/kWh	4.03 ¢/kWh

Table 3.B.2: Composition of the constructed test cases. Number of prosumers having PV and/or ESS for each test case used. In parenthesis, name assigned to participant in plot results when applicable.

Number of prosumers with	Total number of prosumers $N =$						
	4	8	10	12	15	20	50
No ESS, No PV	1 (D)	3 (A,D,H)	4	2	1	5	6
No ESS, PV	1 (A)	1 (C)	2	2	4	5	14
Small ESS, No PV	1 (C)	0	0	1	3	1	3
Small ESS, PV	0	2 (E,F)	2	4	3	3	12
Big ESS, No PV	0	1 (G)	0	1	1	2	6
Big ESS, PV	1 (B)	1 (B)	2	2	3	4	9

3.B Description of test cases for numerical implementations

All test cases are constructed by taking generation and consumption timeseries for residential buildings from the Resstock database [45]. We pick the census microdata area in California with the largest number of buildings with PV installations in the dataset, and filter the data so that only single-family houses remain. The test cases are built by arbitrarily picking buildings with and without solar photovoltaic. The data does not include energy storage systems (ESS), so battery ESS are arbitrarily assigned to some of the buildings. The characteristics of the ESS and the utility prices are taken equal to those reported in [36] and are summarized in Table 3.B.1.

Table 3.B.2 describes the types of agents included in each of the test cases considered. For the numerical tests of Section 4, all 365 days in the dataset were used. For the validation of the sampling method, one day in the data set was selected randomly.

The implementation was done in python using the *pyomo* modelling package and solved with *Gurobi*. All tests are run on a laptop with 2.7GHz Intel Core i5 and 8GB of RAM.

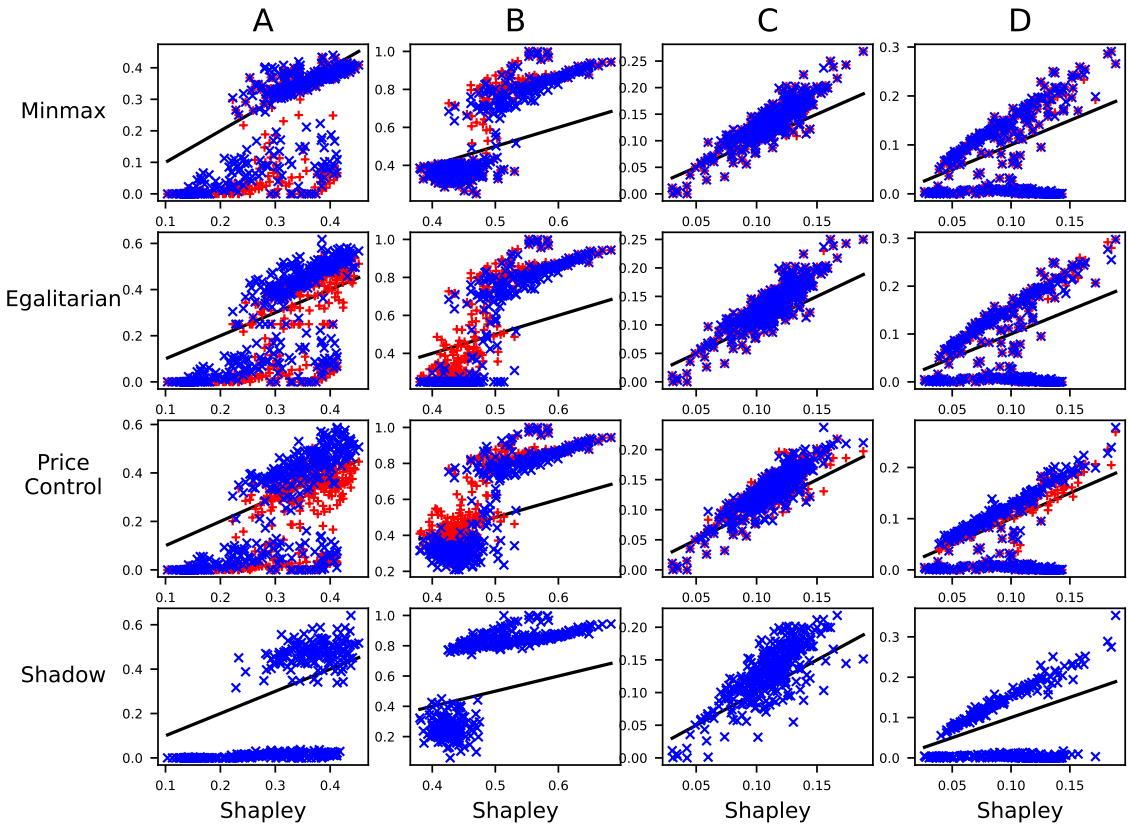

Figure 3.C.1: Scatter plot of proportion of savings allocated to each participant vs. corresponding Shapley allocation, for the four mechanisms considered. Each row corresponds to a mechanism, each column to a participant. Each point corresponds to a day in the year. The solid black line represents the $y = x$ line, so points above and under the line are overallocated and underallocated respectively, with respect to the Shapley allocation. $\times$ for allocations allowing for different selling and buying prices. $+$ for allocations restricted to having equal selling and buying prices. The shadow imputation has identical selling and buying prices.

3.C Extended results of numerical implementations

3.C.1 Optimization framework for most fair uniform price allocation

Figures 3.C.1 and 3.C.2 show detailed results of the numeric tests performed on the test case with $n = 4$ participants. Figure 3.C.3 show the results for the case with $n = 8$ participants.

Figure 3.C.4 shows the annual savings per participant under the shadow imputation for different market sizes. The results show that while it is true that the range of savings achieved by different participants vary significantly, all participants achieve positive savings, with a majority of the savings in the range of \$100's.

Figure 3.C.2: Proportion of savings allocated to each participant for the four mechanisms considered, case with $n = 4$ participants. Error bars show the range of allocations obtained during the 365 days. Main bars show the average across the year. Projected Shapley is the uniform price allocation in the core that is closest to the Shapley value in ℓ_1 norm.

3.C.2 Validation of sampling methodology

The results of the validation tests for the sampling methodology for the other mechanisms are presented in Figures 3.C.5, 3.C.6 and 3.C.7.

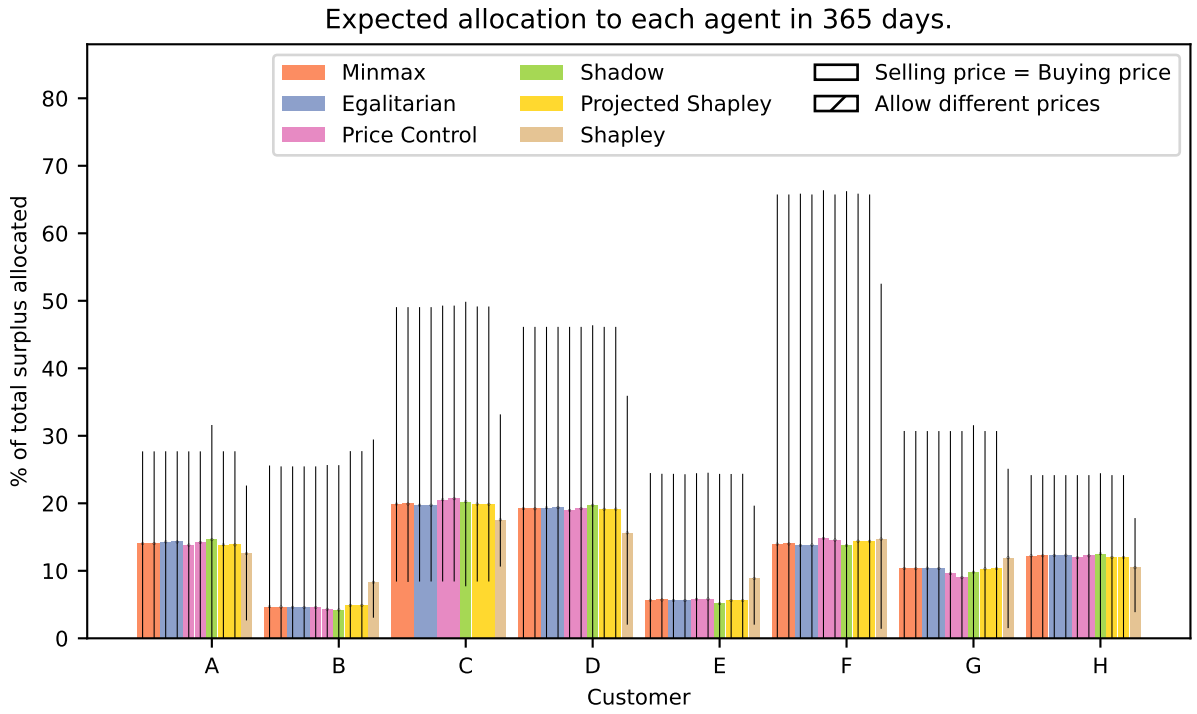

Figure 3.C.3: Proportion of savings allocated to each participant for the four mechanisms considered, case with $n = 8$ participants. Error bars show the range of allocations obtained during the 365 days. Main bars show the average across the year. Projected Shapley is the uniform price allocation in the core that is closest to the Shapley value in ℓ_1 norm.

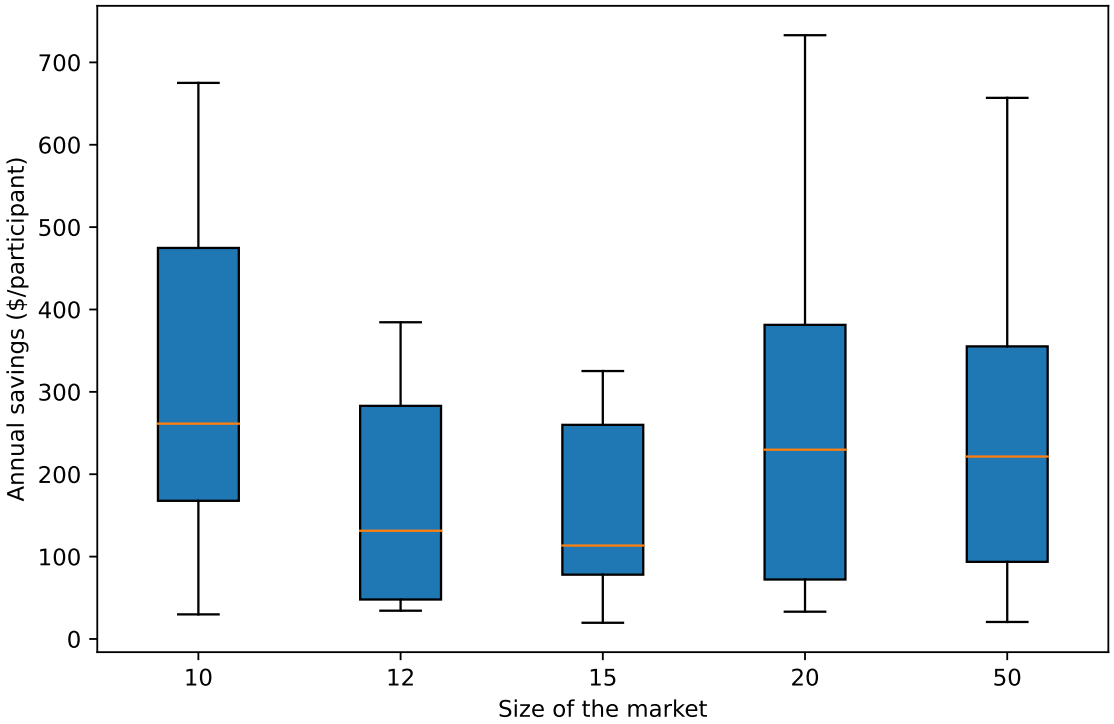

Figure 3.C.4: Boxplot showing the distribution of savings per participant under the shadow price imputation for different market sizes, over the number of participants in each market. The box extends from the first quartile (Q1) to the third quartile (Q3) of the data, with a line at the median. Whiskers cover the whole range of data.

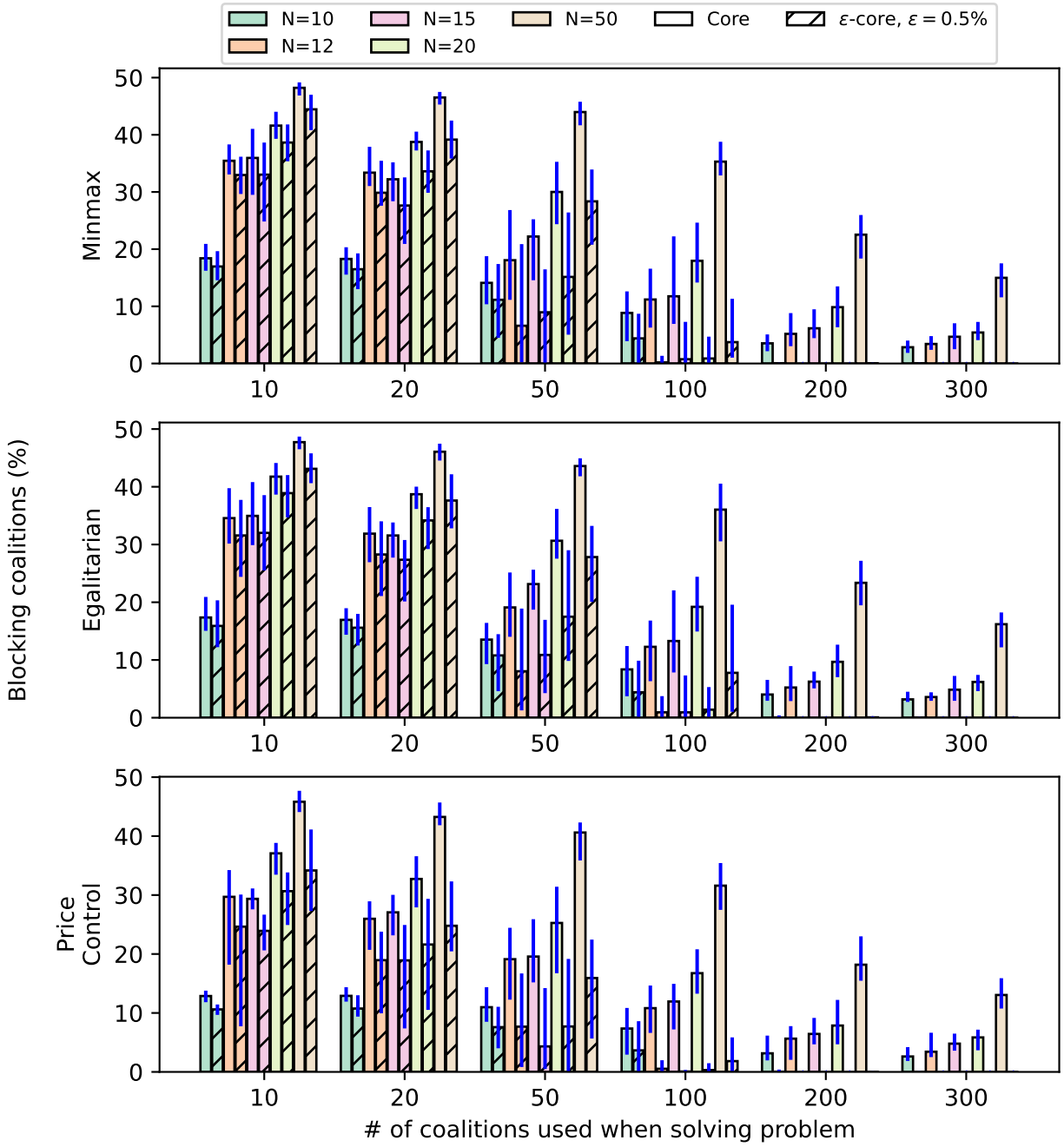

Figure 3.C.5: Blocking coalitions found for obtained allocations, for different market and sample sizes, for all mechanisms. Error bars show the range of results obtained over 10 repetitions. Main bars show the average. The proportion of coalitions found to be blocking by at least a proportion ε of the collective bill, for $\varepsilon = 0$ and $\varepsilon = 0.005$ are shown.

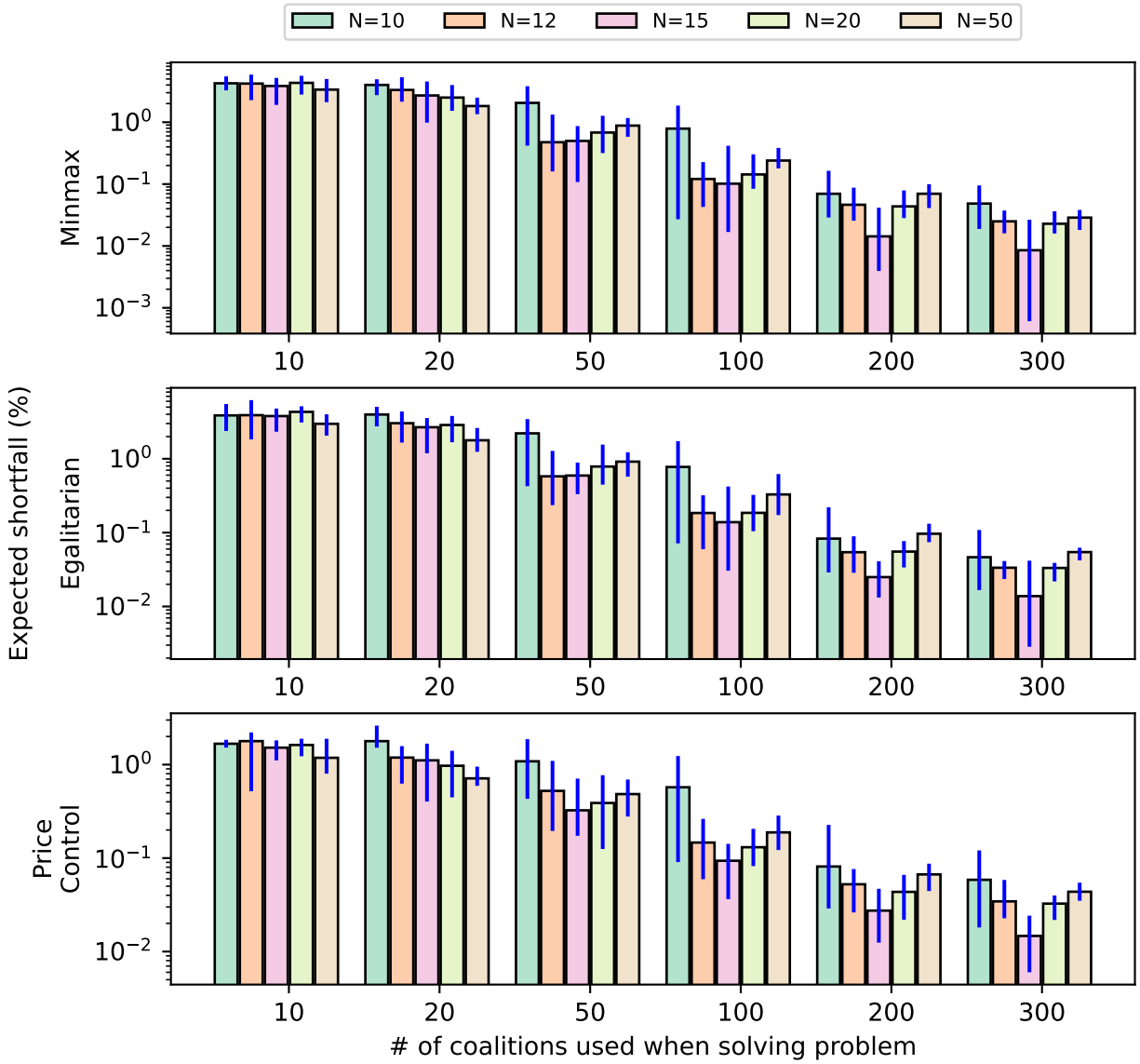

Figure 3.C.6: Expected shortfall for blocking coalitions, for different market and sample sizes, for all mechanisms. Expected conditional shortfall[a] expressed as a proportion of collective bill in log scale. Main bars represent the average over 10 repetitions. Error bars show the whole range of results obtained.

[a] Let Λ be the collection of blocking coalitions, i.e. $\Lambda = \{S \subseteq N : \sum_{i \in S} b_i > C(S)\}$, then the conditional expected shortfall shown is $(1/|\Lambda|) \sum_{S \in \Lambda} \left(\sum_{i \in S} b_i - C(S)\right) / \left(\sum_{i \in S} b_i\right)$

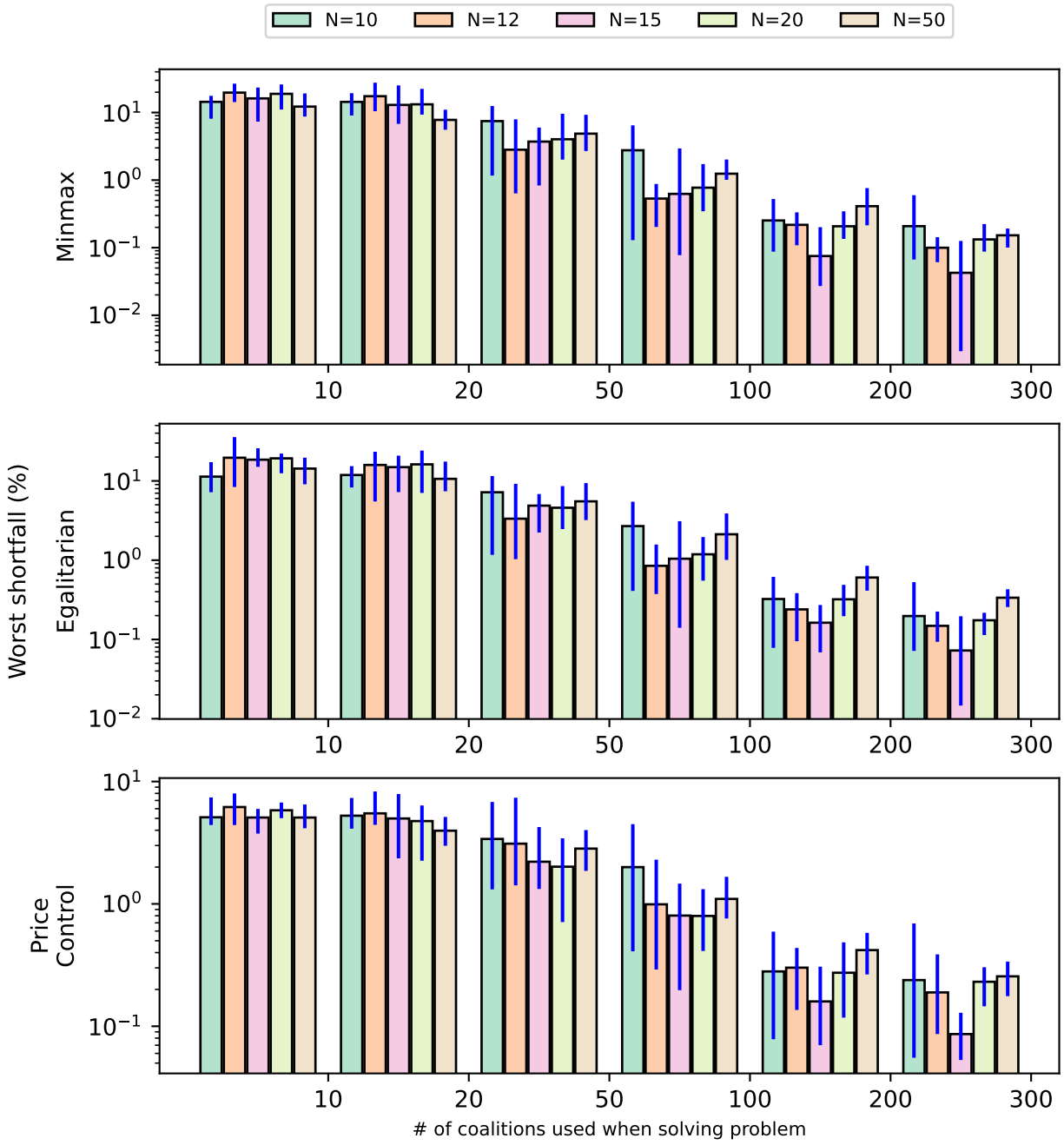

Figure 3.C.7: Worst shortfall for blocking coalitions, for different market and sample sizes, for all mechanisms. Shortfall expressed as a proportion of collective bill in log scale. Error bars show the range of allocations obtained during the 365 days. Main bars show the average across the year.

References

[1] T. Valencia Zuluaga and S. S. Oren, "Data-Driven Sizing of Co-Located Storage for Uncertain Renewable Energy," *Policy and Regulation IEEE Transactions on Energy Markets*, vol. 1, no. 4, pp. 348–359, Dec. 2023, conference Name: Policy and Regulation IEEE Transactions on Energy Markets. [Online]. Available: https://ieeexplore.ieee.org/abstract/document/10129826?casa_token=M6MrYXkTDkoAAAAA:aCPo6T-tANnuaM6PIYWMUZl_gKcEnr82TfrK3egy02dNUaEgu7c5jq18OrnSNsYTZxhi7NR7LA

[2] ——, "Cost Sharing Mechanism with Statistical Learning for Peer-to-Peer Energy Trading," in *2023 IEEE Power & Energy Society General Meeting (PESGM)*, Jul. 2023, pp. 1–5, iSSN: 1944-9933. [Online]. Available: https://ieeexplore.ieee.org/abstract/document/10253145

[3] ——, "Sizing Co-located Storage for Uncertain Renewable Energy Sold Through Forward Contracts," in *Proceedings of the 11th Bulk Power Systems Dynamics and Control Symposium (IREP 2022)*, Banff, Canada, 2022. [Online]. Available: https://arxiv.org/abs/2207.12619

[4] T. Valencia Zuluaga, "Optimization of electricity systems under uncertainty," Ph.D. dissertation, UC Berkeley, 2024.

[5] H. E. Kankaya and N. Akar, "Solving Multi-Regime Feedback Fluid Queues," *Stochastic Models*, vol. 24, no. 3, pp. 425–450, Aug. 2008, publisher: Taylor & Francis.

[6] J. H. Kim and W. B. Powell, "Optimal Energy Commitments with Storage and Intermittent Supply," *Operations Research*, vol. 59, no. 6, pp. 1347–1360, Dec. 2011, publisher: INFORMS.

[7] E. Y. Bitar, R. Rajagopal, P. P. Khargonekar, K. Poolla, and P. Varaiya, "Bringing Wind Energy to Market," *IEEE Transactions on Power Systems*, vol. 27, no. 3, pp. 1225–1235, Aug. 2012.

[8] C. J. Dent, J. W. Bialek, and B. F. Hobbs, "Opportunity Cost Bidding by Wind Generators in Forward Markets: Analytical Results," *IEEE Transactions on Power Systems*, vol. 26, no. 3, pp. 1600–1608, Aug. 2011.

[9] P. Harsha and M. Dahleh, "Optimal Management and Sizing of Energy Storage Under Dynamic Pricing for the Efficient Integration of Renewable Energy," *IEEE Transactions on Power Systems*, vol. 30, no. 3, pp. 1164–1181, May 2015.

[10] Y. Ru, J. Kleissl, and S. Martinez, "Storage Size Determination for Grid-Connected Photovoltaic Systems," *IEEE Transactions on Sustainable Energy*, vol. 4, no. 1, pp. 68–81, Jan. 2013.

[11] A. Loukatou, P. Johnson, S. Howell, and P. Duck, "Optimal valuation of wind energy projects co-located with battery storage," *Applied Energy*, vol. 283, p. 116247, Feb. 2021.

[12] D. Mitra, "Stochastic Theory of a Fluid Model of Producers and Consumers Coupled by a Buffer," *Advances in Applied Probability*, vol. 20, no. 3, pp. 646–676, 1988, publisher: Applied Probability Trust.

[13] D. Gaver and R. Miller, "Limiting distributions for some storage problems," in *Studies in applied probability and management science*, K. Arrow, S. Karlin, and H. Scarf, Eds. Stanford University Press, 1962, pp. 110–126.
[14] S. S. Oren and S. H. Wan, "Optimal Strategic Petroleum Reserve Policies: A Steady State Analysis," *Management Science*, vol. 32, no. 1, pp. 14–29, Jan. 1986, publisher: INFORMS.
[15] X. Chen, K.-C. Leung, and A. Y. S. Lam, "Power Output Smoothing for Renewable Energy System: Planning, Algorithms, and Analysis," *IEEE Systems Journal*, vol. 14, no. 1, pp. 1034–1045, Mar. 2020.
[16] V. Deulkar, J. Nair, and A. A. Kulkarni, "Sizing Storage for Reliable Renewable Integration," in *2019 IEEE Milan PowerTech*, Jun. 2019, pp. 1–6.
[17] V. Kulkarni, "Fluid Models for Single Buffer Systems," in *Frontiers in Queueing: Models and Applications in Science and Engineering*, J. H. Dshalalow, Ed. CRC Press, Jan. 1997, pp. 321–338.
[18] B. Sericola, "A Finite Buffer Fluid Queue Driven by a Markovian Queue," *Queueing Systems*, vol. 38, no. 2, pp. 213–220, Jun. 2001.
[19] B. Sericola and B. Tuffin, "A fluid queue driven by a Markovian queue," *Queueing Systems*, vol. 31, no. 3, pp. 253–264, Jul. 1999.
[20] N. Akar and K. Sohraby, "Infinite- and finite-buffer Markov fluid queues: a unified analysis," *Journal of Applied Probability*, vol. 41, no. 2, pp. 557–569, Jun. 2004, publisher: Cambridge University Press.
[21] V. V. Lopes, T. Scholz, A. Estanqueiro, and A. Q. Novais, "On the use of Markov chain models for the analysis of wind power time-series," in *2012 11th International Conference on Environment and Electrical Engineering*, May 2012, pp. 770–775.
[22] J. Tang, A. Brouste, and K. L. Tsui, "Some improvements of wind speed Markov chain modeling," *Renewable Energy*, vol. 81, pp. 52–56, Sep. 2015.
[23] K. Xie, Q. Liao, H.-M. Tai, and B. Hu, "Non-Homogeneous Markov Wind Speed Time Series Model Considering Daily and Seasonal Variation Characteristics," *IEEE Transactions on Sustainable Energy*, vol. 8, no. 3, pp. 1281–1290, Jul. 2017.
[24] K. Brokish and J. Kirtley, "Pitfalls of modeling wind power using Markov chains," in *2009 IEEE/PES Power Systems Conference and Exposition*, Mar. 2009, pp. 1–6.
[25] G. Papaefthymiou and B. Klockl, "MCMC for Wind Power Simulation," *IEEE Transactions on Energy Conversion*, vol. 23, no. 1, pp. 234–240, Mar. 2008.
[26] T. Scholz, V. V. Lopes, and A. Estanqueiro, "A cyclic time-dependent Markov process to model daily patterns in wind turbine power production," *Energy*, vol. 67, pp. 557–568, Apr. 2014.
[27] M. Bolinger, J. Seel, C. Warner, and D. Robson, "Utility-Scale Solar, 2021 Edition," Lawrence Berkeley National Laboratory, Technical Report, Oct. 2021. [Online]. Available: https://emp.lbl.gov/sites/default/files/utility_scale_solar_2021_edition_slides.pdf
[28] NREL, "Wind generation profile in 2012," National Renewable Energy Laboratory, Tech. Rep., Mar. 2016. [Online]. Available: https://www.dropbox.com/s/a67gw17wz1clk50/34843-2012.csv?dl=0

[29] K. Mongird, V. Viswanathan, J. Alam, C. Vartanian, V. Sprenkle, and R. Baxter, "2020 Grid Energy Storage Technology Cost and Performance Assessment," Pacific Northwest National Laboratory, Tech. Rep. DOE/PA-0204, Dec. 2020.

[30] D. P. Bertsekas, *Dynamic programming and optimal control*, 4th ed. Belmont, Mass: Athena Scientific, 2012.

[31] I. Penn, "California Panel Backs Solar Mandate for New Buildings," *The New York Times*, Aug. 2021. [Online]. Available: https://www.nytimes.com/2021/08/11/business/energy-environment/california-solar-mandates.html

[32] P. Milgrom and M. Watt, "Linear Pricing Mechanisms for Markets without Convexity," in *Proceedings of the 23rd ACM Conference on Economics and Computation*, ser. EC '22. New York, NY, USA: Association for Computing Machinery, Jul. 2022, p. 300. [Online]. Available: https://dl.acm.org/doi/10.1145/3490486.3538310

[33] T. Capper, A. Gorbatcheva, M. A. Mustafa, M. Bahloul, J. M. Schwidtal, R. Chitchyan, M. Andoni, V. Robu, M. Montakhabi, I. J. Scott, C. Francis, T. Mbavarira, J. M. Espana, and L. Kiesling, "Peer-to-peer, community self-consumption, and transactive energy: A systematic literature review of local energy market models," *Renewable and Sustainable Energy Reviews*, vol. 162, p. 112403, Jul. 2022. [Online]. Available: https://www.sciencedirect.com/science/article/pii/S1364032122003112

[34] S. Malik, M. Duffy, S. Thakur, B. Hayes, and J. Breslin, "A priority-based approach for peer-to-peer energy trading using cooperative game theory in local energy community," *International Journal of Electrical Power & Energy Systems*, vol. 137, p. 107865, May 2022. [Online]. Available: https://www.sciencedirect.com/science/article/pii/S0142061521010796

[35] L. Han, T. Morstyn, and M. McCulloch, "Incentivizing Prosumer Coalitions With Energy Management Using Cooperative Game Theory," *IEEE Transactions on Power Systems*, vol. 34, no. 1, pp. 303–313, Jan. 2019, conference Name: IEEE Transactions on Power Systems.

[36] J. Li, Y. Ye, D. Papadaskalopoulos, and G. Strbac, "Computationally Efficient Pricing and Benefit Distribution Mechanisms for Incentivizing Stable Peer-to-Peer Energy Trading," *IEEE Internet of Things Journal*, vol. 8, no. 2, pp. 734–749, Jan. 2021, conference Name: IEEE Internet of Things Journal.

[37] X. Chen and J. Zhang, "A Stochastic Programming Duality Approach to Inventory Centralization Games," *Operations Research*, vol. 57, no. 4, pp. 840–851, Aug. 2009, publisher: INFORMS. [Online]. Available: https://pubsonline.informs.org/doi/10.1287/opre.1090.0699

[38] G. Owen, "On the core of linear production games," *Mathematical Programming*, vol. 9, no. 1, pp. 358–370, Dec. 1975. [Online]. Available: https://doi.org/10.1007/BF01681356

[39] H. Moulin, *Fair division and collective welfare / Hervé Moulin.* Cambridge, Mass: MIT Press, 2003, publication Title: Fair division and collective welfare.

[40] F. Perea, J. Puerto, and F. R. Fernández, "Avoiding unfairness of *Owen* allocations in linear production processes," *European Journal of Operational Research*, vol. 220, no. 1, pp. 125–131, Jul. 2012. [Online]. Available: https://www.sciencedirect.com/science/article/pii/S0377221712000331

[41] W. Tushar, T. K. Saha, C. Yuen, P. Liddell, R. Bean, and H. V. Poor, "Peer-to-Peer Energy Trading With Sustainable User Participation: A Game Theoretic Approach," *IEEE Access*, vol. 6, pp. 62 932–62 943, 2018, conference Name: IEEE Access. [Online]. Available: https://ieeexplore.ieee.org/document/8490655

[42] A. Mas-Colell, M. D. Whinston, and J. R. Green, "Social Welfare Functions and Social Optima," in *Microeconomic theory*. New York: Oxford University Press, 1995, pp. 825–831, section: 22.C.

[43] B. Dutta and D. Ray, "A Concept of Egalitarianism Under Participation Constraints," *Econometrica*, vol. 57, no. 3, pp. 615–635, 1989, publisher: [Wiley, Econometric Society]. [Online]. Available: https://www.jstor.org/stable/1911055

[44] E. Balkanski, U. Syed, and S. Vassilvitskii, "Statistical Cost Sharing," *arXiv:1703.03111 [cs]*, Mar. 2017, arXiv: 1703.03111. [Online]. Available: http://arxiv.org/abs/1703.03111

[45] E. Wilson, A. Parker, A. Fontanini, E. Present, J. Reyna, R. Adhikari, C. Bianchi, C. CaraDonna, M. Dahlhausen, J. Kim, A. LeBar, L. Liu, M. Praprost, L. Zhang, P. DeWitt, N. Merket, A. Speake, T. Hong, H. Li, N. Mims Frick, Z. Wang, A. Blair, H. Horsey, D. Roberts, K. Trenbath, O. Adekanye, E. Bonnema, R. El Kontar, J. Gonzalez, S. Horowitz, D. Jones, R. Muehleisen, S. Platthotam, M. Reynolds, J. Robertson, K. Sayers, and Q. Li, "End-Use Load Profiles for the U.S. Building Stock: Methodology and Results of Model Calibration, Validation, and Uncertainty Quantification," NREL, Tech. Rep. NREL/TP-5500-80889, 1854582, MainId:78667, Mar. 2022. [Online]. Available: https://www.osti.gov/servlets/purl/1854582/

[46] C. P. U. Commission, "CPUC Modernizes Multi-Tenant and Multi-Property Solar and Storage Tariffs and Strengthens Solar Consumer Protections," Nov. 2023, docket number: R.20-08-020. [Online]. Available: https://www.cpuc.ca.gov/news-and-updates/all-news/cpuc-modernizes-multi-tenant-and-multi-property-solar-and-storage-tariffs-2023

[47] K. Misbrener, "CPUC undermines the economic value of California schools, apartments going solar," Nov. 2023. [Online]. Available: https://www.solarpowerworldonline.com/2023/11/cpuc-undermines-economic-value-california-schools-apartment-solar/

[48] S. Borenstein, M. Fowlie, and J. Sallee, "Designing Electricity Rates for An Equitable Energy Transition," Next 10 & Energy Institute at Haas, Tech. Rep., Feb. 2021. [Online]. Available: https://www.next10.org/publications/electricity-rates

[49] S. M. Barrager and E. G. Cazalet, *Transactive energy: a sustainable business and regulatory model for electricity*. Reston: Public Utilities Reports, Inc, 2016.

[50] J. R. Birge and F. Louveaux, *Introduction to Stochastic Programming*. Springer Science & Business Media, Jun. 2011, google-Books-ID: Vp0Bp8kjPxUC.

[51] N. A. Uhan, "Stochastic linear programming games with concave preferences," *European Journal of Operational Research*, vol. 243, no. 2, pp. 637–646, Jun. 2015. [Online]. Available: https://www.sciencedirect.com/science/article/pii/S0377221714010261